



CIVIL ENGINEERING STUDIES  
Illinois Center for Transportation Series No. 09-052  
UILU-ENG-2009-2033  
ISSN: 0197-9191

# **MECHANISTIC-EMPIRICAL DESIGN CONCEPTS FOR JOINTED PLAIN CONCRETE PAVEMENTS IN ILLINOIS**

Prepared By  
**Amanda Bordelon**  
**Jeffery Roesler**  
University of Illinois at Urbana-Champaign

**Jacob Hiller**  
Michigan Technological University

Research Report ICT-09-052

A report of the findings of  
**ICT-R57**  
**Evaluation and Implementation of Improved CRCP And JPCP Design**  
Illinois Center for Transportation

July 2009

1. Report No. FHWA-ICT-09-052		2. Government Accession No.		3. Recipient's Catalog No.	
4. Title and Subtitle  Mechanistic-Empirical Design Concepts for Jointed Plain Concrete Pavements in Illinois				5. Report Date July 2009	
				6. Performing Organization Code	
				8. Performing Organization Report No. ICT-09-052 UILU-ENG-2009-2033	
7. Author(s) A. Bordelon, J. Roesler, and J. Hiller				9. Performing Organization Name and Address Illinois Center for Transportation University of Illinois at Urbana Champaign 205 North Mathews Ave. – MC 250 Urbana, Illinois 61801	
12. Sponsoring Agency Name and Address Illinois Department of Transportation Bureau of Materials and Physical Research 126 East Ash Street Springfield, Illinois 62704				10. Work Unit ( TRAIS)	
				11. Contract or Grant No. ICT-R57	
				13. Type of Report and Period Covered	
15. Supplementary Notes				14. Sponsoring Agency Code	
16. Abstract  The Illinois Department of Transportation (IDOT) currently has an existing jointed plain concrete pavement (JPCP) design method based on mechanistic-empirical (M-E) principles. The objective of this research was to provide IDOT with an improved design process for JPCP based on new research findings over the past 15 years. Existing JPCP methods such as the Mechanistic Empirical Pavement Design Guide (MEPDG) were reviewed. Two conclusions from the review of current design methods were that a geographic specific temperature and site specific load spectra analysis were not necessary at this time to produce reasonable concrete thicknesses. A single climate zone and the ESAL concept to represent mixed truck traffic are therefore still recommended for the state of Illinois based on current rigid pavement design technology. A new mechanistic-empirical design process was proposed based on the principles of the current IDOT method. This new design process was implemented into a spreadsheet program to allow for rapid plotting of design charts and also to enable pavement engineers to readily conduct special design studies that may be warranted when certain inputs fall outside the recommended values used to plot the new design charts. The new design inputs are pavement layer and slab geometry, material layer properties, concrete strength, ESALs, slab-base interface bond condition, temperature curling analysis type, shoulder type, and a reliability-based fatigue algorithm derived from laboratory beam tests. Due to the limited JPCP performance data, the recommended design process did not use a field calibrated damage-to-cracking model but was verified against the existing JPCP method.					
17. Key Words Pavement, design, jointed plain concrete pavement, JPCP			18. Distribution Statement No restrictions. This document is available to the public through the National Technical Information Service, Springfield, Virginia 22161.		
19. Security Classif. (of this report) Unclassified		20. Security Classif. (of this page) Unclassified		21. No. of Pages 255	
				22. Price	

## **ACKNOWLEDGMENT**

This publication is based on the results of ICT-R57 **Evaluation and Implementation of Improved CRCP and JPCP Design Methods for Illinois**. ICT-R57 was conducted in cooperation with the Illinois Center for Transportation; the Illinois Department of Transportation, Division of Highways; and the U.S. Department of Transportation, Federal Highway Administration. The authors would also like to acknowledge the contributions of University of Illinois graduate students, Mr. Matthew Beyer and Mr. Victor Cervantes along with Mr. Dong Wang for his assistance in the preliminary evaluation of the MEPDG software in Appendix B.

Members of the Technical Review Panel are:

Amy Schutzbach, IDOT (TRP chair)  
David Lippert, IDOT  
Paul Niedernhofer, IDOT  
LaDonna Rowden, IDOT  
Hal Wakefield, FHWA  
Charles Wienrank, IDOT  
Mark Gawedzinski, IDOT

## **DISCLAIMER**

The contents of this report reflect the views of the authors, who are responsible for the facts and the accuracy of the data presented herein. The contents do not necessarily reflect the official views or policies of the Illinois Center for Transportation, the Illinois Department of Transportation, or the Federal Highway Administration. This report does not constitute a standard, specification, or regulation.

## EXECUTIVE SUMMARY

The Illinois Department of Transportation (IDOT) currently has an existing jointed plain concrete pavement (JPCP) design method based on mechanistic-empirical (M-E) principles. The objective of this research was to provide IDOT with an improved design process for JPCP based on new research findings over the past 15 years. Existing JPCP methods such as the Mechanistic Empirical Pavement Design Guide (MEPDG) were reviewed. Two conclusions from the review of current design methods were that a geographic-specific temperature and site-specific load spectra analysis were not necessary at this time to produce reasonable concrete thicknesses. A single climate zone and the ESAL concept to represent mixed truck traffic are therefore still recommended for the state of Illinois based on current rigid pavement design technology. A new mechanistic-empirical design process was proposed based on the principles of the current IDOT method. This new design process was implemented into a spreadsheet program to allow for rapid plotting of design charts, and also to enable pavement engineers to readily conduct special design studies that may be warranted when certain inputs fall outside the recommended values used to plot the new design charts. The new design inputs are pavement layer and slab geometry, material layer properties, concrete strength, ESALs, slab–base interface bond condition, temperature curling analysis type, shoulder type, and a reliability-based fatigue algorithm derived from laboratory beam tests. Due to the limited JPCP performance data, the recommended design process did not use a field-calibrated damage-to-cracking model, but was verified against the existing JPCP method.



# CONTENTS

<b>Acknowledgment.....</b>	<b>i</b>
<b>Disclaimer .....</b>	<b>i</b>
<b>Executive Summary .....</b>	<b>ii</b>
<b>Chapter 1. Introduction.....</b>	<b>1</b>
1.1 Background .....	1
1.2 Objectives.....	2
<b>Chapter 2. Evaluation of Existing Design Methods for         Application in Illinois .....</b>	<b>3</b>
2.1 IDOT M-E Design Procedure (1991) .....	3
2.2 MEPDG (NCHRP 1-37A).....	3
2.3 Rigid Pavement Analysis for Design Program.....	5
2.4 Summary of Design Guide evaluation .....	8
<b>Chapter 3. Design Equations.....</b>	<b>9</b>
3.1 Inputs.....	11
3.2 Tensile Stress Calculations .....	15
3.3 Fatigue Calculations .....	29
3.4 Fatigue Damage Calculations .....	30
3.5 Reliability .....	33
3.6 Thickness Design .....	36
<b>Chapter 4. JPCP Design Sensitivity.....</b>	<b>37</b>
4.1 Design Charts.....	37
4.2 Sensitivities.....	40
<b>Chapter 5. Conclusions and Recommendations.....</b>	<b>47</b>
5.1 Future work Advancements .....	48
<b>References .....</b>	<b>49</b>
<b>Appendix A. Review of IDOT’s Existing JPCP Design Method</b>	<b>A-1</b>
A.1 Objective .....	A-1
A.2 Background .....	A-1
A.3 Inputs .....	A-2
<b>Appendix B. JPCP and CRCP Design Comparisons Using         MEPDG and IDOT Design Methods .....</b>	<b>B-1</b>
B1. Introduction .....	B-1
B2. JPCP Design.....	B-1
B3. CRCP Design.....	B-16
B4. JPCP Versus CRCP.....	B-23
B5. Design Guide Summary .....	B-25
<b>Appendix C. Characterization of Traffic for JPCP Design: Load         Spectra Analysis Versus ESAL.....</b>	<b>C-1</b>
C1. Objective .....	C-1
C2. Location Traffic .....	C-1
C3. Input Parameters .....	C-16
C4. Climate.....	C-21
C5. Percentage Slab Cracking .....	C-22

C6. Thickness Design.....	C-23
C7. Summary.....	C-27
<b>Appendix D. Built-In Curling in Jointed Plain Concrete</b>	
<b>Pavements .....</b>	<b>D-1</b>
D1. Introduction .....	D-1
D2. Stress Analysis .....	D-3
D3. Case studies .....	D-7
D4. Summary.....	D-10
<b>Appendix E. Development of a Mechanistic-Empirical Fatigue</b>	
<b>Analysis Procedure.....</b>	<b>E-1</b>
E1. Introduction.....	E-1
E2. Results using the RadiCAL Software .....	E-Error! Bookmark not defined.12
E3. Critical Damage Locations .....	E-17
E4. Design Parameters Resulting in Alternative Fatigue Failure Modes .....	E-18
E5. Conclusions of Initial Mechanistic-Empirical Damage Study.....	E-24
<b>Appendix F. Non-Linear Temperature Effects on Concrete</b>	
<b>Pavement Slab Response.....</b>	<b>F-1</b>
F1. Introduction.....	F-1
F2. Quadratic Temperature Profile Method .....	F-3
F3. NOLA Concept .....	F-8
F4. Piecewise Non-Linear Temperature Profile Stress Calculation.....	F-15
F5. Comparison of Quadratic to Piecewise Non-Linear Temperature Stresses.....	F-18
F6. Comparison of True NOLA to Piecewise Non-Linear Temperature Stresses ..	F-23
F7. Effect of Non-Linear Temperature Stresses on Fatigue Damage .....	F-27
F8. Summary on Non-Linear Temperature.....	F-33
<b>Appendix G. Design Verification of In-Service Jointed Plain</b>	
<b>Concrete Pavements.....</b>	<b>G-1</b>
G1. Introduction.....	G-1
G2. RPPR Sections.....	G-1
G3. UCPRC Sections.....	G-7
G4. Conclusions on Design Verification of In-Service California JPCP Sites .....	G-33
<b>Appendix H. Comparison of Jointed Plain Concrete Pavement</b>	
<b>Design Prediction Methods .....</b>	<b>H-1</b>
H1. Introduction.....	H-1
H2. Conclusions On Design Methodology Comparison.....	H-25
<b>Appendix I. Ramp Reinforcement for Jointed Plain Concrete</b>	
<b>Pavements .....</b>	<b>I-1</b>
I1. Introduction.....	I-1
I2. Analysis of Minimum Steel Required.....	I-1
I3. Summary .....	I-4

# CHAPTER 1. INTRODUCTION

## 1.1 BACKGROUND

Many pavement design procedures that were developed in the past used an empirical approach to pavement design based on observations of pavement sections and their respective features affecting the performance. Over the years, many researchers have employed mechanistic variables in design such as stress, strain, or deflection to supplement empirically observed behavior of a concrete pavement. Mechanistic-empirical design of concrete pavements can be dated as far back as 1922, when the results of the Bates Road experiment were used to relate the corner stress due to a wheel load to the concrete thickness (Older, 1924). Stress computations based on medium-thick plate theory were employed by Westergaard (1927, 1948) starting in the 1920s and have subsequently been used in mechanistic-empirical rigid pavement design procedures through the years. Pickett and Ray (1951) expanded on Westergaard's prediction methods by developing charts that incorporated multiple wheel loads. Technological breakthroughs in computers allowed finite element analysis (FEA) to become the preferred method of rigid pavement stress prediction starting in the late 1970s (Huang and Wang, 1973; Tabatabaie, 1977; Tabatabaie and Barenberg, 1978) and is currently the state-of-the-art.

The first wide-spread mechanistic-empirical analysis for highway design was employed in the zero-maintenance design concept by Darter (1977). This thickness method incorporated a stress ratio approach for fatigue with the inclusion of mechanical load and environmental stresses such as temperature and moisture gradients. The Portland Cement Association (PCA, 1984) also developed a widely used method that incorporated a tensile bending stress from FEA into a thickness design procedure, while also accounting for erodibility of the underlying layers (Packard and Tayabji, 1985). The PCA method did not incorporate the effects of temperature or moisture stresses. Two national research studies, NCHRP 1-26 (Thompson and Barenberg, 1992) and NCHRP 1-30 (Darter et al., 1995), provided improved methods for incorporating curling analyses into a mechanistic-empirical design procedure for concrete pavements.

IDOT was among the first state highway agencies to adopt a mechanistic-empirical design method for concrete pavements based on research completed at the University of Illinois (Zollinger and Barenberg, 1989a, 1989b). Recently, a mechanistic-empirical method for rigid pavement design has been developed under NCHRP 1-37A (ARA, 2007), also called the Mechanistic-Empirical Pavement Design Guide (MEPDG). This method improves on existing methods by incorporating issues such as steer-drive axle spacing, non-linear temperature effects, bottom-up and top-down transverse cracking prediction, faulting predictions, climatic influences, and nationally calibrated models from field test sites across North America. Most recently, Hiller (2007) developed an analysis program, called RadiCAL, to evaluate alternative cracking locations on rigid pavements, especially for loading near the transverse joint, which were associated with longitudinal and corner cracks observed in Western states.

With the recent release of the MEPDG, many states are evaluating its applicability against their existing design methods. Some features included in the MEPDG software (ARA, 2007) are already considered by IDOT in its design method. However, there are other features which IDOT should evaluate, such as how to deal with load spectra, or account for it based on existing collected traffic data, climatic factors, and effective built-in curling.

## **1.2 OBJECTIVES**

The objectives of this study were to refine the JPCP design method based on new findings from the past 15 years, and to develop and refine a JPCP design process that IDOT can use for routine design which accounts for the major factors that affect the performance of jointed plain concrete pavements. The following tasks were completed to meet these objectives:

1. Review MEPDG and its applicability to IDOT with specific focus on climate and traffic characterization.
2. Review available fatigue models and strength data to better define the repeated load characteristics of rigid pavements.
3. Characterize the effective built-in curling on Illinois JPCP.
4. Identify potential alternative cracking locations on jointed plain concrete pavements.
5. Propose and implement a JPCP thickness design process in a spreadsheet.
6. Review IDOT's JPCP ramp reinforcement design (see Appendix I).

## CHAPTER 2. EVALUATION OF EXISTING DESIGN METHODS FOR APPLICATION IN ILLINOIS

In order to evaluate the possible improvements to IDOT's current JPCP design procedure, all available mechanistic-empirical (M-E) design guides needed to be evaluated. Since the implementation of the IDOT JPCP M-E design method in 1989, only the MEPDG and the pavement analysis program RadiCAL have been developed.

### 2.1 IDOT M-E DESIGN PROCEDURE (1991)

IDOT currently has a mechanistic-empirical design guide for JPCP based on research developed by Zollinger and Barenberg (1989a, 1989b) at the University of Illinois, who were also actively involved in NCHRP 1-26 calibrated mechanistic pavement design (Thompson and Barenberg, 1992). The design concepts for IDOT were well documented in several reports, but changes in the design inputs and equations during the implementation phase were not as well documented. Appendix A is a review of the design concepts and inputs that were eventually used to define the existing JPCP curves in Chapter 54 of the Illinois Bureau of Design and Environment (BDE) manual (IDOT, 2002). Figure 1 is an example of IDOT's design curves for tied concrete or asphalt shoulders with a fair soil type. There are separate curves for poor and granular subgrade soils.

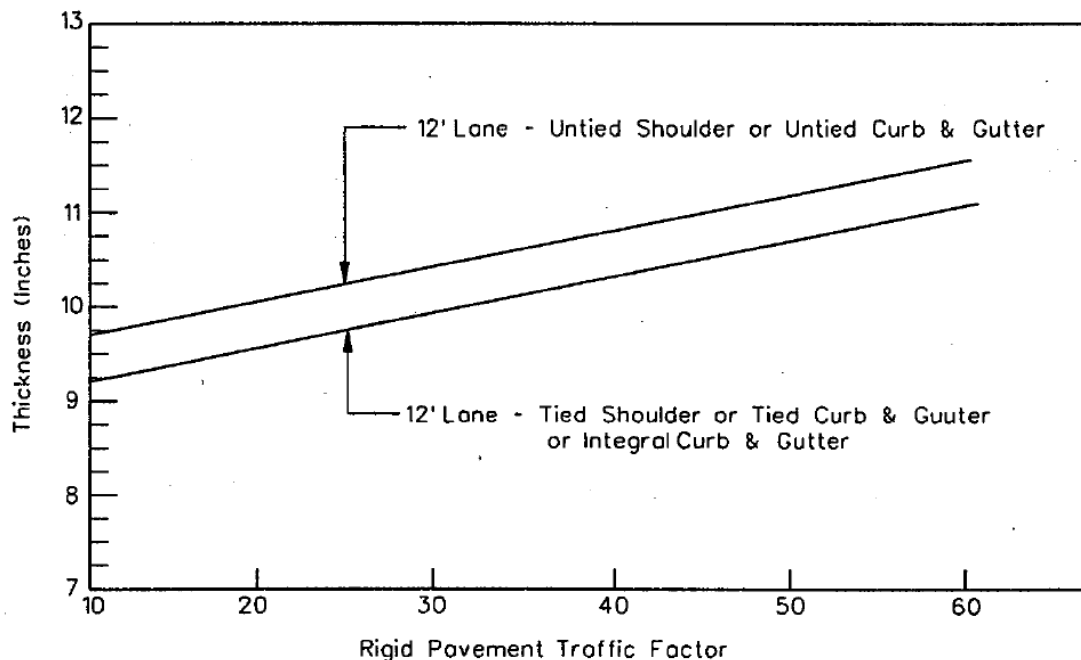


Figure 1. IDOT's design curves for JPCP for fair subgrade soil conditions and Traffic Factor between 10 and 60 (IDOT, 2002).

### 2.2 MEPDG (NCHRP 1-37A)

The MEPDG (ARA, 2007) was developed under NCHRP 1-37A as robust software for the design of new or for the rehabilitation of existing asphalt and concrete pavements. This program uses engineering mechanics to find stresses, strains, and

deflections and uses these outputs to predict performance of the pavement over its design life. Traffic is characterized using a load spectra concept while accounting for steer-drive axle spacings, as well as the individual axle spacing on a tandem, tridem, and quad axle. The MEPDG has the ability to predict environmental (climate) impacts on pavement response and design at virtually any location in the United States. One of the more singular features of the MEPDG is the ability to account for a variety of material inputs and their impact on pavement response to better capture the deterioration of the pavement and improve design predictions. For JPCPs, the MEPDG uses a fatigue equation originally derived from field slab test results of the U.S. Army Corps of Engineers and a nationally calibrated performance equation that relates fatigue damage to observed slab cracking. The MEPDG uses a stress prediction neural network in conjunction with the fatigue transfer function previously mentioned to predict either bottom-up or top-down transverse fatigue cracking near the mid-slab edge. The MEPDG also allows for user-specified failure criteria in terms of both reliability and percentage of slabs cracked.

To evaluate the additional features of the MEPDG software (Version 0.91) over existing M-E guides, a preliminary analysis was completed on several hypothetical JPCP and CRCP sections in Illinois. The MEPDG results were compared with IDOT's current design procedure for JPCP and CRCP. The design inputs were shoulder type (AC shoulder, tied shoulder, and widened lane), climate zone (the Chicago, Champaign, and Carbondale areas), and traffic level (2, 10, 60, and 230 million equivalent single-axle loads [ESALs] or an equivalent load spectra). A summary of the inputs and preliminary analysis of the MEPDG software (Version 0.91) for JPCP and CRCP can be found in Appendix B.

For JPCP, the biggest difference between the MEPDG and the IDOT method was that the fatigue failure mode predicted was primarily top-down cracking for the MEPDG versus bottom-up cracking for the IDOT method. The MEPDG showed a significant slab thickness difference between JPCP designed near Lake Michigan and other locations in Illinois, even Dupage County. This 1- to 2.5-in. difference between Midway Airport and Dupage Airport climate was deemed an anomaly, which may be theoretically correct, but the MEPDG appears to be overly sensitive to this particular type of local temperature changes. Overall, there was not a significant climatic effect on JPCP design for a given set of concrete material properties in Illinois based on Version 0.91 of the MEPDG. For both IDOT and MEPDG methods, the shoulder type affected the concrete slab thickness. The IDOT method produced greater slab thicknesses for tied shoulder relative to the MEPDG, but thinner thicknesses for widened lanes. The concrete thickness requirement for tied shoulders or widened lanes was similar for the MEPDG.

The IDOT design gave thinner CRCP slabs for 2 million ESALs relative to the MEPDG, but the IDOT method gave thicker slabs for traffic levels greater than 2 million. No climatic effect was observed for CRCP thickness designs using the MEPDG. The rule of thumb that CRCP thickness is 80 to 90% of JPCP thickness was not consistent across traffic levels and shoulder types for both the IDOT and MEPDG methods. The use of load spectra in MEPDG (Version 0.91) for either CRCP or JPCP did not appear to provide significant advantages over the ESALs-based IDOT method for the inputs evaluated.

Several of the main features of the MEPDG are the analysis of rigid pavement structures in any climate zone and with any load spectra. To explore these two variables in more detail, additional runs of the MEPDG (Version 1.0) were completed. The main objective of these MEPDG runs was to make a decision as to whether a climate-based design (or designs) based on local traffic spectra were necessary. For example, to

answer such questions as, whether changes in geographical location or load spectra (for a given ESAL count) give a significant enough difference in concrete slab thickness to warrant a design method change for IDOT, Appendix C provides a summary of the Illinois climate zone and load spectra analysis using the MEPDG.

The review of the MEPDG Version 1.0 showed that local temperature effects did alter the required slab thickness for a given traffic distribution; much more than Version 0.91. However, there was not a logical way to account for the climate effects in terms of geographical location in the state going from north to south. Second, for a given magnitude of ESALs and fixed climate location, a variety of load spectra distributions taken from weigh scale or WIM stations in Illinois affected the required concrete slab thickness by less than 0.5 in.

## 2.3 RIGID PAVEMENT ANALYSIS FOR DESIGN PROGRAM

The design of rigid pavements has traditionally focused on mitigating fatigue cracking at the mid-slab longitudinal edge, such as with the MEPDG and IDOT's current method. With the advances in characterizing built-in slab curling and proper modeling of steer-drive axle spacing effect, the location of maximum fatigue damage and subsequent cracking mode cannot easily be ascertained without a detailed analysis. Residual negative gradients due to built-in temperature curling and differential drying shrinkage can cause corner, longitudinal, or transverse cracking in rigid pavements and should be considered for incorporation into mechanistic-empirical rigid design procedures. Using the process of the Equivalent Built-in Temperature Difference (EBITD) backcalculation developed by Rao and Roesler (2005a), the frequency distribution of equivalent temperature gradients tends to shift toward negative values, thus increasing the likelihood of alternative fatigue cracking modes. The EBITD for several JPCP in Illinois were measured and are summarized in Appendix D. It was found that the absolute magnitude of EBITD was on average less than -10 °F for JPCP in Illinois (see Table 1), which was smaller than the default assumption in the MEPDG of -10 °F.

Table 1. Backcalculated EBITD Values for US-20 near Freeport, Illinois.

Section ID	Joint Spacing (feet)	All		Hinge Joints		Doweled Joints		Notes
		Mean (°F)	Standard Deviation (°F)	Mean (°F)	Standard Deviation (°F)	Mean (°F)	Standard Deviation (°F)	
H	15	-4.1	1.1	n/a	n/a	-4.1	1.1	
G4	40	-19.9	9.1	-26.6	9.3	-14.6	4.3	a
G3	13.3	2.0	0.0	n/a	n/a	2.0	0.0	b
F	20	-7.0	4.8	n/a	n/a	-7.0	4.8	
E	15	-6.3	3.3	n/a	n/a	-6.3	3.3	
D	40	-11.2	8.0	-12.9	10.8	-9.4	3.4	a
C	20	-1.2	0.5	n/a	n/a	-1.2	0.5	

<sup>a</sup> Structural transverse crack near mid-slab

<sup>b</sup> JPCP with tie bar at joints and dowels at every third joint

A mechanistic analysis procedure named RadiCAL was developed (Hiller 2007), building off an extensive initial finite element analysis that determined the sensitivity of many of the variables involved in determining both traditional and alternative cracking

mechanisms in jointed plain concrete pavements,. This procedure uses an influence line analysis using an existing finite element program to model an axle or set of axles passing over a slab for a range of input parameters. RadiCAL uses both the maximum and minimum stress levels at nodes along the longitudinal edge and transverse joint, as these axles move statically across the slab. Using statistical distribution of input parameters such as site-specific temperature profiles, shoulder type, joint type, lateral wander, and vehicle characteristics in conjunction with Miner's Hypothesis for fatigue damage accumulation, RadiCAL allows for the prediction of relative damage profiles, as well as absolute damage to assess both the timing and location of potential fatigue cracks. A more detailed description of the development of RadiCAL can be reviewed in Appendix E.

Due to the unrestrained slabs (no dowels or tie bars), short slabs, and arid climate, RadiCAL was initially developed to analyze cracking distress in California JPCP. Significant levels of transverse, longitudinal, and corner cracking have been found throughout the California highway network (Harvey et al., 2000b). Using a linear temperature assumption in RadiCAL, it was found that the use of a stress range fatigue approach (Tepfers, 1979) tended to predict more realistic critical fatigue damage locations noted on many California jointed plain concrete pavements in comparison with the maximum stress fatigue approach using the Zero-Maintenance equation (Darter, 1977).

To supplement the RadiCAL program, a non-linear temperature parameter named NOLA (NON-Linear Area) was developed, which allows for the calculation of self-equilibrating stresses that are not typically accounted for in rigid pavement analyses. The NOLA for a given temperature profile represents the difference in area between a quadratic temperature profile (three temperatures at three depths) and an assumed linear profile (temperature at top and bottom of the slab). This method allows for a simple visualization of the level of non-linearity for a given temperature profile and a simple direct calculation of the self-equilibrating stresses at any depth of interest within the concrete slab. The detailed derivation of the NOLA parameter can be reviewed in Appendix F. Conducting both stress and fatigue damage analyses using RadiCAL, it was found that by using only the linear temperature differences, bottom-up stresses are generally overpredicted and top-down stresses are subsequently underpredicted. This omission can lead to an underprediction of fatigue damage in cases with no to low built-in curl (bottom-up failures) and overprediction of fatigue damage in high built-in curl cases (top-down cracking mechanisms).

Eleven JPCP sections in California were analyzed to attempt to validate RadiCAL's ability to predict fatigue cracking locations. This was conducted using site-specific geometry, load transfer, EBITD, climate, load spectra, and vehicle class distribution using linear and non-linear temperature profiles for stress range (Tepfers, 1979) and the MEPDG fatigue transfer functions (ARA, 2007). When substantial replications of EBITD were available, the stress range approach using linear temperature considerations tended to produce realistic damage profiles in comparison with the observed cracking patterns. When considering non-linear temperature, the MEPDG fatigue algorithm implemented into RadiCAL tended to predict existing transverse and longitudinal cracking fairly well. While a clear picture was not found in terms of the best fatigue transfer function to predict locations of cracking, the results show that the use of several known concrete fatigue functions can be used in conjunction with calibration to design against both traditional and alternative cracking mechanisms for JPCPs. Appendix G summarizes the design verification study of the RadiCAL program with in-service JPCP in California.



In terms of both predicted thickness and critical damage locations, the RadiCAL program was compared with both the Illinois Department of Transportation mechanistic-empirical design method (IDOT, 2002) and Version 1.0 of the MEPDG (ARA, 2007). The level of built-in curl significantly affects the required thickness both in the MEPDG and RadiCAL methods. While both of these methods flipped from bottom-up to top-down transverse cracking as critical at a built-in curl level of -10 °F, a slightly different trend of required thickness was noticed using RadiCAL. In RadiCAL cases without built-in curl, the required thickness was larger than with EBITD of -10 °F. For the cases studied, the MEPDG design method was found to be more sensitive to joint spacing and climate in terms of thickness design in comparison with RadiCAL using the same fatigue, cracking, and reliability functions. When using either a tied PCC shoulder or a widened slab, the MEPDG, IDOT, and RadiCAL methods all predict similar trends and thickness reductions from a standard asphalt shoulder design. These relative thickness reductions were quite similar for the tied PCC and widened slab cases in the majority of cases.

In terms of critical cracking locations, the MEPDG, IDOT, and RadiCAL methods tended to match quite well in asphalt shoulder cases for all fatigue transfer functions available in RadiCAL. When tied shoulders were used, the critical damage locations were generally similar, although RadiCAL predicts a variety of secondary fatigue cracking locations at significant damage levels, producing a high potential for either bottom-up or top-down longitudinal cracking. For widened lane cases, RadiCAL generally predicted that the critical damage location remains at the transverse joint, producing longitudinal cracking emanating along the wheel path. In comparison, both the IDOT and MEPDG methods predict bottom-up transverse cracking to be critical in these cases. The results from RadiCAL suggest that special attention should be paid to widened slab designs using the MEPDG or IDOT methods, as the critical damage location in these methods probably does not protect against these alternative cracking mechanisms. A detailed summary of the design comparisons can be reviewed in Appendix H.

The development of RadiCAL and the subsequent damage location verification study provides several practical recommendations to either increase JPCP fatigue life or reduce the likelihood of alternative cracking mechanisms. A few of the main recommendations are listed below:

- The use of dowels to promote long-term load transfer along transverse joints generally limits the fatigue damage found at the transverse joint for asphalt shoulder cases. However, this is not necessarily the case when a tied PCC shoulder is also used. Due to the reduced stresses found at the mid-slab longitudinal edge location with a tied PCC shoulder, RadiCAL predicts that some probability of longitudinal cracking may ensue from high relative stresses at the transverse joint, even when dowels are used in the design. The probability of occurrence would increase as the joint spacing is decreased.
- The use of joint spacing less than 15 ft generally limits excessive curling stresses with typical JPCP thicknesses that may lead to transverse cracking before the design life is completed. However, shorter joint spacing (12 ft) may lead to an increased probability of longitudinal cracking emanating either at or between the wheel path without the use of dowels. Careful consideration of these factors should be made when considering extremely short joint spacing for standard lane widths.
- From the perspective of differential drying shrinkage and built-in construction curling, limiting the level of EBITD generally leads to transverse cracking fatigue failures that can be rehabilitated with dowel bar retrofitting techniques. This EBITD reduction can be realized through the use of extensive water curing (particularly in arid regions) of

newly-placed PCC slabs or by paving during less extreme conditions (late in the construction season or night construction). The selection of concrete materials in terms of water–cement ratio, cement content, and type will also have an effect on EBITD level. While these techniques will not likely eliminate the EBITD of a given JPCP section, the impact of this factor should be limited to a moderate level.

- The use of widened lanes may delay the onset of fatigue cracking in terms of absolute damage, but analysis using RadiCAL suggests that the cracking mechanism may result in longitudinal cracking in the wheel path. An excessive reduction in thickness from a typical asphalt shoulder case may result in premature fatigue cracking as well. This should be considered when deciding to use this particular lane width option.

## **2.4 SUMMARY OF DESIGN GUIDE EVALUATION**

The MEPDG and IDOT JPCP design methods were reviewed along with a rigid pavement analysis method (RadiCAL) that addresses alternative cracking modes such as longitudinal and corner cracking. The current IDOT method has been serving the state of Illinois adequately for 17 years. IDOT's JPCP method does have some limitations that need to be addressed, such as accommodating higher traffic volumes, variable joint spacing, and an interactive design spreadsheet for special design studies. The MEPDG is an attractive program because of its large number of available inputs and relative ease of operation. Several of the key features addressed in the review of the MEPDG were climate effects and load spectra versus ESALs. Based on the design review documented in Appendix C, there is no geographically rational way to accommodate climate in a design guide for IDOT and there does not seem to be an overwhelming advantage at this time to implement load spectra over ESALs.

RadiCAL, which was originally developed for California conditions with particular interest in transverse joint loading, has less appeal, since Illinois JPCP have shown very few corner and longitudinal breaks and low levels of built-in curling (see Appendix D). Furthermore, IDOT employs favorable slab dimensions (15 ft by 12 ft) with tied concrete shoulders, which reduces the propensity for longitudinal and corner cracking. To fully implement RadiCAL as a design method, additional input parameters would need to be added to make the program more general, which would take significant effort. These efforts would likely not pay off since the advantages of RadiCAL primarily lie in the prediction of alternative cracking locations. Several key findings for IDOT from the RadiCAL program are the thickness restrictions that should be placed on widened lanes which should not be less than tied concrete shoulders with high load transfer (see Appendix H). As long as built-in curling levels remain small, then alternative cracking modes will have a low probability of occurrence. RadiCAL also has shown that inclusion of nonlinear temperature gradients offers benefits in rigid pavement design. However, without the use of an alternative fatigue algorithm such as one proposed by Tepfers (1979; Tepfers and Kutti 1979) and a more realistic cracking model based on fracture mechanics principles, the nonlinear stresses calculated can make the design method overly sensitive to extreme temperature events.

## CHAPTER 3. DESIGN EQUATIONS

Based on the evaluation of existing methods, it was decided not to implement the MEPDG or RadiCAL program for Illinois at this time, but to refine the current IDOT M-E method into a user-friendly spreadsheet format (see Figure 2) that can be used easily by pavement designers, and more important, can be updated more readily in the future. As discussed in Chapter 2, the current IDOT JPCP curves were based on runs of a FORTRAN program developed at the University of Illinois (Zollinger and Barenberg, 1989a, 1989b). This chapter documents the input parameters and design equations implemented into the proposed design spreadsheet. Subsequently, JPCP design charts can then be generated by IDOT personnel for incorporation into Chapter 54 of the BDE Manual (IDOT, 2002).

TRAFFIC			STRESSES									
Design ESALs	Allowable ESALs		Allowed Stress Ratio	Equivalent Damage Ratio	Westergaard Edge Stress	Slab Size Effect	3 Layers Effect	Shoulder Type Effect	Total Edge Stress	Temperature Curling Impact	Temperature Curling Stress	Total Stress
$n$	$N$		SR	EDR	$\sigma_{west}$	$f_1$	$f_2$	$f_3$	$\sigma_e = \sigma_{west} * f_1 * f_2 * f_3$	$R$	$\sigma_{curl}$	$\sigma_{total} = \sigma_{west} * f_1 * f_2 * f_3 + R * \sigma_{curl}$
-	ACPA		-	-	psi	-	-	-	psi	ILLJOINT	psi	psi
9.54E+07	2.36E+13		0.456	0.05	247.26	0.980	0.993	1.000	240.46	1.124	94.22	346.4
						with aeq and l 2P	with aeq and l	with aeq and leff	with aeq and l			
INPUTS					FATIGUE							
Geometry					Allowed Fatigue based on Daytime Stress	Allowed Fatigue based on Zero Gradient	Allowable ESALs	Fatigue Damage Ratio	Percent Cracking (%) - 95% Reliability	% Cracking Failure Criteria		
$h$	Trial Concrete Thickness	10	in.		Zero-Maintenance	3.75E+09	1.07E+12	1.61E+13	0.000	2.2	20	pass
$h_2$	Slab-Base Bonding Condition	Unbonded	layers		ACPA	2.63E+05	1.57E+12	2.36E+13	4.526	20	-	fail
	Initial Thickness of Base Layer	4	in.		MEPDG	1.61E+05	1.35E+08	2.02E+09	7.410	155.2	20	fail
	Shoulder Type	Asphalt Shoulder			Load and Temp stress Load stress only combined day/nighttime							
$L$	Slab Length	15	feet		blue numbers are user inputs							
$L$	Slab Length	180	in.		orange numbers denote value not used							
$D$	Widen Lane Extension	2	feet		black numbers are computed							
$W$	Lane width	12	feet									
Traffic Loads												
	Single Axle Load	18,000	lb									
	Tire Pressure	120	psi									
$P$	Single Tire Load	4500	lb									
$a$	Radius of Applied Load	3.455	in.									
$S$	Spacing Between Dual Tires	12	in.									
$\bar{D}$	Mean Wander Distance from Edge	18	in.									
Material Properties												
$E$	Elastic Modulus of the Concrete	4,600,000	psi									
$\nu$	Poisson's Ratio	0.15	-									
$MOR$	Modulus of Rupture, Flexural Strength at 28 days for 3rd Day Bend Test	759	psi									
$E_2$	Elastic Modulus of the Base Layer	600,000	psi									
$k$	Modulus of Subgrade Reaction (k-value)	100	pci									
$k_s$	Static k-value	100	pci									
$LTE$	Shoulder Load Transfer Efficiency	70.0	%									
$AGG$	Shoulder Aggregate Interlock Factor	1.50E+04	psi		78.07%, 100 ksi							
$AGG/k_l$	Non-dimensional Shoulder Stiffness	3.36										
Climate Factors												
$CTE$	Coefficient of Thermal Expansion	5.5E-06	in./in./°F									
	Temperature Determination Method	Effective Temperature Gradient										
	Slab Positive Temperature Gradient	1.65	°F/in.		Current IDOT procedure has 1.65 °F/in. for 25% for daytime positive gradient							
	Percent Time for Temperature Gradient	25%										
$\gamma$	Unit weight of concrete	0.087	pci									
$DG$	dimensionless parameter of the relative defl	4.383	-									
$DP$	dimensionless parameter of the deflection	22.950	-									
$\Delta T$	Temperature Differential	16.5	°F									
$DT$	Temperature	9.08	-									
Reliability for ACPA												
$R'$	Reliability	95%										
$P_{cr}$	Percent Cracking	20%			Salsilli damage equation assumes 50% cracking							
$R^*$	Effective Reliability	98%										

Figure 2. Screenshot of the design spreadsheet for the proposed JPCP design.

### 3.1 INPUTS

Table 2 lists all of the input parameters required in the design of JPCP, along with a range of typical values and their respective units. Further details about these geometric, traffic, material, and climatic inputs are described in the following sections.

Table 2. Input Parameters for JPCP

Description	Symbol	Unit	Typical Value or Selections
Design equivalent single-axle loads	<i>ESALs</i>	-	up to 60 million (from IDOT, 2002)
Concrete fatigue algorithm	-	-	Zero-Maintenance (Darter, 1977), ACPA (Riley et al., 2005) or MEPDG (ARA, 2007)
Concrete thickness	<i>h</i>	in.	6 to 14 ( $L/l > 3$ )
Slab-base bonding condition	-		Bonded or unbonded
Thickness of base layer	<i>h<sub>2</sub></i>	in.	0 to 24
Shoulder type	-	-	Asphalt, tied or widened lane
Widened lane extension	<i>D</i>	ft.	1 to 2
Slab length	<i>L</i>	ft.	10 to 20 ( $L/l > 3$ )
Spacing between dual tires	<i>S</i>	in.	12 to 16
Offset distance between outer face of tire and slab edge (mean wander distance from edge)	$\bar{D}$	in.	0, 12, or 18
Concrete elastic modulus	<i>E</i>	psi	3,000,000 to 5,000,000
Modulus of rupture – mean flexural strength from 3 <sup>rd</sup> -point bending at 90 days	<i>MOR</i>	psi	650 to 850
Elastic modulus of the base layer (if applicable)	<i>E<sub>2</sub></i>	psi	100,000 to 800,000
Modulus of subgrade reaction	<i>k</i>	pci	50 to 200
Shoulder load transfer efficiency (used with tied shoulders)	<i>LTE</i>	%	40 to 90
Coefficient of thermal expansion	$\alpha$	in./in./°F	3.9 E-6 to 7.3 E-6
Temperature determination method	-	-	Temperature distribution or effective temperature gradient
Temperature stress superposition factor	<i>R</i>	-	ILLICON (Barenberg, 1994), Lee and Darter (1994), Salsilli (1991), or ILLIJOINT
Slab positive temperature gradient (used with effective temperature gradient)	$\Delta T/h$	°F/in.	+1 to +2 (IDOT currently suggests +1.65)
Percent time for temperature gradient (used with effective temperature gradient)	-	%	25 to 60 (IDOT currently suggests 25 for daytime)
Reliability (for ACPA method)	<i>R'</i>	%	80 to 99
Percent cracking (for ACPA method)	<i>P<sub>cr</sub></i>	%	20 to 50

### 3.1.1 Pavement Layer Geometry Inputs

A trial concrete thickness is required in the determination of JPCP design. For the final or desired concrete thickness, the initial thickness selection and design inputs can be altered until the desired fatigue damage, cracking level, or stress levels are achieved. In terms of the overall pavement structure, the program requires information about thickness ( $h_2$ ) and modulus ( $E_2$ ) of the base layer and the interface condition with the concrete slab (bonded or unbonded), as well as the modulus of subgrade reaction or  $k$ -value. The geometric dimensions of the slab are also required inputs: slab length  $L$  and lane (or paving slab) width  $W$ . Currently,  $W$  is set at the standard 12 ft, with the exception of a widened lane where  $W$  is extended by a distance  $D$  (measured in feet).

The three shoulder type choices available are:

- an asphalt shoulder (assumes no load transfer along the longitudinal edge);
- a tied concrete shoulder (assumes that a 10-ft concrete shoulder is placed along the pavement and that the load transfer efficiency [LTE]—for example, 40% for tied separated concrete shoulder or 70% for a tied monolithic shoulder—must be input by the user); or
- a widened lane with an extra width of  $D$ .

The aggregate interlock factor or joint stiffness (AGG) across the tied concrete shoulder can be estimated based on a deflection load transfer efficiency (LTE) value measured by a falling weight deflectometer test. Ioannides and Korovesis (1990) proposed the correlation between the LTE and a non-dimensional stiffness  $AGG / (k * l)$  shown in Figure 3. An equation to compute this non-dimensional stiffness is later described in Section 3.2.2.3.

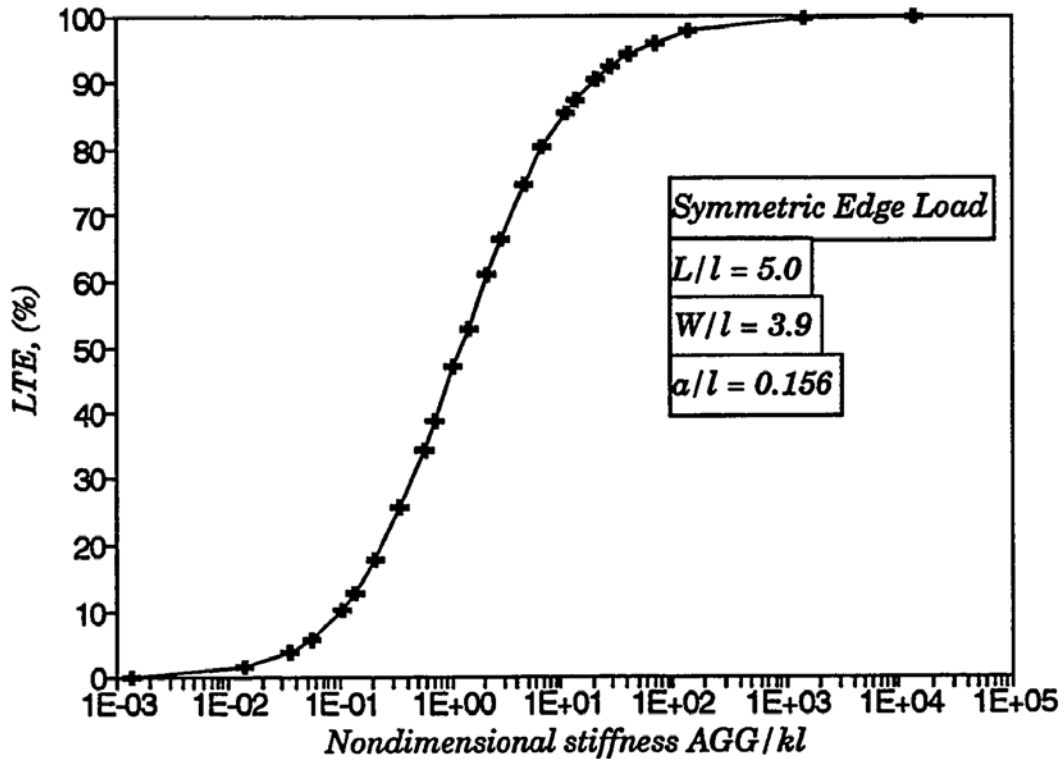


Figure 3. Correlation between the LTE measured from a FWD test to the non-dimensional stiffness of the joint  $AGG / (k \cdot l)$  (Ioannides and Korovesis, 1990).

### 3.1.2 Traffic

The AASHTO design guide has traditionally used equivalent single-axle loads (ESALs) to quantify the effects of mixed truck traffic on pavement damage. Several mechanistic-empirical design methods, such as the PCA (1984), StreetPave (ACPA, 2005), and the MEPDG (ARA, 2007), use load spectra to individually characterize how each axle type or vehicle type, or both, affect the pavement damage. Appendix C describes a study completed in this research which specifically investigated the difference between ESAL and load spectra-based thickness design using the MEPDG. In terms of the required concrete slab thickness, there was not a significant difference found when using either ESALs or load spectra as the traffic input. This finding led to the decision to continue using ESALs as the traffic input, mainly because of its simplicity and its availability in terms of being calculated by Illinois engineers—in spite of some of the known limitations with the ESAL concept.

The geometry of the applied load is defined by the tire contact pressure, total axle load, and wheel configuration, such as the spacing between the dual tires ( $S$ ). With ESALs being used in the design, the load of a single axle is therefore fixed at 18,000 lb and a dual-tire configuration (4 tires per axle) is assumed such that each tire load ( $P$ ) is set to 4,500 lb with a fixed tire pressure of 120 psi. The radius of applied load ( $a$ ) is calculated based on these inputs and is adjusted to an equivalent radius ( $a_{eq}$ ) based on a formulation proposed by Salsilli (1991) as described in Section 3.2. The influence of wander in traffic is accounted for in the design guide with use of the quantity ( $\bar{D}$ ). This variable is defined as the mean wander distance from the edge of the slab to the outside edge of the tire and is typically 12 or 18 in. This distance is required to determine the

equivalent damage ratio (*EDR*), which is required to account for the reduced number of expected repetitions causing damage at the mid-slab edge.

### 3.1.3 Material Properties

The material properties, particularly the concrete flexural strength, are used as design inputs. The concrete material's Poisson's ratio  $\mu$  is fixed at 0.15. The elastic modulus of the concrete is related to the strength of the concrete, but is required as a separate input into the program. It is recommended that the mean concrete flexural strength or modulus of rupture (MOR) be measured using 3<sup>rd</sup>-point (also known as 4-point) bending tests (ASTM, 2003a, 2003b) at 90 days. For testing performed at different concrete ages or using a different test method, see Appendix A for suggested conversions.

The *k*-value or modulus of subgrade reaction can vary with moisture levels in the ground and thus varies drastically throughout the year. For this design procedure, only a single *k*-value is required as an input. This value can be the weighted average *k*-value over the entire year determined from a dynamic test method, or an estimated *k*-value. For determination of temperature curling stresses in this design program, a static *k*-value is set to 100 psi/in.

The coefficient of thermal expansion (CTE) was tested as part of the Strategic Highway Research Program's Long Term Pavement Performance study. For Illinois, the average CTE was  $5.7 \times 10^{-6}$  in./in./°F based on 86 cores; the summary of the test results are shown in Table 3.

Table 3. Coefficient of Thermal Expansion Values for Illinois

	CTE Value	
	$10^{-6}$ in./in./°C	$10^{-6}$ in./in./°F
Lowest 10%	8.2	4.6
Mid 80%	10.3	5.7
Highest 10%	11.9	6.6
Minimum	7.1	3.9
Maximum	13.1	7.3
Overall (average $\pm$ standard deviation)	$10.2 \pm 1.0$	$5.7 \pm 0.6$

### 3.1.4 Pavement Temperature Data

Pavement temperature data was generated and organized into temperature differential versus frequency distributions using the Enhanced Integrated Climatic Model (Larson and Dempsey, 1997). The input can be either a cumulative damage analysis using the full temperature differential distribution or a single effective temperature gradient value and the equivalent percent time of occurrence. The current IDOT procedure uses +1.65 °F/in. of positive temperature differential for 25% of the time, -0.65 °F/in. of negative temperature differential for 35% of the time, and zero gradient for 40% of the time. It is suggested that the positive temperature gradient and 25% time of occurrence be used when analyzing the curling stresses. The fatigue damage caused by the zero and nighttime gradient is negligible in terms of the overall damage at the bottom of the mid-slab edge.



A brief study was done using the current MEPDG Version 1.0 software to investigate the influence of climate (selected based on locations throughout Illinois) on percent cracking for the same thickness, and the minimum thickness that produced 20% cracking. The results of this study can be found in Appendices B and C. Although the climate (or location) did have an influence on the amount of cracking seen in the pavement section, there was no clear trend found between regions or locations in Illinois and the required slab thickness. Therefore, one climate zone is adequate for all of Illinois.

Various studies have been performed in the past which investigated the correlation between curling stresses along with load-related stresses on total stress calculations. From these studies, different regression equations were developed for this stress calculation. The program computes the curling stress and a correction factor  $R$  according to the regression equations found in Salsilli's thesis (1991), the spreadsheet developed by Salsilli, the ILLICON code (Barenberg, 1994), the ILLIJOINT code (reported in Zollinger and Barenberg, 1989a, 1989b) and from Lee and Darter (1994). For all of the curling stress calculations, a static  $k$ -value is fixed at 100 psi/in. Details about the calculations for each regression equation can be found in Section 3.2.3.1.

For the temperature differential distribution option, the frequency distribution was recorded for each 2.5 °F for a JPCP in Champaign, Illinois. The stresses and corresponding fatigue damage (using one of the selected correction factor  $R$  equations and fatigue damage calculation methods) were computed and summed for all temperature differential levels.

### 3.2 TENSILE STRESS CALCULATIONS

To compute the stresses in the pavement structure, the program uses Westergaard's (1948) edge stress, and then uses various adjustment factors to correct the computed stress based on the slab size, slab–base interface condition, the shoulder type, and temperature curling stresses. The equations for the stress calculation and factors are shown in the next section.

#### 3.2.1 Westergaard Edge Stress

According to Westergaard's theory for an infinite slab (assuming the length of the slab  $L$  measured in inches is greater than or equal to 5 times the radius of relative stiffness  $l$ ), the edge stress  $\sigma_{west}$  is computed based on an equivalent loaded area (stress in the slab based on each tire loaded onto the slab and their location in relation to the edge). The calculation of Westergaard's edge stress  $\sigma_{west}$  (psi) is shown in Equation (1):

$$\sigma_{west} = \frac{3(1 + \mu)P}{\pi(3 + \mu)h^2} \left[ \ln \frac{Eh^3}{100ka_{eq}^4} + 1.84 - \frac{4\mu}{3} + \frac{1 - \mu}{2} + 1.18(1 + 2\mu)(a_{eq}/l) \right] \quad (1)$$

where  $P$  is the equivalent tire load, or twice the load of a single tire (lb); and  $l$  is the radius of relative stiffness (in.) equal to

$$l = \left( \frac{Eh^3}{12(1 - \mu^2)k} \right)^{0.25} \quad (2)$$

where:

$\mu$  = Poisson's ratio of the concrete;  
 $h$  = the concrete slab thickness (in.);  
 $E$  = the concrete's elastic modulus (psi); and  
 $k$  = the modulus of subgrade reaction (psi/in.).

For single-axle dual-wheel loading, Salsilli (1991) developed an equation to compute an equivalent radius of applied loading  $a_{eq}$  (in.) which gives the same bending stress as a dual-wheel load, separated by a distance  $S$  (measured in inches), as follows:

$$a_{eq} = a \left[ 0.909 + 0.339485 \left( \frac{S}{a} \right) + 0.103946 \left( \frac{a}{l} \right) - 0.017881 \left( \frac{S}{a} \right)^2 - 0.045229 \left( \frac{S}{a} \right)^2 \left( \frac{a}{l} \right) + 0.000436 \left( \frac{S}{a} \right)^3 - 0.301805 \left( \frac{S}{a} \right) \left( \frac{a}{l} \right)^3 + 0.034664 \left( \frac{S}{a} \right)^2 \left( \frac{a}{l} \right)^2 + 0.001 \left( \frac{S}{a} \right)^3 \left( \frac{a}{l} \right) \right] \quad (3)$$

where  $a$  is the radius (in.) of applied load for one tire.

According to Salsilli, the equation for equivalent radius of applied loading is valid when  $0 < (S/a) < 20$  and  $0.05 < (a/l) < 0.5$ , assuming a lane width of 12 ft. The set of tires closest to the centerline joint of the pavement contribute negligible stress to the mid-slab edge stress, and thus were omitted from the calculations. Other equivalent radii of applied loading equations were developed by Salsilli (1991) for various axle configurations, such as tandem and tridem axles, but are not covered in this report since ESALs rather than load spectra is the standard traffic input. The equivalent radius of applied loading ( $a_{eq}$ ) is to be used in all subsequent equations in the design process.

### 3.2.2 Stress Factors

The theoretical edge stress calculation developed by Westergaard is corrected based on various adjustment factors to account for finite slab sizes, bonded or unbonded base layers and shoulder conditions. These factors are defined in the following sections.

#### 3.2.2.1 Slab Size

To account for a finite slab length, an adjustment factor  $f_l$  was derived by Salsilli (1991) as described in Equation (4) where  $L$  is the length of the slab measured in inches.

$$f_l = \left[ 0.582282 - 0.533078 \left( \frac{a_{eq}}{l} \right) + 0.181706 \left( \frac{L}{l} \right) - 0.019824 \left( \frac{L}{l} \right)^2 + 0.109051 \left( \frac{a_{eq}}{l} \right) \left( \frac{L}{l} \right) \right] \quad (4)$$

The slab size factor is validated for  $3 \leq (L/l) \leq 5$  and  $0.05 \leq (a_{eq}/l) \leq 0.3$ . The slab size factor  $f_1$  should be a maximum of 1, and for cases in which  $L/l$  is greater than 5, the slab size factor is also equal to 1.

### 3.2.2.2 Bonded/Unbonded Base

The layer below the concrete is considered the stabilized base layer which may be bonded or unbonded to the concrete. A factor  $f_2$  is used to account for how the interface condition reduces the tensile bending of the pavement. To calculate this adjustment factor, the effective thickness  $h_{eff}$  must be computed for a bonded or unbonded interface. In the case of an unbonded slab–base interface, the unbonded effective thickness ( $h_{eff,u}$ ) measured in inches and stress factor  $f_2$  are computed based on Equations (5) and (8) from Ioannides et al. (1992).

$$h_{eff,u} = \left[ h^3 + h_2^3 \frac{E_2 h_2}{E h} \right]^{1/3} \quad (5)$$

$$\sigma_{eff} = \frac{3(1 + \mu)P}{\pi(3 + \mu)h_{eff}^2} \left[ \ln \frac{E h_{eff}^3}{100 k a_{eq}^4} + 1.84 - \frac{4\mu}{3} + \frac{1 - \mu}{2} + 1.18(1 + 2\mu)(a_{eq}/l_{eff}) \right] \quad (6)$$

$$\sigma_{1,u} = \frac{h}{h_{eff,u}} \sigma_{eff} \quad (7)$$

$$f_2 = \frac{\sigma_1}{\sigma_{west}} \quad (8)$$

The concrete thickness  $h$  (in.), concrete elastic modulus  $E$  (psi), base layer thickness  $h_2$  (in.), and base layer elastic modulus  $E_2$  (psi) are required to compute the effective thickness. An effective radius of relative stiffness  $l_{eff}$  is computed according to Equation (2) and the effective edge stress  $\sigma_{eff}$  at the bottom of the equivalent section is calculated from Equation (6) using the effective thickness  $h_{eff,u}$  instead of  $h$ . The maximum bending stress  $\sigma_1$  at the bottom of the surface concrete layer is calculated from Equation (7). The interface correction factor  $f_2$  in Equation (8) is computed as the ratio of the computed tensile stress at the bottom of the concrete slab for the effective three layer system divided by the Westergaard edge tensile stress for the two-layer slab system (slab and foundation).

For the bonded base layer, the concrete and base layer act as a composite pavement and the neutral axis NA of the composite section is shown in Figure 4.

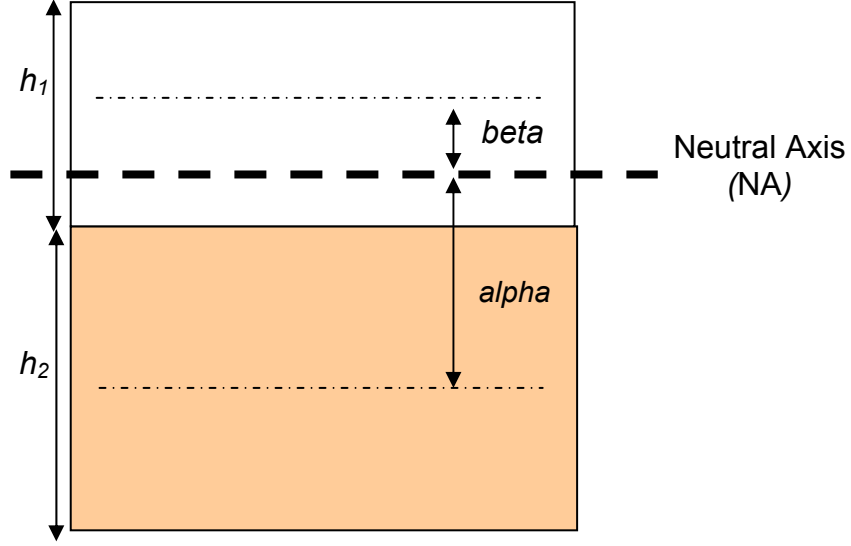


Figure 4. Schematic of concrete and base layer geometry.

An adjusted thickness (measured in inches) for the concrete and base layer ( $h_f$  and  $h_{2f}$ , respectively) are computed based on the location of the neutral axis NA in the composite section according to Equations (9) through (13) based on the Ioannides et al. (1992) formulation.

$$\alpha = \frac{0.5h * (h + h_2)}{h + h_2 * (E_2 / E)} \quad (9)$$

$$\beta = 0.5(h + h_2) - \alpha \quad (10)$$

$$h_f = (h^3 + 12 * h * \beta^2)^{1/3} \quad (11)$$

$$h_{2f} = (h_2^3 + 12 * h_2 * \alpha^2)^{1/3} \quad (12)$$

$$NA = \frac{Eh^2/2 + E_2h_2(h + h_2/2)}{Eh + E_2h_2} \quad (13)$$

An effective concrete thickness  $h_{eff,b}$  can also be computed for the bonded base layer case, as seen in Equation (14). Similarly to the unbonded case, the maximum edge stress at the bottom of the concrete slab must be computed, as shown in Equation (15). The interface correction factor for a bonded base layer  $f_2$  is determined according to Equation (8), except using the bonded  $h_{eff,b}$  for  $h_{eff}$  and the bonded stress  $\sigma_{1,b}$  instead of  $\sigma_1$ .

$$h_{eff,b} = \left[ h_f^3 + h_{2f}^3 \frac{E_2 h_{2f}}{E h_f} \right]^{1/3} \quad (14)$$

$$\sigma_{l,b} = \frac{h - NA}{h_{eff}/2} \sigma_{eff} \quad (15)$$

If no base layer exists (in other words, the concrete pavement is placed directly on the subgrade or on a material with substantially lower modulus), a stress factor  $f_2$  of 1.0 will result.

### 3.2.2.3 Shoulder Type

The three types of shoulders considered for JPCP design are widened lane, tied concrete shoulder, and asphalt shoulder. For each case, an adjustment factor  $f_3$  is computed. When asphalt concrete is employed as the shoulder, it is assumed that no stress reduction occurs and therefore  $f_3$  can be set to 1.

For a widened lane, the critical tensile stress could occur at the bottom of the mid-slab edge, the interior of the slab, or at the transverse joint. Salsilli (1991) derived an equation to predict the adjustment factor  $f_{3w}$  to the Westergaard edge stress due to the effects of a widened lane for loading near the mid-slab edge, as seen in Equation (16).

$$f_{3w} = [0.454147 + 0.013211\left(\frac{l}{D}\right) + 0.386201\left(\frac{a_{eq}}{D}\right) - 0.24565\left(\frac{a_{eq}}{D}\right)^2 + 0.053891\left(\frac{a_{eq}}{D}\right)^3] \quad (16)$$

where  $D$  is the offset distance between the outer face of the wheel and the slab edge (in.). The adjustment factor  $f_{3w}$  is valid when  $0.125 \leq (D/l) \leq 3$  and  $0.05 \leq (a_{eq}/l) \leq 0.3$ . However, when  $D/l < 0.125$ , the influence of the widened lane on reducing edge stresses can be considered negligible, and thus,  $f_{3w} = 1$  should be used. As shown in Appendices E and H, widened lanes tend to produce critical cracking locations at the transverse joint, even with a small amount of built-in curling. Based on the findings in Appendix H, it is recommended that the widened lane thickness never be less than the tied concrete shoulder thickness to avoid the potential for longitudinal or corner cracking.

For a tied concrete shoulder, the reduction in the edge stress will depend on the effectiveness of the aggregate interlock between the shoulder and the slab. The shoulder non-dimensional aggregate interlock factor  $AGG / kl$  is computed based on the expected LTE according to Equation (17).

$$\frac{AGG}{kl} = \left[ \frac{\frac{1}{LTE} - 0.01}{0.012} \right]^{-\frac{1}{0.849}} \quad (17)$$

The adjustment factor  $f_{3T}$  for tied concrete shoulder can be computed according to Equations (18) and (19), based on Salsilli (1991). The tied shoulder adjustment factors are valid for  $0.05 \leq (a_{eq}/l) \leq 0.3$ .

For  $5 \leq (AGG / kl) \leq 50,000$ :

$$f_{3T} = \left[ 0.99864 - 0.51237 \left( \frac{a_{eq}}{l} \right) + 0.0762 \left( \ln \left( \frac{AGG}{kl} \right) \right) + 0.00315 \left( \ln \left( \frac{AGG}{kl} \right) \right)^2 + 0.015936 \left( \frac{a_{eq}}{l} \right)^2 \left( \ln \left( \frac{AGG}{kl} \right) \right)^2 \right] \quad (18)$$

else for  $0 \leq (AGG / kl) \leq 5$ ,

$$f_{3T} = \left[ 1 - 0.025169 \left( \frac{AGG}{kl} \right) - 0.086034 \left( \frac{a_{eq}}{l} \right) \left( \frac{AGG}{kl} \right) \right] \quad (19)$$

### 3.2.3 Temperature Curling Stress

The slab's temperature profile affects the location and magnitude of the critical stress state in the pavement. To greatly simplify the stress analysis, the temperature-induced stresses are analyzed separately from the load-induced stresses. As stated earlier, these stresses cannot be simply added together unless the curling and load stress analysis have the same boundary conditions. Because the slab curls off its support, there is some error associated with the superposition assumption and therefore a correction factor must be applied. The total stresses  $\sigma_{total}$  (psi) at the mid-slab edge are finally computed from Salsilli (1991) according to Equation (20).

$$\sigma_{total} = \sigma_{west} * f_1 * f_2 * f_3 + R * \sigma_{curl} \quad (20)$$

where  $R$  is the superposition correction factor to account for temperature curling of the slab, as described later in Section 3.2.3.1; and  $\sigma_{curl}$  is the Westergaard (1927) curling stress (psi), calculated as follows:

$$\sigma_{curl} = \frac{C * E * \alpha * \Delta T}{2} \quad (21)$$

where:

$C$  = the slab length coefficient determined from Equation (22);  
 $\alpha$  = the coefficient of thermal expansion (measured in in./in./°F); and  
 $\Delta T$  = the temperature differential from the top to bottom in the concrete slab (°F).

$$C = 1 - \left( \frac{2 \cos(\lambda) \cosh(\lambda)}{\sin(2\lambda) + \sinh(2\lambda)} \right) \left( \tan(\lambda) + \frac{\sinh(\lambda)}{\cosh(\lambda)} \right) \quad (22)$$

where  $\lambda = \frac{L}{l_s * \sqrt{8}}$  and  $l_s = \left( \frac{Eh^3}{12(1 - \mu^2)k_s} \right)^{0.25}$  is the radius of relative stiffness determined from a static test,  $k_s$ . One discrepancy when comparing the proposed procedure with

other methods is the static  $k_s$  used for curling stresses and the  $k$  used in the load-based stress calculation are not necessarily the same.

### 3.2.3.1 Superposition Correction Factor $R$

The determination of the superposition correction factor  $R$  to account for temperature curling stress has been studied by several researchers, with each study addressing different JPCP cases. As a result, different equations have evolved based on calibrating the stresses of each data set. After an extensive review of these equations, it is recommended that the original ILLIJOINT  $R$  factor be used. The other  $R$  factor equations are provided herein and in the spreadsheet for future application. In the original JPCP design methods, Salsilli (1991) determined the  $R$  equation shown in Equations (23) and (24) based on ILLI-SLAB simulations.

For  $250 \leq k_s \leq 750$ :

$$\begin{aligned}
 R = & [0.481898 + 0.003919 * L + 8.5391 * 10^{-5} * DT * k_s / h \\
 & + 0.694626 * \log_{10}^3 (C) * DT / h + 8.382 * 10^{-12} * h * E * L \\
 & - 0.013247 * DT^2 / h + 0.187668 * \log_{10}^4 (C) * (DT / h)^3 \\
 & + 0.000106 * DT^2 * L / h^2 + 0.000334 * h * DT + 0.1475 * \log_{10}^3 (C) \\
 & - 5.547 * 10^{-9} * h * E - 0.040857 * (DT / h)^2 * \log_{10} (1 / I_s) - 5.405 * 10^{-6} * L^2 \\
 & + 0.547185 * \log_{10}^2 (C)]
 \end{aligned} \tag{23}$$

else, for  $50 \leq k_s \leq 250$ :

$$\begin{aligned}
 R = & [0.901768 - 0.689151 * \log_{10}^4 (C) * DT / h + 0.749635 * \log_{10}^4 (C) * (DT / h)^3 \\
 & + 1.416192 * \log_{10}^3 (C) * (DT / h)^3 + 0.831476 * \log_{10}^2 (C) * (DT / h)^3 \\
 & + 0.000126 * DT * k_s - 0.000989 * DT * k_s / h \\
 & + 0.122626 * \log_{10} (C) * (DT / h)^3 + 4.0 * 10^{-10} * E * k_s * \log_{10} (1 / I_s) \\
 & + 0.821965 * \log_{10}^2 (C) - 0.110462 * \log_{10}^4 (C) * (DT / h)^2 \\
 & + 1.921 * 10^{-12} * E * k_s * L]
 \end{aligned} \tag{24}$$

where  $DT = \alpha * \Delta T * 10^5$  and is valid for  $-40 \leq \Delta T \leq 40$ . Note that Equation (24) is computed in the design spreadsheet for a fixed  $k_s$  of 100 psi/in. The calculation of the  $R$  factor for  $k_s > 250$  pci shown in Equation (23) is not used due to the assumption that curling stresses have a smaller  $k$ -value than the dynamic  $k$ -value felt under the wheel load. Furthermore, it was reported by Salsilli that Equation (24) has a standard error of the estimate of 0.37 and a coefficient of variation at 34%, which are extremely large for that predictive equation. The Salsilli equations are still included in the design spreadsheet because they are part of the evolution of concrete pavement design.

Salsilli later developed a spreadsheet for computing the stresses and damage induced in a JPCP design. This spreadsheet contained a calculation of the  $R$  factor as seen in Equation (25).

$$\begin{aligned}
R = & [1.38302 - 0.139374/(a_{eq}/l_s) + 0.012349/(a_{eq}/l_s)^2 - 0.000329/(a_{eq}/l_s)^3 \\
& + 23.637919*(L/l_s)^{-3} - 0.864308*(L/l_s)^{-2}*DT \\
& + 0.00204*(L/l_s)^{-1}*DT^2]
\end{aligned} \tag{25}$$

According to other research studies, the  $R$  factor is determined as shown in Equations (26) through (30). The  $R$  factor in the ILLICON code (Barenberg, 1994) is computed as follows:

$$\begin{aligned}
R = & [1.062 - 0.0157568*DT - 0.0000876*k_s - 1.068*(L/l_s*0.01) \\
& + 0.387317*DT*(L/l_s*0.01) + 1.17*10^{-11}*E*DT*k_s \\
& - 1.81*10^{-12}*E*DT^2*k_s - 1.051*10^{-9}*E*(L/l_s*0.01)^2*k_s*DT \\
& + 1.84*10^{-11}*E*DT^2*(L/l_s*0.01)*k_s - 1.7487*(L/l_s*0.01)^2*DT \\
& + 0.00003435123724*DT^3 + 86.97*(L/l_s*0.01)^3 \\
& - 0.00816396*DT^2*(L/l_s*0.01)]
\end{aligned} \tag{26}$$

Zollinger and Barenberg (1989a) developed a JPCP design program called ILLIJOINT that was subsequently used to determine the design charts for IDOT. This program computed the  $R$  factor and a regression equation for the mid-slab edge curling stress  $\sigma_{curl}$  (psi), as shown in Equations (27) and (28).

$$\begin{aligned}
R = & [0.48039 + 0.01401*h - 0.27278*(T/h) - 0.00403*(L/12) \\
& + 0.19508*\log_{10}(k_s) + 0.45187*(T/h)*\log_{10}(h) - 0.00532*(T/h)^2 \\
& + 0.01246*(T/h)*(L/12) - 0.00622*(T/h)*(L/12)*\log_{10}(k_s) \\
& + 8.7872*\log_{10}(h^3/k_s)/h^2 - 0.11846*(T/h)*\log_{10}(h^3/k_s)]
\end{aligned} \tag{27}$$

$$\begin{aligned}
\sigma_{curl} = & [(T/h)*(0.06712*k_s + 79.07391*\log_{10}(k_s) + 11.7269*(L/12) \\
& - 0.0072*(L/12)*k_s - 3.22139*(L/12)*\log_{10}(k_s) - 204.39477*h/k_s \\
& - 38.08854*(L/12)/h - 8.36842*h*\log_{10}(k_s) \\
& + 0.20845*(L/12)*h*\log_{10}(k_s) + 0.00058*(L/12)*h*k_s]
\end{aligned} \tag{28}$$

where  $T$  is the temperature difference from the top to bottom of the slab (measured in °F). For the IDOT design spreadsheet the curling stress equation regressed by Zollinger and Barenberg for ILLIJOINT was not used, since it was deemed that the Westergaard curling stress would suffice.

Lee (1994) and Lee and Darter (1994) derived  $R$  factor equations based on systematic runs of ILLI-SLAB for daytime and nighttime curling conditions, as seen in Equations (29) and (30), respectively. For daytime curling:

$$R = 0.94825 + 0.15054*\phi_1 + 0.03724*\phi_2 + 0.03395*\phi_3 \tag{29}$$



$$\text{where } \Phi_1 = \begin{cases} -2.5575 + 0.8003ATX_1 & ATX_1 \leq 3 \\ -2.6338 + 1.1038ATX_1 - 0.0914ATX_1^2 & 3 < ATX_1 \leq 7 \\ 0.7564 - 0.0155ATX_1 & ATX_1 > 7 \end{cases},$$

$$\Phi_2 = \begin{cases} -0.6788 + 0.0107ATX_2 & ATX_2 \leq 3 \\ 3.7674 - 2.297ATX_2 + 0.2963ATX_2^2 & 3 < ATX_2 \leq 7 \\ -7.0337 + 1.2945ATX_2 & ATX_2 > 7 \end{cases},$$

$$\Phi_3 = \begin{cases} 4.0843 + 4.8241ATX_3 & ATX_3 \leq -1 \\ 0.1815 + 0.0541ATX_3 - 1.0899ATX_3^2 & -1 < ATX_3 \leq 0.5 \\ 0.0453 + 0.0383ATX_3 & ATX_3 > 0.5 \end{cases},$$

$$ATX_1 = [-0.04724*W/I_s + 0.56954*L/I_s - 0.08408DT + 0.20033*a_{eq}/I_s \\ - 0.26647*D_G + 0.00375*D_P + 0.73881*a_{eq}*L/I_s^2 - 0.01142*DT*L/I_s \\ + 0.0953*D_G*L/I_s + 0.01121*D_G*W/I_s],$$

$$ATX_2 = [0.03869*W/I_s + 0.35781*L/I_s + 0.09078*DT - 0.04054*a_{eq}/I_s \\ + 0.86388*D_G + 0.01635*D_P - 0.31246*a_{eq}*L/I_s^2 + 0.00552*DT*L/I_s \\ - 0.12677*D_G*L/I_s - 0.01765*D_G*W/I_s],$$

$$ATX_3 = [0.58567*W/I_s + 0.25804*L/I_s + 0.14784*DT + 0.14984*a_{eq}/I_s \\ + 0.12743*D_G - 0.05012*D_P + 0.72295*a_{eq}*L/I_s^2 - 0.0131*DT*L/I_s \\ - 0.01304*D_G*L/I_s - 0.06591*D_G*W/I_s],$$

$$D_G = \frac{\gamma h^2}{k_s I_s^2} * 10^5, \text{ and } D_P = \frac{2Ph}{k_s I_s^4} * 10^5$$

For nighttime curling:

$$R = 0.76068 + 0.2849*\Phi_4 + 0.10707*\Phi_5 + 0.10048*\Phi_6 \quad (30)$$

$$\text{where } \Phi_4 = \begin{cases} -2.5301 + 0.3866ATX_4 & ATX_4 \leq 6 \\ -4.0938 + 0.8799ATX_4 - 0.0395ATX_4^2 & 6 < ATX_4 \leq 12 \\ 0.3181 + 0.0435ATX_4 & ATX_4 > 12 \end{cases},$$

$$\Phi_5 = \begin{cases} -1.498 - 1.1359ATX_5 & ATX_5 \leq -1 \\ -0.4956 - 0.0892ATX_5 + 0.0174ATX_5^2 & -1 < ATX_5 \leq 5 \\ -1.1278 + 0.1075ATX_5 & ATX_5 > 5 \end{cases},$$

$$\Phi_6 = \begin{cases} 3.6341 + 0.6512ATX_6 & ATX_6 \leq -7 \\ -0.2683 - 0.6808ATX_6 - 0.1116ATX_6^2 & -7 < ATX_6 \leq -1 \\ 0.1966 - 0.2061ATX_6 & ATX_6 > -1 \end{cases},$$

$$\begin{aligned}
ATX_4 &= [-0.13971*W/l_s + 0.85779*L/l_s + 0.07003*|DT| + 0.19562*a_{eq}/l_s \\
&\quad + 0.365897*D_G + 0.0595*D_P - 0.24211*a_{eq}*L/l_s^2 + 0.07242*D_G*L/l_s \\
&\quad - 0.00482*D_P*L/l_s + 0.00797*|DT|*L/l_s + 0.0122*|DT|*W/l_s], \\
ATX_5 &= [-0.15106*W/l_s + 0.08443*L/l_s + 0.28234*|DT| - 0.48812*a_{eq}/l_s \\
&\quad + 0.17449*D_G - 0.03194*D_P - 0.78445*a_{eq}*L/l_s^2 - 0.01999*D_G*L/l_s \\
&\quad + 0.00206*D_P*L/l_s - 0.06949*|DT|*L/l_s - 0.00419*|DT|*W/l_s], \text{ and} \\
ATX_6 &= [0.1096*W/l_s - 0.60315*L/l_s - 0.26836*|DT| + 0.06965*a_{eq}/l_s \\
&\quad - 0.71547*D_G - 0.12704*D_P + 0.02846*a_{eq}*L/l_s^2 + 0.13364*D_G*L/l_s \\
&\quad + 0.01088*D_P*L/l_s + 0.02248*|DT|*L/l_s + 0.0026*|DT|*W/l_s].
\end{aligned}$$

The Lee and Darter (1994) equations for the  $R$  factor are valid for  $0.05 \leq a_{eq}/l_s \leq 0.3$ ,  $3 \leq L/l_s \leq 15$ ,  $3 \leq W/l_s \leq 15$ ,  $5.5 \leq DT \leq 22$ ,  $1.06 \leq D_G \leq 9.93$ , and  $2.61 \leq D_P \leq 140.74$ . Note that for the nighttime temperature curling cases, the  $ATX$  equations contain the absolute value of  $DT$ . Although this was not described in Lee and Darter (1994), only the absolute value of  $DT$  allows for the equations to be true for negative temperature values and was verified to produce closer correlation to ILLI-SLAB simulations.

Comparisons of these various  $R$  factor equations were made to ILLI-SLAB simulations and it was determined that the ILLIJOINT and ILLICON superposition  $R$  factors gave the closest total stress correlation with ILLI-SLAB. In the design spreadsheet, it is recommended that the correction factor  $R$  from Zollinger and Barenberg's ILLIJOINT program be used [see Equation (27)].

### 3.2.3.2 Slab Temperature Differential Results

In the design spreadsheet, the temperature stresses and  $R$  factor can be determined from a user-defined effective temperature gradient with a percent time of occurrence, or with a temperature differential distribution based on post-processed EICM data for Champaign, Illinois (see Table 4 and Appendix D). For the case of the user-defined effective temperature gradient, only one temperature gradient value is input into the design (+1.65 °F/in.), which represents the positive temperature curling which adds to the wheel load tensile stress at the bottom of the slab.

Table 4. Temperature Distribution for Champaign, Illinois for 8-, 10-, 12-, and 14-in..  
JPCP Thicknesses.

8-in. PCC Thickness					10-in. PCC Thickness				
T degF	Frequency	(%)	Temperature Statistics		T degF	Frequency	(%)	Temperature Statistics	
-30	0	0.0	Max.	22.8	-30	0	0.0	Max.	25.3
-27.5	0	0.0	Min.	-27.1	-27.5	2	0.0	Min.	-28.8
-25	2	0.0	Average	0.0	-25	0	0.0	Average	0.0
-22.5	0	0.0	Median	-0.5	-22.5	0	0.0	Median	-0.5
-20	0	0.0			-20	22	0.0		
-17.5	27	0.0			-17.5	97	0.2		
-15	128	0.2			-15	394	0.6		
-12.5	593	1.0			-12.5	941	1.5		
-10	1502	2.4			-10	1960	3.2		
-7.5	3340	5.4			-7.5	3889	6.3		
-5	6380	10.4			-5	6438	10.5		
-2.5	10084	16.4			-2.5	9152	14.9		
0	10948	17.8			0	9800	16.0		
2.5	8965	14.6			2.5	8389	13.7		
5	6749	11.0			5	6585	10.7		
7.5	5347	8.7			7.5	5052	8.2		
10	3958	6.4			10	4084	6.7		
12.5	2043	3.3			12.5	2465	4.0		
15	907	1.5			15	1307	2.1		
17.5	304	0.5			17.5	538	0.9		
20	72	0.1			20	195	0.3		
22.5	17	0.0			22.5	45	0.1		
25	2	0.0			25	11	0.0		
27.5	0	0.0			27.5	2	0.0		
30	0	0.0			30	0	0.0		

12-in. PCC Thickness					14-in. PCC Thickness				
T degF	Frequency	(%)	Temperature Statistics		T degF	Frequency	(%)	Temperature Statistics	
-30	0	0.0	Max.	27.2	-30	2	0.0	Max.	28.7
-27.5	2	0.0	Min.	-29.9	-27.5	0	0.0	Min.	-31.2
-25	0	0.0	Average	0.0	-25	3	0.0	Average	0.0
-22.5	23	0.0	Median	-0.5	-22.5	44	0.1	Median	-0.4
-20	63	0.1			-20	113	0.2		
-17.5	192	0.3			-17.5	348	0.6		
-15	581	0.9			-15	732	1.2		
-12.5	1225	2.0			-12.5	1448	2.4		
-10	2295	3.7			-10	2511	4.1		
-7.5	4024	6.6			-7.5	4115	6.7		
-5	6379	10.4			-5	6239	10.2		
-2.5	8506	13.9			-2.5	7932	12.9		
0	9175	15.0			0	8608	14.0		
2.5	7967	13.0			2.5	7658	12.5		
5	6388	10.4			5	6367	10.4		
7.5	5099	8.3			7.5	4989	8.1		
10	3982	6.5			10	4026	6.6		
12.5	2723	4.4			12.5	2904	4.7		
15	1541	2.5			15	1706	2.8		
17.5	759	1.2			17.5	956	1.6		
20	308	0.5			20	431	0.7		
22.5	103	0.2			22.5	153	0.2		
25	24	0.0			25	62	0.1		
27.5	9	0.0			27.5	13	0.0		
30	0	0.0			30	8	0.0		

For the distributed temperature option, the program selects the hourly temperature differential frequency data generated from the EICM for Champaign, Illinois for the appropriate concrete thickness. For each temperature differential, the curling stress  $\sigma_{curl}$  and  $R$  factors are computed. The total fatigue damage is the summation of the wheel load stress, plus individual temperature curling stress times the  $R$  factor multiplied by the frequency of occurrence.

### 3.2.4 Erosion

Many concrete pavement design guides consider erosion of the support layers in the design process. Erosion leads to loss of support and cracking of the slab. Pumping can be thought as a special case of erosion where fines are ejected through joints or cracks. The factors affecting erosion are the presence of water, rate of water movement beneath the slab, erosion potential of the support layers, magnitude and number of load repetitions, and slab deflection (Huang 2004). A model to consider all these factors mechanistically still does not exist today. However, the PCA method and the MEPDG both have mechanistic-based procedures to account for the potential for erosion that addresses all the aforementioned factors. Since some of the factors are handled empirically, the PCA and MEPDG models are termed “calibrated models.” In the current version of the IDOT JPCP design, erosion is considered in the final slab thickness selection, as shown in Figure 5 below, and will be described a little later.

The AASHTO Guide (1986) for concrete pavement design includes the AASHTO Road Test data which experienced significant erosion of the base and subgrade material. Therefore the AASHTO Guide empirically considered erosion in the design equations. The 1986 AASHTO Guide further refined the erosion of materials by establishing layer drainage coefficients for flexible pavements and the loss of support (LS) factor and drainage coefficient for rigid pavements. Essentially these factors increase the required slab thickness, the need for dowels, or the use of stabilized base layers.

The PCA method (Packard 1984), now called StreetPave, has two criteria for concrete pavement failure: slab cracking and erosion. The PCA method considers the pavement corner deflection as the key indicator of erosion. The erosion potential decreases with the use of a stabilized base layer, dowelled transverse joints, and tied concrete shoulders. In general, slab cracking controls the thickness design for lower traffic levels while heavier traffic levels result in erosion factor controlling the slab thickness.

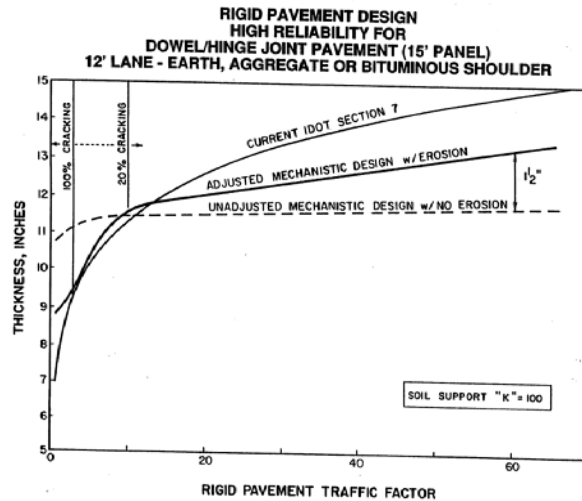


Figure 15. Mechanistic Jointed PCC Design Curve Adjusted for Erosion

Figure 5. Erosion adjusted concrete slab thickness curves (Barenberg 1991)

NCHRP 1-37A has an excellent review of erosion and pumping and can be found in ARA (2004). The MEPDG (ARA 2007) considers erosion of the support layers similarly to the PCA method. The main difference is that a differential energy concept which considers the factors affecting deflection and joint load transfer efficiency at the corner loading position is implemented into the model. The differential energy term is linked to the potential for joint faulting. Design features and materials which reduce corner deflections improve the resistance to erosion and subsequent faulting. For CRCP, the MEPDG assumes a void is created over time under the slab based on the type of base material. This approach is similar to the erosion process originally used in the IDOT JPCP design described next.

Field evaluations of distressed concrete pavements in Illinois have found erosion of the base layer with all types of stabilized base layers, e.g., CAM I, CAM II, and BAM. To account for this erosion for high traffic volumes, Zollinger and Barenberg (1989a) conducted an ILLISLAB analysis in which a 60-in. width along the entire longitudinal edge was assumed to be unsupported. Figure 6 shows the increase in tensile stress at various slab thickness values and degrees of edge erosion. The increase in tensile stress for a 60-in.-wide loss of support was then added to the wheel load stress under full support conditions and the temperature curling stress. The resultant stress required an increase in the slab thickness of 1.5-inch at a traffic factor (TF) of 60. It was also recommended that at  $TF < 10$ , little to no erosion would be assumed. In the final design charts, the design slab thickness at  $TF = 60$  was connected with a straight line to the slab thickness required at  $TF = 10$ .

## WLS Increase

Erodible Subbase

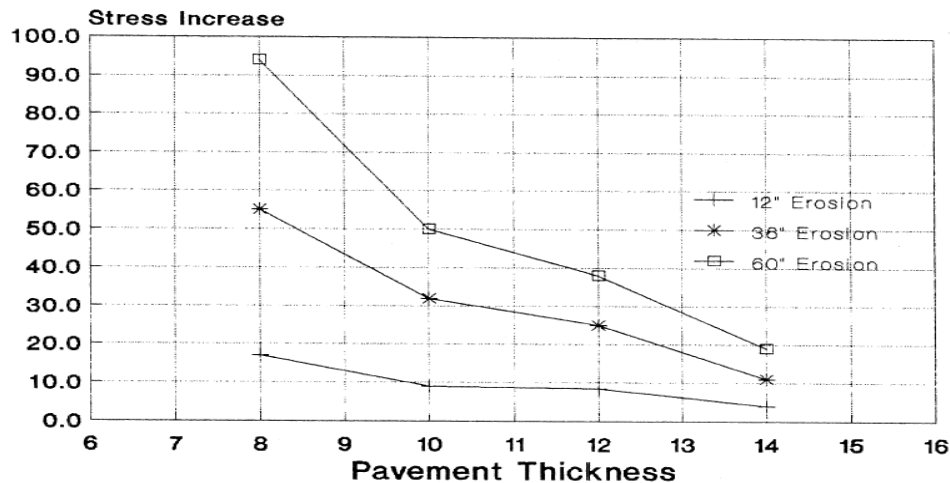


Figure 6. Effect of slab thickness and erosion along the longitudinal edge on tensile stress at mid-slab edge (from Zollinger and Barenberg, 1989a).

IDOT has stated that half of JPCP are built on aggregate base courses. Therefore, completely eliminating the potential for erosion of the base layer does not seem reasonable at this time. The options for considering erosion in the IDOT JPCP are to maintain the existing erosion magnification factor (1.5-inch at TF=60), modify the erosion factor, or eliminate it. First of all, eliminating the erosion factor would require a secondary process to assure the pavement designer that the slab thickness and base layer combination would not erode prematurely. A laboratory procedure to quantify the potential for slab-base erosion is a subject of a research study in Texas A&M (Zollinger 2009).

A finite element analysis with ILLISLAB (Khazanovich 1994) was conducted similar to the analysis completed by Zollinger and Barenberg (1989a). For the current analysis, a single slab was run to determine the tensile stress increase as the area along the edge had its support value set to 0 psi/in. The analysis assumptions were the following: slab thickness of 10 inch, k-value of 100 psi/in, elastic modulus of 4,000 ksi, single wheel edge load of 9-kips (80 psi contact pressure), and slab length and width of 15 ft and 12 ft, respectively. A slab thickness of 10 inches was chosen since it is the approximate slab thickness required at TF=60 without any erosion consideration. The unsupported area was varied from 0 to 72 inches from the edge to determine the sensitivity of tensile stresses to support area. The analysis determined that the critical tensile stress increased approximately 40 psi for a 72 inch eroded area, which was less than the values published by Zollinger and Barenberg. However, they likely used different assumptions in the slab model that were not documented in their report and thus cannot be easily replicated. The additional tensile stress increase translates into an additional 1-inch slab thickness with the proposed JPCP process to maintain the same cracking level at failure. Therefore, the slab thickness should be adjusted upward 1-inch at TF=60 to account for the potential for erosion until a more mechanistic approach is developed.

There is no overwhelming field justification to extend the erosion bump factor to a higher traffic factor ( $TF > 60$ ) and thus any slab thickness greater than this traffic level has a constant 1-inch erosion magnification factor. The slab thickness requirement at  $TF = 60$  is then connected with a straight line to the required slab thickness at  $TF = 10$ . As a point of reference, the proposed CRCP design process by Beyer and Roesler (2009) does not consider erosion directly since the procedure is calibrated against Illinois CRCP sections.

### 3.2.5 Stress Ratio

After computing the total tensile stress at the bottom of the mid-slab edge, as described in Equation (20), the stress ratio  $SR$  is computed according to Equation (31) and used to determine the fatigue life of the concrete slab.

$$SR = \frac{\sigma_{total}}{MOR} \quad (31)$$

## 3.3 FATIGUE CALCULATIONS

Various types of fatigue equations exist for computing the allowable load repetitions  $N$  for a given total stress level in the concrete pavement. The Zero-Maintenance, ACPA, and MEPDG fatigue equations are included in the design program as options. The details of the calculation of each fatigue equation are described in the following section. These different fatigue equations are not expected to give the same results since they were originally developed under different assumptions and use different performance equations to relate the fatigue damage to the observed slab cracking in the field.

### 3.3.1 Zero-Maintenance

The Zero-Maintenance fatigue Equation (32) was derived by Darter (1977) based on a compilation of several laboratory beam fatigue studies into a single equation with 50% probability of failure.

$$\log N = 17.67 - 17.61 * SR \quad (32)$$

### 3.3.2 ACPA

Recently, a research study was undertaken (Titus-Glover et al., 2005; Riley et al., 2005) to re-evaluate the original data set that Darter (1977) used and to which were added additional fatigue test results to derive a fatigue equation that allows the user the ability to set the level of reliability of the fatigue equation, which is essentially a means of setting the overall reliability of the design. Since this new fatigue equation assumes that at 50% reliability, 50% of the slabs are cracked when the fatigue damage is equal to 1.0, Equation (34) adjusts the percent slabs cracked at failure for a damage of 1.0 based on the effective reliability  $R^*$ , or the probability of survival of the pavement.

$$\log N = \left[ -\frac{SR^{-10.24} \log(R^*)}{0.0112} \right]^{0.217} \quad (33)$$

$$R^* = 1 - \frac{(1 - R') * P_{cr}}{0.5} \quad (34)$$

where  $R'$  is the desired reliability of having a given percent of cracked slabs ( $P_{cr}$ ) at fatigue damage of 1.0. Based on IDOT's current JPCP design procedure, it is suggested that 20% cracking be set as a fatigue limit for  $TF > 10$  and 100% for  $TF = 3$  or less. For  $3 \leq TF \leq 10$ , percent cracking is linear between 100 and 20%.

### 3.3.3 MEPDG

The Mechanistic-Empirical Pavement Design Guide (MEPDG) software predicts the fatigue cracking, faulting, and roughness performances of various pavement types based on similar design inputs. According to MEPDG Version 1.0 program (ARA, 2007), the number of allowable load repetitions based on a given stress level is shown in Equation (35). The fatigue equation is then used in conjunction with a fatigue cracking performance curve to predict the level of slab cracking in the field.

$$\log N = 2 * SR^{-1.22} \quad (35)$$

## 3.4 FATIGUE DAMAGE CALCULATIONS

Once the allowable load repetitions are computed and the estimated or design traffic is known, then the level of fatigue damage can be calculated. The estimated traffic must be further reduced to account for wander. The truck traffic is assumed to have a normal distribution of lateral wander from the actual edge of the pavement. The mean wander distance  $\bar{D}$  (in.) from the pavement edge has been found to be 12 to 18 in. Zollinger and Barenberg (1989a, 1989b) computed an equivalent damage ratio ( $EDR$ ) which determines the percent of expected truck traffic at the exact edge of the slab that produces the same fatigue damage as the normally distributed truck traffic across the lane width. These  $EDR$  values are reproduced in Table 5 for each shoulder type. The determination of a "medium load transfer" is set in the program to an LTE less than 70%. An LTE greater than 70% will be classified as a "high load transfer" case.



Table 5. Equivalent Damage Ratios (after Zollinger and Barenberg, 1989b)

Asphalt Shoulder				
$\bar{D}$ (in.)	18		12	
$k$ -value (psi/in.)	100	200	100	200
Thickness $h$ (in.)				
8	0.05	0.05	0.12	0.12
10	0.05	0.05	0.12	0.12
12	0.06	0.06	0.14	0.14

Tied Shoulder (10 ft) Medium Load Transfer				
$\bar{D}$ (in.)	18		12	
$k$ -value (psi/in.)	100	200	100	200
Thickness $h$ (in.)				
8	0.07	0.06	0.18	0.17
10	0.09	0.09	0.19	0.19
12	0.17	0.17	0.22	0.22

Tied Shoulder (10 ft) High Load Transfer				
$\bar{D}$ (in.)	18		12	
$k$ -value (psi/in.)	100	200	100	200
Thickness $h$ (in.)				
8	0.12	0.13	0.24	0.18
10	0.21	0.22	0.27	0.23
12	0.34	0.33	0.36	0.32

Widened Lane (extended by 2 ft)				
$\bar{D}$ (in.)	18		12	
$k$ -value (psi/in.)	100	200	100	200
Thickness $h$ (in.)				
8	0.11	0.14	0.17	0.19
10	0.17	0.2	0.24	0.25
12	0.25	0.28	0.31	0.34

### 3.4.1 Fatigue Damage

The estimated amount of fatigue is computed based on the sum of the ratio of expected design ESALs  $n$  to allowable load repetitions  $N$ . For the calculation of fatigue damage  $FD$ , the  $EDR$  must be multiplied by this ratio, as shown in Equation (36).

$$FD = \sum_i \frac{n * PO_i}{N_i} * EDR \quad (36)$$

where  $PO_i$  is the percent occurrence of a given condition and  $N_i$  is the allowable fatigue repetitions calculated for that condition. For example, assume that a temperature gradient of +1.65 °F/in. is applied to occur 25% of the time, and for the remainder of the

time, a zero gradient is assumed;  $PO_1$  would be 25% and  $N_1$  would be the allowable repetitions produced by this temperature gradient and load stress. Then  $PO_2$  would be 75% and  $N_2$  would be the allowable repetitions corresponding to only load stress. For the ACPA fatigue equation, failure of the JPCP occurs when the fatigue damage ( $FD$ ) is greater than or equal to 1. For the Zero-Maintenance and MEPDG fatigue equations, the  $FD$  is related to a slab cracking performance equation described in the next section.

### 3.4.2 Percent of Cracking

In the past, a fatigue damage of 1.0 did not necessarily guarantee that the pavement section had failed. Thus, researchers have related various fatigue damage levels to the percent of slabs cracked in the field. Field-calibrated fatigue models are highly dependent on the quality of the distress data, the accuracy of the inputs (traffic, climate, pavement layer geometry, material properties, etc.), and the process used to calibrate the equation. The models generally do not give acceptable results without re-calibration when new stress algorithms, fatigue equations, or new inputs are included in the pavement design procedure.

The current JPCP thickness method (IDOT, 2002) uses the Zero-Maintenance fatigue curve to calculate the fatigue damage. Two field-calibrated models were developed to predict the level of slab cracking for 50% ( $P_{cr}^{50\%}$ ) and for 95% ( $P_{cr}^{95\%}$ ) reliability levels, as shown in Equations (37) and (38), respectively. These calibrated equations used the COPES database (Becker et al., 1984).

$$P_{cr}^{50\%} = 1 / \left[ 0.01 + .00000421 * \left( 44.5^{-\text{Log}FD} \right) \right] \quad (37)$$

$$P_{cr}^{95\%} = 1 / \left[ 0.01 + .00000235 * \left( 32.6^{-\text{Log}FD} \right) \right] \quad (38)$$

For the MEPDG fatigue algorithm, the fatigue damage is again related to the slab cracking at 50% ( $P_{cr}^{50\%}$ ) and 95% ( $P_{cr}^{95\%}$ ) reliability levels, as shown in Equations (39) and (40), respectively. These calibrated slab cracking equations are based on observed cracking on JPCP taken from field sections primarily in the LTPP database.

$$P_{cr}^{50\%} = \frac{1}{1 + FD^{-1.98}} \quad (39)$$

$$P_{cr}^{95\%} = P_{cr}^{50\%} + 1.64 * Se \quad (40)$$

where  $Se = (5.3116 P_{cr}^{50\%})^{0.3903} + 2.99$  is the standard error determined from the national calibration. It should be noted that the MEPDG program has been calibrated using different stress prediction equations; therefore, even by using their fatigue and performance equations in the design spreadsheet, different thickness results should be expected. If the MEPDG fatigue algorithm is to be used, recalibration of Equations (39) and (40) will be required.

### 3.5 RELIABILITY

Over the years there have been different approaches in handling reliability in concrete pavement design. In the 1986 AASHTO Guide, a reliability concept was introduced to the design equation since the original design equation utilized mean inputs and thus inherently resulted in 50% design reliability. The PCA method (Packard 1984) for “Thickness Design for Concrete Highway and Street Pavements” utilized a “load safety factor” to account for unpredicted truck loads and volumes and thus can be considered factor of safety approach to design reliability. The traditional FAA method (1995) does not require any input for reliability but the concrete fatigue algorithm provided a design factor (safety factor) of 1.3 in the fatigue algorithm for 5,000 design coverages. The MEDPG (ARA 2007) has a similar approach to reliability as the current IDOT design method (Zollinger and Barenberg, 1989b), which is based on the reliability of the fatigue cracking prediction.

One way to compare the various design methods reliability is to calculate a traffic multiplier (TM), i.e., the amount of equivalent traffic required to achieve the design thickness. For 50% reliability, the traffic multiplier is equal to 1.0. Based on past experience in Illinois, 95% reliability has been used for high-type rigid and flexible pavement systems (Thompson and Cation, 1986; Zollinger and Barenberg, 1989b). For full-depth HMA pavement, a traffic multiplier of 4.0 (based on the variation in deflection measurements) has been used in the past to account for design uncertainties.

The traffic multiplier can be derived from the AASHTO Design Guide (1986) for concrete pavements from the following equation:

$$TM = \frac{W_{18}}{10^{\text{Log}W_{18} - Z_R S_0}} \quad (41)$$

where  $W_{18}$  is the expected design ESALs,  $Z_R$  is the standard normal deviate, and  $S_0$  is the overall standard deviation of the design. For typical concrete pavements,  $S_0$  is 0.35, and for 95% reliability,  $Z_R = -1.645$ . Plugging these assumptions into the above equation, results in a traffic multiplier of 3.77, which is valid for any level of design ESALs. For a reliability of 90% ( $Z_R = -1.282$ ), the traffic multiplier drops down to 2.81.

IDOT’s current JPCP method doesn’t directly use a traffic multiplier, but it can be calculated based on the calibrated cracking to fatigue damage functions. The current JPCP thickness method (IDOT, 2002) uses the Zero-Maintenance fatigue curve to calculate the fatigue damage. Two field-calibrated models were developed (see Figure 7) to predict the level of slab cracking for 50% ( $P_{cr}^{50\%}$ ) and for 95% ( $P_{cr}^{95\%}$ ) reliability levels, as shown in Equations (42) and (43), respectively, based on the COPES database (Becker et al., 1984). For any level of slab cracking the ratio of fatigue damage (FD) at 50% to 95% is the TM. This translates into a TM between 2.2 to 2.5 depending on the selected slab cracking level.

$$P_{cr}^{50\%} = 1 / \left[ 0.01 + .00000421 * \left( 44.5^{-\text{Log}FD} \right) \right] \quad (42)$$

$$P_{cr}^{95\%} = 1 / \left[ 0.01 + .00000235 * \left( 32.6^{-\text{Log}FD} \right) \right] \quad (43)$$

## Mean Values; COPES, ILL

LogN = 17.61 - 17.61R

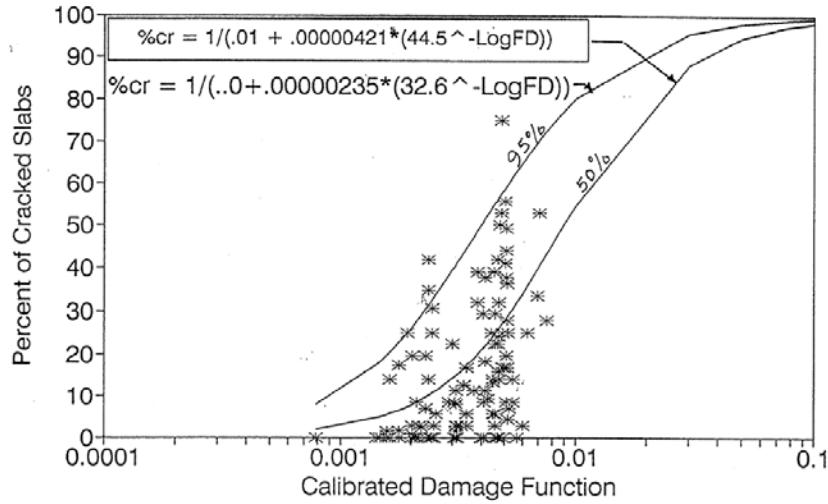


Figure 7. Percent slab cracking versus fatigue damage for concrete pavement in Illinois (Barenberg, 1991)

As in the above slab cracking equations, a fatigue damage of 1.0 does not necessarily guarantee that the pavement section has failed. These field-calibrated fatigue models are highly dependent on the quality of the distress data, the accuracy of the inputs (traffic, climate, pavement layer geometry, material properties, etc.), and the process used to calibrate the equation. The models generally do not give acceptable results without re-calibration when new stress algorithms, fatigue equations, or new inputs are included in the pavement design procedure.

For the MEPDG fatigue algorithm for JPCP, the fatigue damage is again related to the slab cracking at 50% ( $P_{cr}^{50\%}$ ) and 95% ( $P_{cr}^{95\%}$ ) reliability levels, as shown in Equations (44) and (45), respectively. These calibrated slab cracking equations are based on observed cracking on JPCP taken from field sections primarily in the LTPP database.

$$P_{cr}^{50\%} = \frac{1}{1 + FD^{-1.98}} \quad (44)$$

$$P_{cr}^{95\%} = P_{cr}^{50\%} + 1.64 * Se \quad (45)$$

where  $Se = (5.3116P_{cr}^{50\%})^{0.3903} + 2.99$  is the standard error in slab cracking determined from the national calibration. Using the two equations above, the traffic multiplier for the MEPDG for 10 and 20% slab cracking at 95% reliability is 2.8 and 1.7, respectively.

For the MEPDG fatigue algorithm for CRCP, the fatigue damage is again related to the number of punchouts at 50% ( $PO_{50\%}$ ) and 95% ( $PO_{95\%}$ ) reliability levels, as shown in Equations (46) and (47), respectively. These calibrated punchout equations are based

on observed punchouts on CRCP taken from field sections primarily in the LTPP database.

$$PO = \frac{a}{1 + b \cdot FD^c} \quad (46)$$

$$PO_{95\%} = PO_{50\%} + 1.64 \cdot Se \quad (47)$$

where the calibration constants are the following:  $a = 216.842$ ,  $b = 33.1579$ , and  $c = -0.58947$ ; and  $Se = 2.2593 \cdot (PO_{50\%})^{0.4882} + 2$  is the standard error in punchouts determined from the national calibration. Using the two equations above, the traffic multiplier for the MEPDG for 10 and 20 punchouts per mile at 95% reliability is 20 and 6.5, respectively. The standard error is high on the MEPDG punchout prediction which results in very large traffic multipliers.

Another approach to reliability can focus on one of the most sensitive components of the design, i.e., the concrete fatigue algorithm. This approach was taken in the concrete fatigue algorithm originally selected for the PCA method. The fatigue equation assumes a 5% probability of failure based on a dataset of concrete fatigue beam tests. Recent research was undertaken (Titus-Glover et al., 2005; Riley et al., 2005) to re-evaluate the original beam fatigue equation that Darter (1977) used to derive the zero-maintenance fatigue curve. Additional fatigue test data was added and a new fatigue equation that allows the user the ability to set the level of reliability of the fatigue equation. The designer now has the ability to choose the overall reliability of the design based on the reliability of the measured concrete fatigue data. The proposed fatigue algorithm that allows user defined reliability was implemented in the most recent release of the ACPA's StreetPave software (2005). In this new fatigue equation, shown in equation (48), 50% of the slabs are cracked when the fatigue damage is equal to 1.0 at a reliability level of 50%. For other levels of cracking, an effective reliability  $R^*$ , or the probability of survival of the pavement, must be calculated as proposed by Riley et al. (2005) in equation (49).

$$\log N = \left[ -\frac{SR^{-10.24} \log(R^*)}{0.0112} \right]^{0.217} \quad (48)$$

$$R^* = 1 - \frac{(1 - R') \cdot P_{cr}}{0.5} \quad (49)$$

where  $R'$  is the desired reliability of having a given percent of cracked slabs ( $P_{cr}$ ) at fatigue damage of 1.0.

It clear from the above review that the implementation of reliability into rigid pavement design has not been uniformly applied over the years. There are multiple methods to account for variability in design. For the proposed IDOT CRCP design framework (Beyer and Roesler 2009), a traffic multiplier approach is used. The traffic multipliers calculated from the MEPDG were too high based on previous published and calculated traffic multipliers that exist. Therefore a single TM of 4 for a 10 punchout per mile criterion is recommended for CRCP. This selected TM is based on the upper bound calculated from the AASHTO method for concrete pavements. For the JPCP

design, experience has shown IDOT's JPCP gives reasonable results. Currently IDOT does not have a sufficient database of JPCP sections with cracking and traffic and therefore only a method based on a traffic multiplier or fatigue algorithm shift is possible. It is recommended that the concrete fatigue algorithm in equations (48) and (49) be used with 95% reliability and no TM.

### **3.6 THICKNESS DESIGN**

To determine the appropriate design concrete thickness, a trial-and-error approach should be performed using various input combinations with a trial thickness until the desired fatigue damage ( $<1.0$ ) or a failure criterion (e.g., 20% slab cracking) is met.

## CHAPTER 4. JPCP DESIGN SENSITIVITY

JPCP design charts were generated by inputting the structural design equations and the suggested inputs into an Excel spreadsheet (see Figure 8 to Figure 10). For each design chart listed in this section, the existing JPCP curves from IDOT's current and proposed JPCP design curves are plotted. All of the standard design charts shown in Sections 4.1 and 4.2 are plotted with the following assumptions: ACPA fatigue algorithm, 95% reliability,  $MOR = 750$  psi, concrete modulus of 4,600 ksi, coefficient of thermal expansion of  $5.5e-6$  in./in./°F, Poisson's ratio of 0.15,  $k_s = 100$  psi/in., effective temperature gradient approach ( $+1.65$  °F/in., 25% of the time), ILLIJOINT superposition  $R$ -factor, slab length of 15 ft, lane width of 12 ft, unbonded slab-base interface, 4-in.-base with  $E_2 = 600,000$  psi, mean wheel path of 18 in., 120 psi tire pressure, 12 in. between tires, 20% slab cracking at traffic factor (TF)  $\geq 10$  and 100% slab cracking for TF = 3, and erosion is accounted for as a 1-inch increase in required thickness for TF  $\geq 60$ . The design charts in Section 4.1 were generated for variable dynamic  $k$ -values of 50, 100, and 200 psi/in. and for asphalt concrete shoulders and tied shoulders with an LTE of 70% (assumed to be equivalent to the widened lane in the current IDOT design procedure). Sensitivity studies (see Figure 11 through Figure 17) on the influence of load transfer efficiency across a tied joint, bonding condition, wander distance, joint spacing,  $MOR$ , temperature curling approach, fatigue algorithm used, and reliability level were all investigated; these are shown in Section 4.2.

### 4.1 DESIGN CHARTS

#### 4.1.1 Poor Subgrade

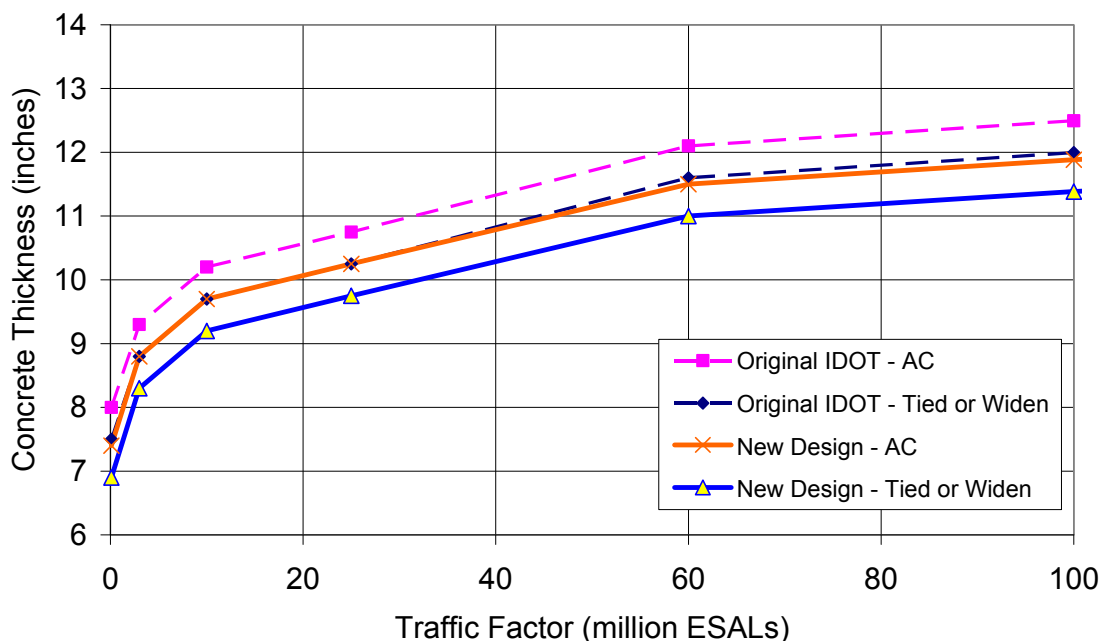


Figure 8. Design chart for poor subgrade condition ( $k = 50$  pci) including asphalt and tied (or widened lane) shoulder conditions for the current IDOT design and from the new design.

#### 4.1.2 Fair Subgrade

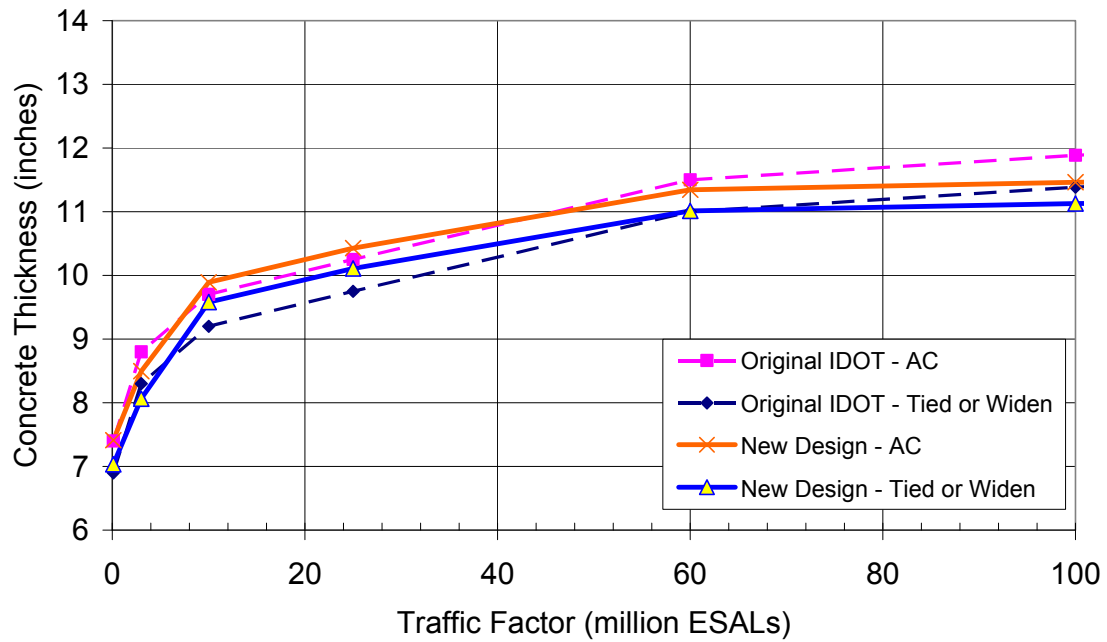


Figure 9. Design chart for fair subgrade condition ( $k = 100$  pci) including asphalt and tied (or widened lane) shoulder conditions for the current IDOT design and from the new design.



### 4.1.3 Granular Subgrade

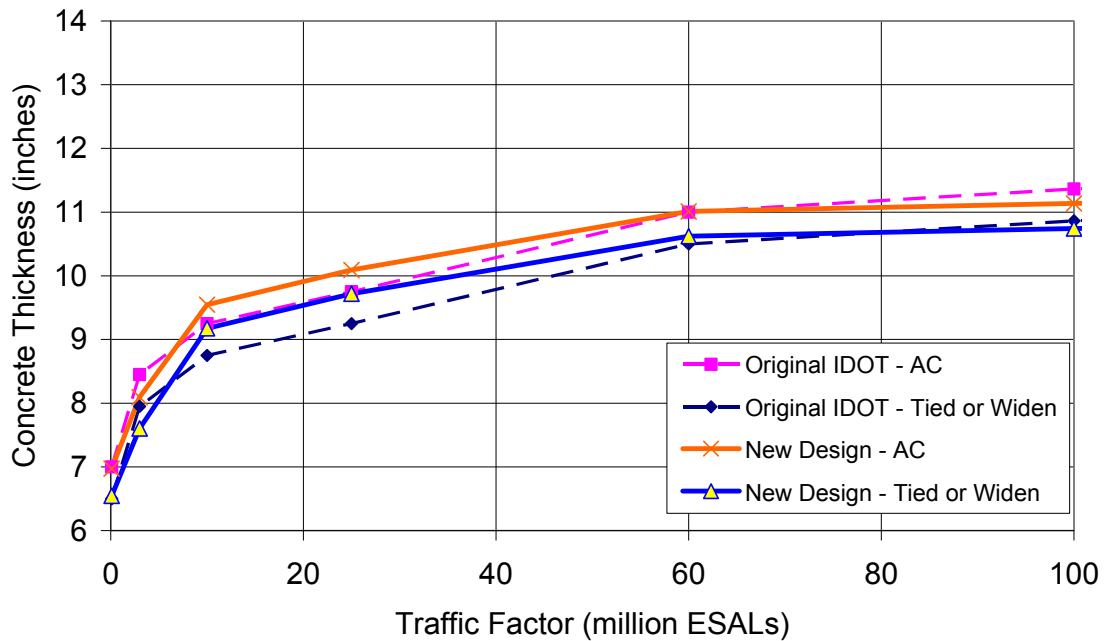


Figure 10. Design chart for granular subgrade condition ( $k = 200$  pci) including asphalt and tied (or widened lane) shoulder conditions for the current IDOT and the new design.

In general, the new design methodology produces slightly thinner pavement thickness especially at higher traffic levels. The main reason for the reduced thickness is a combination of the different concrete fatigue algorithm, reliability scheme, and stress prediction algorithms. The use of a tied shoulder has generally the same sensitivity between the current and new method.

## 4.2 SENSITIVITIES

### 4.2.1 Load Transfer Efficiency for Tied Shoulder

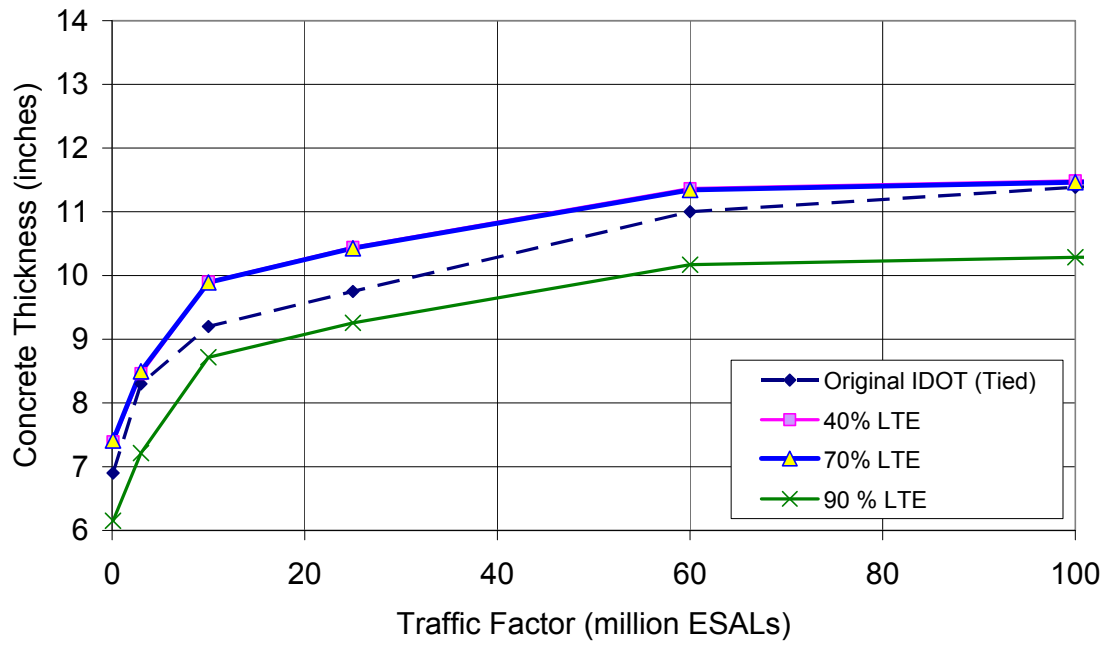


Figure 11. Sensitivity chart of 40, 70, and 90% load transfer efficiency across a tied shoulder compared to current IDOT design.

#### 4.2.2 Bonding Condition

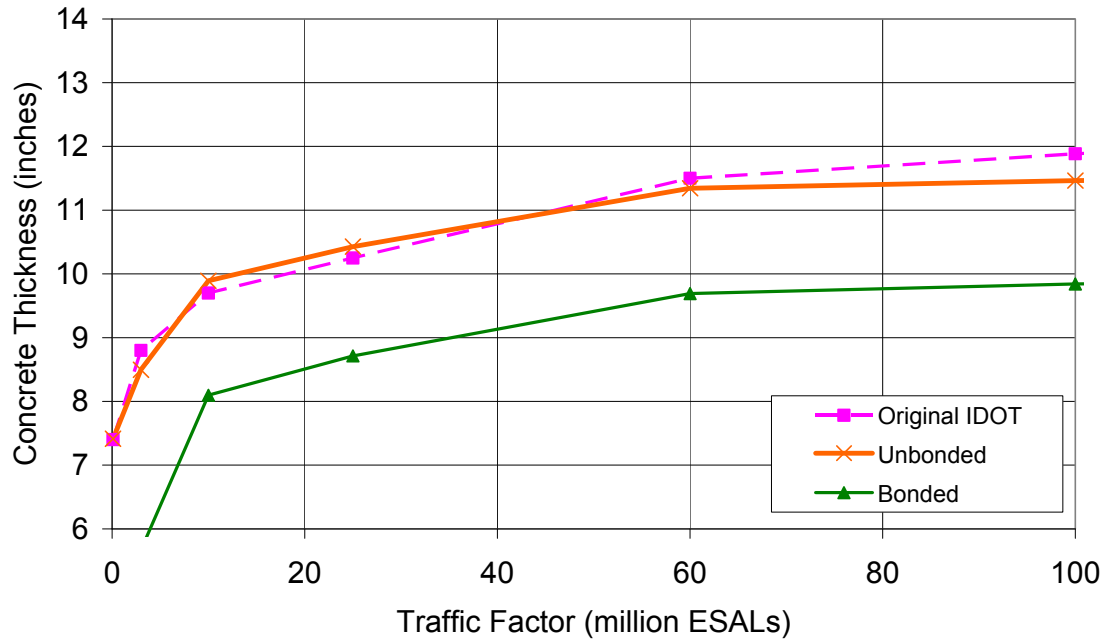


Figure 12. Sensitivity chart assuming the JPCP is unbonded or bonded to the base layer and compared to current IDOT design.

### 4.2.3 Traffic Wander

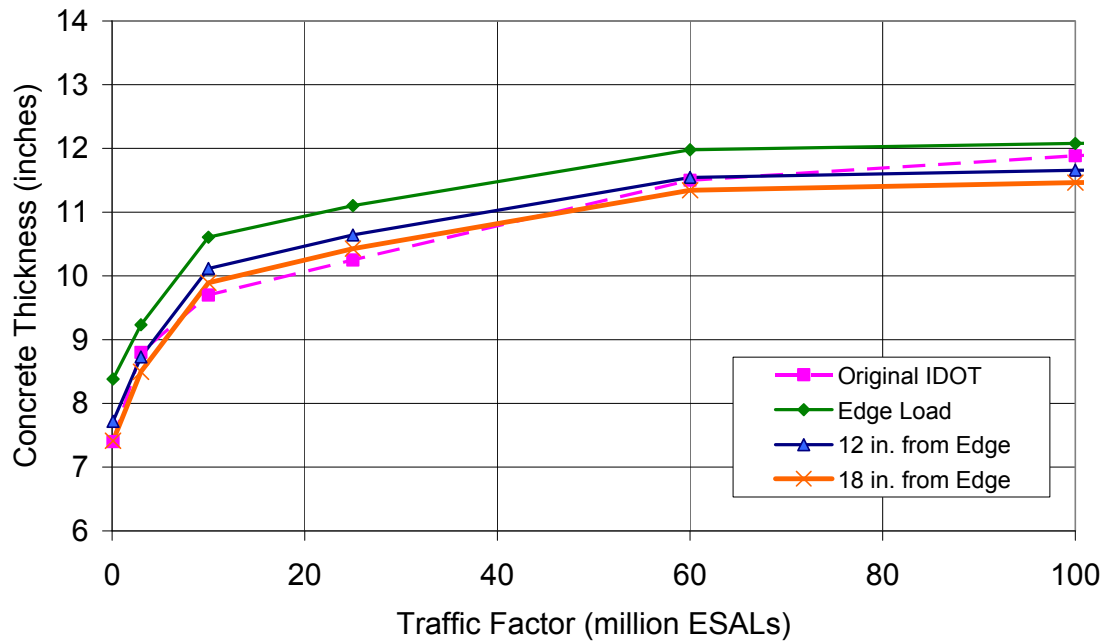


Figure 13. Sensitivity chart of accounting for 0-, 12-, or 18-in. mean distance of traffic wander from the edge of the slab (comparison to current IDOT design also shown).

#### 4.2.4 Joint Spacing

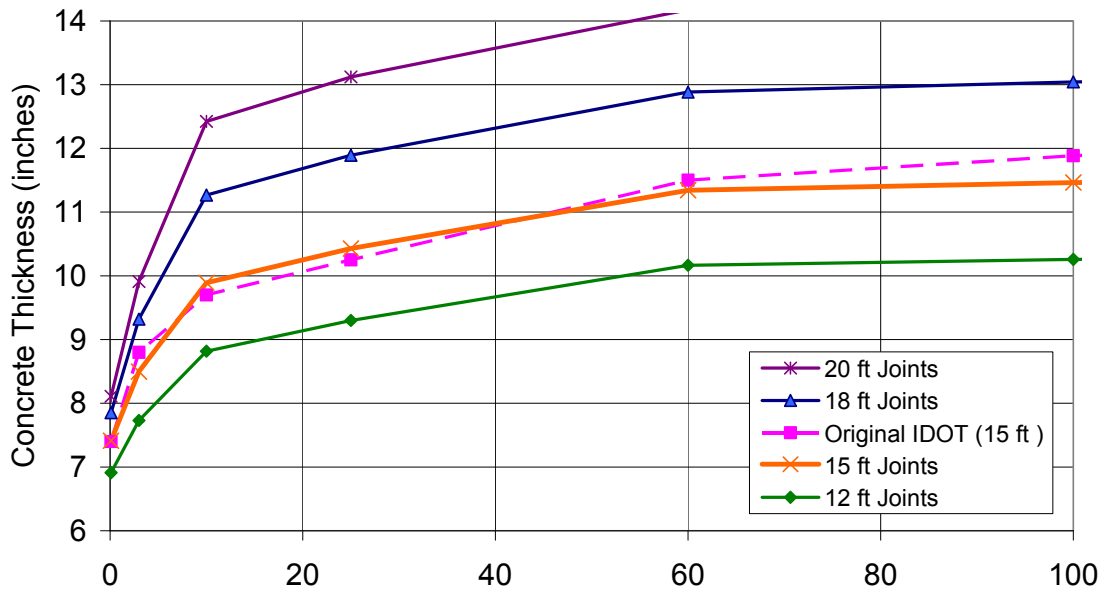


Figure 14. Sensitivity chart for 12-, 15-, 18-, and 20-ft joint spacing using the new design and compared to current IDOT design (assumes 15-ft joint spacing).

#### 4.2.5 Concrete Strength

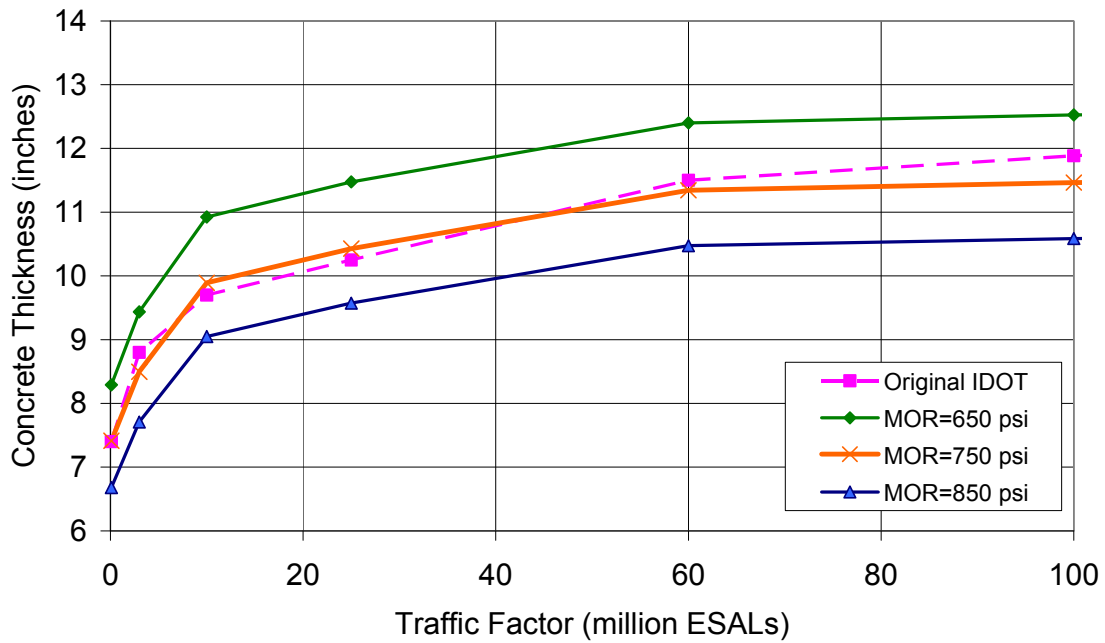


Figure 15. Sensitivity chart of the mean concrete flexural strength (using 3<sup>rd</sup>-point bending) at 650, 750, and 850 psi and compared to current IDOT design.

#### 4.2.6 Temperature Determination Method

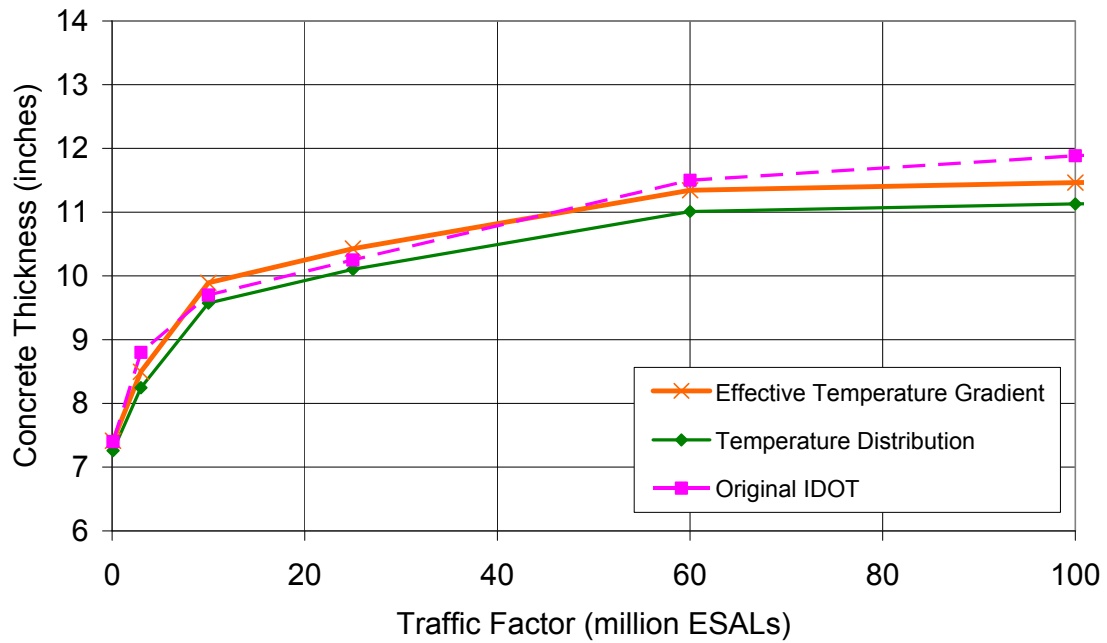


Figure 16. Sensitivity of the design based on Effective Temperature Gradient or Temperature Distribution approach compared to current IDOT design.

#### 4.2.7 Reliability

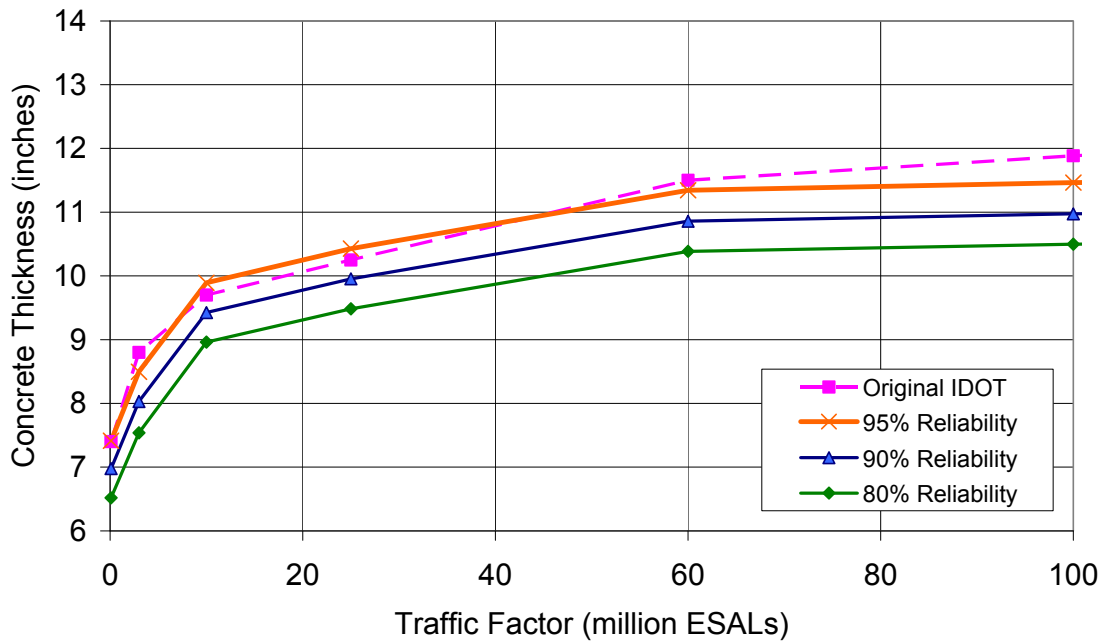


Figure 17. Sensitivity chart showing the influence of different Reliability levels (80, 90, and 95%) with the ACPA fatigue algorithm compared to current IDOT design.

The design sensitivity study has confirmed that many of the assumptions made in Section 4.1, such as the shoulder load transfer efficiency of 70%, concrete flexural strength of 750 psi, unbonded slab–base interface, 18-in. mean wheel path, and 95% reliability, are valid. The most sensitive design inputs were the slab–base interface, concrete flexural strength, and the slab length. The concrete strength directly affects the fatigue life of the slab and the slab length affects the curling stress calculation. Reducing or increasing the slab size may be required on special projects to accommodate existing pavement geometry, but generally, 15-ft. slabs are recommended. It is also recommended that the slab–base interface not be changed to “bonded” due to its significant effect on slab thickness and the difficulty in assuring bond through the life of the slab. Both methods to characterize the variation in temperature distribution in the slab gave similar slab thickness results.



## CHAPTER 5. CONCLUSIONS AND RECOMMENDATIONS

A mechanistic-empirical method to design jointed plain concrete pavements has been used in the state of Illinois for the past two decades to limit slab fatigue cracking to an acceptable level. The current IDOT method, the Mechanistic Empirical Pavement Design Guide (MEPDG), and a rigid pavement analysis program for design (RadiCAL) were thoroughly reviewed to determine what possible changes needed to be made based on research over the past 15 years. The initial research focused on the necessity of a JPCP method that accounted for geographic location in the state of Illinois, as well as site-specific load spectra data to characterize truck traffic.

For multiple locations in Illinois, the MEPDG evaluation produced some required slab thickness differences suggesting that temperature changes have an effect. However, there was no clear geographical demarcation to the results and thus, a single temperature zone for the state of Illinois is still deemed sufficient. Another major feature of the MEPDG is implementation of site-specific load spectra for a design. An analysis of MEPDG using site-specific load spectra collected at a variety of Illinois weigh stations and one WIM site showed there was less than 0.5 in. difference in the required slab thickness for a given temperature zone and ESAL count. Thus, IDOT's use of ESALs or traffic factors is still just as valid for predicting fatigue cracking as using load spectra analysis. A field FWD study found that JPCP in Illinois had low levels of built-in curling; thus, the likelihood of alternative modes of cracking such as longitudinal or corner cracks is not very probable assuming there is no slab geometry or there are no concrete material changes. Finally, the effect of nonlinear temperature profile on the tensile stresses was evaluated in the program RadiCAL. Although the nonlinear temperature stresses affect the magnitude of the total tensile stresses, especially for top-down cracking, for mid-slab edge load stress analysis using the ESAL concept, it will not significantly affect the design thickness. Thus, use of a linear temperature profile is still recommended.

The existing JPCP design charts for Illinois conditions were based on a computer program called ILLIJOINT. A new design procedure is proposed, using mechanistic-empirical principles similar to the current method, and is implemented into a user-friendly spreadsheet program. The proposed JPCP design process uses published load stress algorithms developed by Salsilli (1991) and accounts for curling stresses based on a single climatic zone in Illinois. The proposed method allows the user to input the pavement layer and slab geometry, layer material property inputs, concrete strength, slab-base interface condition, and expected number of design lane ESALs. The three shoulder types that are considered are asphalt concrete, tied concrete, and widened lane. Several fatigue algorithms were coded into the proposed design process, but the ACPA fatigue algorithm is recommended, since it takes into account reliability and is based on the fatigue failure of laboratory concrete beam specimens. Due to the limited set of available JPCP field performance data in Illinois, the proposed method was compared with the existing method for reasonableness without the need for fatigue damage to slab cracking calibration. Further field verification needs to be completed based on currently constructed JPCP in Illinois.

Design charts developed from this proposed design procedure indicate required slab thicknesses are most sensitive to shoulder type, concrete strength, slab size, and interface bonding condition. Subgrade stiffness has only a minor effect on the fatigue life of concrete pavements. Based on findings from the program RadiCAL, the required thickness of widened lanes is recommended to be no thinner than that of tied concrete shoulders with high load transfer to avoid alternative cracking modes emanating from the

transverse joint. The slab–base interface condition should be assumed to be unbonded until sufficient data on the long-term bond level is known for Illinois concrete pavement sections. A joint spacing of 15 ft should continue to be used, but a 12-ft spacing can be used in locations that have experienced premature cracking. The recommended design concrete flexural strength at 90 days using 3<sup>rd</sup>-point loading is 750 psi. This MOR should be used for all designs, since it approximately represents mean design strength of concrete mixtures in Illinois based on their current mixture design specifications.

## **5.1 FUTURE WORK ADVANCEMENTS**

The current M-E design methods (MEPDG, RadiCAL, and current IDOT design) are principally similar and only differ in terms of how, the location, and the number of times the stresses are calculated. Further refinement of how often stresses are calculated won't make much difference in the final design answer, since the weakest links in the design methods are the selection of the fatigue algorithm, material fracture properties, and the assumption that concrete does not progressively fail. For future design principles to be more powerful, they will need to account for the structure–material interaction and the progressive cracking of the concrete material under mechanical and environmental conditions. The use of fracture mechanics is sure to be part of any next-generation concrete pavement design methods. Another key aspect of longer-life concrete pavement is quantifying the interaction between the concrete slab and the underlying support layers to prevent premature loss of support or erosion.

## REFERENCES

- AASHTO (1986). *Guide for Design of Pavement Structures*. American Association of State Highway and Transportation Officials, Washington, DC.
- ACPA (2005), *StreetPave* (concrete thickness design software), American Concrete Pavement Association, Skokie, IL
- ARA (2004). "Appendix JJ: Transverse Joint Faulting Model," National Cooperative Highway Research Program Project 1-37A.
- ARA, Inc. (2007). *Interim Mechanistic-Empirical Pavement Design Guide Manual of Practice*. Final Draft. National Cooperative Highway Research Program Project 1-37A.
- Armaghani, J.M., T.J. Larsen, and L.L. Smith (1987). "Temperature Response of Concrete Pavements", *Transportation Research Record 1121*, TRB, National Research Council, Washington, D.C., pp. 23-33.
- ASTM C 2487-02 (2003). "Classification of Soils for Engineering Purposes" *2003 Annual Book of ASTM Standards*, Vol. 04.02. Philadelphia, PA.
- ASTM C 293-02 (2003). "Standard Test Method for Flexural Strength of Concrete (Using Simple Beam With Center-Point Loading)." *2003 Annual Book of ASTM Standards*, Vol. 04.02. Philadelphia, PA.
- ASTM C 78-02 (2003). "Standard Test Method for Flexural Strength of Concrete (Using Simple Beam with Third-Point Loading)." *2003 Annual Book of ASTM Standards*, Vol. 04.02. Philadelphia, PA.
- Awad, M.E. and H.K. Hilsdorf (1974). "Strength and Deformation Characteristics of Plain Concrete Subjected to High Repeated and Sustained Loads," *Fatigue of Concrete: Abeles Symposium*, Detroit, MI, ACI Publication SP-41, ACI, Farmington Hills, MI, pp. 1-13.
- Ballinger, C.A. (1972), "Cumulative Fatigue Damage Characteristics", *Highway Research Record No. 370*, Highway Research Board, National Research Council, Washington, D.C., pp. 48-60.
- Banan, M-R. (1995). Data-based Mathematical Modeling: Development and Application. PhD dissertation, University of Illinois, Urbana, IL.
- Barenberg, E.J. (1991), Review of Illinois Department of Transportation Rigid Pavement Design Curves, 35 pp.
- Barenberg, E.J. (1991), Development of Revised J-PCC Design Curve for IDOT, Memo to IDOT, 11 pp.
- Barenberg, E.J. (1994). ILLICON computer code. University of Illinois, Urbana, IL.

- Beckemeyer, C.A., L. Khazanovich, and H.T. Yu (2002). "Determining the Amount of Built-in Curling in JPCP: A Case Study of Pennsylvania I-80," *Transportation Research Record: Journal of the Transportation Research Board*, No. 1809, Transportation Research Board of the National Academies, Washington, D.C., pp. 85-92.
- Becker, J.M., M.I. Darter, M.B. Snyder, and R.E. Smith (1984). *Concrete Pavement Evaluation System (COPES)*, NCHRP Report No. 227, Final Report, NCHRP Project 1-19.
- Beyer, M. and Roesler, J.R. (2009), *Mechanistic-Empirical Design Concepts for Continuously Reinforced Concrete Pavements in Illinois*, Final Report, Illinois Center for Transportation, University of Illinois, Urbana, IL, 85 pp.
- Boresi, A.P. (1965). *Elasticity in Engineering Mechanics*, Prentice-Hall, Englewood Cliffs, N.J., pp. 222-223.
- Bradbury, R.D. (1938). *Reinforced Concrete Pavements*. Wire Reinforcement Institute, Washington, D.C.
- Byrum, C.R. (2000). "Analysis by High Speed Profile of Jointed Concrete Pavement Slab Curvatures", *Transportation Research Record 1730*, TRB, National Research Council, Washington, D.C., pp. 1-9.
- Byrum, C.R., and W. Hansen (1994). "Influence Function Approach to Analysis of Jointed Portland Cement Concrete Pavement," *Transportation Research Record 1449*, TRB, National Research Council, Washington, D.C., pp. 148-158.
- Choubane, B., and M. Tia (1992). "Nonlinear Temperature Gradient Effect on Maximum Warping Stresses in Rigid Pavements," *Transportation Research Record 1370*, TRB, National Research Council, Washington, D.C., pp. 11-19.
- Choubane, B., and M. Tia (1995), "Analysis and Verification of Thermal-Gradient Effects on Concrete Pavement," *Journal of Transportation Engineering*, Vol. 121, No. 1, ASCE, Reston, VA, pp. 75-81.
- Darter, M.I. (1977). *Design of Zero-Maintenance Plain Jointed Pavements*. Report FHWA-RD-77-111. Federal Highway Administration, U.S. Department of Transportation, Washington, D.C..
- Darter, M.I., K.T. Hall, and C. Kuo (1995). *Support Under Portland Cement Concrete Pavements*. NCHRP Report 372. TRB, National Research Council, Washington, D.C..
- Darter, M.I., L. Khazanovich, M.B. Snyder, S. Rao, and J. Hallin (2001). "Development and Calibration of a Mechanistic Design Procedure for Jointed Plain Concrete Pavements," *Proceedings of the 7th International Conference on Concrete Pavements*, Orlando, FL, Vol. 1, pp. 113-131.
- Domenichini, L. and A. Marchionna (1981). "Influence of Stress Range on Plane Concrete Pavement Fatigue Design," *Proceedings of the Second International Conference on Concrete Pavement Design*, Purdue University. West Lafayette, IN, pp. 55-65.

Eisenmann, J., and G. Leykauf (1990a). "Effects of Paving Temperature on Pavement Performance," *Proceedings of the 2nd International Workshop on the Theoretical Design of Concrete Pavements*, Siquenza, Spain.

Eisenmann, J., and G. Leykauf (1990b). "Simplified Calculation of Slab Curling Caused by Surface Shrinkage," *Proceedings of the 2nd International Workshop on the Theoretical Design of Concrete Pavements*, Siquenza, Spain, pp. 185-197.

ERES Consultants (1999). *ISLAB2000 Finite Element Code for Rigid Pavement Analysis*. Version 3.6, Champaign, IL.

Federal Airport Administration. (1995). "Airport Pavement Design and Evaluation." *Advisory Circular 150/5320-6D*, Federal Aviation Administration, Washington, DC.

Grasley, Z.C. (2003). Internal Relative Humidity, Drying Stress Gradients, and Hygrothermal Dilation of Concrete. MS thesis. University of Illinois at Urbana-Champaign, Urbana, IL.

Hansen, W., E.A. Jensen, and P. Mohr (2001). *The Effects of High Strength and Associated Concrete Properties on Pavement Performance*. Report FHWA-RD-00-161. Federal Highway Administration, U.S. Department of Transportation, Washington, D.C..

Harik, I.E., P. Jianping, H. Southgate, and D. Allen (1994). "Temperature Effects on Rigid Pavements," *Journal of Transportation Engineering*, Vol. 120, No. 1, ASCE, Reston, VA, pp. 127-143.

Harvey, J.T., A. Chong, and J.R. Roesler (2000a). *Climate Regions for Mechanistic-Empirical Pavement Design in California and Expected Effects on Performance*, Draft Report, Pavement Research Center, University of California-Berkeley, Richmond, CA.

Harvey, J.T., J.R. Roesler, J. Farver, and L. Liang (2000b). *Preliminary Evaluation of Proposed LLPRS Rigid Pavement Structures and Design Inputs*, Final Report, FHWA/CA/OR-2000/02, Pavement Research Center, University of California-Berkeley, Richmond, CA.

Hatt, W. K. (1923). "The Effect of Moisture on Concrete," *ASCE Transactions*, Vol. 89, ASCE, Reston, VA, pp. 271-315.

Heath, A.C., and J.R. Roesler (2000). "Top-Down Cracking of Rigid Pavements Constructed with Fast-Setting Hydraulic Cement Concrete," *Transportation Research Record: Journal of the Transportation Research Board*, No. 1712, TRB, National Research Council, Washington, D.C., pp. 3-12.

Heath, A.C., J.R. Roesler, and J.T. Harvey (2003) "Modeling Longitudinal, Corner and Transverse Cracking in Jointed Concrete Pavements," *International Journal of Pavement Engineering*, Vol. 4, No. 1, pp. 51-58.

Hiller, J.E., and J.R. Roesler (2002) "Transverse Joint Analysis for Use in Mechanistic-Empirical Design of Rigid Pavements," *Transportation Research Record: Journal of the*

*Transportation Research Board, No. 1809*, Transportation Research Board of the , National Academies, Washington, D.C., pp. 42-51.

Hiller, J.E., and J.R. Roesler (2005a) "Determination of Critical Concrete Pavement Fatigue Damage Locations Using Influence Lines," *Journal of Transportation Engineering*, Vol. 131, No. 8, ASCE, Reston, VA, pp. 599-607.

Hiller, J.E., and J.R. Roesler (2005b) *User's Guide for Rigid Pavement Analysis for Design in California (RadiCAL) Software*. Version 1.2, Pavement Research Center, University of California-Berkeley, Richmond, CA.

Hiller, J.E., and J.R. Roesler (2006). "Alternative Failure Modes for Long-life Jointed Plain Concrete Pavements," *Proceedings of the International Conference on Long-Life Concrete Pavements*, Chicago, IL.

Hiller, J.E. (2007). *Development of Mechanistic-Empirical Principles for Jointed Plain Concrete Pavement Fatigue Design*, PhD dissertation. University of Illinois at Urbana-Champaign, Urbana, IL.

Huang, Y.H. (1993). *Pavement Analysis and Design*. Prentice Hall, Englewood Cliffs, NJ

Huang, Y.H. (2004). *Pavement Analysis and Design*. Prentice Hall, Englewood Cliffs, NJ, 2<sup>nd</sup> Edition.

Huang, Y.H. and Wang, S.T. (1973), "Finite-Element Analysis of Concrete Slabs and Its Implications for Rigid Pavement Design," *Highway Research Record 466*, Highway Research Board, pp. 55-69.

Hveem, F. N. (1951). "Slab Warping Affects Pavement Joint Performance," *Journal of American Concrete Institute*, Vol. 47, ACI, Skokie, IL, pp. 797-808.

IDOT (2002). *Bureau of Environment and Design Manual*, Chapter 54: Pavement Design. Illinois Department of Transportation, Springfield, IL.

Ioannides, A.M. (1984). *Analysis of Slabs on Grade for a Variety of Loading and Support Conditions*. PhD dissertation. University of Illinois at Urbana-Champaign, Urbana, IL.

Ioannides A. M., and G.T. Korovesis (1990). "Aggregate Interlock: A Pure-Shear Load Transfer Mechanism," *Transportation Research Record 1286*, TRB, National Research Council, Washington, D.C., pp. 14-24.

Ioannides, A.M., and L. Khazanovich, (1998). "Nonlinear Temperature Effects on Multilayered Concrete Pavements," *Journal of Transportation Engineering*, Vol. 124, No. 2, ASCE, Reston, VA, pp. 128-136.

Ioannides, A.M., L. Khazanovich, and J.L. Becque. (1992), "Structural Evaluation of Base Layers in Concrete Pavement Systems," *Transportation Research Record 1370*, TRB, National Research Council, Washington D.C., pp. 20-28.

Ioannides, A.M., and R. Salsilli-Murua (1999). "Temperature Curling in Rigid Pavement: An Application of Dimensional Analysis", *Transportation Research Record 1227*, TRB, National Research Council, Washington, D.C., pp. 1-11.

Janssen, D.J., and M.B. Snyder (2000). "Temperature-Moment Concept for Evaluating Pavement Temperature Data," *Journal of Infrastructure Systems*, Vol. 6, No. 2, ASCE, Reston, VA, pp. 81-83.

Jeong, J.H., and D.G. Zollinger (2005). "Environmental Effects on the Behavior of Jointed Plain Concrete Pavements," *Journal of Transportation Engineering*, Vol. 131, No. 2, ASCE, Reston, VA, pp 140-148.

Kannekanti, V., and J.T. Harvey (2006). "Sensitivity Analysis of 2002 Design Guide Distress Prediction Models for Jointed Plain Concrete Pavement," *Transportation Research Record: Journal of the Transportation Research Board*, No. 1947, Transportation Research Board of the National Academies, Washington, D.C., pp. 91-100.

Kesler, C.E. (1953), "Effect of Speed of Testing on Flexural Fatigue Strength of Plain Concrete," , *Highway Research Board Proceedings*, Vol. 32, Highway Research Board, National Research Council, Washington, D.C., pp. 251-258.

Khazanovich, L. (1994). Structural Analysis of Multi-Layered Concrete Pavement Systems. PhD dissertation. University of Illinois at Urbana-Champaign, Urbana, IL.

Khazanovich, L., and J.R. Roesler (1997) "DIPLOBACK: Neural-Network-based Backcalculation Program for Composite Pavements," *Transportation Research Record 1570*, TRB, National Research Council, Washington, D.C., pp. 143-150.

Khazanovich, L., O.I. Selezneva, H.T. Yu, and M.I. Darter (2001) "Development of Rapid Solutions for Prediction of Critical Continuously Reinforced Concrete Pavement Stresses," *Transportation Research Record: Journal of the Transportation Research Board*, No. 1778, TRB, National Research Council, Washington, D.C., pp. 64-72.

Korovesis, G. T. (1990). Analysis of Slabs-on-Grade Pavement Systems Subjected to Wheel and Temperature Loadings. PhD dissertation. University of Illinois at Urbana-Champaign, Urbana, IL.

Larson, G. and B.J. Dempsey (1997). *Enhanced Integrated Climatic Model Version 2.0 (EICM)*. University of Illinois at Urbana-Champaign, Urbana, IL.

Lee, Y.-H. (1994), Development of pavement prediction models, PhD dissertation, University of Illinois at Urbana-Champaign, Urbana, IL.

Lee, Y.-H., and M.I. Darter (1993). "Mechanistic Design Models of Loading and Curling in Concrete Pavements," *Proceedings, Airport Pavement Innovations – Theory to Practice*, Vicksburg, MS, ASCE Specialty Conference, ASCE, Reston, VA.

Lee, Y.-H. and M.I. Darter. (1994), "Loading and Curling Stress Models for Concrete Pavement Design," *Transportation Research Record 1449*, TRB, National Research Council, Washington, D.C., pp. 101-113.

Lu, Q., T. Le, J.T. Harvey, J. Lea, R. Quinley, D. Redo, and J. Avis (2001) *Truck Traffic Analysis using WIM Data in California*, Draft Report, Pavement Research Center, University of California-Berkeley, Richmond, CA.

Masad, E., R. Taha, and B. Muhunthan (1996). "Finite Element Analysis of Temperature Effects on Plain-Jointed Concrete Pavements," *Journal of Transportation Engineering*, Vol. 122, No. 5, ASCE, Reston, VA, pp. 388-398.

McCullough, B.F. and T. Dossey (1999). "Considerations for High-Performance Concrete Paving: Recommendations from 20 Years of Field Experience in Texas," *Transportation Research Record 1684*, TRB, National Research Council, Washington, D.C., pp. 17-24.

McCullough, B.F., D.G. Zollinger, and T. Dossey (2000). *Evaluation of the Performance of Texas Pavements Made with Different Coarse Aggregates*, Report No. 7-3925-1, Center for Transportation Research and Texas Transportation Institute, College Station, TX.

McGhee, K.H. (1995). Design, Construction, and Maintenance of PCC Pavement Joints. *NCHRP Synthesis of Highway Practice 211*. TRB, National Research Council, Washington, D.C.

Miner, M.A. (1945). "Cumulative Damage in Fatigue," *Transactions of the ASME*, Vol. 67, ASME, New York, NY, pp. A159-A164.

Mirambell, E. (1990). "Temperature and Stress Distributions in Plain Concrete Pavements under Thermal and Mechanical Loads," *Proceedings of the Second International Workshop on the Design and Rehabilitation of Concrete Pavements*, Siguenza, Spain, pp. 121-135.

Mohamed, A.R., and W. Hansen (1997). "Effect of Nonlinear Temperature Gradient on Curling Stresses in Concrete Pavements," *Transportation Research Record 1568*, TRB, National Research Council, Washington, D.C., pp. 65-71.

Murdock, J.W. and C.E. Kesler, (1958). "Effect of Range of Stress on Fatigue Strength of Plain Concrete Beams," *Journal of the American Concrete Institute*, Vol. 30, No. 2, ACI, Farmington Hills, MI, pp. 221-231.

Older, C. (1924). "Highway Research in Illinois," *Transactions of the American Society of Civil Engineers*, Vol. 87, ASCE, Reston, VA, pp. 1180-1224.

Packard, R.G. (1984). *Thickness Design for Concrete Highway and Street Pavements*. Portland Cement Association, Skokie, IL.

Packard, R.G. and S.D. Tayabji (1985). "New PCA Thickness Design Procedure for Concrete Highway and Street Pavements," *Proceedings, 3rd International Conference on Concrete Pavement Design*. Purdue University, West Lafayette, IN, pp. 225-236.

Pickett, G., and G.K. Ray (1951). "Influence Charts for Concrete Pavements," *Transactions of the American Society of Civil Engineers*, Vol. 116, ASCE, Reston, VA.



- Poblete, M., A. Garcia, J. David, P. Ceza, and R. Espinosa (1990). "Moisture Effects on the Behaviour of PCC Pavements," *Proceedings of the 2nd International Workshop on the Theoretical Design of Concrete Pavements*, Siquenza, Spain.
- Poblete, M., R. Salsilli, R. Valenzuela, A. Bull, and P. Spratz (1988). "Field Evaluation of Thermal Deformations in Undoweled PCC Pavement Slabs," *Transportation Research Record 1207*, TRB, National Research Council, Washington, D.C., pp. 217-228.
- Portland Cement Association. (1984). *Thickness Design for Concrete Highway and Street Pavements*. Report No. EB109-01P, Skokie, IL, 47 pp.
- Post-Tensioning Institute (1991). Design and Construction of Post-Tensioned Slabs on Ground, Phoenix, AZ.
- Raithby, K.D. and J.W. Galloway (1974), "Effects of Moisture Condition, Age and Rate of Loading on Fatigue of Plain Concrete," *Fatigue of Concrete: Abeles Symposium*, , Detroit, MI, ACI Publication SP-41, ACI, Farmington Hills, MI, pp.15-34.
- Rao, C.B., E.J. Barenberg, M.B. Snyder, and S.K. Schmidt (2001). "Effects of Temperature and Moisture on the Response of Jointed Concrete Pavements," *Proceedings of the 7th International Conference on Concrete Pavements*, Orlando, FL, Vol. 1, pp. 23-38.
- Rao, S. (2005). Characterization of Built-In Curling, Damage, and Cracking in Accelerated-Pavement-Tested Restrained Concrete Slabs at Palmdale, CA. PhD dissertation. University of Illinois at Urbana-Champaign, Urbana, IL.
- Rao, S., and J.R. Roesler (2003). *Analysis and Estimation of Effective Built-In Temperature Difference for North Tangent Slabs*, Draft report to Pavement Research Center, University of California-Berkeley, Richmond, CA.
- Rao, S., and J.R. Roesler (2004). "Cumulative Fatigue Damage Analysis of Concrete Pavement using Accelerated Pavement Testing Results," *Proceedings of the 2nd International Conference on Accelerated Pavement Testing*, Minneapolis, MN.
- Rao, S., and J.R. Roesler (2005a). "Nondestructive Testing of Concrete Pavements for Characterization of Effective Built-In Curling," *ASTM Journal of Testing and Evaluation*, Vol. 33, No. 5, ASCE, Reston, VA, pp. 356-363.
- Rao, S., and J.R. Roesler (2005b), "Characterizing Effective Built-In Curling from Concrete Pavement Field Measurements," *ASCE Journal of Transportation Engineering*, Vol. 131, No. 4, ASCE, Reston, VA, pp. 320-327.
- Rasmussen, R O and McCullough, B.F. (1998). *A Foundation for High Performance Jointed Concrete Pavement Design and Construction Guidelines*, Transtec Consultants, Austin, TX.
- Reed, C. and Schutzbach, A. (1993). Evaluating Pavement Design Features – Five Year Performance Evaluation of FA 401 and FA 409. Division of Highways, Bureau of Materials and Physical Research, Illinois Department of Transportation, Springfield, IL..

- Riley, R.C., L. Titus-Glover, J. Mallela, S. Waalkes, and M. Darter, (2005). "Incorporation of Probabilistic Concepts Into Fatigue Analysis of Ultrathin Whitetopping as Developed for the American Concrete Pavement Association," *Proceedings of Conference on Best Practices in Ultrathin and Thin Whitetoppings*, Denver, CO, pp.288-317.
- Rodden, R. (2006). Analytical Modeling of Environmental Stresses in Concrete Slabs. MS thesis. University of Illinois at Urbana-Champaign, Urbana, IL.
- Rufino, D.M. (2003). Mechanistic Analysis of In-Service Airfield Concrete Pavement Responses. PhD dissertation, University of Illinois at Urbana-Champaign, Urbana, IL.
- Salsilli-Murua, R.A. (1991). Calibrated Mechanistic Design Procedure for Jointed Plain Concrete Pavements. PhD dissertation, University of Illinois at Urbana-Champaign, Urbana, IL.
- Schmidt, S.K. (2001). Analysis of "Built-In" Curling and Warping in PCC Pavements. MS thesis. University of Minnesota, Minneapolis, MN.
- Smith, K.D., M.J. Wade, D.G. Peshkin, L. Khazanovich, H.T. Yu, and M.I. Darter (1998). *Performance of Concrete Pavements; Volume II—Evaluation of In-service Concrete Pavements*. FHWA-RD-95-110, Federal Highway Administration, U.S. Department of Transportation, Washington, DC.
- Tabatabaie-Raissi, A.M. (1977). Structural Analysis of Concrete Pavement Joints, PhD dissertation, University of Illinois at Urbana-Champaign, Urbana, IL.
- Tabatabaie, A.M., and E.J. Barenberg, (1978). "Finite Element Analysis of Jointed of Cracked Concrete Pavements", *Transportation Research Record 671*, TRB, National Research Council, Washington, D.C., pp. 11-18.
- Teller, L.W., and E.C. Sutherland, (1935). "The Structural Design of Concrete Pavements, Part 2: Observed Effects of Variations in Temperature and Moisture on the Size, Shape and Stress Resistance of Concrete Pavement Slabs," *Public Roads*, Vol. 15, No. 9, pp. 169-197.
- Tepfers, R. (1979). "Tensile Fatigue Strength of Plain Concrete," *Journal of the American Concrete Institute*, Vol. 76, ACI, Farmington Hills, MI, pp. 919-933.
- Tepfers, R. and Kutti, T (1979). "Fatigue Strength of Plain, Ordinary, and Lightweight Concrete," *Journal of the American Concrete Institute*, Vol. 76, ACI, Farmington Hills, MI, pp. 635-652.
- Thomlinson, L. (1940). "Temperature Variations and Consequent Stresses Produced by Daily and Seasonal Temperature Cycles in Concrete Slabs," *Concrete Constructional Engineering*, Vol. 36. No. 6, pp. 298-307 and Vol. 36. No. 7, pp. 352-260, London, U.K.
- Thompson, M. R. and Cation, K., (1986). *A Proposed Full-Depth Asphalt Concrete Thickness Design Procedure*, Research Report FHWA/IL/UI 213, Illinois Cooperative

Highway and Transportation Research Program, University of Illinois at Urbana-Champaign, Urbana, IL, 1986.

Thompson, M.R. and E.J. Barenberg (1992). *Calibrated Mechanistic Structural Analysis Procedure for Pavements - Phase 2*, NCHRP Report 1-26, HRB, National Research Council, Washington, D.C.

Timoshenko, S., and J.M. Lessells (1925). *Applied Elasticity*. Westinghouse Technical Night School Press, East Pittsburgh, PA., pp. 272–273.

Titus-Glover, L., J. Mallela, J. Darter, G. Voigt, and S. Waalkes, (2005). “Enhanced Portland Cement Concrete Fatigue Model for StreetPave,” *Transportation Research Record: Journal of the Transportation Research Board*, No. 1919, Transportation Research Board of the National Academies, Washington, D.C., pp. 29-37.

Vandenbossche, J.M. (2003). *Interpreting Falling Weight Deflectometer Results for Curled and Warped Portland Cement Concrete Pavements*. PhD dissertation. University of Minnesota, Minneapolis, MN.

Westergaard, H.M. (1927), “Analysis of Stresses in Concrete Pavements Due To Variations of Temperature,” *Highway Research Board, Proceedings*, Vol. 6, Highway Research Board, National Research Council, Washington D.C., pp. 201-217.

Westergaard, H.M. (1948). “New Formulas for Stresses in Concrete Pavements for Airfields,” *Transactions*, ASCE, pp. 113.

Yu, H.T., L. Khazanovich, M.I. Darter, and A. Ardani (1998), “Analysis of Concrete Pavement Responses to Temperature and Wheel Loads Measured from Instrumented Slabs,” *Transportation Research Record* 1639, TRB, National Research Council, Washington, D.C., pp. 94-101.

Yu, H.T., and L. Khazanovich (2001). “Effects of Construction Curling on Concrete Pavement Behavior,” *Proceedings of the 7th International Conference on Concrete Pavements*, Orlando, FL, Vol. 1, pp. 55-68.

Zollinger, D. G. and E. J. Barenberg (1989a) “Background for Development of Mechanistic Based Design Procedure for Jointed Concrete Pavements,” *Civil Engineering Studies, Transportation Engineering Series No. 56*, Illinois Cooperative Highway Research Program Series No. 224, Project IHR-518, Urbana, IL.

Zollinger, D.G., and E.J. Barenberg (1989b). *Proposed Mechanistic Based Design Procedures for Jointed Concrete Pavements*. Report No. FHWA/IL/UI 225, University of Illinois at Urbana-Champaign, IL.

Zollinger, D. (2009), personal communication.

# APPENDIX A. REVIEW OF IDOT'S EXISTING JPCP DESIGN METHOD

## A.1 OBJECTIVE

The purpose of this review is to summarize what is documented as the method used to generate the existing IDOT JPCP thickness design curves, and the related inputs (e.g., see Figure A.1, in Chapter 54 of the BDE Manual [IDOT, 2002]). Multiple sources will be used for this summary, including the following references: Zollinger and Barenberg (1989a), Zollinger and Barenberg (1989b), and several written memos between IDOT and the University of Illinois in the summer of 1991.

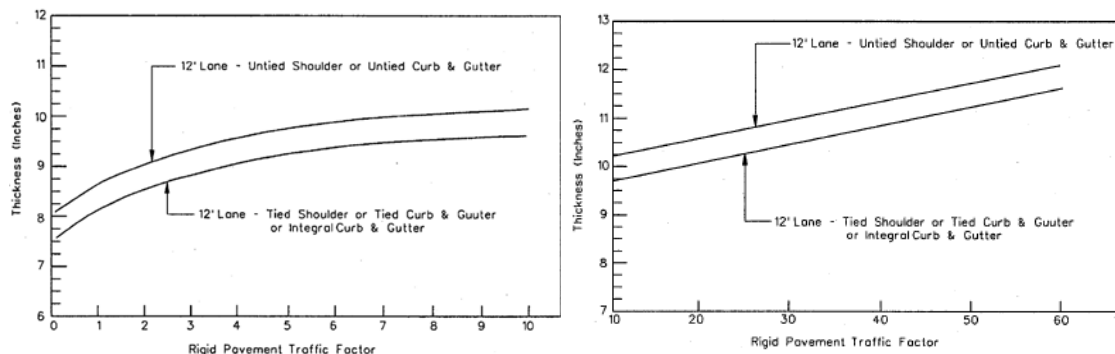


Figure A.1. Rigid pavement design charts for poor subgrade soil (IDOT, 2002).

## A.2 BACKGROUND

The current IDOT JPCP method is considered a mechanistic-empirical (M-E) design procedure and was one of the first state-developed mechanistic-empirical processes in the United States. The procedure was first introduced in 1989 and the final modification adopted into practice in 1991. The process of IDOT's M-E procedure is selecting the appropriate values for the input variables such as layer material properties and traffic and then defining the initial design options such as shoulder type, base type, reliability, and transverse joint type. The structural model, ILLISLAB (Tabatabaie and Barenberg, 1978; Ioannides, 1984), was used to calculate the critical mid-slab edge tensile stress at the bottom of the slab, which included both load and temperature curling stresses. A fatigue analysis was completed to linearly sum the fatigue damage for various conditions of load and temperature stresses, as well as to develop a consideration for wander. Finally, a performance algorithm related the calculated fatigue damage to a level of slab cracking in the field for a certain degree of reliability.

The creation of the IDOT JPCP design curves from the mechanistic-empirical process described in Zollinger and Barenberg (1989a, 1989b) was done through a FORTRAN program called ILLIJOINT, which is documented in Zollinger and Barenberg (1989a). Since IDOT didn't finalize the JPCP design curves until 1991, all inputs assumed in this published program were not necessarily the same as the final inputs. The University of Illinois at Urbana-Champaign (UIUC) research team was not able to locate the final version of the ILLIJOINT program that was used to generate the curves, but the following documentation is believed to be the inputs and assumptions that were made to create IDOT's current slab thickness curves.

## **A.3 INPUTS**

### **A.3.1 Concrete Properties**

The concrete modulus of elasticity was assumed to be  $4 \times 10^6$  psi, the Poisson's ratio 0.15, and the coefficient of thermal expansion  $5 \times 10^{-6}/^{\circ}\text{F}$ . The selection of the design flexural strength of the concrete was the subject of much discussion in many memos between IDOT and Professor Barenberg after the publication of the research reports by Zollinger and Barenberg (1989a, 1989b). IDOT specified the concrete flexural strength under center-point loading to be a minimum of 650 psi at 14 days. This 14-day minimum strength translates into a mean strength at 14 days of 838 psi, assuming a 15% coefficient of variation (COV) and 93% reliability (1.5 standard deviations). Furthermore, a 14-day center-point loading was approximately equivalent to a 90-day third-point loading configuration ( $0.85 \times 1.08 \times 1.1 = 1.01$ ). Third-point loading is 85% of center-point loading and the 14 to 28- and 28 to 90-day strength gains are 8 and 10%, respectively. The mean COPES database flexural strength was finally assumed to be 752 psi and IDOT's MISTIC database from 1986–1990 found that the average flexural strength was 855 psi with a COV of 13%. From the various memos and data sets, it appeared that a design flexural strength of less than 650 psi did not make sense, and in fact, the mean strength at 90 days should be greater than 650 psi. In the creation of the IDOT design curves, it is believed that the final design strength was 750 psi. In a locally calibrated method, the magnitude of the design strength is not critical, as long as the strengths from the calibration are consistent with the design input strength values.

### **A.3.2 Subgrade Support**

The three moduli of subgrade reaction values available for Illinois soils are 50, 100, and 200 psi/in. for wheel load analysis. The documentation by Zollinger and Barenberg (1989b) states that the  $k$ -value had a spring value for one-third of the year and two-thirds of the year assumes a summer/fall/winter  $k$ -value. This assumption does not appear to show up in the ILLIJOINT code, but the program does allow for input of  $k$ -value for various percentages of times during the year. For the curling stress calculations, the  $k$ -value of the soil was always assumed to be 100 psi/in. This eliminated the potential for an increase in slab thickness, as the support layers, specifically the subgrade, became stiffer.

### **A.3.3 Traffic**

Mixed truck traffic is characterized by ESALs. IDOT has its own method for calculating the design lane ESALs based on the mixture of passenger cars and single- and multiple-unit trucks. This procedure can be found in Chapter 54 of the BDE Manual (IDOT, 2002). The mean distance from the edge of pavement to the outside edge of the traffic lane is assumed to be 18 in., although 12 in. was also an option. This is also referred to elsewhere as the mean wheel path location or lateral distribution distance. The standard deviation for this distribution is assumed to be 10 in.

### **A.3.4 Slab Geometry**

The standard slab size for the JPCP method was a 15-ft length x 12-ft width. The extended lane option added a maximum of 2-ft width to the lane and the tied concrete shoulder option was assumed to be 10 ft.

### A.3.5 Shoulder Type

Three shoulder types were used in the original development of the JPCP curves: asphalt concrete shoulders, tied concrete shoulders, and widened lane. In the 1991 design manual, the widened lane solution was eliminated since it was not being used. The tied concrete shoulder assumed that there was medium or high load transfer efficiency (LTE) across the lane-shoulder joint, which translated to 85 to 95% deflection LTE, but was not specifically documented in the ILLIJOINT program.

### A.3.6 Base Type

The base type was assumed to be a non-erodible material that would provide uniform support, control frost penetration depth, and facilitate drainage. In Zollinger and Barenberg (1989a), the base was assumed to be unbonded in the stress analysis using ILLISLAB. The authors stated that the type of bases included were CAM I, CAM II, and BAM. However, in the ILLIJOINT code, there was no input to accommodate for variation of the base type.

### A.3.7 Load and Curl Stress Algorithms

Regression equations to predict the maximum tensile stress at the bottom of the mid-slab edge were developed based on a factorial of ILLISLAB runs (Zollinger and Barenberg, 1989a) for an 18-kip single-axle load. A regression equation was also developed to predict the curling stress at the same location. The Westergaard/Bradbury equation for curling stress was not used due to its assumption that full contact condition had to be maintained between the slab and support layer. It was assumed based on field measurements and previous work by Bradbury (1938) that positive gradients occur 25% of the time, negative gradients occur 35% of the time, and zero gradients happen 40% of the time. The final equivalent gradients assumed in developing the thickness charts were +1.65°F/in. for daytime conditions and -0.65°F/in. for nighttime conditions. The following is the curling stress equation included in the ILLIJOINT program.

$$CS = \frac{(G)ET}{5 \times 10^{-6}} \left( 0.06712(K) + 79.07391 \log_{10} K + 11.72690(L) - 0.00720 KL \right. \\ \left. - 3.22139L \log_{10} K - 204.39477 \frac{H}{(K)} - 38.08854 \frac{L}{(H)} \right. \\ \left. - 8.36842 H \log_{10} K + 0.20845 LH \log_{10} K + 0.00058 LHK \right)$$

where:

CS = curl stress

H = PCC slab thickness, inches

G = thermal gradient through slab, °F/in.

K = modulus of foundation support, psi/in.

L = joint spacing, feet

ET = thermal coefficient of contraction of PCC 1oF

The coefficient of thermal expansion was not explicitly stated in the background to the design, but is  $5 \times 10^{-6}$  based on the evaluation of the ILLIJOINT code.

In general, load and temperature stresses cannot simply be added together unless the same boundary conditions exist. When slabs separate from their support at certain locations, then the superposition assumption is violated and leads to some level of error in the calculation of total stresses. To better predict the total stresses, a correction factor  $R$  is multiplied to the curling stress. This  $R$ -factor for the ILLIJOINT program is given in the main body of the text (Equation 27). The total stress is then the wheel load stress plus  $R$  multiplied by the curling stress.

### **A.3.8 Concrete Fatigue and Cracking**

The concrete beam fatigue curve used to relate the stress ratio to the allowable repetitions to failure (coded in several versions of the ILLIJOINT program) was the following equation from the Zero-Maintenance study by Darter (1977):

$$\text{Log } N = 16.61 - 17.61R$$

where  $R$  is the ratio between the tensile stress and concrete flexural strength. This equation was developed based on a probability of failure of 24% for the experimental beam fatigue data. In the proposed mechanistic-empirical method report by Zollinger and Barenberg (1989a, 1989b), they listed the 50% probability fatigue equations from Darter (1977):

$$\text{Log } N = 17.61 - 17.61R$$

This equation was used to calibrate the slab cracking performance curves discussed next. The slab cracking-to-fatigue-damage relationship was developed based on 137 sections of jointed concrete pavement with 100-ft slab sizes from the COPES database (Becker et al., 1984). A slab fatigue damage of 1.0 didn't necessarily equate to failure of the concrete pavement as originally proposed by Miner (1945) for laboratory specimen sizes. The slab cracking versus fatigue damage curves are shown in Figure A.2 along with the respective performance equations for two levels of reliability. Note, the second equation should start in the denominator with 0.01. The correlation coefficient was noted to be poor for these equations, but no other JPCP data was available at the time. For Illinois, concrete failure was defined as 20% slab cracking above a TF of 10 and 100% slab cracking at a TF of 3, with slab cracking values linearly interpolated between these two points.

## Mean Values; COPES, ILL

LogN = 17.61 - 17.61R

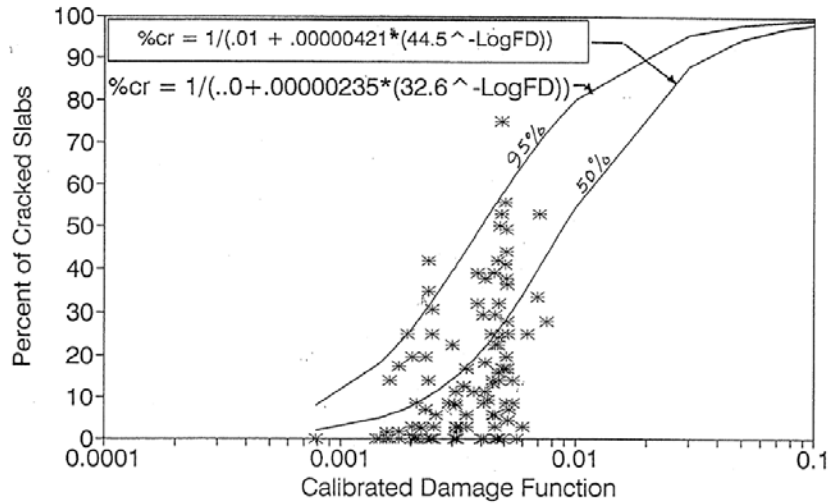


Figure A.2. Calibrated slab cracking curves for 50 and 95% reliability.

### A.3.9 Erosion

In the past, field evaluation of distressed concrete pavements have discovered voids or areas of the base not intimately supported by the concrete pavement with all types of stabilized base layers; e.g., CAM I, CAM II, and BAM. To account for this erosion for high traffic volumes, Zollinger and Barenberg (1989a) conducted an ILLISLAB analysis in which a 60-in. width along the entire longitudinal edge was assumed to be unsupported. Figure A.3 shows the increase in tensile stress at various slab thickness values and degrees of edge erosion. The increase in tensile stress for a 60-in.-wide loss of support was then added to the wheel load stress under full support conditions and the temperature curling stress. The resultant stress required an increase in the slab thickness of 1.5 in. at a TF of 60. It was also recommended that at TF < 10, little to no erosion would be assumed. Thus, the design thickness at TF = 60 was linearly connected to the thickness required at TF of 10. Figure A.4 shows the final adjustment that was made to account for erosion of the base layer.



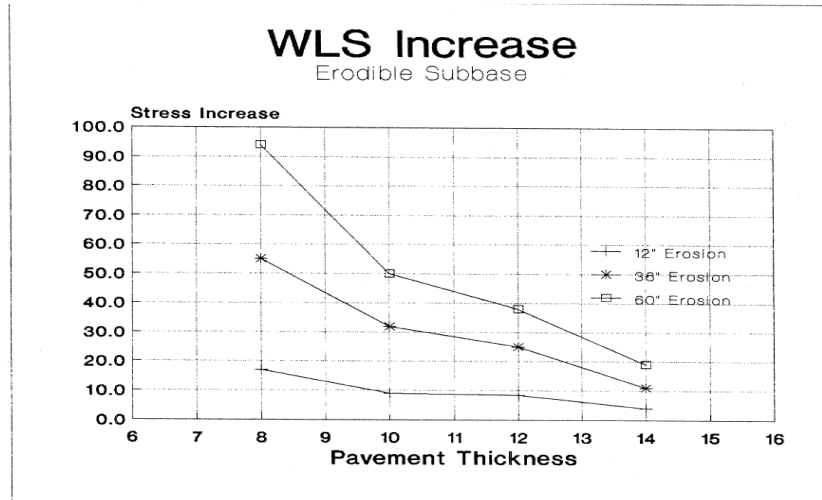


Figure 2.3 Load Stress Increase Due to Unsupported Pavement Conditions

Figure A.3. Effect of slab thickness and erosion along the longitudinal edge on tensile stress increase at mid-slab edge (Zollinger and Barenberg, 1989a).

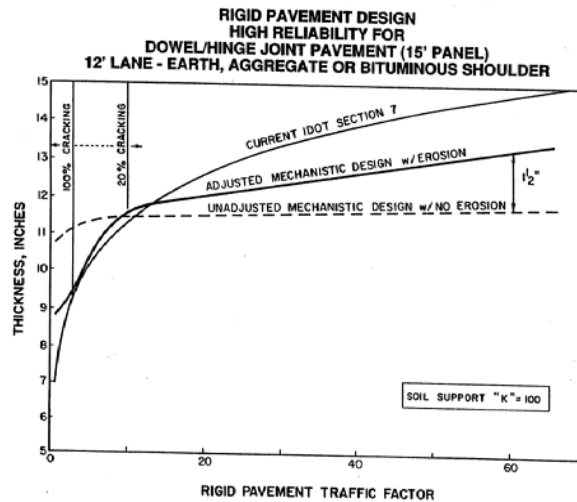


Figure 15. Mechanistic Jointed PCC Design Curve Adjusted for Erosion

Figure A.4. IDOT-adjusted concrete slab thickness curve for erosion.

# APPENDIX B. JPCP AND CRCP DESIGN COMPARISONS USING MEPDG AND IDOT DESIGN METHODS

## B1. INTRODUCTION

A series of Jointed Plain Concrete Pavement (JPCP) and Continuously Reinforced Concrete Pavement (CRCP) designs were conducted at the University of Illinois at Urbana-Champaign beginning in May 2006. The rigid pavement design methods used were the Mechanistic-Empirical Pavement Design Guide (MEPDG) and the Illinois Department of Transportation Design (IDOT). The MEPDG was implemented by using the computer software available from the internet (Version 0.91) which was developed under the National Cooperative Highway Research Program (NCHRP) project 1-37A; while the IDOT method was carried out using design nomographs presented in Chapter 54 in the Illinois Bureau of Design and Environment Manual (2002).

The main objective of these pavement designs is to compare JPCP/CRCP design results from the IDOT and MEPDG procedures and determine the sensitivity of each design method to traffic level (ESALs and load spectra), Illinois climatic zones, and shoulder type in terms of pavement slab thickness. The following appendix summarizes the inputs, assumptions, and results for JPCP and CRCP design using the IDOT and MEPDG procedures.

## B2. JPCP DESIGN

### B2.1. Mechanistic-Empirical Pavement Design Guide

#### B2.1.1. Design Inputs

The following is a list of the design inputs required for the NCHRP 1-37A design guide:

- 1) Design life: 30 years
- 2) Pavement construction: August
- 3) Pavement analysis: probabilistic
- 4) Performance criteria

Initial IRI (International Roughness Index) (in./mi):	82
Terminal IRI (in./mi):	172 <b>(N/A)</b>
Transverse cracking (% slabs cracked):	20 <b>(Failure Definition)</b>
Mean joint faulting (in.):	0.12 or 0.25 <b>(N/A)</b>
Design reliability (%):	95

The transverse cracking at failure was assumed to be 20% for all traffic levels. In reality, IDOT's design manual defines failure at 20% slab cracking at traffic levels greater than 10 million ESALs (TF = 10) and has a variable failure criteria between traffic factors of 3 and 10, from 100% (TF = 3) to 20% (TF = 10). In future runs, IDOT's specific failure criteria for transverse cracking will be used.

- 5) Traffic

Initial two-way AADTT (Annual Average Daily Truck Traffic):
390, 1,950, 11,665 and 44,716 (which correspond to 18-kip ESALs of 2.01, 10.03, 60, and 230 million, respectively)

Number of lanes in design direction: 2  
 Percent of trucks in design direction (%): 50  
 Percent of trucks in design lane (%): 95  
 Vehicle operational speed (mph): 60  
 Traffic Monthly Adjustment Factors (MAF): level 3, default values in MEPDG software  
 (All are equal to 1.00 for different vehicle classes in any month)

Vehicle class distribution (based on weigh station data from I-55, Bolingbrook, Illinois northbound lanes):

Class 4: 1.6%  
 Class 5: 4.6%  
 Class 6: 3.7%  
 Class 7: 0.0%  
 Class 8: 6.7%  
 Class 9: 79.0%  
 Class 10: 0.9%  
 Class 11: 3.5%  
 Class 12: 0.0%  
 Class 13: 0.0%

Traffic Growth Factor: No Growth

Vehicle axle load distribution factors: The default values in the MEPDG were used for the Bolingbrook, Illinois facility (I-55).

Mean wheel location from the lane marking (in.): 18  
 Traffic wander standard deviation (in.): 10  
 Design lane width (ft): 12  
 Number of axles per truck: default values used in the MEPDG (see *Table B.1*).

Table B.1. Default Values of Number of Axles per Truck in the MEPDG.

Vehicle Class	Single Axle	Tandem Axle	Tridem Axle	Quad Axle
Class 4	1.62	0.39	0.00	0.00
Class 5	2.00	0.00	0.00	0.00
Class 6	1.02	0.99	0.00	0.00
Class 7	1.00	0.26	0.83	0.00
Class 8	2.38	0.67	0.00	0.00
Class 9	1.13	1.93	0.00	0.00
Class 10	1.19	1.09	0.89	0.00
Class 11	4.29	0.26	0.06	0.00
Class 12	3.52	1.14	0.06	0.00
Class 13	2.15	2.13	0.35	0.00

Hourly truck traffic distribution: default values used in MEPDG (see

*Table B.2*).

Table B.2. Default Values of Hourly Truck Traffic Distribution in the MEPDG.

Time Period	Distribution (%)	Time Period	Distribution (%)
12:00 a.m. – 1:00 a.m.	2.3	12:00 p.m. – 1:00 p.m.	5.9
1:00 a.m. – 2:00 a.m.	2.3	1:00 p.m. – 2:00 p.m.	5.9
2:00 a.m. – 3:00 a.m.	2.3	2:00 p.m. – 3:00 p.m.	5.9
3:00 a.m. – 4:00 a.m.	2.3	3:00 p.m. – 4:00 p.m.	5.9
4:00 a.m. – 5:00 a.m.	2.3	4:00 p.m. – 5:00 p.m.	4.6
5:00 a.m. – 6:00 a.m.	2.3	5:00 p.m. – 6:00 p.m.	4.6
6:00 a.m. – 7:00 a.m.	5.0	6:00 p.m. – 7:00 p.m.	4.6
7:00 a.m. – 8:00 a.m.	5.0	7:00 p.m. – 8:00 p.m.	4.6
8:00 a.m. – 9:00 a.m.	5.0	8:00 p.m. – 9:00 p.m.	3.1
9:00 a.m. – 10:00 a.m.	5.0	9:00 p.m. – 10:00 p.m.	3.1
10:00 a.m. – 11:00 a.m.	5.9	10:00 p.m. – 11:00 p.m.	3.1
11:00 a.m. – 12:00 p.m.	5.9	11:00 p.m. – 12:00 a.m.	3.1

6) Axle configuration

Average axle width (edge-to-edge) outside dimensions (ft):	8.5
Dual tire spacing (in.):	12
Single tire (psi):	120
Dual tire (psi):	120

Percent of trucks with different average axle spacing (MEPDG default) (see *Table B.3*).

Table B.3. Percent of Trucks with Different Axle Spacing.

	Short	Medium	Long
Average axle spacing (ft)	12	15	18
Percent of trucks	33	33	34

The tire pressure for single and dual tires was assumed to be higher than in the IDOT Design Manual. The increased tire pressure assumption will likely not affect the results, but can be changed to 80 psi for future runs.

7) Climate

The climatic data from five weather stations in MEPDG were considered in this study. Three of these stations are located in Chicago areas; i.e., Chicago/Midway, Chicago/O'Hare and Chicago/Dupage. The other two are Champaign and Carbondale. The three Chicagoland weather stations were used to assess the lake effect on pavement temperature profiles and their subsequent designs.

8) Structure–Design features

Permanent curl/warp effective temperature difference (°F):	-10
--	-----

Joint design	
Joint spacing (ft):	15

Sealant type:	Silicone
Dowel diameter (in.):	1.5
Dowel bar spacing (in.):	12

For the runs presented, silicone sealant was assumed for the transverse joints. IDOT has not sealed its transverse joints since 2004. It is expected that choosing to seal or not to seal joints will not affect the cracking results, but would affect the faulting predictions with the MEPDG.

#### Edge support

Three types of shoulder are considered in this study: asphalt concrete shoulder, tied shoulder, and widened slab. The long-time load transfer efficiency (LTE ) across the lane–shoulder joint was 40% or 80%.

Normal slab width (ft) :	12
Widened slab width (ft):	14

#### Base properties

Base type:	Asphalt-treated
Erodibility index:	Extremely resistant
Base/slab friction coefficient:	0.65
PCC–base interface:	Bonded
Loss of bond age (months):	60

#### Structure -- ICM (Integrated Climatic Model) properties

Surface shortwave absorptivity:	0.85
---------------------------------	------

#### Drainage parameters

Infiltration:	Moderate (50%)
Drainage path length (ft):	12 feet
Pavement cross slope (%):	2

#### Structure—Layers

##### Layer 1—JPCP

##### General properties

PCC material	JPCP
Layer thickness (in.):	Variable
Unit weight (pcf):	150
Poisson's ratio:	0.15

#### Thermal properties

Coefficient of thermal expansion (per F° x 10 <sup>-6</sup> ):	5.6
Thermal conductivity (BTU/hr-ft-F°):	1.25
Heat capacity (BTU/lb-F°):	0.28

#### Mix properties

Cement type:	Type 1
Cementitious material content (lb/yd <sup>3</sup> ):	550
Water/cement ratio:	0.377
Aggregate type:	Limestone
PCC zero-stress temperature (F°)	Derived

Ultimate shrinkage at 40% R.H. (microstrain)	Derived
Reversible shrinkage (% of ultimate shrinkage):	50
Time to develop 50% of ultimate shrinkage (days):	35
Curing method:	Curing compound

IDOT currently specifies that the cementitious content should be 565 lb/cubic yard for central mix plants and 605 lb/cubic yard for truck mix concrete.

#### Strength properties

Input level:	Level 3
28-day PCC modulus of rupture (psi):	650
28-day PCC compressive strength (psi):	N/A

A modulus of rupture (MOR) of 650 psi (3<sup>rd</sup>-point loading) was chosen at 28-day age for the runs presented in this technical note. IDOT currently specifies a minimum flexural strength of 650 psi at 14 days using a center-point loading configuration. The MOR strength value chosen for the runs herein is approximately 10% greater than the IDOT requirements. In future runs, the required strength at 28 days can be reduced accordingly.

#### Layer 2—Asphalt concrete

Material type:	Asphalt concrete
Layer thickness (in.):	4

#### General properties

Reference temperature (F°):	70
-----------------------------	----

#### Volumetric properties as built

Effective binder content (%):	11
Air voids (%):	8.5
Total unit weight (pcf):	148

Poisson's ratio:	0.35
------------------	------

#### Thermal properties

Thermal conductivity asphalt (BTU/hr-ft-F°):	0.67
Heat capacity asphalt (BTU/lb-F°):	0.23

#### Asphalt mix

Cumulative % retained 3/4-in. sieve:	20
Cumulative % retained 3/8-in. sieve:	45
Cumulative % retained #4 sieve:	65
% passing #200 sieve:	5

#### Asphalt binder

Option:	Conventional viscosity grade
Viscosity grade:	AC 10

#### Layer 3—Fine-grained soil CH (A-7-6)

Unbound material:	A-7-6
-------------------	-------

Thickness (in.):	Semi-infinite
Strength properties	
Input level:	Level 3
Analysis type:	ICM inputs (ICM calculated modulus)
Poisson's ratio:	0.35
Coefficient of lateral pressure, Ko:	0.5
Modulus (input) (psi):	7500
ICM inputs	
Gradation and plasticity index	
Plasticity index, PI:	40
Passing #200 sieve (%):	90
Passing #4 sieve (%):	99
D60 (mm):	0.01
Calculated/derived parameters	
Maximum dry unit weight (pcf):	82.2 (derived)
Specific gravity of solids, Gs:	2.77 (derived)
Saturated hydraulic conductivity (ft/hr):	3.25e-05 (derived)
Optimum gravimetric water content (%):	28.8 (derived)
Calculated degree of saturation (%):	89.4 (calculated)
Soil water characteristic curve parameters:	Default values

### **B2. 1. 2. Design Results**

A summary of the JPCP slab design thickness based on MEPDG simulation results for different traffic levels, climatic zones, and shoulder types are shown in Section B.2.3 and at the end of this appendix.

### **B2. 2. IDOT Design**

IDOT has a mechanistic-empirical pavement design method for JPCP based on work by Zollinger and Barenberg (1989a), which is currently implemented into design charts. The reliability level for the charts is 95%. One difference between the IDOT and MEPDG methods is the handling of traffic inputs. MEPDG requires the use of load spectra, whereas IDOT uses ESALs (traffic factor). One limiting factor in the IDOT JPCP design method is that the slab thickness ranges from 6 in. to 12 in. with a maximum ESAL count of 60 million. The main IDOT design parameters are as follows:

- Traffic factor  
Traffic factor is defined as the projected total 18-kip ESALs, expressed in millions, to be carried by the design lane during the design period (IDOT, 2002). For the IDOT design simulations, the traffic factors were 2, 10, 60, and 230.
- Edge support conditions  
Two types of shoulder are currently considered in IDOT design procedure: tied shoulder (long-term LTE = 85%) and asphalt concrete shoulder. Note that the original proposed method by Zollinger and Barenberg (1989a) included charts for widened lane.

- Design subgrade support rating (SSR)

The design SSR accounts for the rating of the subgrade support in IDOT design method for JPCP. There are three types of SSR: poor, fair, and granular. A poor SSR was used for the JPCP design simulations.

It should be noted that there is no climatic zone consideration for the IDOT method. The JPCP slab design thickness results based on the IDOT design are shown in Section B.2.3 and at the end of this appendix.

### **B2. 3. JPCP Design Comparison**

To facilitate the comparisons of concrete slab thickness results obtained from the MEPDG and IDOT methods, bar charts are plotted by using the data from these simulations shown at the end of the appendix. PCC slab thickness determined from the IDOT design charts is rounded up to the nearest 0.25 in., while the MEPDG designs are rounded up to the nearest 0.5 in. to obtain the slab design thickness, which may cause some small discrepancies. The following summarizes the bar charts presented below:

Figures B.1, B.2 & B.3: MEPDG (referred to as DG2002) and IDOT design comparisons for JPCP with different types of shoulder (AC, tied shoulder, and widened slab) in Chicago/Midway climate under different traffic levels.

Figures B.4, B.5 & B.6: MEPDG (DG2002) and IDOT design comparisons for JPCP with different type of shoulders (AC, tied shoulder, and widened slab) in Champaign climate under different traffic levels.

Figures B.7, B.8 & B.9: MEPDG (DG2002) and IDOT design comparisons for JPCP with different type of shoulders (AC, tied shoulder, and widened slab) in Carbondale climate under different traffic levels.

Figure B.10: Effects of five climatic zones on the PCC slab thicknesses for the JPCP with AC shoulder using MEPDG.

Figures B.11 & B.12: MEPDG and IDOT design comparisons for the effects of shoulder types on the PCC slab thicknesses in Champaign climate



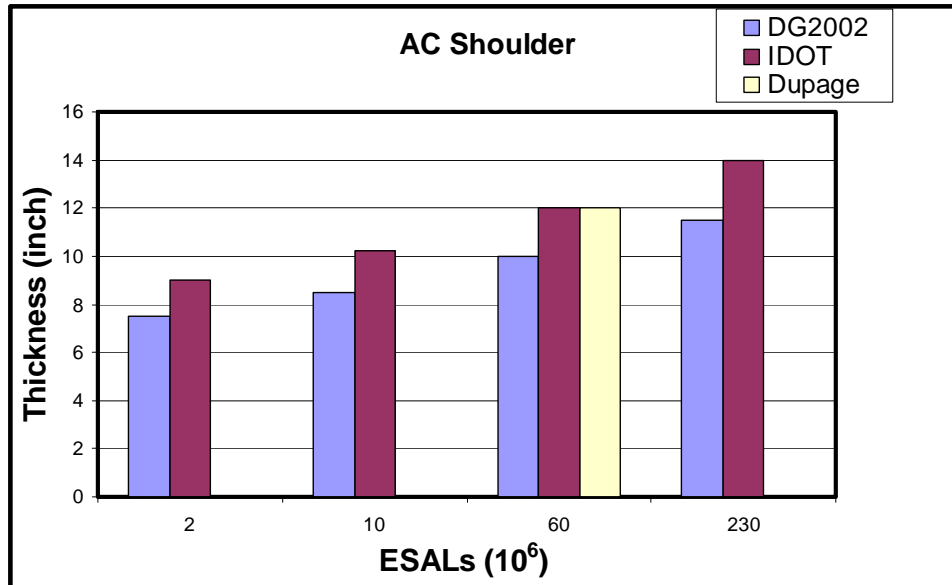


Figure B.1. Chicago (Midway climate) JPCP with AC shoulder.

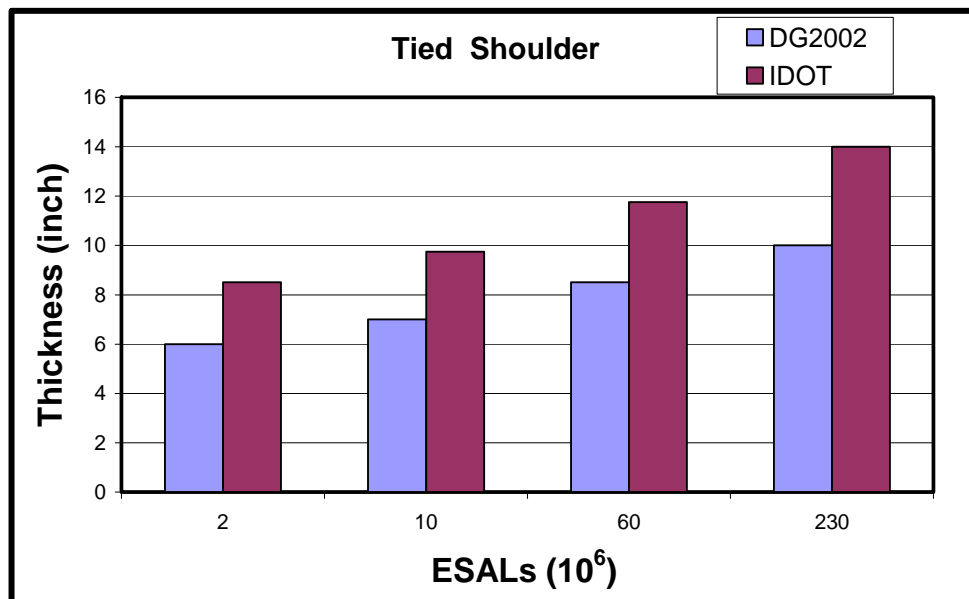


Figure B.2. Chicago (Midway climate) JPCP with tied shoulder.

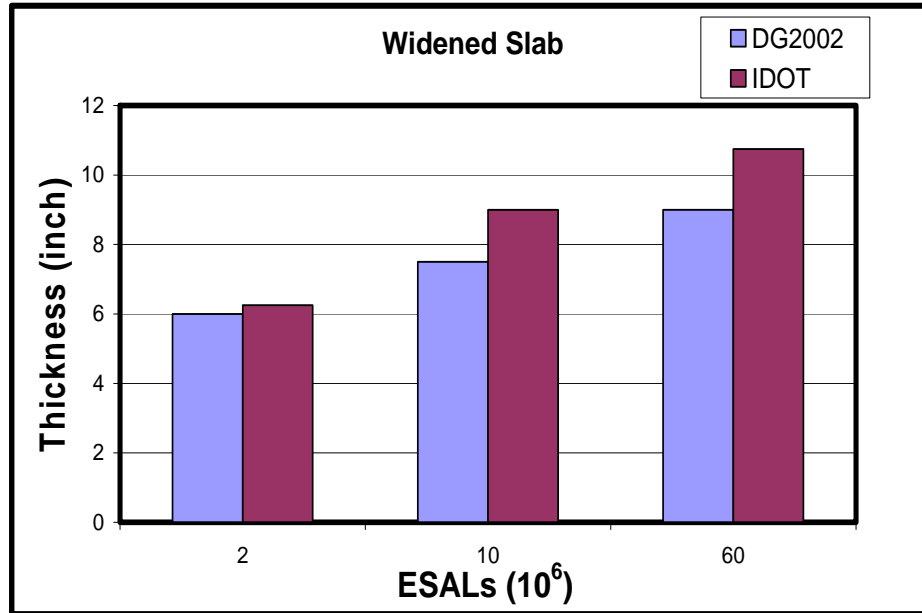


Figure B.3. Chicago (Midway climate) JPCP with widened lane.

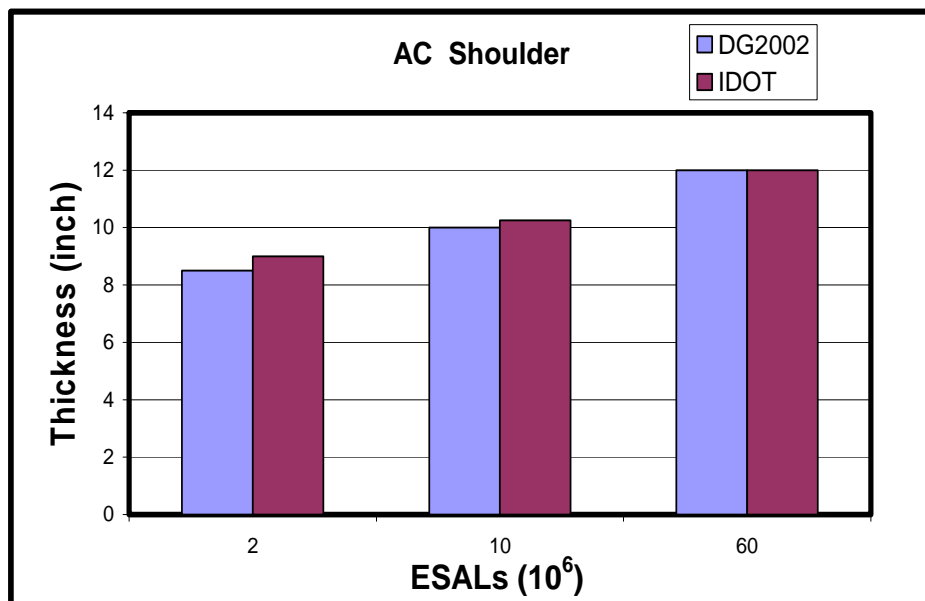


Figure B.4. Champaign (climate) JPCP with AC shoulder.

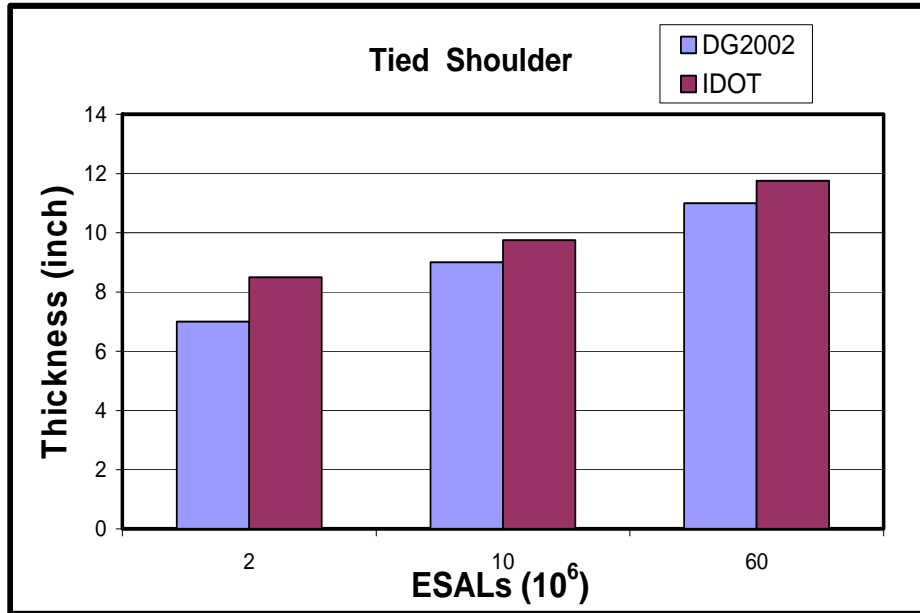


Figure B.5. Champaign (climate) JPCP with tied shoulder.

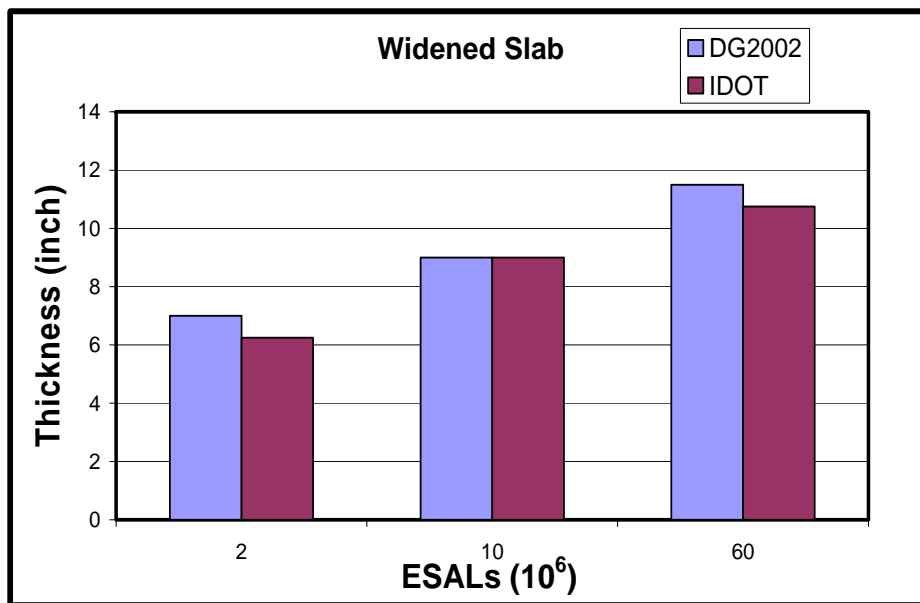


Figure B.6. Champaign (climate) JPCP with widened slab.

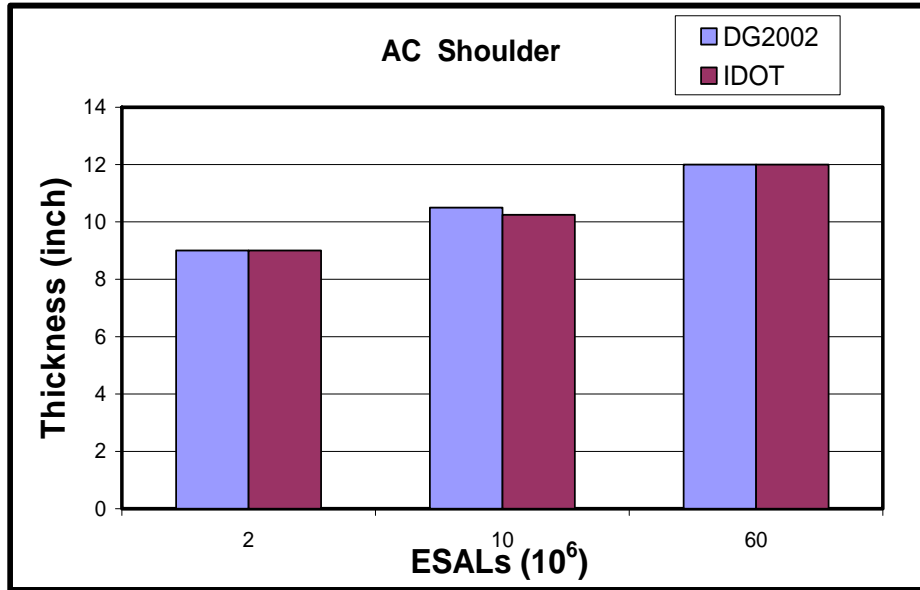


Figure B.7. Carbondale (climate) JPCP with AC shoulder.

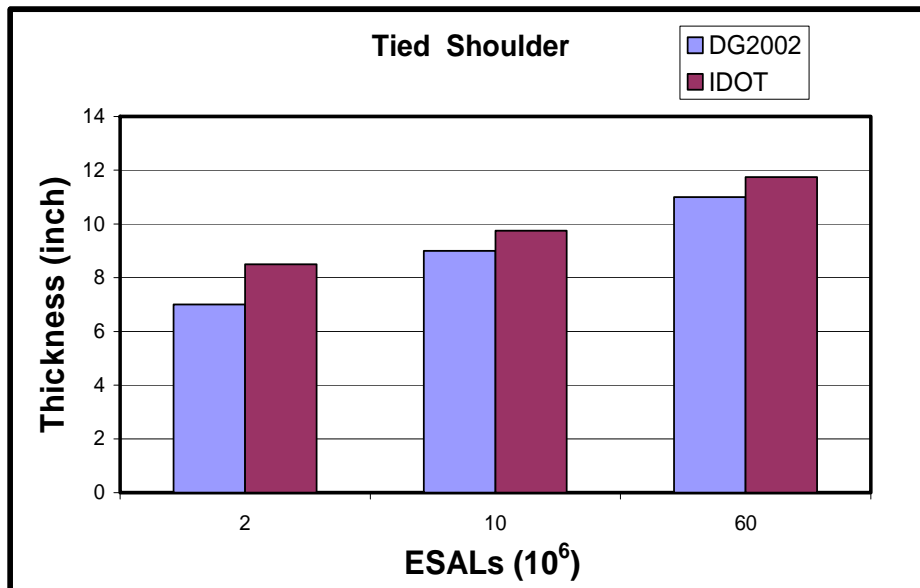


Figure B.8. Carbondale (climate) JPCP with tied shoulder.

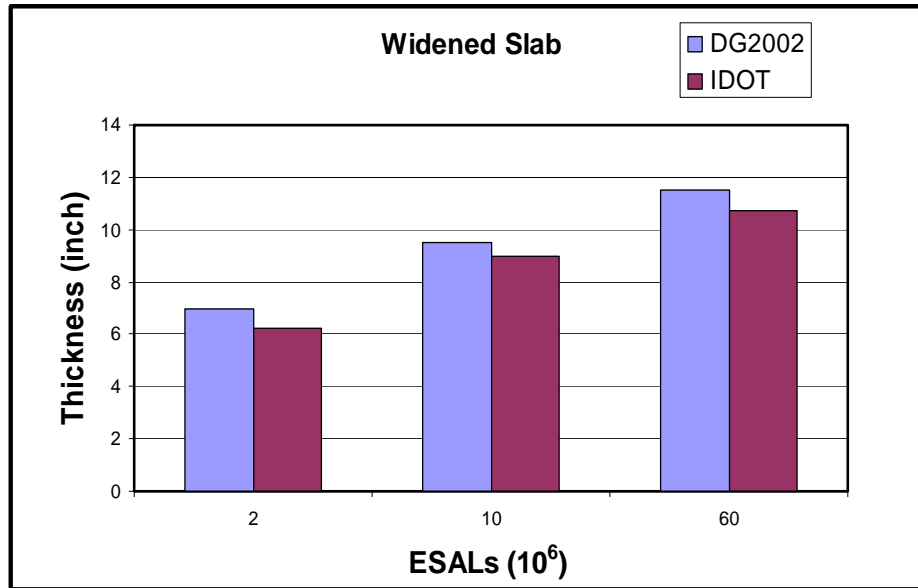


Figure B.9. Carbondale (climate) JPCP with widened slab.

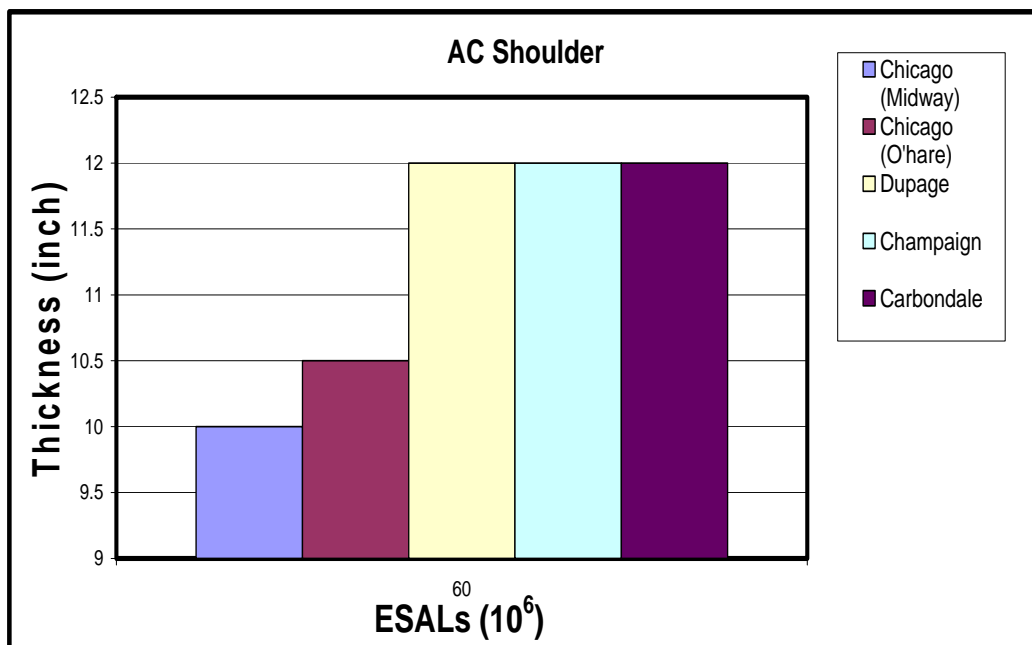


Figure B.10. Climatic zone effects on JPCP with AC shoulder.

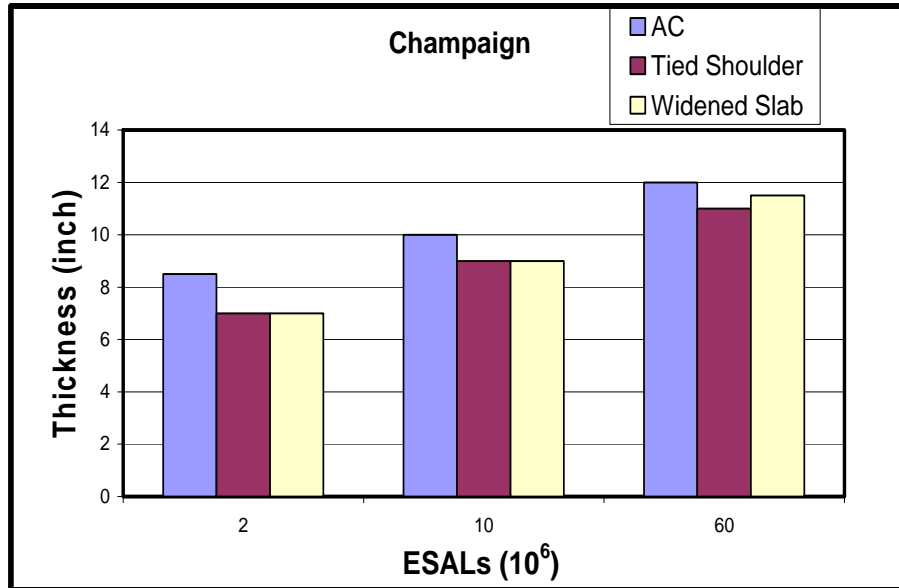


Figure B.11. Effects of shoulder types on the JPCP slab thickness by using MEPDG (Champaign climate).

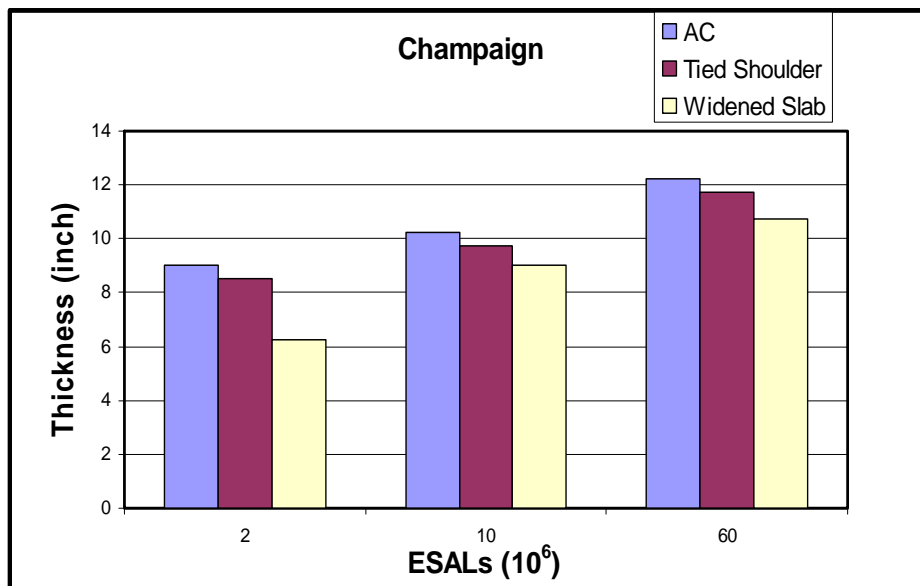


Figure B.12. Shoulder effects on the JPCP slab thickness by using IDOT design methods.

## B2. 4. JPCP Summary

The following is a summary of the JPCP design guide runs.

### B2. 4. 1. Slab Fatigue Cracking

In MEPDG, the slab fatigue cracking mode can be bottom-up or top-down cracking near the mid-slab edge. Given the vehicle class distribution data and the statistical average truck axle

spacing, in addition to other data in the above design inputs, the different slab cracking damage modes are related to the traffic level. The IDOT method only predicts bottom-up transverse fatigue cracking at the mid-slab edge. Overall, as the traffic level increased, the required slab thickness increased.

- Low traffic volume (ESALs = 2 million)  
For the Chicago climate and JPCP with AC shoulder, the dominant slab cracking mode is top-down cracking. For JPCP with tied shoulder, bottom-up cracking is the dominate mode. For the Champaign and Carbondale climates, for the JPCP with AC shoulder or tied concrete shoulder, the top-down cracking is the dominant fatigue damage mode (see data at end of appendix).
- Medium traffic volume (ESALs = 10 million)  
For the JPCP in all climatic zones and shoulder types, top-down cracking is the dominant fatigue damage mode.
- High traffic volume (ESALs = 60 or 230 million)  
For high level traffic volume, top-down cracking is the dominant fatigue damage mode in JPCP design. This holds true for all climatic areas and shoulder types considered in this study.

It is worth mentioning that top-down cracking controls the fatigue damage mode for all JPCP with widened lane design. This is valid for all climatic areas and traffic levels. It should be re-stated that bottom-up cracking is the only failure mode considered in the IDOT method for JPCP. However, the failure mode predicted from the MEPDG runs is primarily top-down cracking, which is quite different from the IDOT method.

#### ***B2. 4. 2. Climatic Zone Effects on Slab Thickness in MEPDG***

By using the climatic data from the above-mentioned five weather stations in MEPDG, the slab design thicknesses are almost the same for the Chicago/Midway and Chicago/O'Hare areas. Similarly, the slab design thicknesses are close to one other for the Chicago/Dupage, Champaign, and Carbondale areas, and the largest slab thickness difference is 0.5 in. under all traffic level and shoulder conditions considered in this report (see Figure B.10 and data at the end of this appendix). The main discrepancy, shown in Figure B.10, is the slab design thickness differences between Chicago/Dupage and Chicago/Midway or Chicago/O'Hare. The slab thickness varied between 1.0 and 2.5 in. for the cases analyzed.

By analyzing the climatic data for the Chicago/Midway, Chicago/Dupage, Mattoon, and Carbondale areas in the MEPDG, and plotting the temperature differential distribution—i.e., the frequency of temperature differential  $\Delta T$  versus the amount of time each  $\Delta T$  is predicted in that area—Figure B.13 shows that Chicago/Midway has the most temperate conditions in terms of  $\Delta T$ . This is probably due to the effect of Lake Michigan on the ambient conditions. While solar radiation effects are probably quite similar for all the Chicago weather stations, Lake Michigan tends to moderate the air temperature, thereby affecting the temperature differential through the PCC slab and resulting in lower calculated thermal curling stresses and PCC design thickness required to compensate for these stresses. This microclimate effect (<30 miles between Dupage and O'Hare) on the design slab thickness appears to be too sensitive in the MEPDG, especially in Version 0.91. For the state of Illinois as a whole, there was little to no climatic effect on thickness design from Chicago/Dupage to Carbondale (350 miles difference), given the same concrete coefficient of thermal expansion.

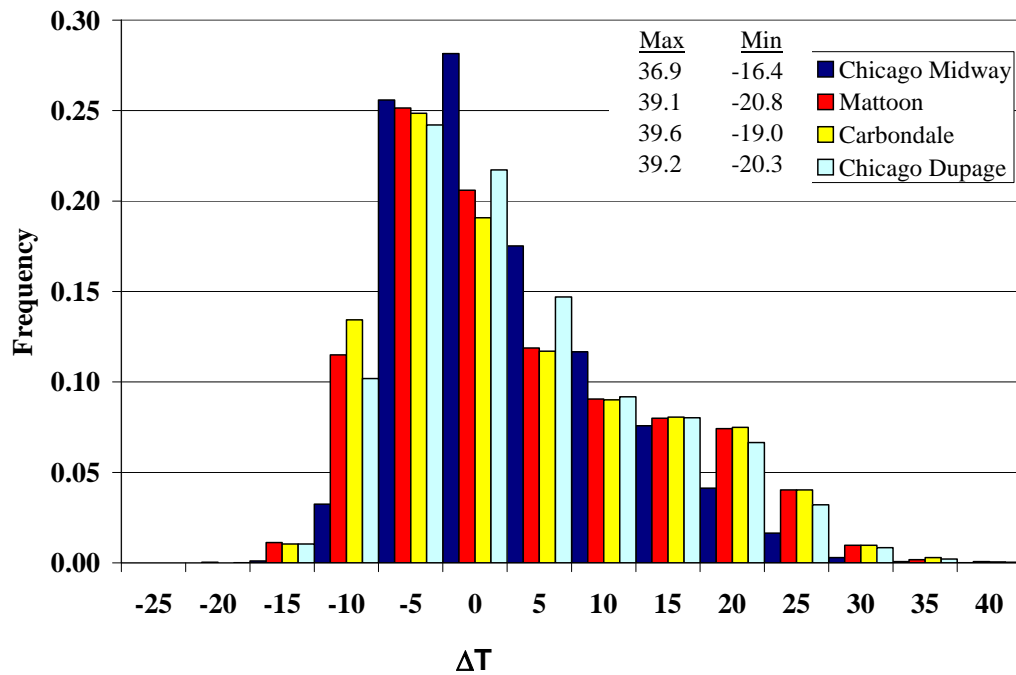


Figure B.13. Frequency distribution of temperature differential for several locations in Illinois.

#### B2. 4. 3. MEPDG and IDOT Design Comparisons for JPCP

Table B.4 shows the slab thickness differences based on MEPDG and IDOT design methods for JPCP, with different shoulder types for different climatic areas (see Figures B.1 to B.9).

Table B.4. Slab Thickness Differences Using MEPDG and IDOT Design Methods (in.)

Shoulder Type	Chicago/Midway ESALs				Champaign ESALs			Carbondale ESALs		
	2M	10M	60M	230M	2M	10M	60M	2M	10M	60M
AC	1.5	1.75	2.0	2.5	0.5	0.25	0	0	-0.25	0
Tied	2.5	2.75	3.25	4.0	1.5	0.75	0.75	1.5	0.75	0.75
Widened Slab	0.25	1.5	1.75		-0.75	0	-0.75	-0.75	-0.5	-0.75

Notes: “-” means that the slab thickness determined by using IDOT design method is thinner than that determined by using MEPDG.

M = Millions.

The IDOT design method does not differentiate between climatic zones. For the Chicago/Midway area, the slab thickness determined by MEPDG Version 0.91 is thinner than the IDOT method, and the slab thickness difference increases as design traffic volume increases for each shoulder type.

For Champaign and Carbondale climates, the slab thicknesses from the MEPDG and IDOT methods for AC shoulders are close to each other. For any design traffic level, the slab thickness for tied concrete shoulders based on MEPDG is thinner than that based on the IDOT



method, which is primarily a result of a higher LTE assumed for the lane–shoulder joint in the IDOT method. The MEPDG gives larger slab thicknesses than the IDOT method for a 14-ft widened lane.

#### **B2. 4. 4. Shoulder Type Effects**

Shoulder type has an effect on slab thickness, as demonstrated in Figures B.11 and B.12 for the Champaign climatic zone. In Figure B.11, when the long-term LTE provided by the tied shoulder is assumed to be 80%, the MEPDG slab thicknesses for tied shoulder are the same with those for widened slab for the low and medium traffic volumes. A small slab thickness difference of 0.5 in. exists for the high traffic volume (ESALs = 60 million). The slab thicknesses are also 1.0 to 1.5 in. thicker for AC shoulders than those for tied shoulders or widened slabs for the MEPDG runs.

In Figure B.12, slab thickness difference between tied shoulder and widened slab is larger when using the IDOT design compared to MEPDG, especially for the low traffic volume case. The long-term LTE for tied shoulder is assumed to be 85% in the IDOT method, and the slab thickness for widened lane in Figure B.12 is calculated based on the assumption that the modulus of subgrade reaction  $k$ -value equals 100 psi/in.

### **B3. CRCP DESIGN**

#### **B3. 1. Mechanistic-Empirical Pavement Design Guide**

##### **B3. 1. 1. Design Inputs**

- 1) Design life: 30 years
- 2) Pavement construction: August
- 3) Pavement analysis: probabilistic
- 4) Performance criteria
 

Initial IRI (International Roughness Index) (in./mi):	82
Terminal IRI (in./mi):	172 <b>(N/A)</b>
CRCP punchouts (per mile):	10 <b>(Critical failure criteria)</b>
Design reliability (%):	95
- 5) Traffic
 

The relevant traffic input parameters are the same as those for the above JPCP designs using the MEPDG.
- 6) Axle configuration
 

Axle configuration is same as that for the MEPDG JPCP designs.
- 7) Climate
 

The climatic data for the Chicago/Midway and Carbondale areas are considered in this study when running MEPDG.
- 8) Structure–design features
 

Permanent curl/warp effective temperature difference (°F):	-10
Steel reinforcement	
Percent steel:	0.8
Steel bar diameter:	0.625 in. (#5)

Steel depth: 3.5 in.

IDOT typically uses 0.8% steel content for extended life CRCP (30-year design life) and 0.7% for CRC pavements with a 20-year design life. In all the CRCP runs for this technical note, a #5 bar was assumed. The choice of a #5 bar for higher steel contents is not exactly correct, since the number of bars required to satisfy the area of steel is not practical. In future runs, #6 or #7 bars should be used to satisfy the steel requirements.

Base properties

Base type:	Asphalt-treated
Erodibility index:	Erosion resistant (3)
Base/slab friction coefficient:	7.5

9) Structure –ICM properties

Surface shortwave absorptivity:	0.85
---------------------------------	------

Drainage parameters

Infiltration:	Moderate (50%)
Drainage path length (ft):	12
Pavement cross slope (%):	2

10) Edge support

Two types of shoulder are considered in this report: asphalt concrete shoulder and tied shoulder. The long-term LTE for tied shoulder in MEPDG is not a variable; it is said that LTE across shoulder is assumed to be 70% (the nondimensional parameter, AGG/kl, is assumed to be equal to 4).

11) Structure-Layers

Layer 1—CRCP

General properties

PCC material	CRCP
Layer thickness (in.):	Variable
Unit weight (pcf):	150
Poisson's ratio:	0.2

Thermal properties

Coefficient of thermal expansion (per $F^{\circ} \times 10^{-6}$ ):	5.5
Thermal conductivity (BTU/hr-ft- $F^{\circ}$ ):	1.25
Heat capacity (BTU/lb- $F^{\circ}$ ):	0.28

Mix properties

Cement type:	Type 1
Cementitious material content (lb/yd <sup>3</sup> ):	550
Water/cement ratio:	0.42
Aggregate type:	Limestone
PCC zero-stress temperature ( $F^{\circ}$ )	Derived
Ultimate shrinkage at 40% R.H. (microstrain)	Derived
Reversible shrinkage (% of ultimate shrinkage):	50
Time to develop 50% of ultimate shrinkage (days):	35

Curing method:

Curing compound

Strength properties

Input level:

Level 3

28-day PCC modulus of rupture (psi):

650

28-day PCC compressive strength (psi):

N/A

Layer 2—Asphalt concrete

Layer 3—Fine-grained soil CH (A-7-6)

The relevant design inputs for the asphalt concrete base and fine-grained soil are the same as those for the JPCP design above.

### **B3. 1. 2. Design Results**

The CRCP slab design thickness results based on the MEPDG for the three different traffic levels, two climatic zones, and two shoulder types are shown in Section B.3.3 and at the end of this appendix.

### **B3. 2. IDOT Design**

IDOT currently does not have a mechanistic-empirical design method for CRCP. IDOT uses a modified (empirical) AASHTO design procedures for CRCP thickness determination (80% of JRPC thickness). The modified AASHTO method used by IDOT does not distinguish between different edge support conditions; i.e., no difference between AC and tied concrete shoulder.

The main design parameters are as follows:

- Class of road and street (facilities)  
There is one separate rigid pavement design nomograph for JPCP and CRCP for Class I facilities, and another design nomograph for Class II, III, and IV facilities [as defined by the BDE Manual (IDOT, 2002)].
- Traffic factor  
Traffic factor is explained in the above-mentioned IDOT method for JPCP.
- Illinois Bearing Ratio (IBR)  
The IBR represents the support provided by the roadbed soils or by unbound granular materials in the modified AASHTO design method. The IBR test procedure is a modified California Bearing Ratio (CBR) procedure and is a soaked lab test (IDOT, 2002). An IBR of 2 was used for the CRCP design.

PCC slab thickness determined from the design charts is rounded up to the nearest 0.25 in. to obtain the design slab thickness.

### **B3. 3. CRCP Design Comparison**

To facilitate the comparison of CRCP slab thickness results based on the MEPDG and IDOT methods, bar charts were plotted using the data from these simulations shown at the end of this appendix. The following is a summary of the figures:

Figures B.14 & B.15: MEPDG (DG2002) and IDOT design comparisons for CRCP with different shoulder types (AC, tied shoulder) for Chicago/Midway climate under different traffic levels.

Figures B.16 & B.17: MEPDG (DG2002) and IDOT design comparisons for CRCP with different shoulder types (AC, tied shoulder) for Carbondale area under different traffic levels.

Figure B.18: Effects of climatic zones on the CRCP slab thickness with AC shoulder using MEPDG.

Figure B.19: Effects of climatic zones on the CRCP slab thickness with tied shoulder using MEPDG.

Figure B.20: CRCP slab thickness comparisons for MEPDG and IDOT design methods.

Figures B.21 & B.22: MEPDG and IDOT design comparisons for JPCP versus CRCP in Champaign climate zone.

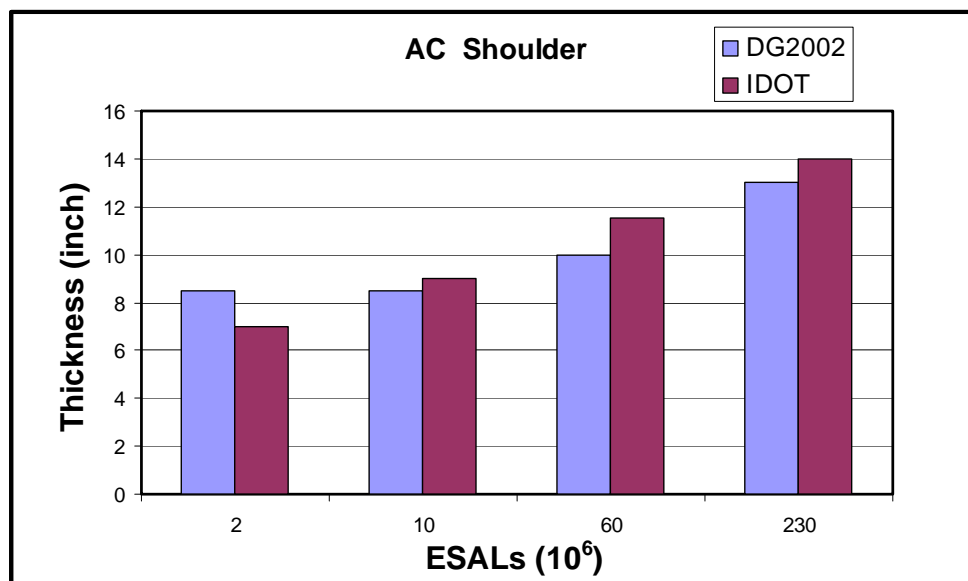


Figure B.14. Chicago (Midway climate) CRCP with AC shoulder.

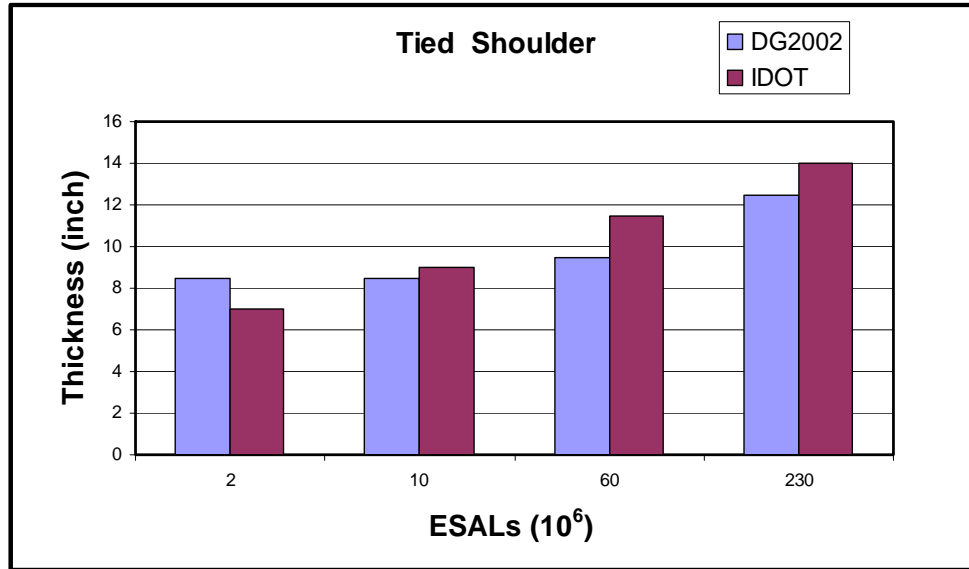


Figure B.15. Chicago (Midway climate) CRCP with tied shoulder (IDOT method is AC shoulder).

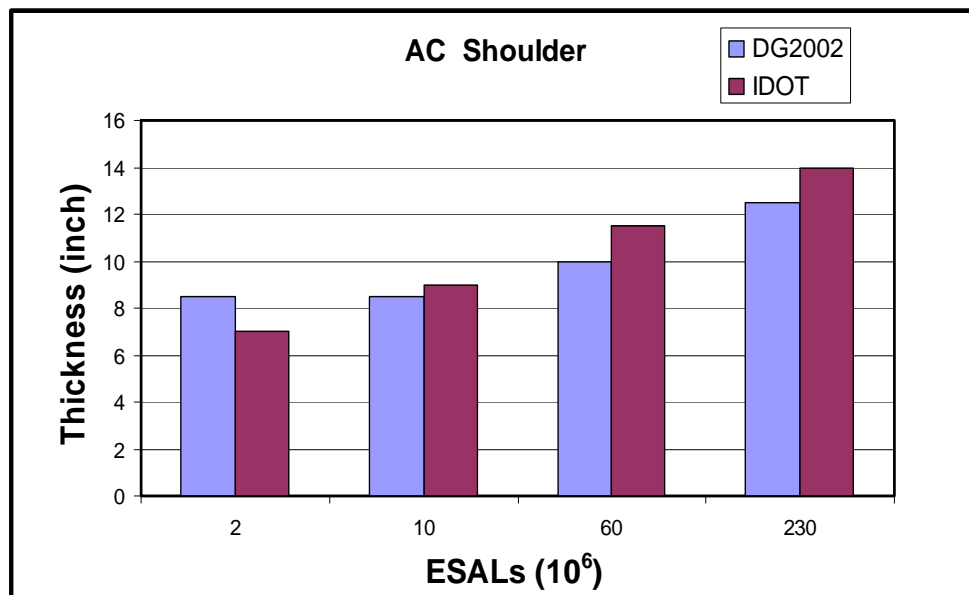


Figure B.16. Carbondale (climate) CRCP with AC shoulder.

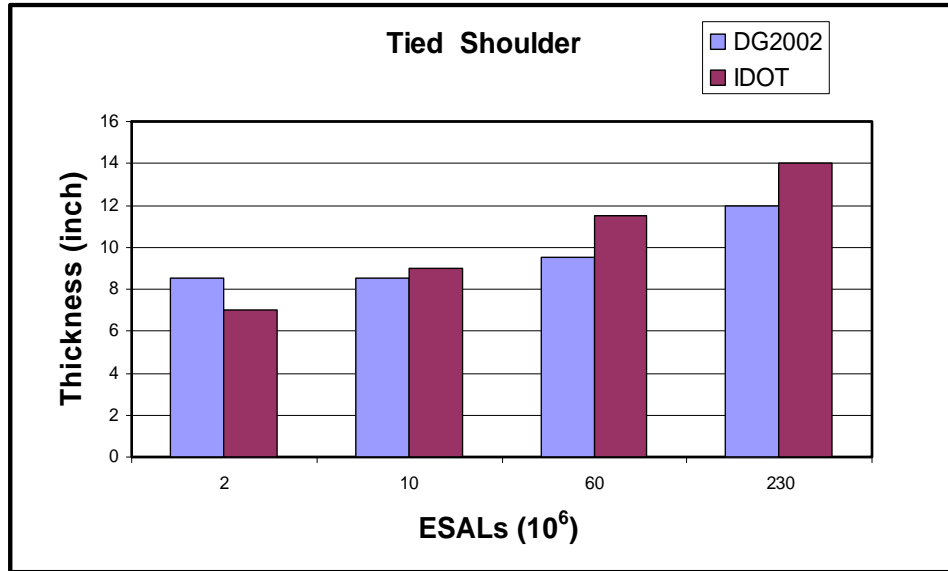


Figure B.17. Carbondale (climate) CRCP with tied shoulder (IDOT method is AC shoulder).

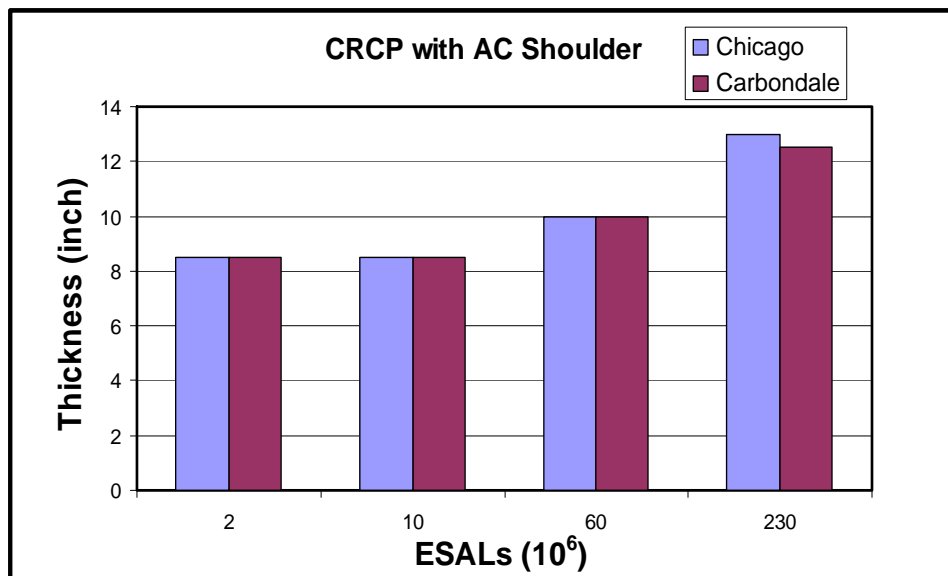


Figure B.18. Climatic zone effects on CRCP with AC shoulder using MEPDG.

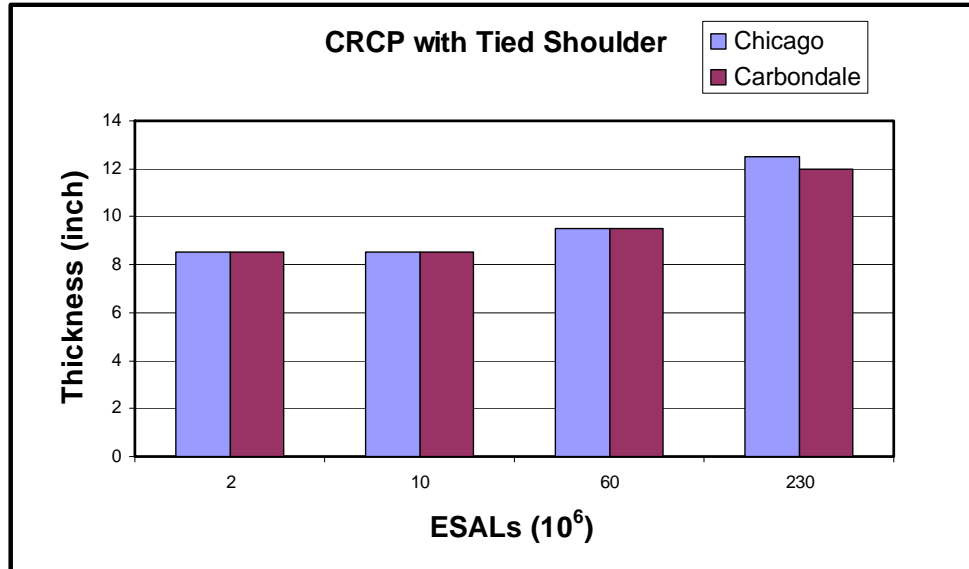


Figure B.19. Climatic zone effects on CRCP with tied shoulder using MEPDG.

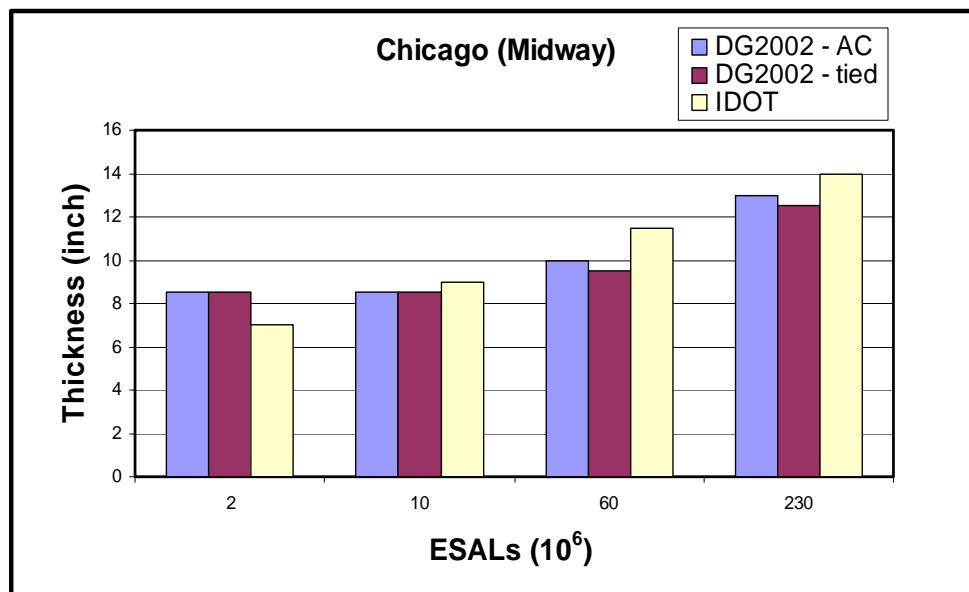


Figure B.20. CRCP slab thickness comparisons for MEPDG and IDOT design methods.

### B3.4. CRCP Summary

The following is a summary of the comparisons in Figures B.14 to B.20.

#### B3.4.1. MEPDG and IDOT Design Comparisons for CRCP

Table B.5 (see also Figures B.14 to B.17) shows the CRCP slab thickness differences between the MEPDG and IDOT design methods for different shoulder types and climatic areas.

Table B.5. CRCP Slab Thickness Differences Between MEPDG and IDOT Design Method (in.)

Shoulder Type	Chicago/Midway ESALs				Carbondale ESALs			
	2M	10M	60M	230M	2M	10M	60M	230M
AC	-1.5	0.5	1.5	1.0	-1.5	0.5	1.5	1.5
Tied*	-1.5	0.5	2.0	1.5	-1.5	0.5	2.0	2.0

Notes: “-” means that the slab thickness determined by using IDOT Design method is thinner than that determined by using MEPDG.

M = millions.

\*IDOT method for CRCP has no tied shoulder, just AC shoulder option

The CRCP slab thickness is less for the IDOT method at low traffic volumes by 1.5 in. but greater than the MEPDG CRCP thickness at greater traffic volumes. Figures B.14 to B.17 indicate that there are no differences in slab thickness between low traffic volume and medium traffic volume in both climatic zones in Illinois. The MEPDG design thicknesses are also shown to be less sensitive to traffic than the IDOT method, which is based off of JRCR thickness designs and not stresses developed with shorter slab lengths.

#### ***B3.4.2. Climatic Zone Effects on Slab Thickness in MEPDG***

Figures B.18 and B.19 show that there is no climatic effect on CRCP slab thickness for CRCP with either AC shoulder or tied shoulder for 2, 10, and 60 million ESAL cases based on the MEPDG. A slight slab thickness difference exists at 230 million ESALs, whereas the required slab thickness for Carbondale area is 0.5 in. thinner compared to Chicago/Midway area.

#### ***B3.4.3. Shoulder Type Effects***

Unlike the MEPDG JPCP design where shoulder type has a greater effect on slab thickness, there is less than 0.5 in. difference between tied and AC shoulders, as seen in Figure B.20.

### **B4. JPCP VERSUS CRCP**

To illustrate the JPCP and CRCP slab thickness difference under the same climatic condition, traffic volume, and shoulder type, the slab thicknesses for JPCP and CRCP in the Champaign climate zone were compared using the MEPDG and IDOT methods. Note that it is assumed that there is no slab thickness difference for CRCP between the Champaign and Carbondale areas.



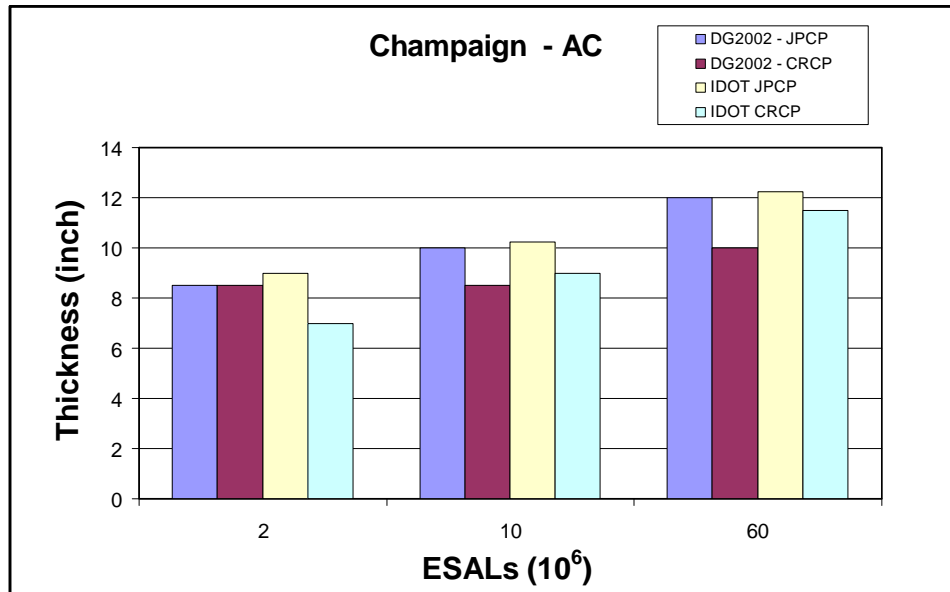


Figure B.21. MEPDG and IDOT Design comparisons for JPCP versus CRCP with AC shoulder in Champaign climate.

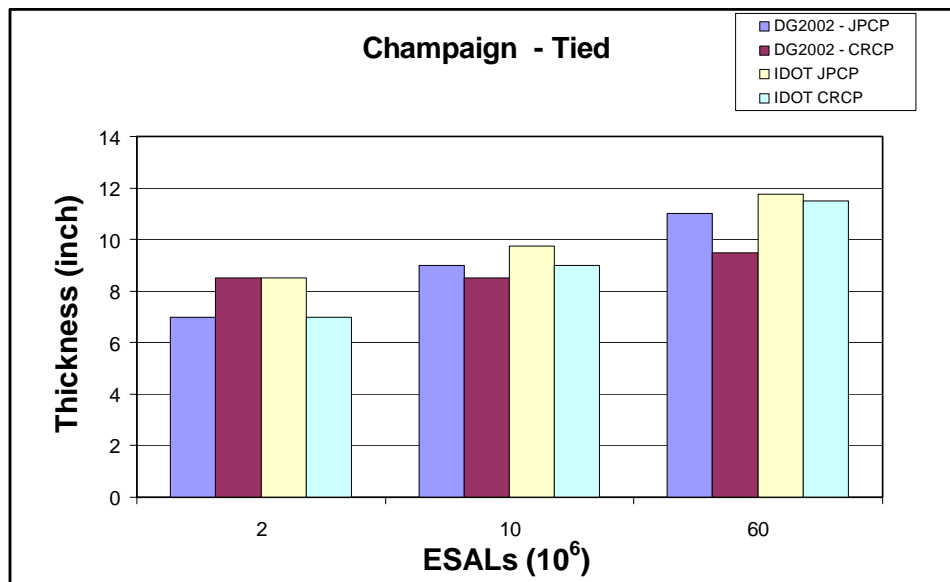


Figure B.22. MEPDG and IDOT Design comparisons for JPCP versus CRCP with tied shoulder in Champaign climate.

The IDOT design method requires thinner slab thickness for CRCP than JPCP with either AC or tied shoulder under all traffic levels, and the slab thickness difference decreases as the traffic level increases.

MEPDG also requires thinner slab thickness for CRCP than JPCP with either AC or tied shoulder for the 10 and 60 million ESALs cases, and the same slab thickness for both designs with AC shoulder at 2 million ESALs. The rule of thumb that CRCP thickness is 80 or 90% of jointed plain was found not to be a constant for all traffic levels and shoulder types.

By using the MEPDG for 10 and 60 million ESALs, the CRCP slab thickness decreased 15 and 16.7% with AC shoulder and 5.6 and 13.6% with tied shoulder, compared to JPCP with the same shoulder type and ESALs.

## **B5. DESIGN GUIDE SUMMARY**

For Illinois inputs, the NCHRP1-37A design guide for rigid pavements (MEPDG Version 0.91) was run for both CRCP and JPCP thickness determination. The MEPDG results were compared with IDOT's current design procedure for JPCP and CRCP. The design inputs varied were shoulder type (AC shoulder, tied shoulder, and widened lane), climate zone (Chicago, Champaign, or Carbondale areas), and traffic level (2, 10, 60, and 230 million ESALs or an equivalent load spectra).

For JPCP, the biggest difference between the MEPDG and IDOT methods was the fatigue failure mode predicted: primarily top-down cracking for MEPDG versus bottom-up cracking for the IDOT method. MEPDG showed a significant slab thickness difference between JPCP designed near Lake Michigan and other locations in Illinois, even Dupage County. This 1- to 2.5-in. difference between Midway Airport and Dupage Airport climate locations was deemed an anomaly, which may be theoretically correct, but MEPDG appears to be overly sensitive to this particular local temperature change. Overall, there is not a significant climatic trend on JPCP thickness design for a given set of concrete material properties in Illinois, based on MEPDG simulations. For IDOT and MEPDG both, the shoulder type did affect the concrete slab thickness. The IDOT method produced higher slab thicknesses for tied shoulders relative to the MEPDG, but thinner thicknesses for widened lanes. The concrete thickness requirements for tied shoulders or widened lanes were similar for MEPDG.

The IDOT design guide gave thinner CRCP slabs for 2 million ESALS relative to the MEPDG, but the IDOT method gave thicker slabs for traffic levels greater than 2 million. No climatic effect was observed for CRCP thickness design using MEPDG. The rule of thumb that CRCP is 80 to 90% of JPCP was not consistent across traffic levels and shoulder types for both the IDOT and MEPDG methods. The use of load spectra in MEPDG for either CRCP or JPCP did not appear to give significant advantages over the ESAL-based IDOT method for the inputs evaluated.

## **APPENDIX C. CHARACTERIZATION OF TRAFFIC FOR JPCP DESIGN: LOAD SPECTRA ANALYSIS VERSUS ESAL**

### **C1. OBJECTIVE**

A study was performed to investigate whether the use of load spectra, obtained from weigh stations (static scales) or weigh-in-motion (WIM), was necessary for JPCP design in Illinois versus the traditional method of converting mixed traffic to ESALs. Load spectra analysis specifically considers vehicle class distribution, axle type, axle spacing, steer-drive axle spacing, and weight in the calculation of concrete pavement stresses. The collection of load spectra data in Illinois is a time-intensive task for IDOT, and the primary question is whether the calibrated JPCP design is more robust when using load spectra or does not make a significant difference when applying the traditional ESAL concept. The Mechanistic-Empirical Pavement Design Guide (MEPDG) program Version 1.0 was used to make this comparison.

### **C2. LOCATION TRAFFIC**

IDOT provided load spectra data for several weigh station locations and one WIM location (Pesotum) as shown in Figure C.1. For each location the vehicle class distribution, as shown in Table C.1 and Figure C.2, and axle load distribution for single, tandem, spread tandem, tridem, and quad axles were recorded. Two default vehicle class distributions from the MEPDG program were also studied: the distribution TTC1 is for mixed single trailer truck routes, while distribution TTC11 is for mixed truck traffic with a high percentage of single trailer units.

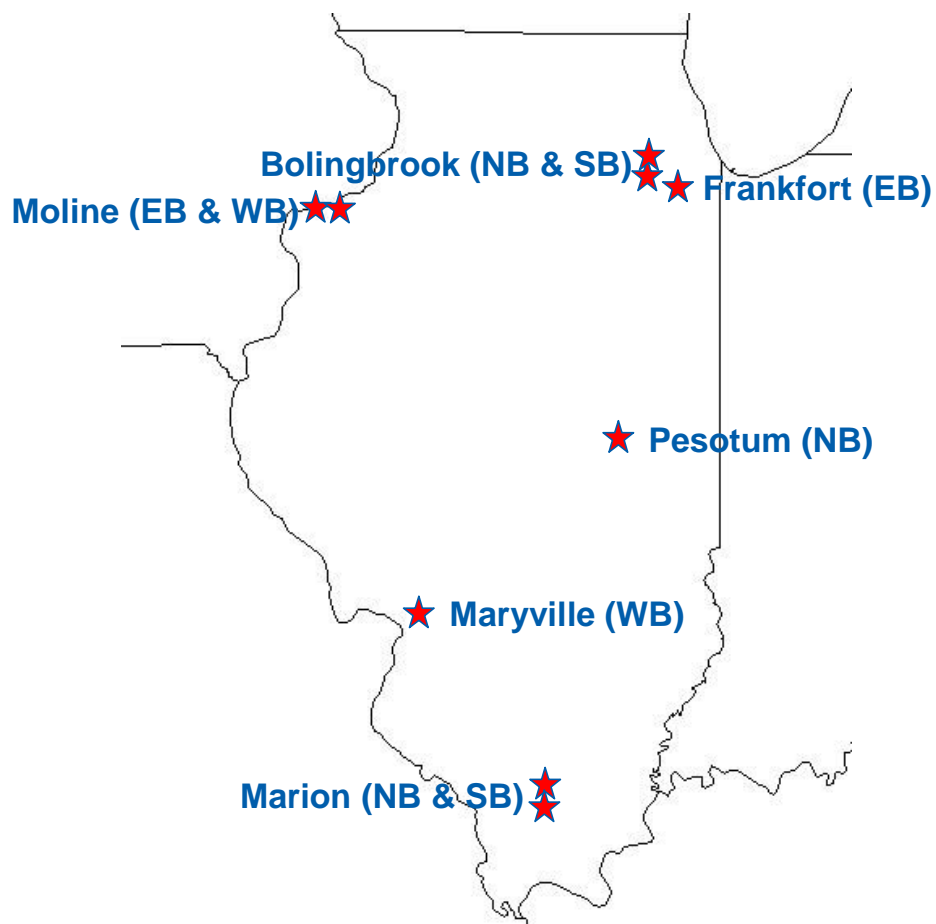


Figure C.1. Weigh and WIM (Pesotum) stations located in Illinois for load spectra analysis.

Table C.1. Vehicle Class Distributions.

FHWA Vehicle Class	Bolingbrook (NB)	Frankfort (EB)	Moline (EB)	Marion (SB)	Marysville (WB)	Pesotum (NB)	MEPDG TTC1	MEPDG TTC11
4	1.58	3.73	0.88	1.14	0.98	2.48	1.30	1.80
5	4.61	1.55	1.32	2.69	1.84	9.31	8.50	24.60
6	3.67	1.42	2.94	2.78	2.15	1.37	2.80	7.60
7	0.01	0.01	0.00	0.00	0.00	0.04	0.30	0.50
8	6.73	3.03	2.64	3.75	2.31	3.69	7.60	5.00
9	78.96	87.49	88.85	84.01	85.94	78.34	74.00	31.30
10	0.95	1.47	0.78	1.07	1.24	0.46	1.20	9.80
11	3.46	1.19	2.40	3.35	4.86	2.51	3.40	0.80
12	0.00	0.00	0.00	0.01	0.05	1.68	0.60	3.30
13	0.02	0.11	0.20	1.20	0.64	0.11	0.30	15.30

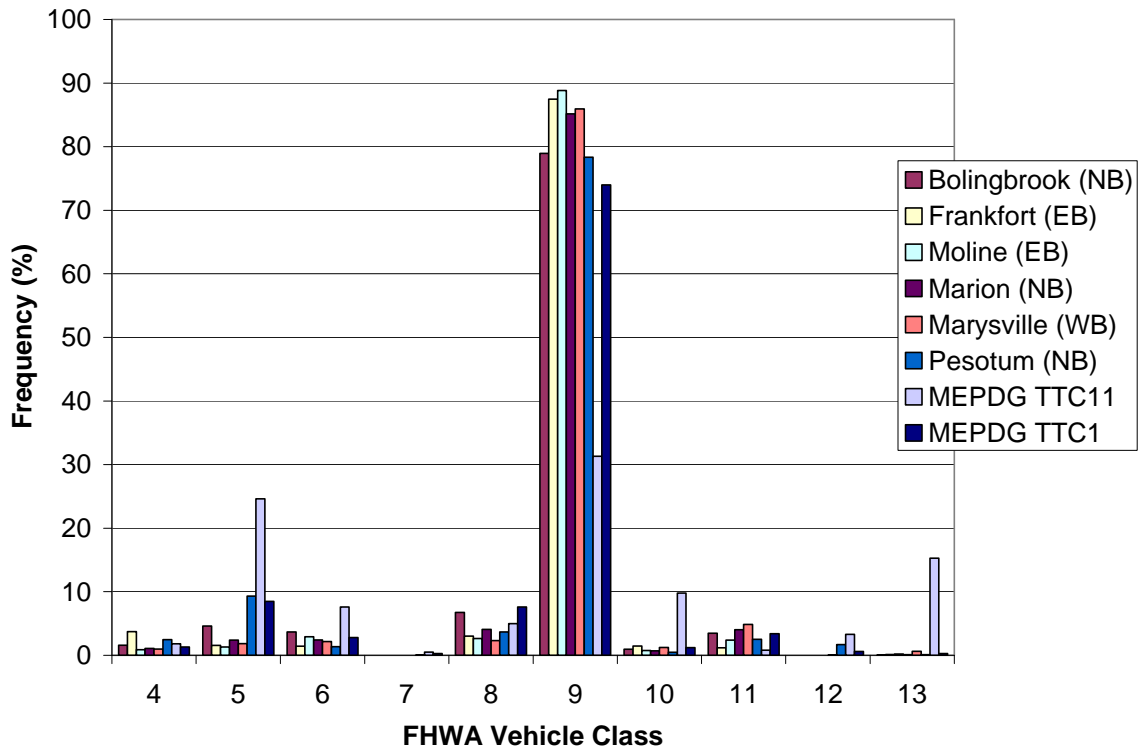


Figure C.2. The frequency of each vehicle class measured for each location or default setting in MEPDG.

The majority of trucks traveling on Illinois highways fall within FHWA class 9. The MEPDG TTC1 seems to match the vehicle class distribution of other locations in Illinois more closely than the default MEPDG TTC11. If one was to look at the tandem axle weight distribution for class 9 vehicles, such as shown in Figure C.3, the variation in distribution is not significant for various locations. Note that the MEPDG axle weights above 38 kips have the greatest frequency of occurrence. There is also a measurable number of axle weights between 34 and 38 kips, which is above the legal tandem axle load.

For each traffic site, vehicle type, axle counts, and the respective axle load, distributions were provided as shown in Table C.2 for Bolingbrook NB. The data in Table C.2 is formatted for input into the MEPDG software and the tandem axle loads are the sum of standard tandem and spread tandem axles. The data for the other weigh scale sites in Illinois are listed in Table C.3 to Table C.6. The Pesotum NB data was measured using a WIM station and every truck spacing and axle load was recorded for each vehicle class over the entire month of February 2006, as shown in Table C.7. Traffic data collected from WIM stations throughout California were summarized in terms of their axle distributions per class of trucks, as shown in Table C.8 to Table C.11 (Hiller, 2007).

A graphical representation of the Bolingbrook NB station's axle load distributions for each FHWA vehicle class containing single, tandem, or tridem axles are shown in Figure C.4 to Figure C.6. For the truck traffic in Illinois, the majority of single-axle vehicles weighed less than 18 kips and there were not many overloaded trucks

measured on the highways. Similarly, the Bolingbrook NB data also suggest very few overloaded tandem axes.

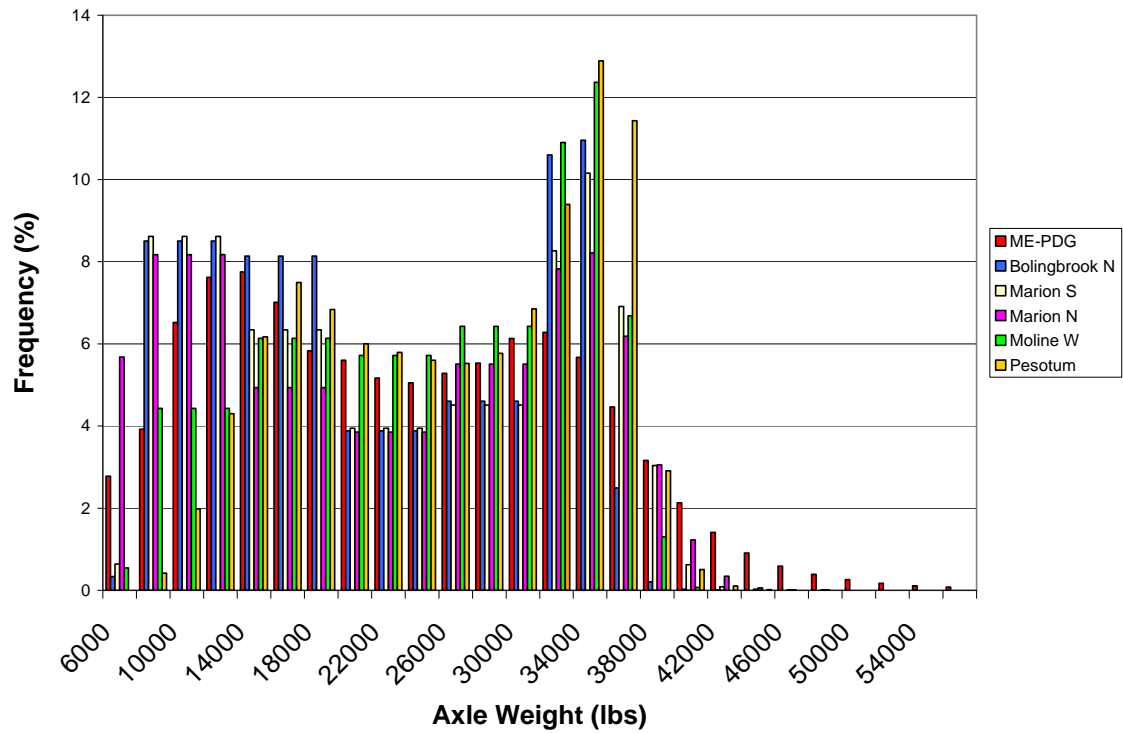


Figure C.3. Tandem axle load distribution for FHWA class 9 vehicles only for each weigh location.

Table C.2. Axle Load Distribution for Bolingbrook NB.

[illegible][illegible][illegible][illegible]

Table C.3. Axle Load Distribution for Frankfurt EB.

Class	Single Axle Load																												
	3000	4000	5000	6000	7000	8000	9000	10000	11000	12000	13000	14000	15000	16000	17000	18000	19000	20000	21000	22000	23000	24000	25000	26000	27000	28000	29000	30000	31000+
4	0.18	6.67	6.67	6.67	6.67	17.64	10.63	10.63	10.63	10.63	2.62	2.62	2.62	2.62	0.67	0.67	0.47	0.21	0.16	0.16	0.03	0.03	0.04	0.04	0.00	0.00	0.00	0.00	0.00
5	0.24	13.40	13.40	13.40	13.40	14.46	5.72	5.72	5.72	5.72	1.81	1.81	1.81	1.81	0.49	0.49	0.24	0.10	0.10	0.10	0.02	0.02	0.00	0.00	0.00	0.00	0.00	0.00	0.00
6	0.76	1.05	1.05	1.05	1.05	11.79	17.70	17.70	17.70	17.70	2.40	2.40	2.40	2.40	0.95	0.95	0.46	0.08	0.19	0.19	0.00	0.00	0.00	0.00	0.02	0.02	0.02	0.02	0.00
7	0.00	0.00	0.00	0.00	0.00	0.00	25.00	25.00	25.00	25.00	0.00	0.00	0.00	0.00	0.00	0.00	0.00	0.00	0.00	0.00	0.00	0.00	0.00	0.00	0.00	0.00	0.00	0.00	0.00
8	3.37	6.17	6.17	6.17	6.17	17.18	10.61	10.61	10.61	10.61	2.25	2.25	2.25	2.25	1.02	1.02	0.60	0.27	0.14	0.14	0.05	0.05	0.00	0.00	0.00	0.00	0.00	0.00	0.00
9	2.22	1.17	1.17	1.17	1.17	4.79	19.38	19.38	19.38	19.38	2.01	2.01	2.01	2.01	1.07	1.07	0.36	0.15	0.02	0.02	0.00	0.00	0.00	0.00	0.00	0.00	0.00	0.00	0.00
10	0.35	0.28	0.28	0.28	0.28	4.85	22.37	22.37	22.37	22.37	0.98	0.98	0.98	0.98	0.11	0.11	0.07	0.00	0.00	0.00	0.00	0.00	0.00	0.00	0.00	0.00	0.00	0.00	0.00
11	0.46	1.91	1.91	1.91	1.91	5.03	12.51	12.51	12.51	12.51	6.26	6.26	6.26	6.26	3.81	3.81	2.05	1.39	0.33	0.33	0.04	0.04	0.00	0.00	0.00	0.00	0.00	0.00	0.00
12	0.00	0.00	0.00	0.00	0.00	0.00	0.00	0.00	0.00	0.00	0.00	0.00	0.00	0.00	0.00	0.00	0.00	0.00	0.00	0.00	0.00	0.00	0.00	0.00	0.00	0.00	0.00	0.00	0.00
13	0.00	0.00	0.00	0.00	0.00	4.31	19.61	19.61	19.61	19.61	3.66	3.66	3.66	3.66	0.00	0.00	0.86	0.00	0.86	0.86	0.00	0.00	0.00	0.00	0.00	0.00	0.00	0.00	0.00

Class	Tandem Axle Load																								
	6000	8000	10000	12000	14000	16000	18000	20000	22000	24000	26000	28000	30000	32000	34000	36000	38000	40000	42000	44000	46000	48000	50000	52000+	
4	2.82	13.38	13.38	13.38	8.39	8.39	8.39	6.65	6.65	6.65	2.44	2.44	2.44	2.61	1.04	0.21	0.31	0.42	0.00	0.00	0.00	0.00	0.00	0.00	0.00
5	0.00	0.00	0.00	0.00	0.00	0.00	0.00	0.00	0.00	0.00	0.00	0.00	0.00	0.00	0.00	0.00	0.00	0.00	0.00	0.00	0.00	0.00	0.00	0.00	0.00
6	8.12	13.75	13.75	13.75	13.90	13.90	13.90	1.27	1.27	1.27	1.14	1.14	1.14	0.81	0.52	0.18	0.15	0.04	0.00	0.00	0.00	0.00	0.00	0.00	0.00
7	0.00	0.00	0.00	0.00	0.00	0.00	0.00	0.00	0.00	0.00	0.00	0.00	0.00	0.00	0.00	0.00	0.00	0.00	0.00	0.00	0.00	0.00	0.00	0.00	0.00
8	18.39	15.28	15.28	15.28	8.39	8.39	8.39	2.95	2.95	2.95	0.49	0.49	0.49	0.13	0.05	0.03	0.03	0.03	0.00	0.00	0.00	0.00	0.00	0.00	0.00
9	4.91	6.37	6.37	6.37	5.76	5.76	5.76	5.65	5.65	5.65	6.55	6.55	6.55	8.55	7.10	4.20	1.70	0.45	0.09	0.01	0.00	0.00	0.00	0.00	0.00
10	1.23	2.71	2.71	2.71	3.95	3.95	3.95	9.44	9.44	9.44	13.35	13.35	13.35	4.40	2.54	1.12	0.63	0.57	0.41	0.38	0.19	0.10	0.10	0.00	0.00
11	12.70	1.01	1.01	1.01	6.14	6.14	6.14	9.65	9.65	9.65	9.83	9.83	9.83	3.52	2.10	1.42	0.24	0.10	0.05	0.00	0.00	0.00	0.00	0.00	0.00
12	0.00	0.00	0.00	0.00	0.00	0.00	0.00	0.00	0.00	0.00	0.00	0.00	0.00	0.00	0.00	0.00	0.00	0.00	0.00	0.00	0.00	0.00	0.00	0.00	0.00
13	1.38	5.92	5.92	5.92	9.67	9.67	9.67	3.88	3.88	3.88	5.05	5.05	5.05	2.07	3.45	5.17	2.76	3.07	2.07	5.80	0.00	0.17	0.17	0.00	0.00

Class	Tridem Axle Load															
	12000	15000	18000	21000	24000	27000	30000	33000	36000	39000	42000	45000	48000	51000	54000	57000+
4	0.00	0.00	0.00	0.00	0.00	0.00	0.00	0.00	0.00	0.00	0.00	0.00	0.00	0.00	0.00	0.00
5	0.00	0.00	0.00	0.00	0.00	0.00	0.00	0.00	0.00	0.00	0.00	0.00	0.00	0.00	0.00	0.00
6	0.00	0.00	0.00	0.00	0.00	0.00	0.00	0.00	0.00	0.00	0.00	0.00	0.00	0.00	0.00	0.00
7	0.00	50.00	50.00	0.00	0.00	0.00	0.00	0.00	0.00	0.00	0.00	0.00	0.00	0.00	0.00	0.00
8	0.00	16.67	16.67	16.67	16.67	0.00	0.00	33.33	0.00	0.00	0.00	0.00	0.00	0.00	0.00	0.00
9	0.00	0.00	0.00	25.00	25.00	0.00	0.00	50.00	0.00	0.00	0.00	0.00	0.00	0.00	0.00	0.00
10	23.95	4.93	4.93	2.65	2.65	5.43	5.43	13.00	14.35	11.30	3.68	2.51	1.52	1.35	1.35	0.06
11	0.00	0.00	0.00	0.00	0.00	0.00	0.00	0.00	0.00	0.00	0.00	0.00	0.00	0.00	0.00	0.00
12	0.00	0.00	0.00	0.00	0.00	0.00	0.00	0.00	0.00	0.00	0.00	0.00	0.00	0.00	0.00	0.00
13	9.09	4.55	4.55	5.37	5.37	2.89	2.89	9.09	6.61	9.09	0.00	8.26	8.26	9.92	6.61	0.46

Class	Quad Axle Load															
	12000	15000	18000	21000	24000	27000	30000	33000	36000	39000	42000	45000	48000	51000	54000	57000+
4	0.00	0.00	0.00	0.00	0.00	0.00	0.00	0.00	0.00	0.00	0.00	0.00	0.00	0.00	0.00	0.00
5	0.00	0.00	0.00	0.00	0.00	0.00	0.00	0.00	0.00	0.00	0.00	0.00	0.00	0.00	0.00	0.00
6	0.00	0.00	0.00	0.00	0.00	0.00	0.00	0.00	0.00	0.00	0.00	0.00	0.00	0.00	0.00	0.00
7	0.00	0.00	0.00	0.00	0.00	0.00	0.00	0.00	0.00	0.00	0.00	0.00	0.00	0.00	0.00	0.00
8	0.00	0.00	0.00	0.00	0.00	0.00	0.00	0.00	0.00	0.00	0.00	0.00	0.00	0.00	0.00	0.00
9	0.00	0.00	0.00	0.00	0.00	0.00	0.00	0.00	0.00	0.00	0.00	0.00	0.00	0.00	0.00	0.00
10	0.00	0.00	0.00	0.00	0.00	0.00	0.00	0.00	0.00	0.00	0.00	0.00	0.00	0.00	0.00	0.00
11	0.00	0.00	0.00	0.00	0.00	0.00	0.00	0.00	0.00	0.00	0.00	0.00	0.00	0.00	0.00	0.00
12	0.00	0.00	0.00	0.00	0.00	0.00	0.00	0.00	0.00	0.00	0.00	0.00	0.00	0.00	0.00	0.00
13	6.25	3.13	3.13	0.00	0.00	6.25	6.25	0.00	6.25	18.75	31.25	18.75	0.00	0.00	0.00	0.00



Table C.4. Axle Load Distribution for Moline EB.

Class	Single Axle Load																													
	3000	4000	5000	6000	7000	8000	9000	10000	11000	12000	13000	14000	15000	16000	17000	18000	19000	20000	21000	22000	23000	24000	25000	26000	27000	28000	29000	30000	31000+	
4	0.09	10.23	10.23	10.23	10.23	17.90	8.07	8.07	8.07	8.07	1.60	1.60	1.60	1.60	0.67	0.67	0.63	0.09	0.18	0.18	0.00	0.00	0.00	0.00	0.00	0.00	0.00	0.00	0.00	
5	0.11	12.81	12.81	12.81	12.81	14.72	6.40	6.40	6.40	6.40	1.69	1.69	1.69	1.69	0.50	0.50	0.28	0.11	0.08	0.08	0.00	0.00	0.00	0.00	0.00	0.00	0.00	0.00	0.00	
6	0.05	0.72	0.72	0.72	0.72	11.80	18.60	18.60	18.60	18.60	1.94	1.94	1.94	1.94	0.61	0.61	0.97	0.41	0.20	0.20	0.05	0.05	0.00	0.00	0.00	0.00	0.00	0.00	0.00	
7	0.00	0.00	0.00	0.00	0.00	0.00	8.33	8.33	8.33	8.33	8.33	8.33	8.33	8.33	16.67	16.67	0.00	0.00	0.00	0.00	0.00	0.00	0.00	0.00	0.00	0.00	0.00	0.00	0.00	
8	2.94	6.20	6.20	6.20	6.20	15.36	10.61	10.61	10.61	10.61	2.71	2.71	2.71	2.71	0.96	0.96	0.68	0.42	0.24	0.24	0.04	0.04	0.00	0.00	0.01	0.01	0.01	0.01	0.00	
9	0.10	0.14	0.14	0.14	0.14	2.60	23.10	23.10	23.10	23.10	1.02	1.02	1.02	1.02	0.11	0.11	0.06	0.02	0.00	0.00	0.00	0.00	0.00	0.00	0.00	0.00	0.00	0.00	0.00	
10	0.20	0.44	0.44	0.44	0.44	7.45	21.47	21.47	21.47	21.47	1.18	1.18	1.18	1.18	0.00	0.00	0.00	0.00	0.00	0.00	0.00	0.00	0.00	0.00	0.00	0.00	0.00	0.00	0.00	
11	0.22	2.13	2.13	2.13	2.13	6.22	12.88	12.88	12.88	12.88	6.84	6.84	6.84	6.84	2.23	2.23	0.67	0.52	0.21	0.21	0.04	0.04	0.00	0.00	0.00	0.00	0.00	0.00	0.00	
12	0.00	0.00	0.00	0.00	0.00	0.00	12.50	12.50	12.50	12.50	12.50	12.50	12.50	12.50	0.00	0.00	0.00	0.00	0.00	0.00	0.00	0.00	0.00	0.00	0.00	0.00	0.00	0.00	0.00	
13	0.00	0.00	0.00	0.00	0.00	3.03	19.95	19.95	19.95	19.95	4.29	4.29	4.29	4.29	0.00	0.00	0.00	0.00	0.00	0.00	0.00	0.00	0.00	0.00	0.00	0.00	0.00	0.00	0.00	

Class	Tandem Axle Load																
	6000	8000	10000	12000	14000	16000	18000	20000	22000	24000	26000	28000	30000	32000	34000	36000	38000
4	4.65	10.08	10.08	10.08	8.91	8.91	8.91	3.88	3.88	3.88	3.49	3.49	3.49	5.81	3.49	3.49	2.33
5	0.00	0.00	0.00	0.00	0.00	0.00	0.00	0.00	0.00	0.00	0.00	0.00	0.00	0.00	0.00	0.00	0.00
6	7.59	12.76	12.76	12.76	10.43	10.43	10.43	2.63	2.63	2.63	1.64	1.64	2.70	3.48	2.75	0.68	0.20
7	0.00	0.00	0.00	0.00	0.00	0.00	0.00	0.00	0.00	0.00	0.00	0.00	0.00	0.00	0.00	0.00	0.00
8	8.15	11.14	11.14	11.14	9.33	9.33	9.33	6.08	6.08	6.08	3.63	3.63	3.63	1.07	0.16	0.05	0.00
9	3.54	4.26	4.26	4.26	5.24	5.24	5.24	5.67	5.67	5.67	7.16	7.16	9.71	10.15	6.51	2.21	0.74
10	0.50	3.61	3.61	3.61	6.79	6.79	6.79	6.07	6.07	6.07	9.33	9.33	9.33	8.81	4.52	5.88	0.67
11	0.00	0.82	0.82	0.82	17.92	17.92	17.92	7.07	7.07	7.07	6.52	6.52	2.01	0.62	0.22	0.14	0.02
12	0.00	0.00	0.00	0.00	0.00	0.00	0.00	16.67	16.67	16.67	16.67	16.67	16.67	0.00	0.00	0.00	0.00
13	0.46	0.93	0.93	0.93	6.46	6.46	6.46	4.85	4.85	4.85	5.78	5.78	5.78	14.09	10.19	18.45	1.85

Class	Tridem Axle Load														
	12000	15000	18000	21000	24000	27000	30000	33000	36000	39000	42000	45000	48000	51000	54000
4	0.00	0.00	0.00	0.00	0.00	0.00	0.00	0.00	0.00	0.00	0.00	0.00	0.00	0.00	0.00
5	0.00	0.00	0.00	0.00	0.00	0.00	0.00	0.00	0.00	0.00	0.00	0.00	0.00	0.00	0.00
6	0.00	0.00	0.00	0.00	0.00	0.00	0.00	0.00	0.00	0.00	0.00	0.00	0.00	0.00	0.00
7	0.00	0.00	0.00	0.00	0.00	0.00	0.00	0.00	0.00	33.33	66.67	0.00	0.00	0.00	0.00
8	14.29	14.29	14.29	14.29	14.29	0.00	0.00	0.00	14.29	14.29	0.00	0.00	0.00	0.00	0.00
9	1.45	6.52	6.52	12.32	12.32	4.35	4.35	5.80	20.29	15.94	5.80	0.00	0.00	0.00	0.00
10	25.07	7.32	7.32	4.51	4.51	5.63	5.63	10.70	10.42	8.45	4.23	2.82	2.25	0.85	0.02
11	0.00	0.00	0.00	0.00	0.00	0.00	0.00	0.00	0.00	0.00	0.00	0.00	0.00	0.00	0.00
12	0.00	0.00	0.00	0.00	0.00	50.00	50.00	0.00	0.00	0.00	0.00	0.00	0.00	0.00	0.00
13	15.69	7.84	7.84	5.88	5.88	3.92	3.92	7.84	3.92	0.00	3.92	7.84	3.92	5.88	7.84

Class	Quad Axle Load														
	12000	15000	18000	21000	24000	27000	30000	33000	36000	39000	42000	45000	48000	51000	54000
4	0.00	0.00	0.00	0.00	0.00	0.00	0.00	0.00	0.00	0.00	0.00	0.00	0.00	0.00	0.00
5	0.00	0.00	0.00	0.00	0.00	0.00	0.00	0.00	0.00	0.00	0.00	0.00	0.00	0.00	0.00
6	0.00	0.00	0.00	0.00	0.00	0.00	0.00	0.00	0.00	0.00	0.00	0.00	0.00	0.00	0.00
7	0.00	0.00	0.00	0.00	0.00	0.00	0.00	0.00	0.00	0.00	0.00	0.00	0.00	0.00	0.00
8	0.00	0.00	0.00	0.00	0.00	0.00	0.00	0.00	0.00	0.00	0.00	0.00	0.00	0.00	0.00
9	0.00	0.00	0.00	0.00	0.00	0.00	0.00	0.00	0.00	0.00	0.00	0.00	0.00	0.00	0.00
10	0.00	0.00	0.00	0.00	0.00	0.00	0.00	0.00	0.00	0.00	0.00	0.00	0.00	0.00	0.00
11	0.00	0.00	0.00	0.00	0.00	0.00	0.00	0.00	0.00	0.00	0.00	0.00	0.00	0.00	0.00
12	0.00	0.00	0.00	0.00	0.00	0.00	0.00	0.00	0.00	0.00	0.00	0.00	0.00	0.00	0.00
13	0.00	0.00	0.00	7.14	7.14	7.14	7.14	0.00	28.57	28.57	0.00	0.00	14.29	0.00	0.00

Table C.5. Axle Load Distribution for Marion SB.

Class	Single Axle Load																													
	3000	4000	5000	6000	7000	8000	9000	10000	11000	12000	13000	14000	15000	16000	17000	18000	19000	20000	21000	22000	23000	24000	25000	26000	27000	28000	29000	30000	31000+	
4	0.00	2.22	2.22	2.22	2.22	18.47	13.55	13.55	13.55	13.55	3.64	3.64	3.64	3.64	1.09	1.09	0.52	0.63	0.26	0.26	0.03	0.03	0.00	0.00	0.00	0.00	0.00	0.00	0.00	
5	0.25	7.74	7.74	7.74	7.74	18.21	9.74	9.74	9.74	9.74	2.14	2.14	2.14	2.14	0.90	0.90	0.61	0.36	0.09	0.09	0.03	0.03	0.01	0.01	0.00	0.00	0.00	0.00	0.00	
6	0.00	0.32	0.32	0.32	0.32	5.02	21.10	21.10	21.10	21.10	1.75	1.75	1.75	1.75	1.04	1.04	0.00	0.05	0.05	0.05	0.03	0.03	0.00	0.00	0.00	0.00	0.00	0.00	0.00	
7	0.00	0.00	0.00	0.00	0.00	0.00	0.00	0.00	0.00	0.00	0.00	0.00	0.00	0.00	50.00	50.00	0.00	0.00	0.00	0.00	0.00	0.00	0.00	0.00	0.00	0.00	0.00	0.00	0.00	
8	0.65	4.21	4.21	4.21	4.21	13.20	12.04	12.04	12.04	12.04	3.74	3.74	3.74	3.74	1.96	1.96	0.99	0.65	0.22	0.22	0.06	0.06	0.02	0.02	0.00	0.00	0.00	0.00	0.00	
9	0.01	0.05	0.05	0.05	0.05	1.10	21.90	21.90	21.90	21.90	2.77	2.77	2.77	2.77	0.00	0.00	0.00	0.01	0.00	0.00	0.00	0.00	0.00	0.00	0.00	0.00	0.00	0.00	0.00	
10	0.00	0.12	0.12	0.12	0.12	1.08	21.78	21.78	21.78	21.78	2.70	2.70	2.70	2.70	0.18	0.18	0.12	0.00	0.00	0.00	0.00	0.00	0.00	0.00	0.00	0.00	0.00	0.00	0.00	
11	0.12	2.94	2.94	2.94	2.94	6.63	11.41	11.41	11.41	11.41	5.41	5.41	5.41	5.41	4.46	4.46	2.67	1.70	0.42	0.42	0.03	0.03	0.00	0.00	0.00	0.00	0.00	0.00	0.00	
12	0.00	2.42	2.42	2.42	2.42	6.45	11.29	11.29	11.29	11.29	4.84	4.84	4.84	4.84	6.45	6.45	3.23	3.23	0.00	0.00	0.00	0.00	0.00	0.00	0.00	0.00	0.00	0.00	0.00	
13	0.00	0.34	0.34	0.34	0.34	2.21	20.06	20.06	20.06	20.06	3.88	3.88	3.88	3.88	0.17	0.17	0.00	0.00	0.17	0.17	0.00	0.00	0.00	0.00	0.00	0.00	0.00	0.00	0.00	

Class	Tandem Axle Load																								
	6000	8000	10000	12000	14000	16000	18000	20000	22000	24000	26000	28000	30000	32000	34000	36000	38000	40000	42000	44000	46000	48000	50000	52000+	
4	0.00	8.21	8.21	8.21	9.74	9.74	9.74	12.31	12.31	12.31	2.56	2.56	2.56	1.54	0.00	0.00	0.00	0.00	0.00	0.00	0.00	0.00	0.00	0.00	0.00
5	0.00	0.00	0.00	0.00	0.00	0.00	0.00	0.00	0.00	0.00	0.00	0.00	0.00	0.00	0.00	0.00	0.00	0.00	0.00	0.00	0.00	0.00	0.00	0.00	0.00
6	17.35	9.60	9.60	9.60	15.71	15.71	15.71	1.14	1.14	1.14	0.62	0.62	0.62	0.55	0.47	0.27	0.07	0.04	0.00	0.02	0.00	0.00	0.00	0.00	0.00
7	0.00	0.00	0.00	0.00	0.00	0.00	0.00	0.00	0.00	0.00	0.00	0.00	0.00	0.00	0.00	0.00	0.00	0.00	0.00	0.00	0.00	0.00	0.00	0.00	0.00
8	2.96	9.92	9.92	9.92	11.17	11.17	11.17	7.95	7.95	7.95	2.78	2.78	2.78	1.25	0.20	0.08	0.03	0.03	0.00	0.00	0.00	0.00	0.00	0.00	0.00
9	0.74	5.62	5.62	5.62	7.93	7.93	7.93	5.22	5.22	5.22	4.76	4.76	4.76	5.83	6.79	5.89	4.36	3.18	1.72	0.71	0.17	0.01	0.01	0.00	0.00
10	0.54	2.39	2.39	2.39	5.29	5.29	5.29	5.24	5.24	5.24	9.93	9.93	9.93	11.81	6.63	3.92	2.25	2.23	2.68	0.81	0.35	0.10	0.10	0.00	0.00
11	0.00	1.65	1.65	1.65	5.28	5.28	5.28	10.76	10.76	10.76	12.66	12.66	12.66	4.87	2.28	1.44	0.31	0.03	0.00	0.00	0.00	0.00	0.00	0.00	0.00
12	0.00	0.00	0.00	0.00	8.33	8.33	8.33	13.89	13.89	13.89	11.11	11.11	11.11	0.00	0.00	0.00	0.00	0.00	0.00	0.00	0.00	0.00	0.00	0.00	0.00
13	0.33	3.40	3.40	3.40	6.60	6.60	6.60	6.93	6.93	6.93	5.54	5.54	5.54	6.53	8.59	6.66	3.30	3.66	2.85	0.23	0.15	0.15	0.15	0.00	0.00

Class	Tridem Axle Load															
	12000	15000	18000	21000	24000	27000	30000	33000	36000	39000	42000	45000	48000	51000	54000	57000+
4	0.00	0.00	0.00	0.00	0.00	0.00	0.00	0.00	0.00	0.00	0.00	0.00	0.00	0.00	0.00	0.00
5	0.00	0.00	0.00	0.00	0.00	0.00	0.00	0.00	0.00	0.00	0.00	0.00	0.00	0.00	0.00	0.00
6	0.00	0.00	0.00	0.00	0.00	0.00	0.00	0.00	0.00	0.00	0.00	0.00	0.00	0.00	0.00	0.00
7	0.00	0.00	0.00	0.00	0.00	0.00	0.00	0.00	100.00	0.00	0.00	0.00	0.00	0.00	0.00	0.00
8	0.00	0.00	0.00	0.00	0.00	14.29	14.29	0.00	28.57	28.57	14.29	0.00	0.00	0.00	0.00	0.00
9	0.00	0.00	0.00	50.00	50.00	0.00	0.00	0.00	0.00	0.00	0.00	0.00	0.00	0.00	0.00	0.00
10	13.11	5.16	5.16	2.53	2.53	2.10	2.10	3.67	10.66	15.03	14.34	8.74	4.02	1.92	2.45	0.40
11	0.00	0.00	0.00	0.00	0.00	0.00	0.00	0.00	0.00	0.00	0.00	0.00	0.00	0.00	0.00	0.00
12	28.57	0.00	0.00	0.00	0.00	28.57	28.57	0.00	14.29	0.00	0.00	0.00	0.00	0.00	0.00	0.00
13	8.50	5.47	5.47	10.12	10.12	7.49	7.49	8.50	4.45	4.45	3.24	0.00	0.81	2.02	3.24	1.16

Class	Quad Axle Load															
	12000	15000	18000	21000	24000	27000	30000	33000	36000	39000	42000	45000	48000	51000	54000	57000+
4	0.00	0.00	0.00	0.00	0.00	0.00	0.00	0.00	0.00	0.00	0.00	0.00	0.00	0.00	0.00	0.00
5	0.00	0.00	0.00	0.00	0.00	0.00	0.00	0.00	0.00	0.00	0.00	0.00	0.00	0.00	0.00	0.00
6	0.00	0.00	0.00	0.00	0.00	0.00	0.00	0.00	0.00	0.00	0.00	0.00	0.00	0.00	0.00	0.00
7	0.00	0.00	0.00	0.00	0.00	0.00	0.00	0.00	0.00	0.00	0.00	0.00	0.00	0.00	0.00	0.00
8	0.00	0.00	0.00	0.00	0.00	0.00	0.00	0.00	0.00	0.00	0.00	0.00	0.00	0.00	0.00	0.00
9	0.00	0.00	0.00	0.00	0.00	0.00	0.00	0.00	0.00	0.00	0.00	0.00	0.00	0.00	0.00	0.00
10	0.00	0.00	0.00	0.00	0.00	0.00	0.00	0.00	0.00	0.00	0.00	0.00	0.00	0.00	0.00	0.00
11	0.00	0.00	0.00	0.00	0.00	0.00	0.00	0.00	0.00	0.00	0.00	0.00	0.00	0.00	0.00	0.00
12	0.00	0.00	0.00	0.00	0.00	0.00	0.00	0.00	0.00	0.00	0.00	0.00	0.00	0.00	0.00	0.00
13	1.89	4.25	4.25	5.19	5.19	8.02	8.02	5.66	14.15	10.38	10.38	14.15	0.94	0.94	0.00	0.41

Table C.6. Axle Load Distribution for Maryville WB.

Class	Single Axle Load																													
	3000	4000	5000	6000	7000	8000	9000	10000	11000	12000	13000	14000	15000	16000	17000	18000	19000	20000	21000	22000	23000	24000	25000	26000	27000	28000	29000	30000	31000+	
4	0.31	5.30	5.30	5.30	5.30	17.13	10.83	10.83	10.83	10.83	3.35	3.35	3.35	3.35	1.61	1.61	0.31	0.52	0.21	0.21	0.05	0.05	0.00	0.00	0.03	0.03	0.03	0.03	0.00	
5	0.53	9.77	9.77	9.77	9.77	17.65	7.82	7.82	7.82	7.82	2.15	2.15	2.15	2.15	0.86	0.86	0.64	0.27	0.05	0.05	0.03	0.03	0.00	0.00	0.01	0.01	0.01	0.01	0.00	
6	0.42	1.52	1.52	1.52	1.52	17.07	16.86	16.86	16.86	16.86	2.07	2.07	2.07	2.07	0.26	0.26	0.10	0.10	0.00	0.00	0.00	0.00	0.00	0.00	0.00	0.00	0.00	0.00	0.00	0.00
7	0.00	0.00	0.00	0.00	0.00	0.00	12.50	12.50	12.50	12.50	0.00	0.00	0.00	0.00	25.00	25.00	0.00	0.00	0.00	0.00	0.00	0.00	0.00	0.00	0.00	0.00	0.00	0.00	0.00	0.00
8	1.45	5.37	5.37	5.37	5.37	14.87	11.22	11.22	11.22	11.22	3.29	3.29	3.29	3.29	1.23	1.23	0.91	0.54	0.08	0.08	0.04	0.04	0.00	0.00	0.00	0.00	0.00	0.00	0.00	0.00
9	0.06	0.34	0.34	0.34	0.34	5.01	23.10	23.10	23.10	23.10	0.26	0.26	0.26	0.26	0.04	0.04	0.02	0.01	0.00	0.00	0.00	0.00	0.00	0.00	0.00	0.00	0.00	0.00	0.00	0.00
10	0.35	0.40	0.40	0.40	0.40	5.62	22.67	22.67	22.67	22.67	0.44	0.44	0.44	0.44	0.00	0.00	0.00	0.00	0.00	0.00	0.00	0.00	0.00	0.00	0.00	0.00	0.00	0.00	0.00	0.00
11	0.12	0.76	0.76	0.76	0.76	3.62	10.14	10.14	10.14	10.14	6.96	6.96	6.96	6.96	7.91	7.91	5.22	2.49	0.58	0.58	0.03	0.03	0.02	0.02	0.00	0.00	0.00	0.00	0.00	0.00
12	0.00	1.04	1.04	1.04	1.04	1.39	9.38	9.38	9.38	9.38	7.29	7.29	7.29	7.29	8.33	8.33	2.78	4.17	1.39	1.39	0.69	0.69	0.00	0.00	0.00	0.00	0.00	0.00	0.00	0.00
13	1.14	2.41	2.41	2.41	2.41	23.86	14.91	14.91	14.91	14.91	0.99	0.99	0.99	0.99	0.00	0.00	1.14	0.00	0.28	0.28	0.00	0.00	0.00	0.00	0.00	0.00	0.00	0.00	0.00	0.00

Class	Tandem Axle Load																
	6000	8000	10000	12000	14000	16000	18000	20000	22000	24000	26000	28000	30000	32000	34000	36000	38000
4	3.70	4.94	4.94	4.94	14.81	14.81	14.81	8.64	8.64	8.64	3.70	3.70	3.70	0.00	0.00	0.00	0.00
5	0.00	0.00	0.00	0.00	0.00	0.00	0.00	0.00	0.00	0.00	0.00	0.00	0.00	0.00	0.00	0.00	0.00
6	6.06	15.01	15.01	15.01	12.39	12.39	12.39	2.45	2.45	2.45	0.89	0.89	0.74	0.68	0.19	0.12	0.00
7	0.00	0.00	0.00	0.00	0.00	0.00	0.00	0.00	0.00	0.00	0.00	0.00	0.00	0.00	0.00	0.00	0.00
8	6.29	8.03	8.03	8.03	13.07	13.07	13.07	7.50	7.50	7.50	2.05	2.05	2.05	0.23	0.46	0.54	0.00
9	0.29	2.17	2.17	2.17	6.33	6.33	6.33	8.10	8.10	8.10	7.42	7.42	7.97	9.11	6.40	2.83	1.07
10	0.95	1.31	1.31	1.31	7.28	7.28	7.28	8.18	8.18	8.18	7.59	7.59	7.59	8.30	9.47	5.39	1.11
11	0.00	0.36	0.36	0.36	10.47	10.47	10.47	5.58	5.58	5.58	6.82	6.82	8.05	6.51	13.95	1.27	0.40
12	0.00	0.00	0.00	0.00	16.67	16.67	16.67	8.33	8.33	8.33	0.00	0.00	0.00	0.00	25.00	0.00	0.00
13	4.99	8.66	8.66	8.66	12.63	12.63	12.63	5.58	5.58	5.58	2.24	2.24	2.24	1.36	2.22	2.36	0.62

Class	Tridem Axle Load												
	12000	15000	18000	21000	24000	27000	30000	33000	36000	39000	42000	45000	48000
4	0.00	0.00	0.00	0.00	0.00	0.00	0.00	0.00	0.00	0.00	0.00	0.00	0.00
5	0.00	0.00	0.00	0.00	0.00	0.00	0.00	0.00	0.00	0.00	0.00	0.00	0.00
6	0.00	0.00	0.00	0.00	0.00	0.00	0.00	0.00	0.00	0.00	0.00	0.00	0.00
7	0.00	0.00	0.00	0.00	0.00	0.00	0.00	0.00	0.00	100.00	0.00	0.00	0.00
8	0.00	6.25	6.25	0.00	0.00	0.00	12.50	12.50	50.00	12.50	0.00	0.00	0.00
9	0.00	0.00	0.00	0.00	0.00	0.00	100.00	0.00	0.00	0.00	0.00	0.00	0.00
10	6.09	4.35	4.35	3.48	3.48	3.91	3.91	13.04	21.74	9.57	13.91	6.09	0.87
11	0.00	0.00	0.00	0.00	0.00	0.00	0.00	0.00	0.00	0.00	0.00	0.00	0.00
12	0.00	0.00	0.00	2.27	2.27	18.18	18.18	27.27	22.73	9.09	0.00	0.00	0.00
13	12.90	16.94	16.94	5.65	5.65	4.84	4.84	9.68	1.61	4.84	0.00	1.61	8.06

Class	Quad Axle Load												
	12000	15000	18000	21000	24000	27000	30000	33000	36000	39000	42000	45000	48000
4	0.00	0.00	0.00	0.00	0.00	0.00	0.00	0.00	0.00	0.00	0.00	0.00	0.00
5	0.00	0.00	0.00	0.00	0.00	0.00	0.00	0.00	0.00	0.00	0.00	0.00	0.00
6	0.00	0.00	0.00	0.00	0.00	0.00	0.00	0.00	0.00	0.00	0.00	0.00	0.00
7	0.00	0.00	0.00	0.00	0.00	0.00	0.00	0.00	0.00	0.00	0.00	0.00	0.00
8	0.00	0.00	0.00	0.00	0.00	0.00	0.00	0.00	0.00	0.00	0.00	0.00	0.00
9	0.00	0.00	0.00	0.00	0.00	0.00	0.00	0.00	0.00	0.00	0.00	0.00	0.00
10	0.00	0.00	0.00	0.00	0.00	0.00	0.00	0.00	0.00	0.00	0.00	0.00	0.00
11	0.00	0.00	0.00	0.00	0.00	0.00	0.00	0.00	0.00	0.00	0.00	0.00	0.00
12	0.00	0.00	0.00	0.00	0.00	0.00	0.00	0.00	0.00	0.00	0.00	0.00	0.00
13	8.33	18.75	18.75	18.75	18.75	4.17	4.17	0.00	0.00	0.00	4.17	4.17	0.00

Table C.7. Pesotum WIM Summary.

	<b>Vehicle Classification</b>															<b>Total</b>
	<b>1</b>	<b>2</b>	<b>3</b>	<b>4</b>	<b>5</b>	<b>6</b>	<b>7</b>	<b>8</b>	<b>9</b>	<b>10</b>	<b>11</b>	<b>12</b>	<b>13</b>	<b>14</b>	<b>15</b>	
Veh Count	0	101,543	33,453	1,953	7,334	1,083	30	2,903	61,706	366	1,979	1,323	87	0	3,736	217,496
% Count	0	47	15	1	3	1	0	1	28	0	1	1	0	0	2	100
Total Gross Weight (1000s)	0	363,776	181,829	46,388	71,075	24,390	1,480	70,134	3,452,850	21,982	104,647	76,774	8,568	0	3,664	4,427,558
Avg. Gross Vehicle Weight	0	3,584	5,438	23,789	9,694	22,625	49,350	24,176	55,994	60,060	52,959	58,031	102,004	0	99,020	20,721
Total ESAL	0	58	65	818	318	316	46	804	89,111	554	2,122	922	475	0	159	95,768
Avg. ESLA	0	0	0	0	0	0	2	0	1	2	1	1	6	0	4	0
Overweight	0	0	0	201	16	100	21	37	3,076	126	15	10	73	0	0	3,675
% Overweight	0	0	0	10	0	9	70	1	5	34	1	1	87	0	0	2

Table C.8. Steer Axle Load Spectra for Average of All California WIM Stations.

Load Level (kips)	FHWA Vehicle Class											
	4	5	6	7	8	9	10	11	12	13	14	15
1	0	0	0	0	0	0	0	0	0	0	0	0
2	0	0	0	0	0	0	0	0	0	0	0	0
3	0	0.00003	0	0	0	0	0	0	0	0	0	0
4	0.00001	0.07904	0.00035	0	0.00417	0.00035	0	0.00005	0.00001	0	0.00001	0.00495
5	0.00005	0.0488	0.00057	0.00001	0.00395	0.00079	0.00001	0.00028	0.00004	0.00001	0.00003	0.00203
6	0.00025	0.03293	0.00095	0.00002	0.00741	0.00205	0.00003	0.00308	0.00029	0.00002	0.00025	0.00149
7	0.0008	0.02913	0.00415	0.00002	0.01522	0.01725	0.00023	0.01913	0.00126	0.00008	0.00244	0.00219
8	0.00153	0.01899	0.01038	0.00004	0.01871	0.06874	0.00085	0.03305	0.00259	0.0002	0.00582	0.00239
9	0.0024	0.01096	0.01367	0.00005	0.01142	0.14719	0.002	0.02355	0.00349	0.00027	0.00636	0.00198
10	0.00237	0.00487	0.0094	0.00003	0.00376	0.15919	0.00206	0.00724	0.00231	0.00019	0.00521	0.00141
11	0.00196	0.00211	0.00493	0.00003	0.00126	0.07537	0.00089	0.00128	0.0006	0.00011	0.00325	0.00083
12	0.00116	0.00093	0.00264	0.00006	0.00034	0.01343	0.00015	0.00009	0.00005	0.00006	0.00126	0.00046
13	0.00054	0.00063	0.0016	0.00013	0.0001	0.00155	0.00002	0.00001	0	0.00003	0.00038	0.00042
14	0.00018	0.00055	0.001	0.00022	0.00004	0.00028	0.00001	0	0	0.00002	0.0001	0.0004
15	0.00007	0.00051	0.0008	0.00039	0.00004	0.00015	0	0	0	0.00001	0.00003	0.00037
16	0.00002	0.00036	0.0006	0.00059	0.00005	0.0001	0	0	0	0.00001	0.00001	0.00027
17	0.00001	0.00021	0.00039	0.00065	0.00005	0.00007	0	0	0	0.00001	0	0.00018
18	0.00001	0.00009	0.00018	0.00036	0.00003	0.00003	0	0	0	0.00001	0	0.00009
19	0	0.00005	0.00009	0.00014	0.00001	0.00001	0	0	0	0.00001	0	0.00005
20	0	0.00003	0.00006	0.00005	0.00001	0.00001	0	0	0	0	0	0.00003
21	0	0.00002	0.00004	0.00001	0	0	0	0	0	0	0	0.00002
22	0	0.00001	0.00002	0	0	0	0	0	0	0	0	0.00002
23	0	0.00001	0.00001	0	0	0	0	0	0	0	0	0.00001
24	0	0.00001	0.00001	0	0	0	0	0	0	0	0	0.00001
25	0	0.00001	0	0	0	0	0	0	0	0	0	0
26	0	0	0	0	0	0	0	0	0	0	0	0
27	0	0	0	0	0	0	0	0	0	0	0	0
28	0	0	0	0	0	0	0	0	0	0	0	0
29	0	0	0	0	0	0	0	0	0	0	0	0
30	0	0	0	0	0	0	0	0	0	0	0	0
31	0	0	0	0	0	0	0	0	0	0	0	0
32	0	0	0	0	0	0	0	0	0	0	0	0
33	0	0	0	0	0	0	0	0	0	0	0	0
34	0	0	0	0	0	0	0	0	0	0	0	0
35	0	0	0	0	0	0	0	0	0	0	0	0
36	0	0	0	0	0	0	0	0	0	0	0	0
37	0	0	0	0	0	0	0	0	0	0	0	0
38	0	0	0	0	0	0	0	0	0	0	0	0
39	0	0	0	0	0	0	0	0	0	0	0	0
40	0	0	0	0	0	0	0	0	0	0	0	0
41	0	0	0	0	0	0	0	0	0	0	0	0
42	0	0	0	0	0	0	0	0	0	0	0	0
43	0	0	0	0	0	0	0	0	0	0	0	0
44	0	0	0	0	0	0	0	0	0	0	0	0

Table C.9. Single-Axle Load Spectra for Average of All California WIM Stations.

Load Level (kips)	FHWA Vehicle Class											
	4	5	6	7	8	9	10	11	12	13	14	15
1	0	0.00157	0	0.00001	0.00462	0.0003	0.00002	0.00035	0.00001	0.00011	0.00007	0.00188
2	0	0.00523	0	0.00003	0.00945	0.00176	0.00001	0.00672	0.00018	0.00017	0.00123	0.00169
3	0	0.00364	0	0.00005	0.00433	0.00317	0.00001	0.02269	0.00081	0.00008	0.0053	0.00203
4	0.00001	0.0231	0	0.00004	0.00367	0.00659	0.00001	0.03307	0.00219	0.00011	0.0096	0.00259
5	0.00001	0.04466	0	0.00005	0.00636	0.00618	0.00001	0.03166	0.00382	0.0002	0.00793	0.00322
6	0.00004	0.03547	0	0.00006	0.00797	0.00344	0.00001	0.02447	0.00351	0.00019	0.00265	0.00263
7	0.00012	0.03353	0	0.0001	0.00985	0.0027	0.00001	0.02408	0.00329	0.00014	0.00098	0.00195
8	0.00023	0.03032	0	0.00016	0.01155	0.00241	0.00001	0.02015	0.00346	0.00011	0.00048	0.0014
9	0.00032	0.02652	0	0.00035	0.01224	0.00241	0.00001	0.01936	0.00392	0.00009	0.00039	0.0012
10	0.00029	0.01786	0	0.00064	0.00988	0.00212	0.00001	0.01799	0.00347	0.00006	0.00044	0.00099
11	0.00026	0.01265	0	0.00082	0.00838	0.00228	0.00001	0.01919	0.00317	0.00005	0.00067	0.00094
12	0.00025	0.00959	0	0.00043	0.00701	0.00286	0.00001	0.02144	0.00278	0.00004	0.00122	0.00092
13	0.0003	0.00826	0	0.0001	0.00647	0.00473	0.00001	0.02767	0.00239	0.00004	0.00268	0.00105
14	0.00033	0.00616	0	0.00002	0.00514	0.00698	0.00001	0.03098	0.00157	0.00004	0.00446	0.00106
15	0.00045	0.00497	0	0	0.00448	0.0091	0.00001	0.03505	0.00102	0.00004	0.00627	0.0011
16	0.00057	0.00376	0	0	0.00359	0.00805	0.00001	0.03166	0.00056	0.00004	0.00636	0.00095
17	0.00058	0.00286	0	0	0.00268	0.0049	0	0.02207	0.00027	0.00004	0.00445	0.00072
18	0.00035	0.00167	0	0	0.00141	0.00176	0	0.00893	0.00009	0.00003	0.00168	0.00037
19	0.0002	0.001	0	0	0.00074	0.00061	0	0.00304	0.00003	0.00003	0.00051	0.00018
20	0.0001	0.00054	0	0	0.00038	0.00022	0	0.00085	0.00001	0.00003	0.00014	0.0001
21	0.00005	0.00031	0	0	0.0002	0.00011	0	0.00023	0	0.00003	0.00004	0.00007
22	0.00002	0.00015	0	0	0.00009	0.00006	0	0.00005	0	0.00002	0.00001	0.00004
23	0.00001	0.00009	0	0	0.00005	0.00004	0	0.00002	0	0.00002	0	0.00003
24	0	0.00005	0	0	0.00003	0.00003	0	0.00001	0	0.00002	0	0.00002
25	0	0.00003	0	0	0.00002	0.00002	0	0	0	0.00001	0	0.00002
26	0	0.00002	0	0	0.00002	0.00001	0	0	0	0.00001	0	0.00001
27	0	0.00001	0	0	0.00001	0.00001	0	0	0	0.00001	0	0.00001
28	0	0.00001	0	0	0.00001	0.00001	0	0	0	0.00001	0	0.00001
29	0	0.00001	0	0	0.00001	0	0	0	0	0	0	0
30	0	0	0	0	0	0	0	0	0	0	0	0
31	0	0	0	0	0	0	0	0	0	0	0	0
32	0	0	0	0	0	0	0	0	0	0	0	0
33	0	0	0	0	0	0	0	0	0	0	0	0
34	0	0	0	0	0	0	0	0	0	0	0	0
35	0	0	0	0	0	0	0	0	0	0	0	0
36	0	0	0	0	0	0	0	0	0	0	0	0
37	0	0	0	0	0	0	0	0	0	0	0	0
38	0	0	0	0	0	0	0	0	0	0	0	0
39	0	0	0	0	0	0	0	0	0	0	0	0
40	0	0	0	0	0	0	0	0	0	0	0	0
41	0	0	0	0	0	0	0	0	0	0	0	0
42	0	0	0	0	0	0	0	0	0	0	0	0
43	0	0	0	0	0	0	0	0	0	0	0	0
44	0	0	0	0	0	0	0	0	0	0	0	0

Table C.10. Tandem Axle Load Spectra for Average of All California WIM Stations.

Load Level (kips)	FHWA Vehicle Class											
	4	5	6	7	8	9	10	11	12	13	14	15
2	0	0.00005	0	0	0.00001	0.00001	0	0	0	0.00001	0	0.00113
4	0	0.0012	0.00018	0	0.00045	0.00114	0	0	0	0.00001	0.00001	0.00108
6	0	0.00195	0.00345	0.00001	0.00136	0.01201	0.00002	0	0.00005	0.00005	0.00013	0.00158
8	0	0.00098	0.00869	0.00004	0.00312	0.04455	0.00013	0	0.00032	0.00014	0.00142	0.00105
10	0.00001	0.00025	0.00621	0.00003	0.00609	0.08533	0.00047	0	0.00106	0.00023	0.00488	0.00094
12	0.00002	0	0.00394	0.00001	0.00524	0.08078	0.00049	0	0.00129	0.00022	0.00302	0.00071
14	0.00008	0	0.00361	0.00001	0.00413	0.0713	0.0004	0	0.00155	0.00019	0.0009	0.00056
16	0.00049	0	0.00326	0.00001	0.0029	0.05286	0.00044	0	0.00173	0.00016	0.00044	0.00039
18	0.00137	0	0.00297	0.00001	0.00224	0.05041	0.00058	0	0.00173	0.00013	0.00027	0.00031
20	0.00165	0	0.00249	0.00002	0.00148	0.04586	0.00059	0	0.00116	0.00008	0.00022	0.00024
22	0.00135	0	0.00235	0.00005	0.00098	0.04739	0.00056	0	0.00058	0.00007	0.00037	0.00025
24	0.00072	0	0.00205	0.00009	0.0006	0.05157	0.00056	0	0.00017	0.00008	0.0008	0.00028
26	0.0005	0	0.00201	0.00017	0.00044	0.07255	0.00061	0	0.00004	0.0001	0.00196	0.00037
28	0.00032	0	0.0019	0.0003	0.00036	0.09383	0.00049	0	0.00001	0.0001	0.00329	0.00044
30	0.00017	0	0.00172	0.00044	0.00032	0.09111	0.00029	0	0	0.00011	0.00317	0.00042
32	0.00006	0	0.00103	0.00042	0.00017	0.04081	0.0001	0	0	0.00009	0.00141	0.00023
34	0.00002	0	0.0006	0.00031	0.00007	0.01217	0.00003	0	0	0.00009	0.00047	0.00011
36	0.00001	0	0.00032	0.00017	0.00002	0.00297	0.00002	0	0	0.00008	0.00013	0.00006
38	0	0	0.00018	0.00009	0.00001	0.00091	0.00001	0	0	0.00006	0.00004	0.00005
40	0	0	0.0001	0.00005	0.00001	0.00033	0.00001	0	0	0.00005	0.00001	0.00003
42	0	0	0.00006	0.00002	0	0.00015	0	0	0	0.00004	0.00001	0.00003
44	0	0	0.00003	0.00001	0	0.00008	0	0	0	0.00003	0	0.00002
46	0	0	0.00002	0	0	0.00005	0	0	0	0.00002	0	0.00002
48	0	0	0.00002	0	0	0.00003	0	0	0	0.00001	0	0.00001
50	0	0	0.00001	0	0	0.00002	0	0	0	0.00001	0	0.00001
52	0	0	0.00001	0	0	0.00001	0	0	0	0.00001	0	0.00001
54	0	0	0.00001	0	0	0.00001	0	0	0	0.00001	0	0
56	0	0	0.00001	0	0	0.00001	0	0	0	0	0	0
58	0	0	0.00001	0	0	0.00001	0	0	0	0	0	0
60	0	0	0.00001	0	0	0	0	0	0	0	0	0
62	0	0	0.00001	0	0	0	0	0	0	0	0	0
64	0	0	0	0	0	0	0	0	0	0	0	0
66	0	0	0	0	0	0	0	0	0	0	0	0
68	0	0	0	0	0	0	0	0	0	0	0	0
70	0	0	0	0	0	0	0	0	0	0	0	0
72	0	0	0	0	0	0	0	0	0	0	0	0
74	0	0	0	0	0	0	0	0	0	0	0	0
76	0	0	0	0	0	0	0	0	0	0	0	0
78	0	0	0	0	0	0	0	0	0	0	0	0
80	0	0	0	0	0	0	0	0	0	0	0	0
82	0	0	0	0	0	0	0	0	0	0	0	0
84	0	0	0	0	0	0	0	0	0	0	0	0
86	0	0	0	0	0	0	0	0	0	0	0	0
88	0	0	0	0	0	0	0	0	0	0	0	0

Table C.11. Tridem Axle Load Spectra for Average of All California WIM Stations.

Load Level (kips)	FHWA Vehicle Class											
	4	5	6	7	8	9	10	11	12	13	14	15
2	0	0	0	0	0	0	0	0	0	0	0	0.00009
4	0	0	0	0	0	0	0.00032	0	0	0.00026	0	0.04522
6	0	0	0	0.00002	0	0	0.00343	0	0	0.0002	0	0.02946
8	0	0	0	0.00015	0	0	0.01449	0	0	0.00049	0	0.0284
10	0	0	0	0.00034	0	0	0.04045	0	0	0.00091	0	0.03945
12	0	0	0	0.0006	0	0	0.05807	0	0	0.00112	0	0.04013
14	0	0	0	0.00076	0	0	0.0465	0	0	0.00126	0	0.02935
16	0	0	0	0.00071	0	0	0.03284	0	0	0.00114	0	0.01592
18	0	0	0	0.00072	0	0	0.03469	0	0	0.00117	0	0.01063
20	0	0	0	0.00077	0	0	0.03518	0	0	0.00115	0	0.00696
22	0	0	0	0.00091	0	0	0.03988	0	0	0.00114	0	0.00597
24	0	0	0	0.00106	0	0	0.0434	0	0	0.00103	0	0.00499
26	0	0	0	0.00147	0	0	0.0457	0	0	0.00119	0	0.00507
28	0	0	0	0.00199	0	0	0.04329	0	0	0.00125	0	0.00484
30	0	0	0	0.00279	0	0	0.05131	0	0	0.00134	0	0.00517
32	0	0	0	0.00345	0	0	0.05209	0	0	0.00112	0	0.00446
34	0	0	0	0.00412	0	0	0.04663	0	0	0.00084	0	0.00352
36	0	0	0	0.0038	0	0	0.03144	0	0	0.00059	0	0.00252
38	0	0	0	0.00343	0	0	0.01807	0	0	0.00057	0	0.00221
40	0	0	0	0.00217	0	0	0.00797	0	0	0.00057	0	0.0017
42	0	0	0	0.00134	0	0	0.00414	0	0	0.00063	0	0.00146
44	0	0	0	0.00073	0	0	0.00219	0	0	0.00055	0	0.00126
46	0	0	0	0.00036	0	0	0.00146	0	0	0.00044	0	0.00093
48	0	0	0	0.0002	0	0	0.00083	0	0	0.00026	0	0.00073
50	0	0	0	0.00011	0	0	0.00042	0	0	0.00016	0	0.00068
52	0	0	0	0.00007	0	0	0.00023	0	0	0.00009	0	0.00048
54	0	0	0	0.00006	0	0	0.00012	0	0	0.00004	0	0.00027
56	0	0	0	0.00003	0	0	0.00005	0	0	0.00003	0	0.00018
58	0	0	0	0.00003	0	0	0.00003	0	0	0.00002	0	0.00013
60	0	0	0	0.00002	0	0	0.00002	0	0	0.00002	0	0.00007
62	0	0	0	0	0	0	0.00002	0	0	0.00001	0	0.00006
64	0	0	0	0	0	0	0.00002	0	0	0.00001	0	0.00006
66	0	0	0	0	0	0	0.00001	0	0	0.00001	0	0.00006
68	0	0	0	0	0	0	0	0	0	0	0	0.00004
70	0	0	0	0	0	0	0	0	0	0	0	0.00004
72	0	0	0	0	0	0	0	0	0	0	0	0.00003
74	0	0	0	0	0	0	0	0	0	0	0	0.00003
76	0	0	0	0	0	0	0	0	0	0.00001	0	0.00003
78	0	0	0	0	0	0	0	0	0	0	0	0.00002
80	0	0	0	0	0	0	0	0	0	0	0	0.00002
82	0	0	0	0	0	0	0	0	0	0	0	0.00002
84	0	0	0	0	0	0	0	0	0	0	0	0.00002
86	0	0	0	0	0	0	0	0	0	0	0	0.00002
88	0	0	0	0	0	0	0	0	0	0	0	0.00001



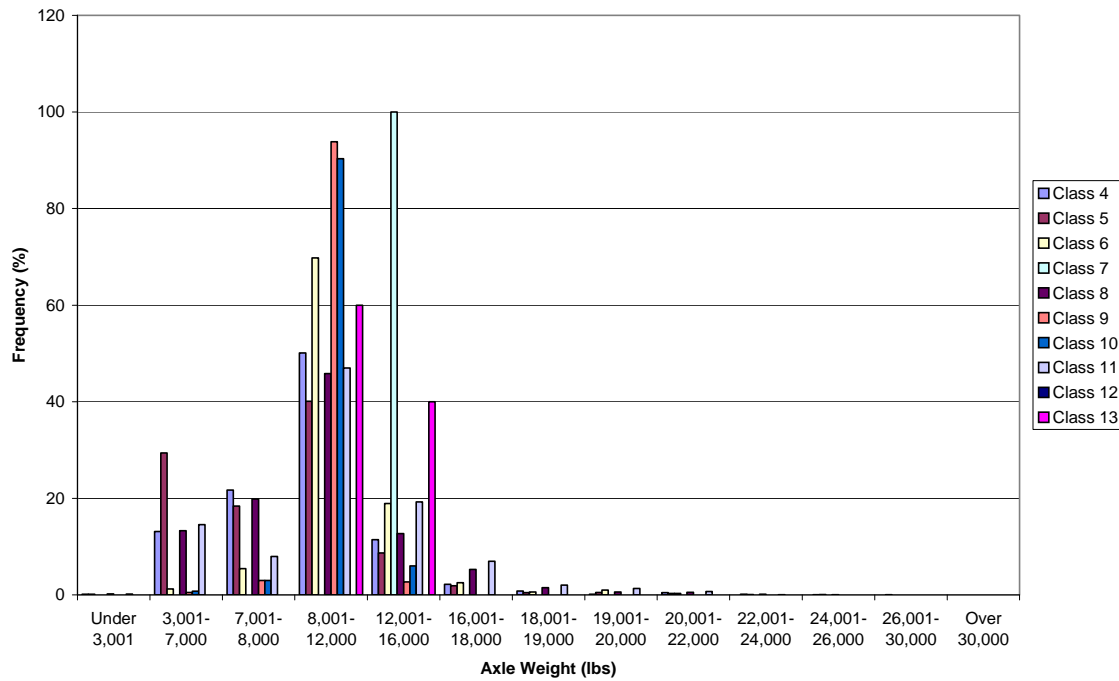


Figure C.4. Axle weight distribution for single axles of various FHWA vehicle classes measured at the Bolingbrook NB weigh scale.

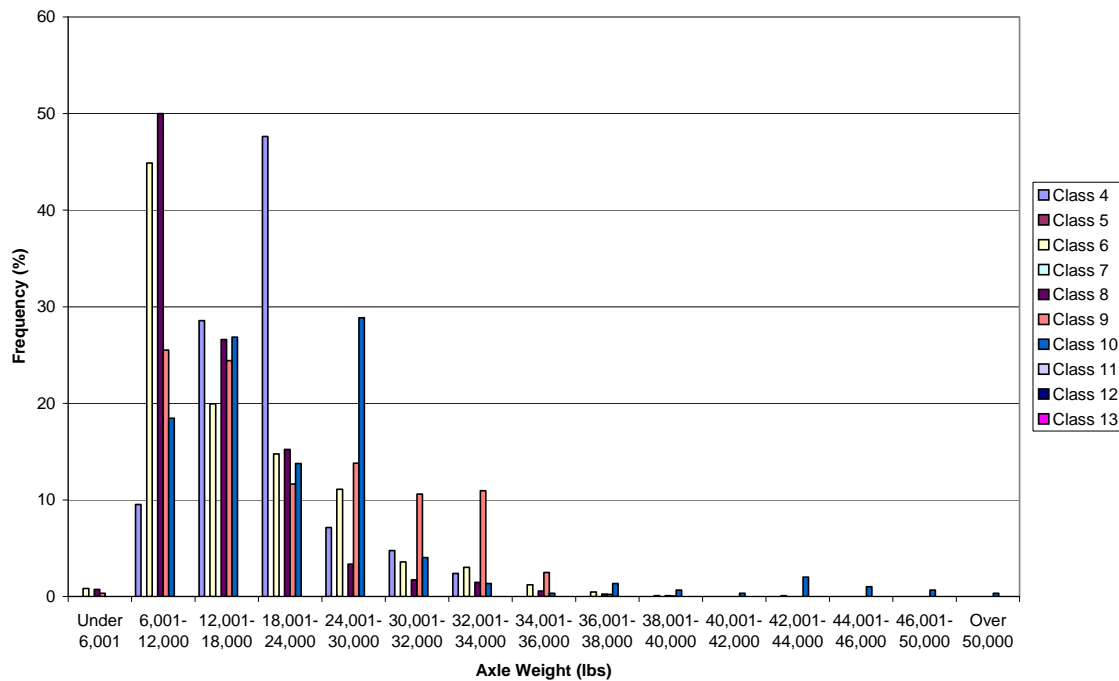


Figure C.5. Axle weight distribution for tandem axles of various FHWA vehicle classes measured at the Bolingbrook NB weigh scale.

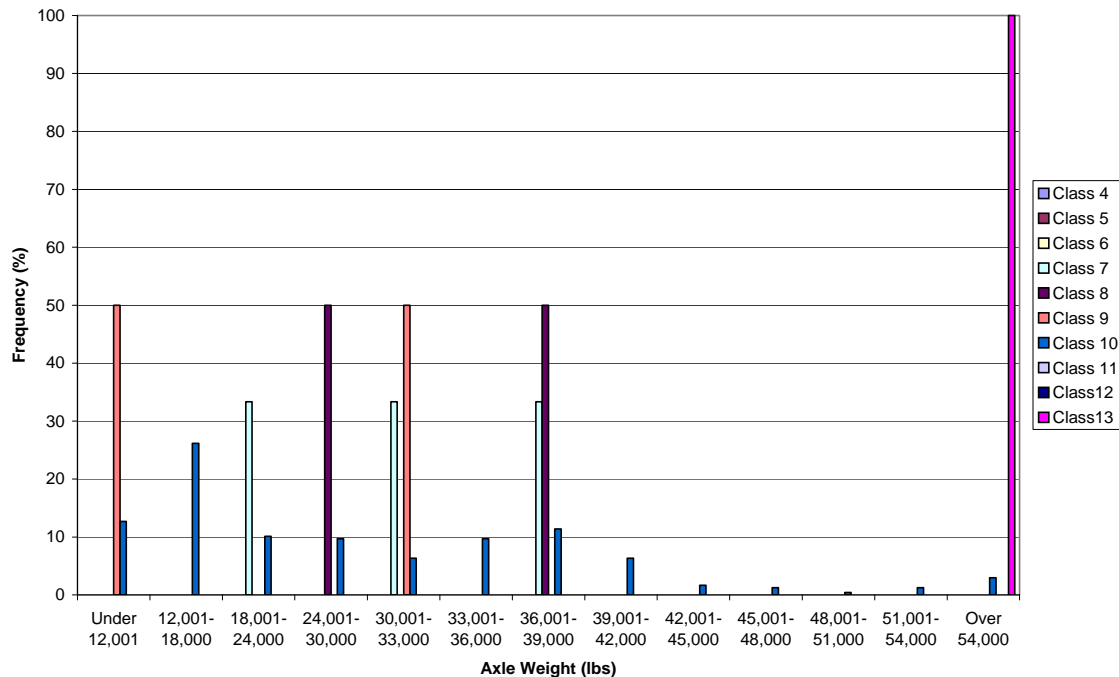


Figure C.6. Axle weight distribution for tridem axles of various FHWA vehicle classes measured at the Bolingbrook NB weigh scale.

### C3. INPUT PARAMETERS

As mentioned previously, the MEPDG software (Version 1.0) was run to determine if the different load spectra distributions in Illinois would influence the required concrete slab thickness given a constant number of ESALs. The primary MEPDG design input parameters used in this study were the following:

- 20-year design life
- 10 in. of a “newly constructed” JPCP with flexural strength of 650 psi (at 28 days)
- Asphalt concrete shoulder; 15-ft joint spacing; 1.5-in. dowel diameters spaced at 12 in.
- 4-in. existing asphalt concrete base with a PG 64-22 grade and an aggregate blend of 0% retained on a  $\frac{3}{4}$  sieve, 35% retained on a  $\frac{3}{8}$  sieve, 50% retained on a  $\frac{1}{4}$  sieve, and 0% passing a #200 sieve.
- Subgrade of A-7-6 with a modulus of 13,000 psi
- ESALs are calculated by the MEPDG based on the load spectra assumptions

Before studying the effects of traffic distribution at different Illinois geographic sites, a climate study had to be performed to look at the effect of Illinois climate change on the percentage of slab cracking for a given traffic distribution. Note that Version 0.91 of the MEPDG was run for the results in the initial MEPDG evaluation documented in Appendix B. The control climate location was Champaign, Illinois (from Williard Airport). The following section lists all the inputs assumed for the MEPDG climate study. All input values were kept to the default values in the MEPDG Version 1.0 program, except for the changes listed above.

## Input Summary Project: CMI

General Information Description:  
 Design Life 20 years  
 Pavement construction: September, 2006  
 Traffic open: October, 2006  
 Type of design JPCP  
 Location: MEPDG default  
 Project ID:  
 Section ID:  
 Principal Arterials - Interstate and Defense Routes  
 Date: 6/26/2008

### Analysis Parameters

Performance Criteria	Limit	Reliability
Initial IRI (in/mi)	63	
Terminal IRI (in/mi)	172	90
Transverse Cracking (% slabs cracked)	15	90
Mean Joint Faulting (in)	0.12	90
Station/milepost format:		
Station/milepost begin:		
Station/milepost end:		
Traffic direction:	East bound	
Default Input Level		
Default input level	Level 3, Default and historical agency values.	

## Traffic

Initial two-way AADTT: 12500  
 Number of lanes in design direction: 2  
 Percent of trucks in design direction (%): 50  
 Percent of trucks in design lane (%): 95  
 Operational speed (mph): 60  
 Traffic -- Volume Adjustment Factors  
 Monthly Adjustment Factors (Level 3, Default MAF)

Month	Vehicle Class									
	Class 4	Class 5	Class 6	Class 7	Class 8	Class 9	Class 10	Class 11	Class 12	Class 13
January	1.00	1.00	1.00	1.00	1.00	1.00	1.00	1.00	1.00	1.00
February	1.00	1.00	1.00	1.00	1.00	1.00	1.00	1.00	1.00	1.00
March	1.00	1.00	1.00	1.00	1.00	1.00	1.00	1.00	1.00	1.00
April	1.00	1.00	1.00	1.00	1.00	1.00	1.00	1.00	1.00	1.00
May	1.00	1.00	1.00	1.00	1.00	1.00	1.00	1.00	1.00	1.00
June	1.00	1.00	1.00	1.00	1.00	1.00	1.00	1.00	1.00	1.00
July	1.00	1.00	1.00	1.00	1.00	1.00	1.00	1.00	1.00	1.00
August	1.00	1.00	1.00	1.00	1.00	1.00	1.00	1.00	1.00	1.00
September	1.00	1.00	1.00	1.00	1.00	1.00	1.00	1.00	1.00	1.00
October	1.00	1.00	1.00	1.00	1.00	1.00	1.00	1.00	1.00	1.00
November	1.00	1.00	1.00	1.00	1.00	1.00	1.00	1.00	1.00	1.00
December	1.00	1.00	1.00	1.00	1.00	1.00	1.00	1.00	1.00	1.00

### Vehicle Class Distribution

(Level 3, Default Distribution)

#### AADTT distribution by vehicle class

Class 4	1.8%
Class 5	24.6%
Class 6	7.6%
Class 7	0.5%
Class 8	5.0%
Class 9	31.3%
Class 10	9.8%
Class 11	0.8%
Class 12	3.3%
Class 13	15.3%

Hourly truck traffic distribution  
by period beginning:

Midnight	2.3%	Noon	5.9%
1:00 am	2.3%	1:00 pm	5.9%
2:00 am	2.3%	2:00 pm	5.9%
3:00 am	2.3%	3:00 pm	5.9%
4:00 am	2.3%	4:00 pm	4.6%
5:00 am	2.3%	5:00 pm	4.6%
6:00 am	5.0%	6:00 pm	4.6%
7:00 am	5.0%	7:00 pm	4.6%
8:00 am	5.0%	8:00 pm	3.1%
9:00 am	5.0%	9:00 pm	3.1%
10:00 am	5.9%	10:00 pm	3.1%
11:00 am	5.9%	11:00 pm	3.1%

Traffic Growth Factor

Vehicle Class	Growth Rate	Growth Function
Class 4	4.0%	No Growth
Class 5	4.0%	No Growth
Class 6	4.0%	No Growth
Class 7	4.0%	No Growth
Class 8	4.0%	No Growth
Class 9	4.0%	No Growth
Class 10	4.0%	No Growth
Class 11	4.0%	No Growth
Class 12	4.0%	No Growth
Class 13	4.0%	No Growth

Traffic -- Axle load distribution Factors

Level 3:	Default
Traffic -- General Traffic Inputs	
Mean wheel location (inches from the lane marking):	18
Traffic wander standard deviation (in):	10
Design lane width (ft):	12
Axle Configuration	
Average axle width (edge-to-edge) outside dimensions,ft):	8.5
Dual tire spacing (in):	12
Tire Pressure (psi):	120
Average Axle Spacing	
Tandem axle(psi):	51.6
Tridem axle(psi):	49.2
Quad axle(psi):	49.2

Number of Axles per Truck

Vehicle Class	Single Axle	Tandem Axle	Tridem Axle	Quad Axle
Class 4	1.62	0.39	0.00	0.00
Class 5	2.00	0.00	0.00	0.00
Class 6	1.02	0.99	0.00	0.00
Class 7	1.00	0.26	0.83	0.00
Class 8	2.38	0.67	0.00	0.00
Class 9	1.13	1.93	0.00	0.00
Class 10	1.19	1.09	0.89	0.00
Class 11	4.29	0.26	0.06	0.00
Class 12	3.52	1.14	0.06	0.00
Class 13	2.15	2.13	0.35	0.00

Wheelbase Truck Tractor

	Short	Medium	Long
Average Axle Spacing (ft)	12	15	18

**Percent of trucks**                      33%        33%        34%

## Climate

icm file: C:\DG2002\Projects\champaign.icm

Latitude (degrees.minutes)	41.47
Longitude (degrees.minutes)	-87.45
Elevation (ft)	619
Depth of water table (ft)	10

## Structure—Design Features

Permanent curl/warp effective temperature difference (°F):	-10
Joint Design	
Joint spacing (ft):	15
Sealant type:	Liquid Sealant
Dowel diameter (in):	1.5
Dowel bar spacing (in):	12
Edge Support	None
Long-term LTE(%):	n/a
Widened Slab (ft):	n/a
Base Properties	
Base type:	Asphalt treated
Erodibility index:	Erosion Resistant (3)
PCC-Base Interface	Full friction contact
Loss of full friction (age in months):	229
Structure--ICM Properties	
Surface shortwave absorptivity:	0.85

## Structure—Layers

### Layer 1 -- JPCP

General Properties	
PCC material	JPCP
Layer thickness (in):	10
Unit weight (pcf):	150
Poisson's ratio	0.2
Thermal Properties	
Coefficient of thermal expansion (per F° x 10- 6):	5.5
Thermal conductivity (BTU/hr-ft-F°) :	1.25
Heat capacity (BTU/lb-F°):	0.28
<i>Mix Properties</i>	
Cement type:	Type I
Cementitious material content (lb/yd^3):	600
Water/cement ratio:	0.42
Aggregate type:	Limestone
PCC zero-stress temperature (F°)	Derived
Ultimate shrinkage at 40% R.H (microstrain)	Derived
Reversible shrinkage (% of ultimate shrinkage):	50
Time to develop 50% of ultimate shrinkage (days):	35
Curing method:	Curing compound
<i>Strength Properties</i>	
Input level:	Level 3
28-day PCC modulus of rupture (psi):	650
28-day PCC compressive strength (psi):	n/a

### Layer 2 -- Asphalt concrete

Material type:	Asphalt concrete
Layer thickness (in):	4
General Properties	
Reference temperature (F°):	70
Volumetric Properties as Built	
Effective binder content (%):	11
Air voids (%):	8.5
Total unit weight (pcf):	148

Poisson's ratio:

0.35 (user entered)

**Thermal Properties**

Thermal conductivity asphalt (BTU/hr-ft-F°):

0.67

Heat capacity asphalt (BTU/lb-F°):

0.23

**Asphalt Mix**

Cumulative % Retained 3/4 inch sieve:

0

Cumulative % Retained 3/8 inch sieve:

35

Cumulative % Retained #4 sieve:

50

% Passing #200 sieve:

0

**Asphalt Binder**

Option: Superpave binder grading

A 10.9800 (correlated)

VTS: -3.6800 (correlated)

High temp. °C	Low temperature, °C						
	-10	-16	-22	-28	-34	-40	-46
46							
52							
58							
64							
70							
76							
82							

**Layer 3 -- A-7-6 (and Layer 4 -- A-7-6)**

Unbound Material:

A-7-6

Thickness(in):

12

(Layer 4 – Semi-Infinite)

**Strength Properties**

Input Level:

Level 3

Analysis Type:

ICM inputs

(ICM Calculated Modulus)

Poisson's ratio:

0.35

Coefficient of lateral pressure,Ko:

0.5

Modulus (input) (psi):

13000

**ICM Inputs**

Gradation and Plasticity Index

Plasticity Index, PI:

30

Liquid Limit (LL)

51

Compacted Layer

No

Passing #200 sieve (%):

79.1

Passing #40

0.0

Passing #4 sieve (%):

94.9

D10(mm)

0.0002309

D20(mm)

0.0005333

D30(mm)

0.001231

D60(mm)

0.01516

D90(mm)

0.6616

Calculated/Derived Parameters

Maximum dry unit weight (pcf):

97.7 (derived)

Specific gravity of solids, Gs:

2.70 (derived)

Saturated hydraulic conductivity (ft/hr):

8.946e-006 (derived)

Optimum gravimetric water content (%):

22.2 (derived)

Calculated degree of saturation (%):

82.7 (calculated)

Soil water characteristic curve parameters:

Default values

Parameters

Value

a 136.42

b 0.51828

c 0.032384

Hr. 500

Sieve	Percent Passing
0.001mm	
0.002mm	
0.020mm	
#200	79.1
#100	
#80	84.9
#60	
#50	
#40	88.8
#30	
#20	
#16	
#10	93.0
#8	
#4	94.9
3/8"	96.9
1/2"	97.5
3/4"	98.3
1"	98.8
1 1/2"	99.3
2"	99.6
2 1/2"	
3"	
3 1/2"	99.9
4"	99.9

## Distress Model Calibration Settings - Rigid (new)

Cracking

Fatigue Coefficients

C1 2

C2 1.22

Cracking Coefficients

C4 1

C5 -1.98

Reliability (CRACK)

Std. Dev.  $\text{POWER}(5.3116 \cdot \text{CRACK}, 0.3903) + 2.99$

### C4. CLIMATE

Various climatic locations across Illinois shown in Figure C.1 were studied using the same traffic (AADTT, vehicle class distribution, and axle load distribution). From this climate sensitivity study it was found that several sites not located near each other had low cracking percentages after 20 years, while other sites also located apart from each other were found to have higher slab cracking. No trends were found with respect to the level of cracking and the geographical location in Illinois; i.e., north to south effect was not discernable. Note that the climate data at Decatur produced the highest amount of cracking for the cases analyzed as shown in Figure C.7. For the subsequent thickness design comparisons for various traffic sites, Champaign, Aurora, and St. Louis climate stations were used, since they represented low, medium, and higher cracking levels for a fixed ESAL count.

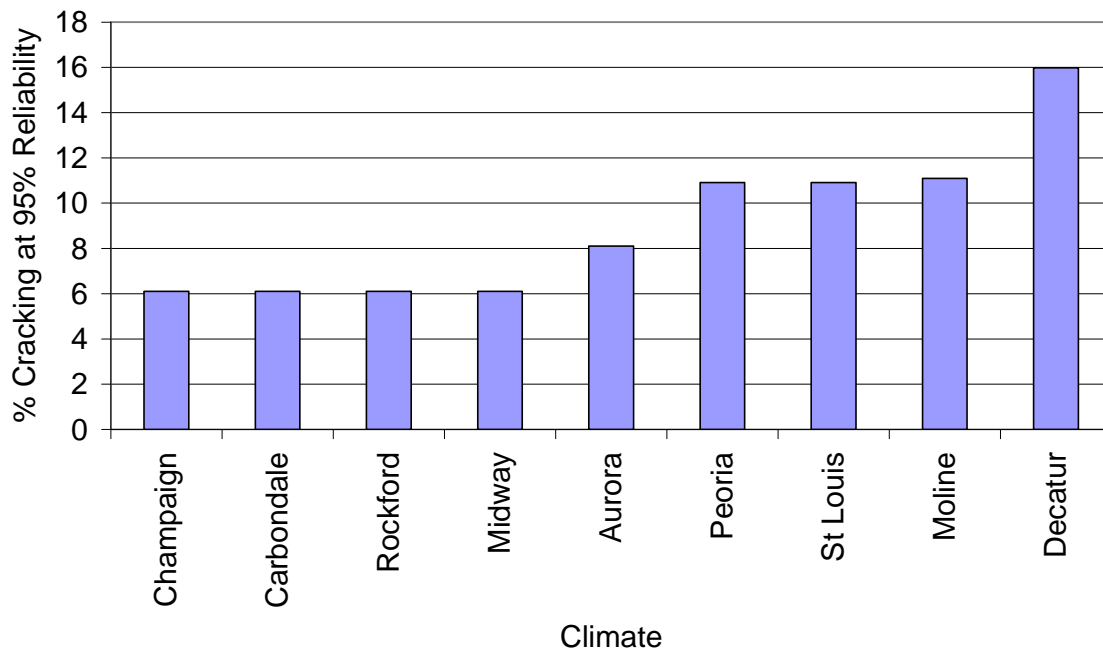


Figure C.7. Climate impact on percentage of cracking using the default MEPDG TTC11 traffic distributions at 80 million ESALs (12,500 AADTT).

## C5. PERCENTAGE SLAB CRACKING

If the site-specific traffic (vehicle and axle) distribution is combined with the local city climate station, the predicted slab cracking at the end of the design life is shown in Figure C.8 for a constant number of ESALs. The slab cracking varies 5 to 20% when using site-specific climate and traffic data. The change in slab cracking could be a result of climate change, load spectra change, or both. If the climate location and ESAL count are fixed and the traffic distribution is varied, then the amount of cracking seen with different load spectra is roughly similar (see Figure C.9). This suggests that the cause of the slab cracking sensitivity in Figure C.8 is related to the climate data change, not the load spectra differences.

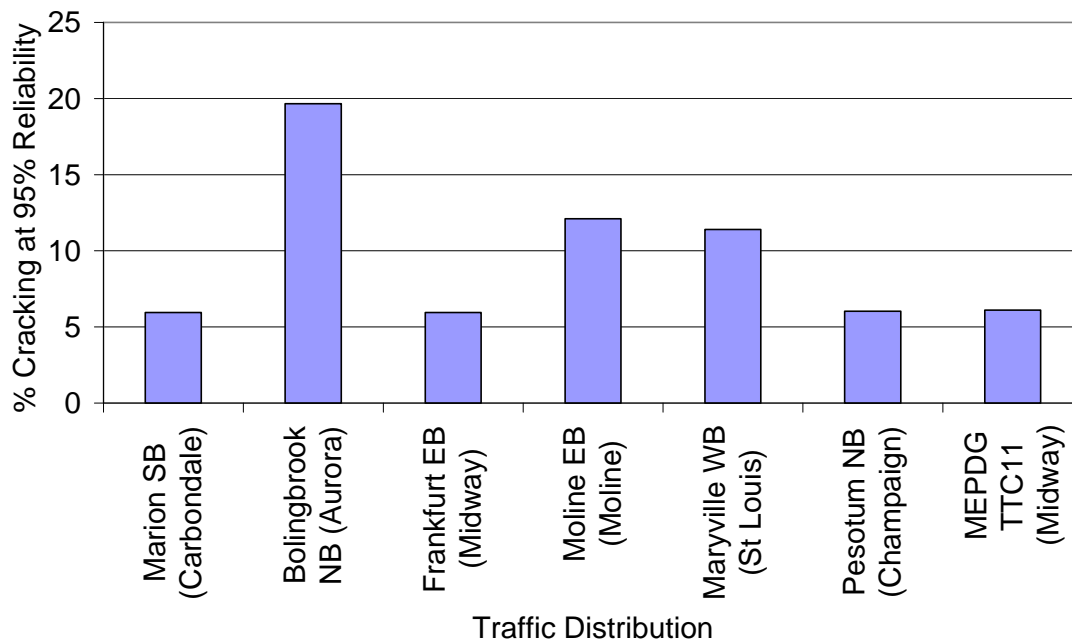


Figure C.8. Percentage of cracking for 80 million ESALs at each location and its corresponding traffic distribution.



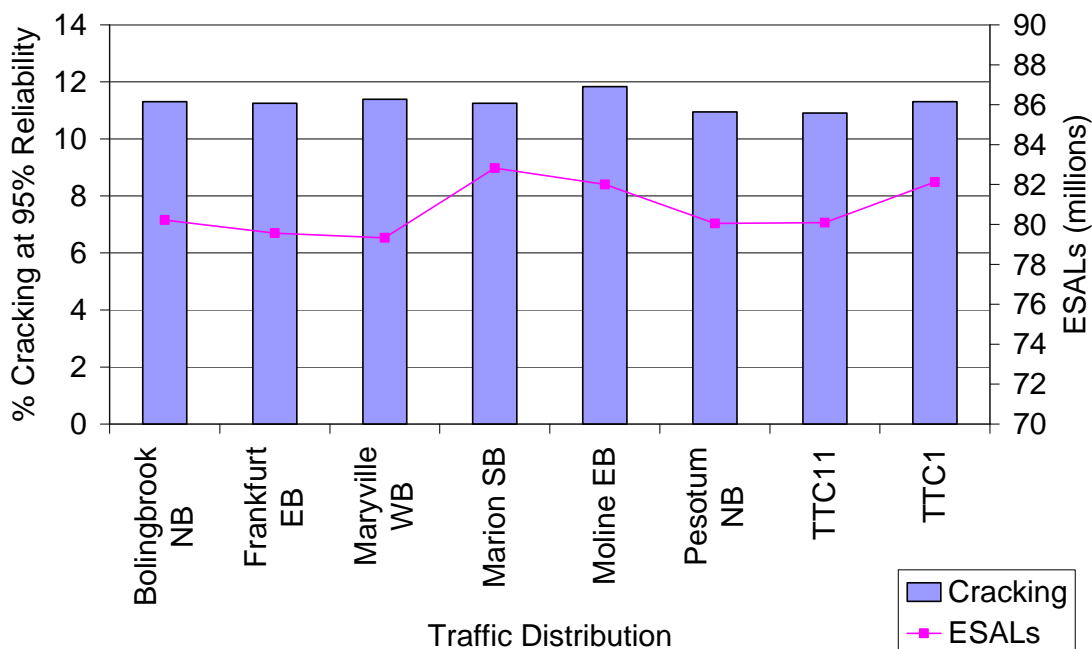


Figure C.9. Percentage of cracking for each traffic distribution with 80 million ESALs and the St. Louis climate.

## C6. THICKNESS DESIGN

A study was performed to determine the effect of climate and load spectra on the required JPCP slab thickness based on the failure criterion of 20% slab cracking at 95% reliability. Since the climate has a more significant influence on cracking than traffic, the traffic analysis was performed at three different locations: St. Louis, Aurora and Champaign. For a 20% slab cracking at 95% reliability, the influence of traffic distributions in terms of allowable ESALs or thickness can be seen in Figure C.10 and Figure C.11 for St. Louis and Aurora climates, respectively. Thinner concrete slabs will result in lower allowable ESALs as expected. From these figures there does seem to be a difference between traffic distributions on the allowable ESALs or thickness design. However, the question still to answer is whether this difference is significant enough such that specific truck and axle weight distributions should be known to improve the JPCP design.

To aid in understanding the significance between traffic distribution and thickness, various design charts determined from the MEPDG runs of the minimum concrete thickness required (to the nearest ½ inch) versus the amount of ESALs applied at various traffic distributions were developed (see Figure C.12 to Figure C.14). In Figure C.12 showing a proposed design chart with the MEPDG default TTC11 distribution, the climate again is shown to produce significant thickness differences. The climate-based differences showed no trend in terms of a north to south effect, and St. Louis produced the greatest thickness for a given level of ESALs, followed by Aurora, and then Champaign, as originally shown in Figure C.7. The other two traffic distributions analyzed in Figure C.13 (Pesotum NB from the WIM) and Figure C.14 (Bolingbrook NB) show the same trends. In addition, Table C.12 summarizes all the values used in Figure C.10 through Figure C.14.

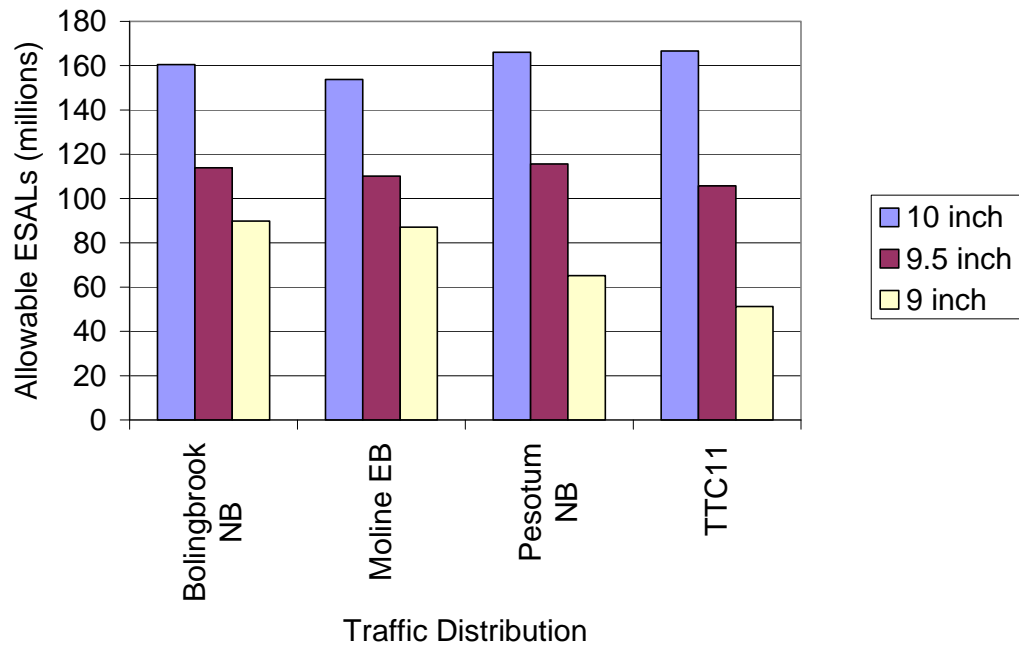


Figure C.10. Allowable ESALs and PCC thickness for each traffic distribution which all produce 20% cracked slabs at 95% reliability for the St. Louis climate.

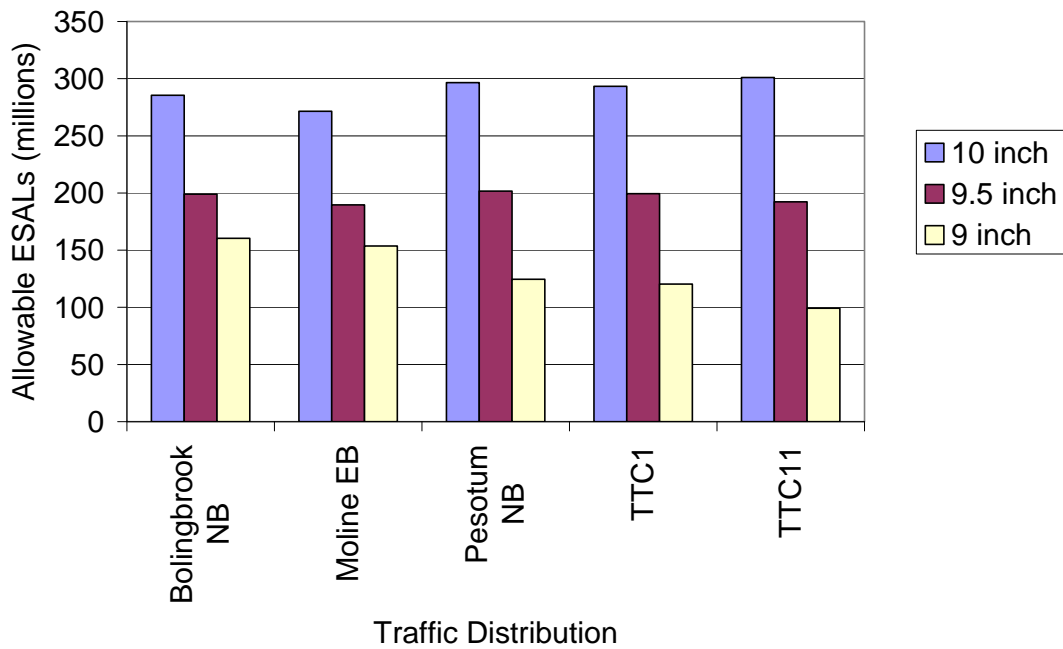


Figure C.11. Allowable ESALs and PCC thickness for each traffic distribution which all produce 20% cracked slabs at 95% reliability for the Aurora climate.

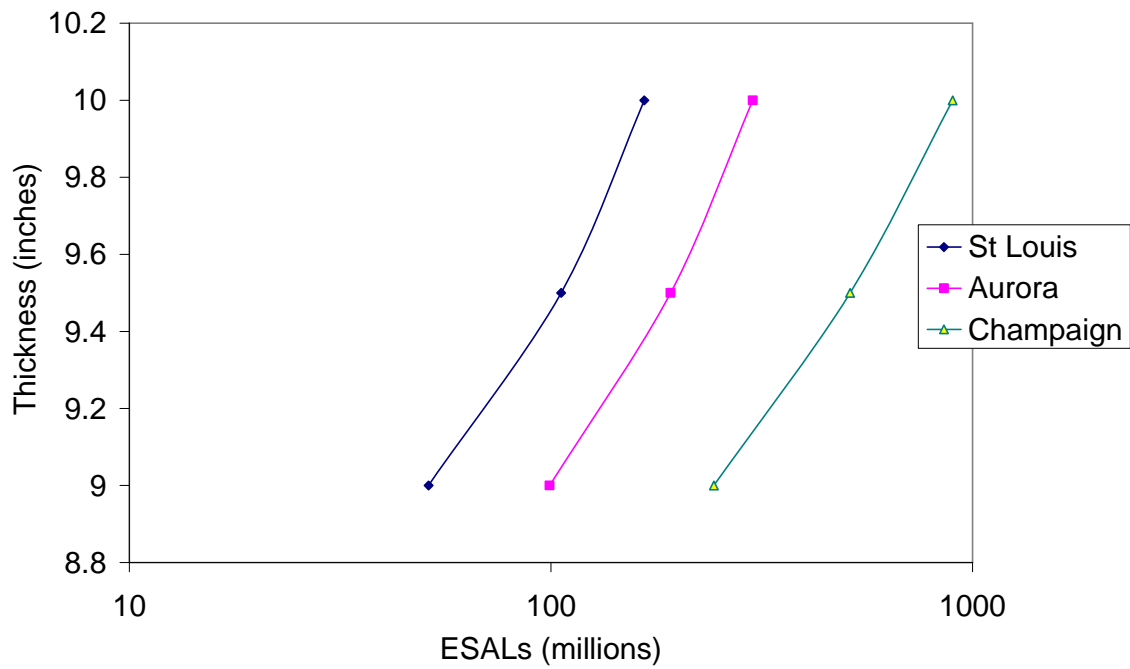


Figure C.12. Minimum slab thickness for given ESALs and climate condition to produce 20% cracking at 95% reliability for TTC11 distribution.

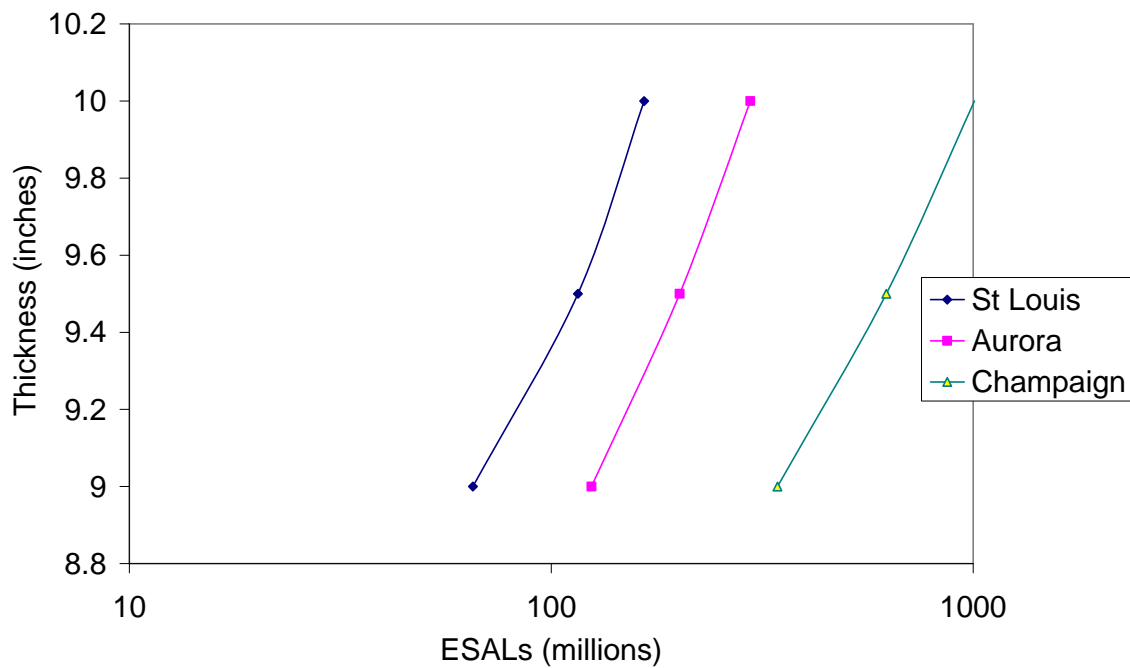


Figure C.13. Minimum slab thickness for given ESALs and climate condition to produce 20% cracking at 95% reliability for Pesotum NB distribution.

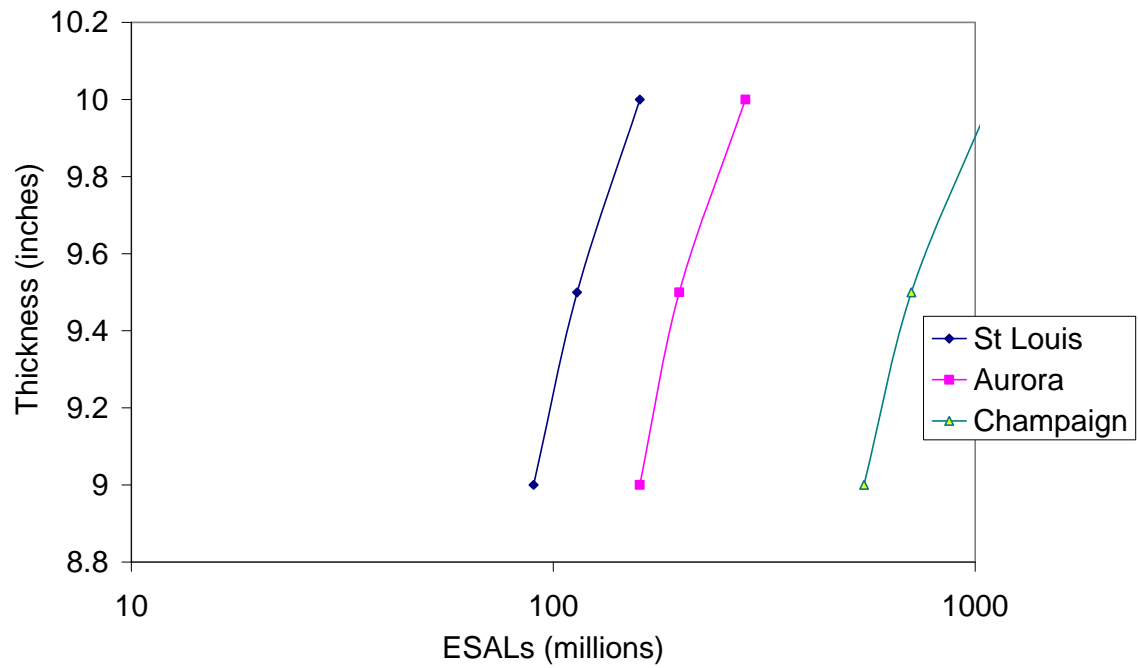


Figure C.14. Minimum slab thickness for given ESALs and climate condition to produce 20% cracking at 95% reliability for Bolingbrook NB distribution.

Table C.12. Thickness Design versus ESALs Summary.

St Louis Climate	10-in. thickness		9.5-in. thickness		9-in. thickness	
	Max ESALs (millions)	Actual % Slabs Cracked	Max ESALs (millions)	Actual % Slabs Cracked	Max ESALs (millions)	Actual % Slabs Cracked
Bolingbrook NB	160.45	19.94	113.92	19.80	89.85	19.82
Moline EB	153.74	20.00	110.18	19.73	87.12	19.51
Pesotum NB	166.03	19.72	115.63	19.94	65.22	19.55
TTC11	166.58	19.81	105.72	19.74	51.26	19.43
Average	161.7	19.9	111.4	19.8	73.4	19.6
Variance	35.8	0.0	19.3	0.0	338.6	0.0

Aurora Climate	10-in. thickness		9.5-in. thickness		9-in. thickness	
	Max ESALs (millions)	Actual % Slabs Cracked	Max ESALs (millions)	Actual % Slabs Cracked	Max ESALs (millions)	Actual % Slabs Cracked
Bolingbrook NB	285.60	19.96	198.96	19.93	160.45	20.00
Moline EB	271.61	19.88	189.61	19.57	153.74	19.47
Pesotum NB	296.48	19.66	201.60	19.61	124.52	19.76
TTC1	293.32	19.94	199.46	19.96	120.26	19.81
TTC11	301.13	19.77	192.21	19.85	99.31	19.70
Average	289.6	19.8	196.4	19.8	131.7	19.7
Variance	133.4	0.0	26.7	0.0	636.0	0.0

For the ranges of thickness analyzed in Table C.12, there is little influence that the load spectra has on thickness design compared to ESAL-based thickness design. For example, if the number of ESALs was 100 million, and one used the St. Louis climate, the design regardless of traffic distribution would always result in a 9.5-in.-thick slab. On the other hand, if the design was for 80 million ESALs and the St. Louis climate was still used, according to Figure C.10 and Table C.12, the traffic distribution in Bolingbrook and Moline would suggest that a 9-in. pavement would be sufficient, and Pesotum and TTC11 would be somewhere between 9.0 and 9.5 in. thick. In the case of the Aurora climate, at 80 million ESALs, a 9-in. slab will be sufficient for all site-specific load spectra.

Since the slab thickness required only varies by 0.5 in. for roughly every 50 million ESALs, regardless of site-specific load spectra, it can be concluded an ESAL-based design could be used confidently over a load spectra design without losing any resolution in the thickness design method. It is postulated that the calibration of various models in the MEPDG software reduces the fatigue cracking sensitivity of the MEPDG to load spectra changes for a constant ESAL level.

## C7. SUMMARY

A sensitivity study was completed using the MEPDG to determine the effect of Illinois geographic location and traffic load spectra changes on the required concrete slab thickness. In Illinois, there was climate zone sensitivity, but this sensitivity could not be simply represented as a north–south effect, and thus, it is recommended that IDOT not adopt a climate-based concrete pavement design in Illinois.

Traffic load spectra data were collected by IDOT at several sites located throughout Illinois. Although the sites do demonstrate some different axle load distribution frequencies, this did not translate into significant concrete pavement thickness differences (<0.5 in. between sites). Thus, the necessity to use load spectra as a means of characterizing traffic is not warranted at this time for fatigue cracking prediction, and IDOT should continue to use ESALs.

## **APPENDIX D. BUILT-IN CURLING IN JOINTED PLAIN CONCRETE PAVEMENTS**

### **D1. INTRODUCTION**

Studies (Vandenbossche, 2003; Beckemeyer et al., 2002; Heath and Roesler, 2000; Yu et al. 1998; Armaghani et al., 1987; Hatt, 1923; Hveem, 1951) have shown that many factors can cause an upward curling of the slab, which suggests that transverse joint loading deserves greater consideration in concrete pavements than previously given. If large positive temperature gradients (temperature of slab is hotter on top than bottom) exist as the concrete hardens shortly after construction, the slab will curl upward as the pavement cools and reaches a zero-gradient condition. This is a common occurrence during the hot summer construction season. This built-in curling can reach magnitudes of 2.5 °F/in. or more (Eisenmann and Leykauf, 1990a). Preliminary analysis has shown that paving under typical nighttime conditions can have an opposite effect on this built-in curl (Schmidt, 2001).

Drying shrinkage profiles in the concrete have been shown to occur to depths of 2 in. (Eisenmann and Leykauf, 1990b; Grasley, 2003) and may extend to the mid-depth of the slab (Rasmussen and McCullough, 1998). In concrete slabs, the top of the slab loses moisture more easily due to its interaction with the ambient environment, while the remaining portion of the slab's volume remains close to saturation level. This effect can be more pronounced in drier, less humid climates. The drying shrinkage through a slab can be influenced by the concrete mix proportions and materials, supporting layers, construction practices, climatic conditions, and the thickness of the concrete slab. These shrinkage distributions have been found in a California study to be high enough such that slabs crack under environmental influences before any traffic loading is even applied (Heath et al., 2003).

Moisture curling effects can be modeled as equivalent temperature gradients by relating their strain measurements to the thermal properties of the concrete and adding these equivalent gradients to actual temperature gradients. Upward curling due to the residual equivalent negative temperature gradients can shift the temperature frequency distribution significantly. Studies have shown that this shift can be on the order of 9 to 20°F (Yu et al., 1998; Armaghani et al., 1987), and in extreme cases, up to 40°F (Rao and Roesler, 2003) towards a negative temperature differential. This shift can ultimately lead to increased importance of axle loads at the transverse joints, which lead to longitudinal fatigue cracking development, due to the amount of unsupported edges and corners in jointed concrete pavements, as seen in Figure D.1.

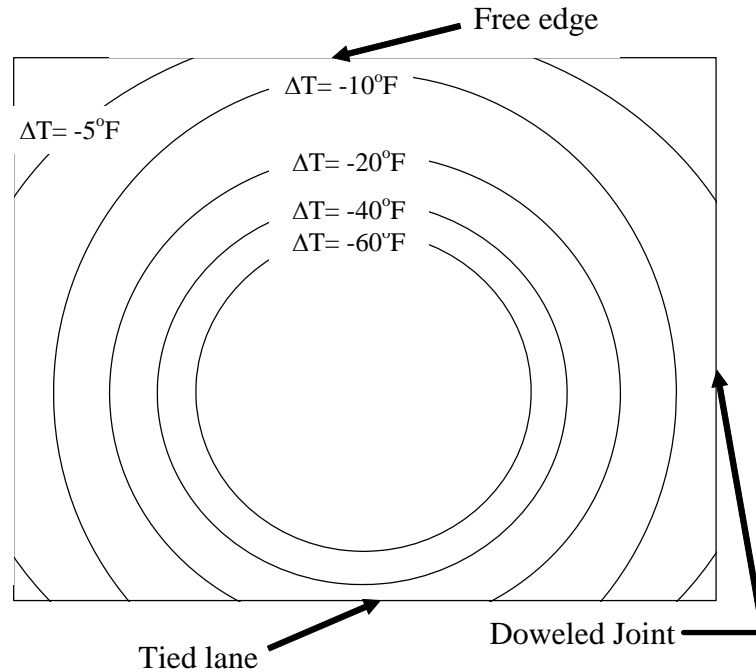


Figure D.1. Example of Unsupported Areas under Different Negative Built-In Curl Levels.

Through irreversible shrinkage, as well as the built-in temperature gradients during the setting of the concrete, a majority of rigid pavements experience a permanent upward curl regardless of the cyclical temperature gradient (Byrum, 2000). This upward curling of concrete slabs has been observed in a variety of different climatic regions (Rao et al., 2001, Yu et al., 1998; Yu and Khazanovich, 2001; Poblete et al., 1988). The magnitude of the total curl varies with cyclical temperature and moisture gradients in the slab, but a certain level of permanent built-in curl always remains. Full-scale test results from the desert climate of Palmdale, California suggest that the levels of permanent curl, in terms of a linear effective built-in temperature difference (EBITD), can exceed  $-40^{\circ}\text{F}$  for unrestrained slabs (Rao and Roesler, 2005a, 2005b). Test sections in Palmdale with more slab restraint such as dowels, tied shoulders, or widened lanes exhibited lower built-in curl levels. Table D.1 demonstrates that the phenomenon of built-in curling exists at numerous geographic locations and climates based on previously published sources. It can also be seen from the Phoenix, Arizona sections that the introduction of tied PCC shoulders or dowels, or both, showed a significant reduction in the amount of built-in curl due to this restraint along the longitudinal edge.



Table D.1. Measured Effective Built-In Temperature Difference (°C).

Location / ID	Built-in Curl (°C)	Comment	Reference
Surface Profiling (using dipstick unless otherwise noted)			
All LTPP GPS3 Sections <sup>a</sup>	Up to -44	Multiple geometries / restraint	Byrum 2000
I-80 in Pennsylvania	-37	Dowels / 20 ft joint spacing	Yu et. al. 2001
AZ1 in Phoenix, Arizona	-15.2 <sup>b</sup>	No dowels / AC shoulder / 15 ft joint spacing	C. Rao et. al. 2001
	-23.9 <sup>c</sup>		
AZ3 in Phoenix, Arizona	-23.1 <sup>b</sup>	No dowels / AC shoulder / 20 ft joint spacing	
	-29.1 <sup>c</sup>		
AZ4 in Phoenix, Arizona	-11.8 <sup>b</sup>	Dowels / Tied PCC shoulder / 20 ft joint spacing	
	-20.0 <sup>c</sup>		
Mankato, Minnesota	-22.8 <sup>b</sup>	No dowels / AC shoulder	
	-27.4 <sup>c</sup>		
Deflection Measurements (using FWD/HWD unless otherwise noted)			
I-70 in Colorado <sup>d</sup>	-11.1	Dowels / Tied PCC shoulder	Yu et. al. 1998
Florida <sup>d</sup>	-5	Undoweled	Armaghani et. al. 1987
Chile	Up to -19.2	Multiple sections	Poblete et. al. 1988
I-80 in Pennsylvania	-8.9	Aggregate base	Yu et. al. 2001
	-6.7	Bituminous base	
Palmdale, California	-22.7	No dowels / AC shoulder	S. Rao and Roesler 2005a
	-9.8	Dowels / Tied PCC shoulder	
	-17.2	Widened lane / AC shoulder	
Ukiah, California	-10	No dowels / AC shoulder	S. Rao and Roesler 2005a
DIA Denver, Colorado <sup>e</sup>	-5 to -8	17.5 inch airfield slabs	Rufino 2003

<sup>a</sup> Using high speed profiling<sup>b</sup> 3 days after construction<sup>c</sup> 40 days after construction<sup>d</sup> Using fixed external surface gages for deflections<sup>e</sup> Using multi-depth deflectometers

## D2. STRESS ANALYSIS

### D2.1. Axle Spacing Effects

With the influence of curling, the spacing between the steer and drive axles and their respective load levels can have an impact on stress development in rigid pavements due to the unsupported edges, as seen in Figure D.1. With 15-ft joint spacing and high levels of negative curling, steer-drive axle spacings as large as 21-ft can influence the critical stress level and promote top-down cracking in the center of the slab. Analysis on weigh-in-motion data from Pesotum, Illinois shows that roughly 77% of steer-drive axle spacings for Class 9 vehicles fall into the 12-ft to 21-ft range that can initiate high stresses at the top of the slab if upward curling

exists. Higher load transfer levels increase the effective length of the slab, and thus, loads placed on adjacent slabs can influence top-down tensile stresses. Figure D.2 shows an example of maximum tensile stress levels at each node from an influence line analysis for multiple steer-drive axle spacings under a large equivalent negative temperature differential ( $-50^{\circ}\text{F}$ ). The effects of axle spacing on top of the slab stresses is less pronounced with lower equivalent temperature differentials, and become non-existent as the slab approaches flat-slab conditions. More details on this analysis can be found in Hiller and Roesler (2005a). For larger axle spacings, the results of the influence line analysis approach the infinite spacing case (tandem only) where the steer axle has no effect on the top-down stress development in the critical slab. For the assumptions in Figure D.2, a 12-ft steer-drive axle is the critical spacing which produces the maximum tensile stress on the top of the slab. Steer-drive axle spacings shorter than 12 ft on a 15-ft slab length start to approach the tandem-only case as well. Steer-drive axle spacings greater than 21 ft and smaller than 9 ft are assumed to be separate single and tandem axle loads, since the axle spacing effect on top-down stress development at these distances is limited.

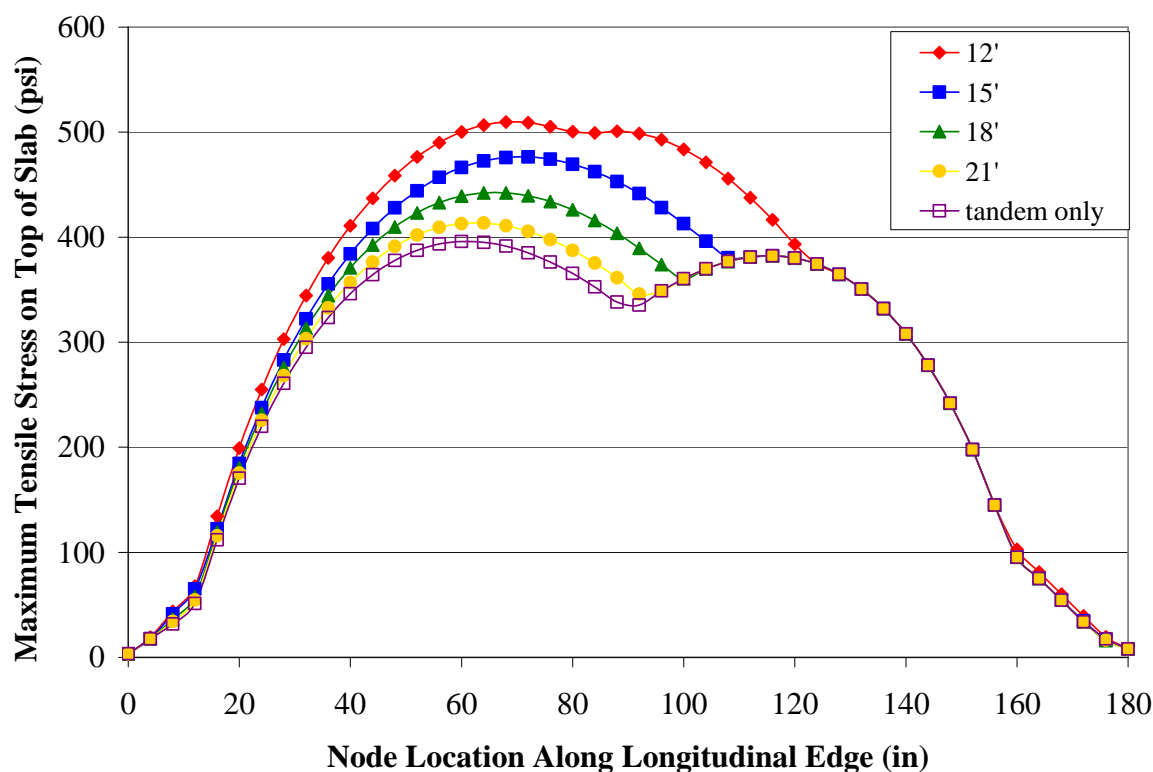


Figure D.2. Effect of Steer-Drive Axle Spacing on Maximum Tensile Stress (12 kip Steer, 44 kip Tandem) for 15-ft Joint Spacing and  $-50^{\circ}\text{F}$  Equivalent Temperature Differential.

## D2.2. Climatic Influences

An important input required for evaluating rigid pavements is the inclusion of EBITD into a mechanistic analysis. The EBITD level is treated as a linear temperature difference in this analysis, which shifts the frequency distribution of the cyclical, reversible slab temperature differences ( $\Delta T$ ) to an equivalent temperature difference, as demonstrated in Figure D.3, for example. For some climatic zones, an EBITD level of  $-30^{\circ}\text{F}$  can shift the equivalent

temperature difference distribution entirely into the negative region, as seen in Figure D.3. Only different levels of upward curl exist under this EBITD level, and the slab would never experience a downward curl or full contact with the underlying base layer.

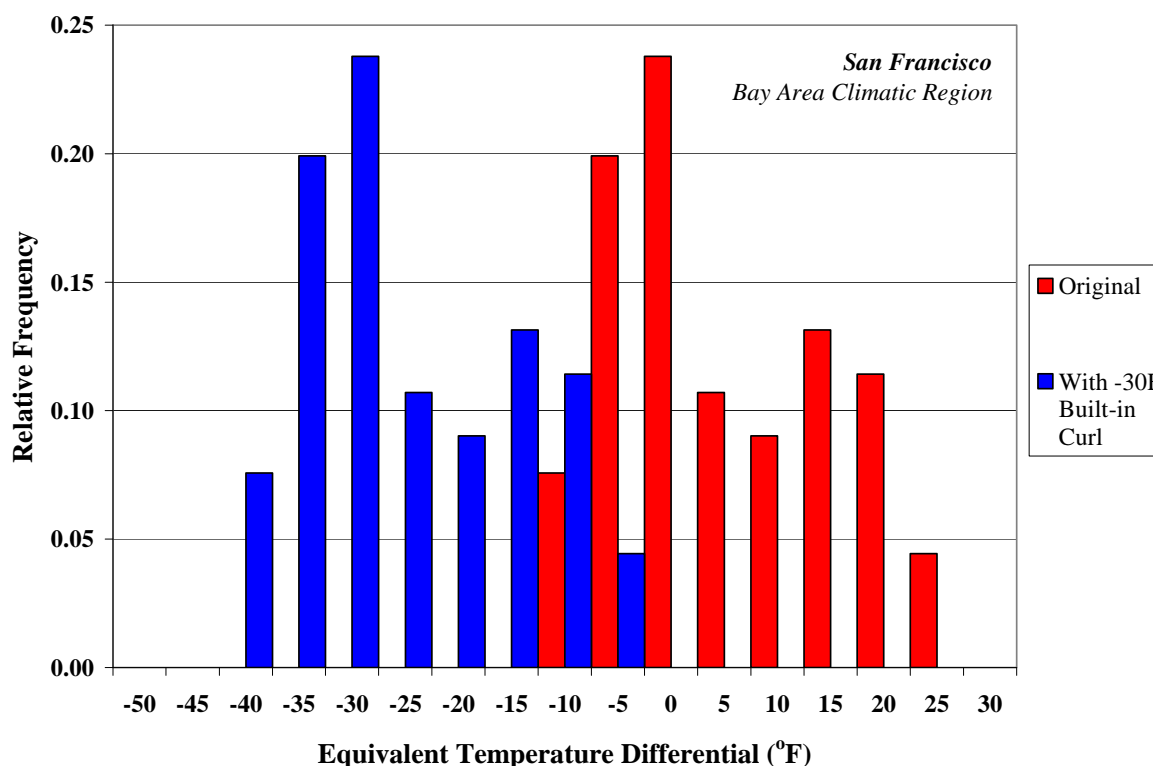


Figure D.3. Frequency Distribution Shift of Temperature Differential due to Effective Built-In Temperature Difference.

In general, the phenomenon of built-in curling can lead to residual stresses that exist in the pavement before any load or temperature curling effects are considered, as seen in Figure D.4. This built-in curling can change the baseline of fatigue damage development in comparison with the old assumption that when no temperature gradient exists, the pavement slabs are without stress. Using built-in curl and finite element analyses, a comprehensive program named *RadiCAL* (Hiller and Roesler 2005b) for determining fatigue damage along both the longitudinal edge and transverse joint was developed. When using the stress range approach in the *RadiCAL* program, the maximum stress is determined from the influence line analysis, while the minimum stress is taken as the residual stress from the combination of EBITD and the cyclical temperature gradient (no mechanical load condition). With 12-ft by 15-ft slabs under a negative gradient, the residual equivalent temperature stresses are higher at the top of the slab along the longitudinal edge, as seen in Figure D.4. If the equivalent temperature difference were positive, the same geometry and restraint conditions would also force the maximum residual stress to be along the longitudinal edge, albeit at the bottom of the slab. These variations in residual stresses create different baselines for the change in stress concept in comparison to a traditional maximum stress analysis. While the maximum stress (load plus curl) along any slab may be at the mid-slab longitudinal edge, the largest change in stress may not be at the location of the highest residual equivalent temperature stress. A maximum stress analysis can be conducted with *RadiCAL*, where the minimum stress is taken as zero.

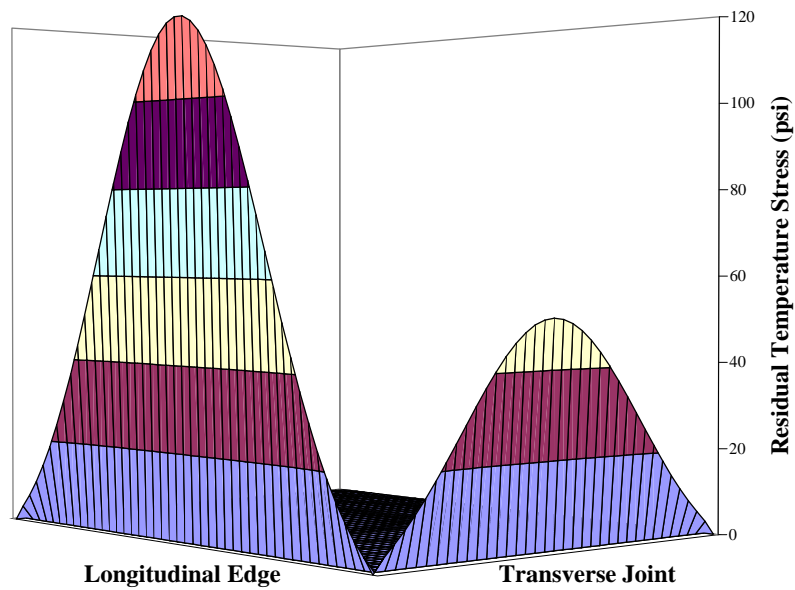


Figure D.4. Residual Equivalent Temperature Stresses for EBITD =  $-30^{\circ}\text{F}$  on 12-ft by 15-ft Slab with No Shoulder Contribution.

### D2.3. Maximum Stress Analysis

Figure D.5a demonstrates the fatigue damage profile along the bottom of the longitudinal edge for asphalt concrete shoulders without the influence of EBITD ( $0^{\circ}\text{F}$ ). The maximum fatigue damage location is at mid-slab edge and is predominantly caused by heavily loaded single axles. This finding supports the traditional analysis approach that the maximum stress and subsequent bottom-up, transverse fatigue cracking are caused by axles placed at the mid-slab edge.

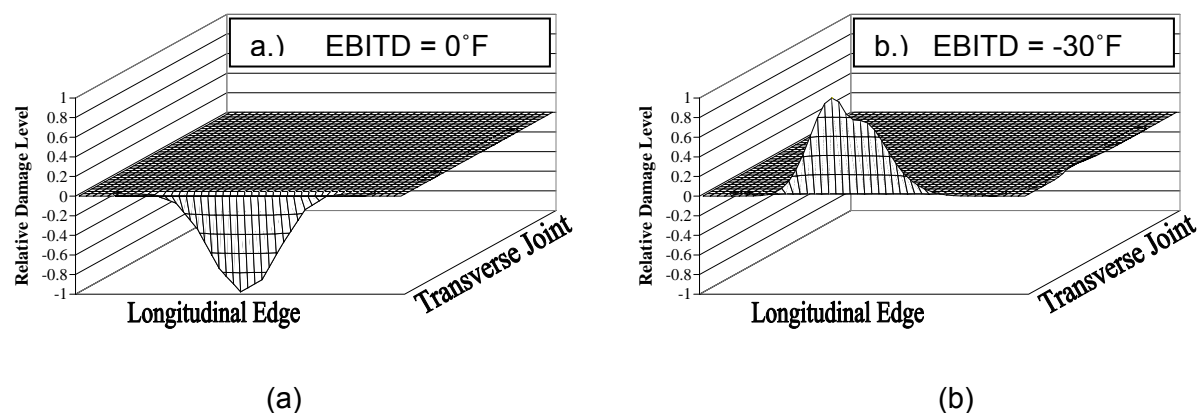


Figure D.5. Example of Damage along Top and Bottom of Slab Edge with  $0^{\circ}\text{F}$  and  $-30^{\circ}\text{F}$  Effective Built-In Temperature Difference.

However, by adding a  $-30^{\circ}\text{F}$  EBITD, the predicted fatigue behavior of the rigid pavement slab is greatly modified, as seen by the damage profile on the right in Figure D.5b. Due to steer-drive axle spacing effects and the lift-off at the slab corners, the critical fatigue damage

location is found within 2 ft of mid-slab, but is top-down instead of the traditional bottom-up cracking mechanism. This result agrees well with the Mechanistic-Empirical Pavement Design Guide (ARA, 2007) for rigid pavements with respect to critical fatigue damage locations (Darter et al., 2001). The steer-drive axle combinations dominate the critical damage level for this case, while single axles only contribute a relatively small portion to the total damage.

## D2.4. Critical Damage Locations

The level of built-in curl can drastically affect the critical fatigue cracking initiation location. Figure D.6 is a demonstration of the critical damage locations found by varying the EBITD level from 0° to -30°F in steps of 5°F, varying the mean lateral wheel load distribution from 18 in. to 24 in. to 30 in., modifying load transfer efficiency, and changing the climatic region in *RadiCAL*. In the asphalt shoulder case, the potential failure zones expand from two to six by using the stress range concept instead of the maximum stress analysis. The stress range concept also leads to potential longitudinal or corner cracking. When using tied shoulders, the potential failure zones expand to four with the stress range approach from the two determined with the maximum stress analysis. The only top-down cracking mechanism for tied shoulders was found to be transverse cracking near the mid-slab edge from steer-drive axle spacing effects. With widened lanes, the maximum stress analysis actually exhibited more potential failure locations (four) relative to the stress range analysis (two).

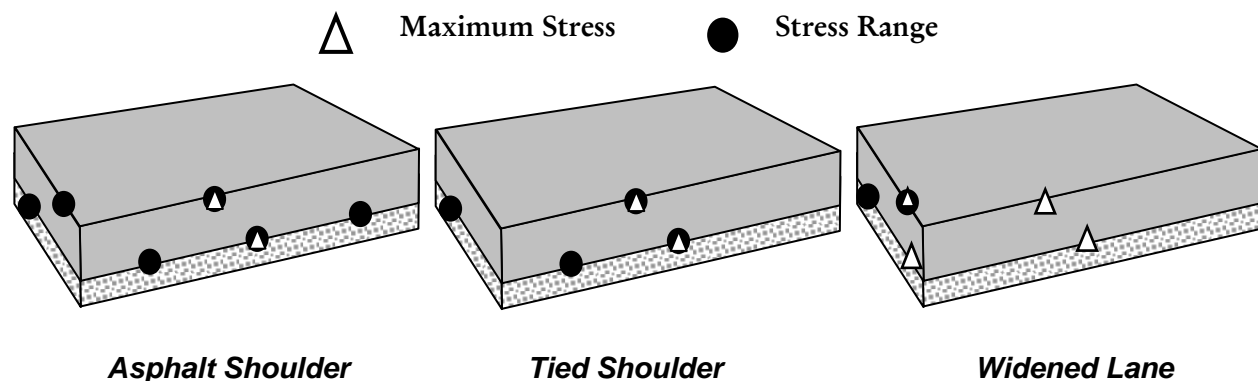


Figure D.6. Potential Maximum Damage Locations Using Maximum Stress or Stress Range Approach.

## D3. CASE STUDIES

### D3.1. US-20 Field Study

In October 2005, IDOT and the University of Illinois tested an in-service section of jointed plain concrete pavement using the FWD to characterize its level of built-in curl. These slabs were located on US-20 just east of Freeport, Illinois and comprised a test section that used different joint spacings (13.3, 15, 20, and 40 ft) and load transfer devices (dowels and hinged joints), as seen in Figure D.7. All of these concrete slabs were designed to be 10 in. thick resting on a 4-in. cement-treated (econocrete) base, tied PCC shoulder, and constructed in the summer of 1986.

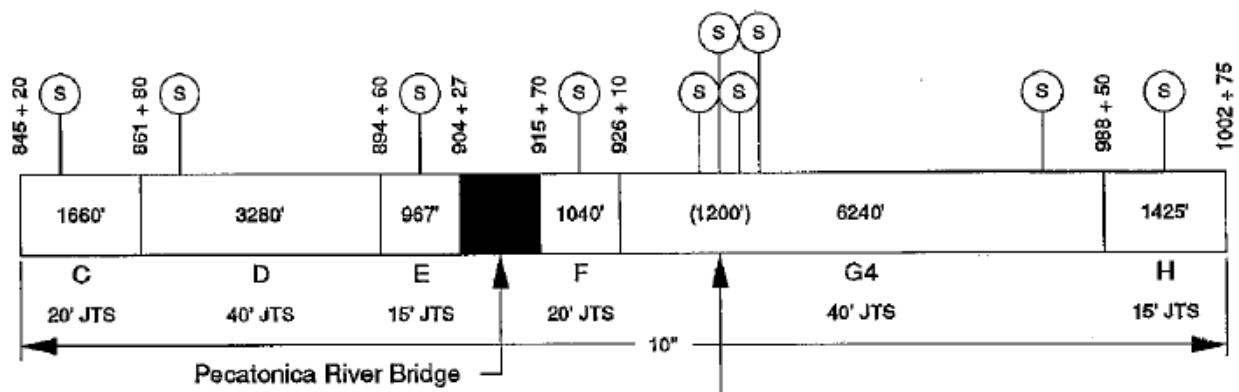


Figure D.7. Site Layout for Test Section on US-20 near Freeport, Illinois (Reed and Schutzbach, 1993).

The FWD testing included three drops at the corner of the slabs and was followed by center slab drops to backcalculate the support conditions and concrete elastic modulus values. For each section, between 6 and 9 corners were tested, depending on the joint type used in that particular section. The three FWD tests at each corner were conducted at different load levels to compare the backcalculated values found at any particular load level.

Load transfer was also tested at the corners of these slabs and was found to be in the range of 85-90% across doweled and hinged joints, and roughly 85% across the tied PCC shoulders. However, the load transfer was found to be below 15% for the structural mid-slab transverse cracks in the 40-ft slab length sections G4 and D, which both were mesh-reinforced JRCP slabs with 40-ft lengths between doweled joints.

Table D.2 shows the section's joint spacing and joint type (doweled joint if not noted elsewhere), as well as the backcalculated EBITD values found from the process developed by Rao and Roesler (2005a). These EBITD values take into account the amount of curling that is due to the actual temperature differences in the slab, and therefore represent the level of equivalent temperature curl that would exist with no temperature difference. In general, Table D.2 shows that the EBITD values were quite low (-7°F) and would be rather insignificant in changing the critical fatigue damage locations when doweled joints were used in conjunction with tied PCC shoulders. However, in those cases with large mid-slab structural transverse cracks, the slab was more free from restraint and did develop significant built-in curling (up to -27°F), which could potentially lead to top-down transverse or longitudinal cracking development before the traditionally predicted bottom-up, mid-slab transverse cracking could develop. This deviation from the designed failure mode would result in a premature fatigue failure using standard mechanistic-empirical design methods.

Table D.2. Backcalculated EBITD Values for US-20 near Freeport, Illinois.

Section ID	Joint Spacing (feet)	All		Hinged Cracks		Joints		Notes
		Mean (°F)	Standard Deviation (°F)	Mean (°F)	Standard Deviation (°F)	Mean (°F)	Standard Deviation (°F)	
H	15	-4.1	1.1	n/a	n/a	-4.1	1.1	
G4	40	-19.9	9.1	-26.6	9.3	-14.6	4.3	a
G3	13.3	2.0	0.0	n/a	n/a	2.0	0.0	b
F	20	-7.0	4.8	n/a	n/a	-7.0	4.8	
E	15	-6.3	3.3	n/a	n/a	-6.3	3.3	
D	40	-11.2	8.0	-12.9	10.8	-9.4	3.4	a
C	20	-1.2	0.5	n/a	n/a	-1.2	0.5	

<sup>a</sup> Structural transverse crack near mid-slab

<sup>b</sup> JPCP with tie bar at joints with dowels at every third joint

### D3.2. US-67 FIELD STUDY

In April 2006, IDOT tested an in-service section of jointed plain concrete pavement using the FWD on westbound US-67 in Morgan County just west of Jacksonville, in west central Illinois. This section is a four-lane divided highway with tied concrete shoulders, constructed in 1999. The pavement is a 10-in. JPCP on a 4-in. base of cement aggregate mixture, and a subgrade stabilized with lime to a depth of 12 in. The joints are doweled, perpendicular, and uniformly spaced at 15 ft. This section had both sealed and unsealed joints to assess the effectiveness of such construction practices and subsequent maintenance on rigid pavement performance.

The sections with sealed joints were found to have a *k*-value of 302 psi/in., while the unsealed section exhibited support of exactly half of that value (156 psi/in.). Load transfer efficiencies were found to be over 80% in both sections, as seen in Table D.3. Using the same backcalculation scheme (Rao and Roesler, 2005a), this section exhibited EBITD values that all fell below the level of -9°F, as was found with the doweled joints on the US-20 site. Low EBITD values were backcalculated due to extremely low deflections under the loaded FWD plate at all load levels (Table D.3). Since the actual temperature difference in the slab during testing was found to be +9°F (top warmer than bottom of slab), all built-in curl levels were found to be less than -9°F, meaning little to no level of EBITD exists on this site.

A second US-67 location was tested in November 2006 by IDOT using FWD, also to determine the level of built-in curl on in-service JPCPs. This site was located on southbound US-67 in Scott County, west-southwest of Manchester, approximately 17 mi from the first US-67 section tested. The pavement is a 9.75-in. JPCP with tied concrete shoulders on a 4-in. base of cement aggregate mixture, and a subgrade stabilized with lime to a depth of 12 in. This section of US-67 was constructed in November of 2004.

For this particular section, mid-slab FWD tests were not conducted, and therefore, information regarding the subgrade support (*k*-value) was not available. While the variable does affect the backcalculation of the built-in curl level, an effort was made to check for the existence of built-in curl at a range of *k*-values, noting that the expected *k*-values at this site would probably be in a similar range of the previously tested US-67 site nearby. The FWD testing for this section was conducted with an actual slab temperature difference of +7°F.

This site had excellent load transfer efficiency across both the transverse joints and tied shoulders, as seen in Table D.3. One explanation for the lower EBITD values was the excellent

LTE at the edges of the slabs. Even under curling conditions from differential shrinkage and built-in temperature difference, the restraint offered by adjacent slabs reduced the resulting permanent curling and deflections under the FWD load. All built-in curl levels on this second US-67 site were found to be less severe than -7°F if reasonable assumptions regarding the support conditions are made, as described earlier. If extremely high  $k$ -values (500 psi/in.) did exist on this site (this would have to be validated with FWD center slab testing), then testing data would support backcalculated built-in curl levels in the range of -10°F to -20°F.

Table D.3. Backcalculated Load Transfer Efficiencies and Average Loaded Deflections for All US-67 Sites.

Testing Date	Location	FWD Load	Transverse Joint LTE	Tied Shoulder LTE	Average Deflection under Load Platen
		pounds	%	%	mils
April-06	US-67 near Jacksonville <sup>a</sup>	9,500	86.9	78.1	5.21
		13,500	88.2	78.2	7.39
		20,500	89.2	79.2	11.28
April-06	US-67 near Jacksonville <sup>b</sup>	9,500	87.2	71.8	5.37
		13,500	84.9	69.7	8.11
		20,500	89.1	73.9	11.32
November-06	US-67 near Manchester	11,000	85.0	90.8	5.62
		14,000	84.8	90.0	7.18
		24,000	86.1	90.9	12.14

<sup>a</sup> Joints sealed

<sup>b</sup> Joint unsealed

#### D4. SUMMARY

The phenomenon of built-in curling has been noted for many years, although the factors involved in causing this, as well as the ability to characterize it, are recent developments in pavement engineering. The importance of built-in curl characterization was addressed from both a residual and total stress standpoint, as well as its impact on fatigue damage development in joint plain concrete pavement design. This built-in curl, in combination with axle spacing effects, can have a profound effect on changing the critical fatigue damage location, resulting in non-traditional cracking and more difficult rehabilitation alternatives for concrete pavements.

FWD testing of two Illinois jointed plain concrete pavement sites was conducted to assess the level of built-in curl existing in typical sections. Both of these sections were designed with tied shoulders that limited the built-in curl potential through restraint. In areas with hinged joints and its associated low-load transfer, the built-in curl was significantly higher than in doweled sections, regardless of joint spacing.



## **APPENDIX E. DEVELOPMENT OF A MECHANISTIC-EMPIRICAL FATIGUE ANALYSIS PROCEDURE**

### **E.1. Introduction**

The study by Hiller and Roesler (2002) on the relative reference stress indicated that software needed to be developed to analyze “damage” from fatigue mechanisms and not just relative stress levels in jointed plain concrete pavements. Traditionally, mechanistic-empirical design of rigid pavements has focused on predicting bottom-up transverse fatigue damage at the edge of the slab. The recent National Cooperative Highway Research Program Project 1-37A (ARA, 2007) accounts for both bottom-up and top-down transverse cracking damage along the longitudinal edge. However, the combination of temperature gradients, moisture shrinkage, and built-in temperature curl increases the number of locations that can potentially exhibit fatigue failure, and a more comprehensive analysis procedure is needed to address this issue.

Through irreversible shrinkage in the top 2 to 3 in. of the concrete slab, as well as the built-in temperature gradients during the setting of the concrete, a majority of rigid pavements experience a permanent upward curl, regardless of the cyclical temperature gradient (Byrum, 2000). This upward curling of concrete slabs has been observed in a variety of different climatic regions (Rao et al., 2001; Yu et al., 1998; Yu and Khazanovich, 2001; Poblete et al., 1988). The magnitude of the total curl varies with cyclical temperature and moisture gradients in the slab, but a certain level of permanent built-in curl always remains. Full-scale test results from the desert climate of Palmdale, California suggest that the levels of permanent curl, in terms of a linear effective built-in temperature difference (EBITD), can exceed -40°F for undoweled slabs (Rao and Roesler, 2005a), as seen in Table E.1. Test sections in Palmdale with more slab restraint, such as dowels, tied shoulders, or widened lanes, exhibited lower built-in curl levels.

Table E.1 also demonstrates that the phenomenon of built-in curling exists at numerous geographic locations and climates based on previously published sources. Through improved characterization of axle-load interactions, as well as permanent and cyclical curling effects in cumulative fatigue damage calculations, the critical location and timing of fatigue cracking in rigid pavements can be better predicted. This portion of the research focuses on improving the prediction of longitudinal, corner, and transverse fatigue cracking phenomena initiating from both the top and bottom of the slab for typical California rigid pavement structures.

Table E.1. Measured Effective Built-In Temperature Difference (°C).

Location / ID	Built-in Curl (°C)	Comment	Reference
Surface Profiling (using dipstick unless otherwise noted)			
All LTPP GPS3 Sections <sup>a</sup>	Up to -44	Multiple geometries / restraint	Byrum 2000
I-80 in Pennsylvania	-37	Dowels / 20 ft joint spacing	Yu et. al. 2001
AZ1 in Phoenix, Arizona	-15.2 <sup>b</sup>	No dowels / AC shoulder / 15 ft joint spacing	C. Rao et. al. 2001
	-23.9 <sup>c</sup>		
AZ3 in Phoenix, Arizona	-23.1 <sup>b</sup>	No dowels / AC shoulder / 20 ft joint spacing	
	-29.1 <sup>c</sup>		
AZ4 in Phoenix, Arizona	-11.8 <sup>b</sup>	Dowels / Tied PCC shoulder / 20 ft joint spacing	
	-20.0 <sup>c</sup>		
Mankato, Minnesota	-22.8 <sup>b</sup>	No dowels / AC shoulder	
	-27.4 <sup>c</sup>		
Deflection Measurements (using FWD/HWD unless otherwise noted)			
I-70 in Colorado <sup>d</sup>	-11.1	Dowels / Tied PCC shoulder	Yu et. al. 1998
Florida <sup>d</sup>	-5	Undoweled	Armaghani et. al. 1987
Chile	Up to -19.2	Multiple sections	Poblete et. al. 1988
I-80 in Pennsylvania	-8.9	Aggregate base	Yu et. al. 2001
	-6.7	Bituminous base	
Palmdale, California	-22.7	No dowels / AC shoulder	S. Rao and Roesler 2005a
	-9.8	Dowels / Tied PCC shoulder	
	-17.2	Widened lane / AC shoulder	
Ukiah, California	-10	No dowels / AC shoulder	S. Rao and Roesler 2005a
DIA Denver, Colorado <sup>e</sup>	-5 to -8	17.5 inch airfield slabs	Rufino 2003

<sup>a</sup> Using high speed profiling<sup>b</sup> 3 days after construction<sup>c</sup> 40 days after construction<sup>d</sup> Using fixed external surface gages for deflections<sup>e</sup> Using multi-depth deflectometers

### E.1.1 Mechanistic Input Characterizations

With the inclusion of built-in temperature gradients and differential shrinkage in the analysis of California rigid pavements, an influence line approach (Byrum and Hansen, 1994) was adopted to determine the location and magnitude of the critical stresses. This approach uses multiple finite element analyses from the ISLAB2000 program (ERES Consultants, 1999) to step an axle or set of axles across a slab by changing the position of the loaded areas 12 in. at a time, and recording up to 89 individual nodal responses for each finite element analysis (see Figure E.1). Depending on the axle configurations and slab geometry, between 17 and 45 loading locations are required to fully traverse the design slab. An example of this process, which can be represented by stress influence lines, is shown in Figure E.2 for two nodal

locations. The advantage of this method is that the influence of a moving axle or set of axles on stress development can be found at each nodal location, along with the maximum stress level and the change in stress. The slab responses at each nodal location were then saved in order to train an artificial neural network (Khazanovich et al., 2001) using Monte Carlo hierarchical adaptive random partitioning (MC-HARP) to reproduce and interpolate the results more efficiently for other input combinations (Banan, 1995; Khazanovich and Roesler, 1997).

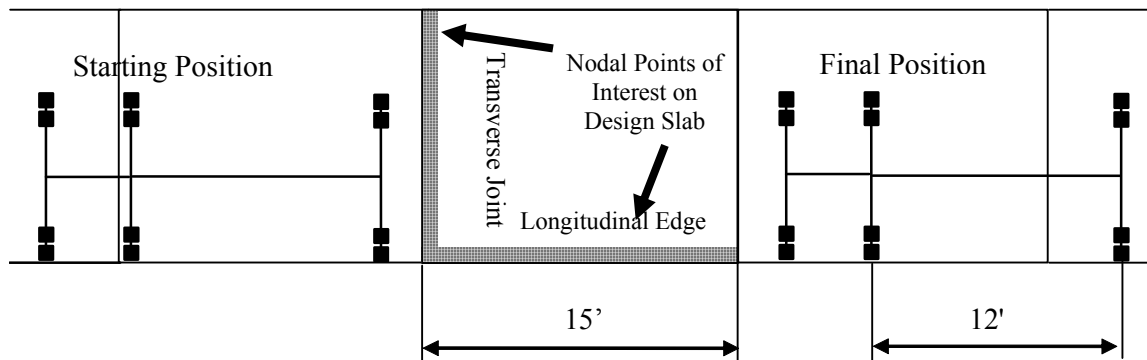


Figure E.1. Locations of starting and ending points for influence line analysis with 12-ft steer-drive axle combination.

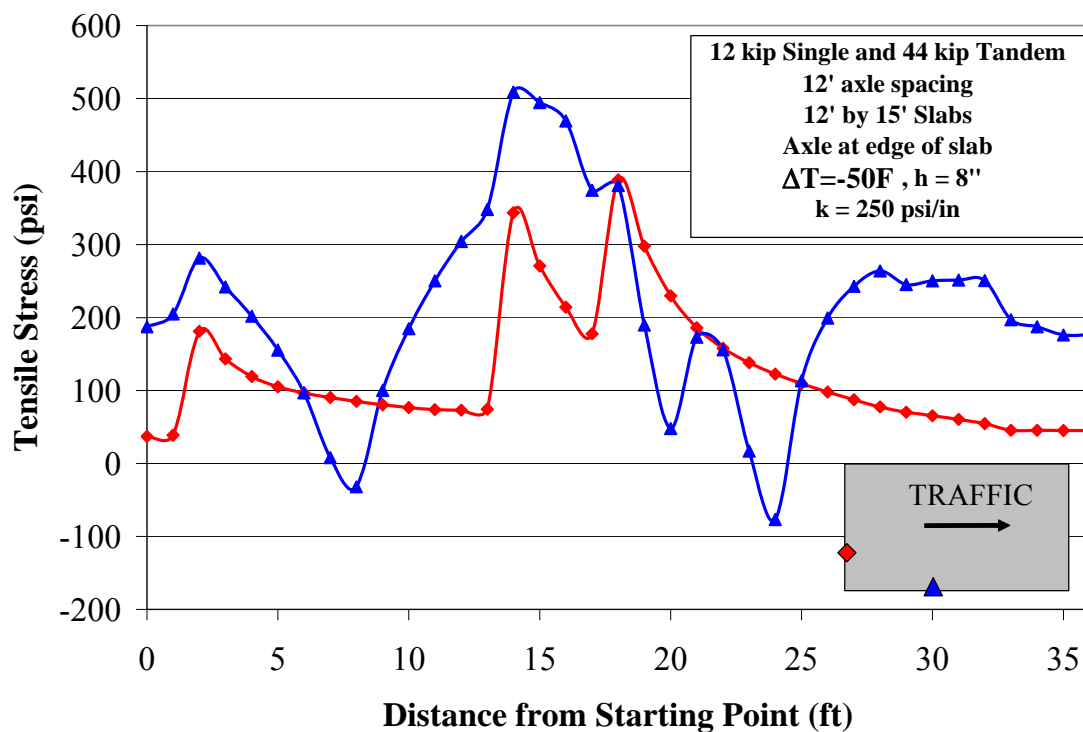


Figure E.2. Example of influence line responses for two nodal locations on top of slab for location between wheel path along transverse joint and 2 ft from mid-slab along longitudinal edge.

To characterize the inputs required for the finite element analyses using the influence line approach, statistical distributions of traffic and climatic conditions were developed. Traffic

and climatic input conditions for the state of California were based on research published by the Pavement Research Center at the University of California-Berkeley.

### ***E.1.2 Traffic Characterization***

Lu et al. (2001) used data from over 100 weigh-in-motion (WIM) stations in California to characterize the load spectra on key California road corridors, as seen in Figure E.3. These load spectra distributions are differentiated by steer, single, tandem, and tridem axles, as seen for California Class 9 vehicles in Figure E.4. The load spectra data helped define the maximum load magnitudes, time-of-day influences, and loaded and unloaded axle ranges, as well as the specific Federal Highway Administration (FHWA) vehicle class distributions for use in mechanistic analyses.

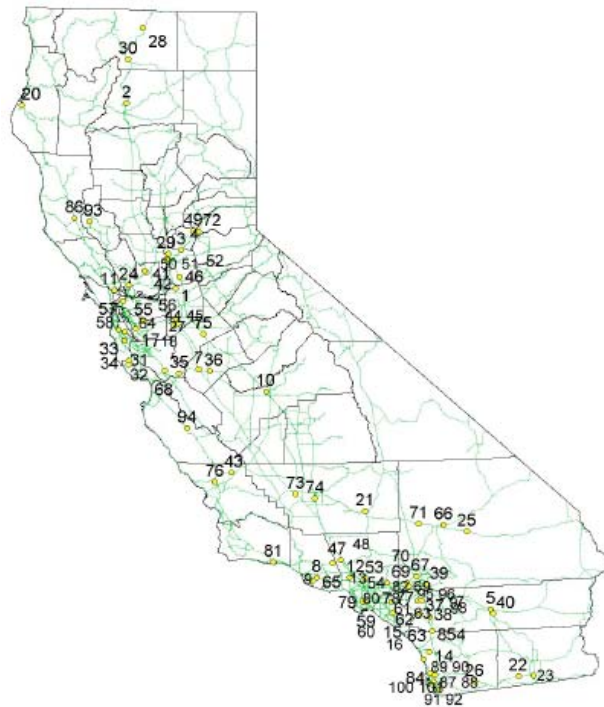


Figure E.3. Locations of California WIM stations (after Lu et al., 2001).

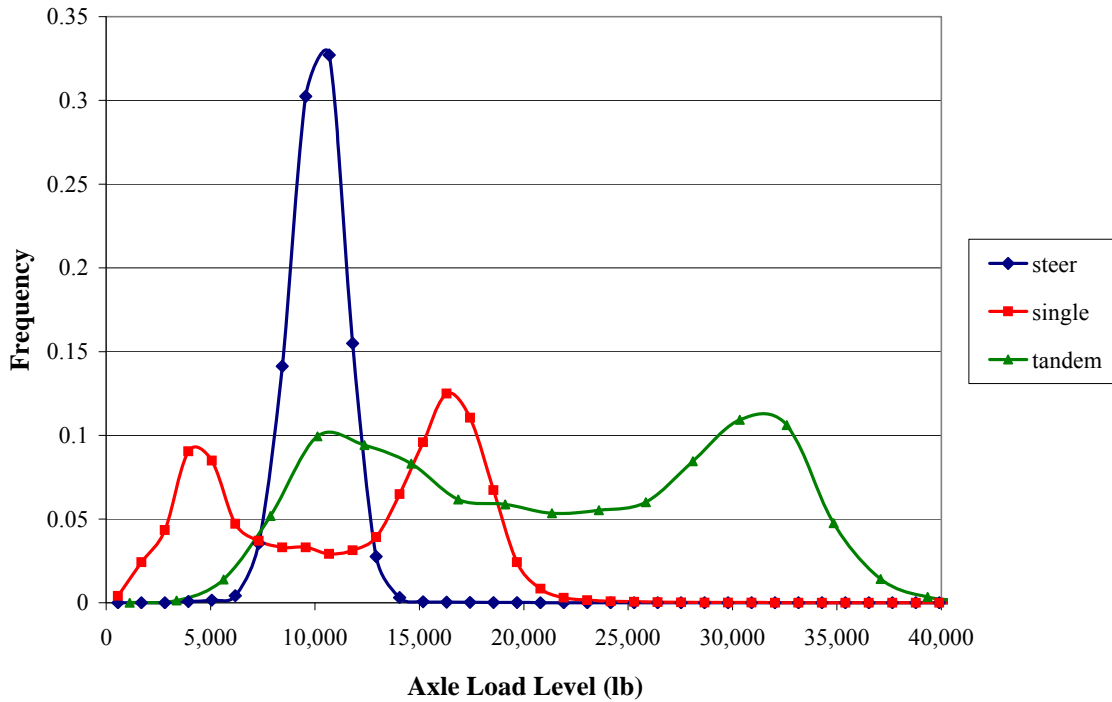


Figure E.4. Example of load spectra by axle type for California class 9 vehicles (after Lu et al., 2001).

In rigid pavements, the stress fields and maximum stress levels are highly dependent on the axle position in relation to the slab edge. To model the lateral wander of applied truck traffic, a standard normal distribution was assumed where the user-specified mean and standard deviation are required according to Equation (E-1).

$$f(x) = \frac{1}{\sigma\sqrt{2\pi}} e^{-\left[\frac{(x-\mu)^2}{2\sigma^2}\right]} \quad (E-1)$$

where:

$f(x)$  = normal distribution function;  
 $x$  = variable representing distance from slab edge to axle;  
 $\mu$  = lateral wheel wander mean; and  
 $\sigma$  = standard deviation.

In the subsequent finite element analysis, the allowable lateral offset of the axles modeled was 0 to 2 ft from the slab edge based on known lateral wander distributions.

### E.1.3 Axle Spacing Effects

With the influence of curling, the spacing between the steer and drive axles and their respective load levels can have an impact on stress development in rigid pavements. An initial analysis found that cases with 15-ft joint spacing and high levels of negative curling, steer-drive axle spacings as large as 12 ft can influence the critical stress level and promote top-down cracking in the center of the slab. Higher load transfer levels increase the effective length of the slab, and thus, loads placed on adjacent slabs can influence top-down tensile stresses. Figure E.5 shows an example of maximum tensile stress levels at each node from an influence line

analysis for multiple steer-drive axle spacings under an equivalent negative linear temperature differential. For larger axle spacings, the results of the influence line analysis approach the infinite spacing case (tandem-only) where the steer axle has no effect on the top-down stress development in the critical slab. Steer-drive axle spacings shorter than 12 ft on a 15-ft slab length start to approach the tandem-only case as well. By modeling maximum stress in this fashion, one single pass of an axle load or a combination of axle loads will result in one repetition and not multiple ones.

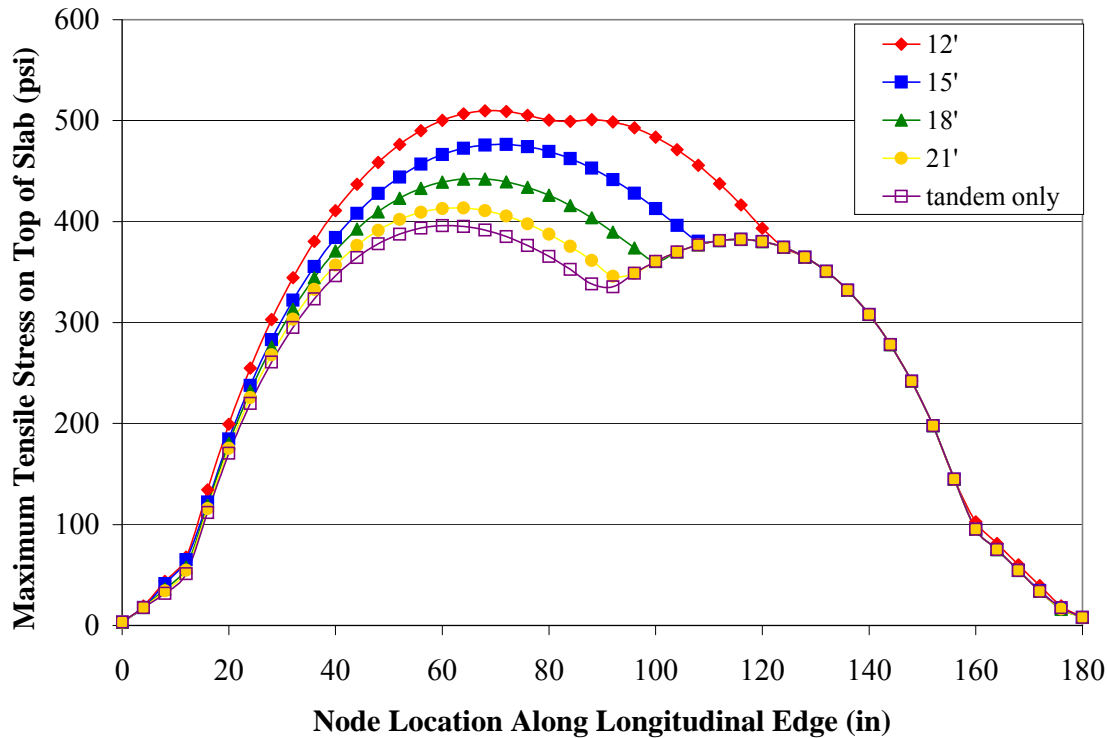


Figure E.5. Effect of steer-drive axle spacing on maximum tensile stress (12-kip steer, 44-kip tandem) for 15-ft joint spacing and  $-50^{\circ}\text{F}$  equivalent temperature differential.

The spacings between the steer and drive axles were determined for the WIM stations in California to form discrete statistical distributions that are highly dependent on the specific FWHA truck classification. The values used for the default axle spacing distributions can be found in Figure E.6. Steer-drive axle spacings greater than 21 ft and smaller than 9 ft are assumed to be separate single and tandem axle loads, since the axle spacing effect on top-down stress development at these distances is limited.

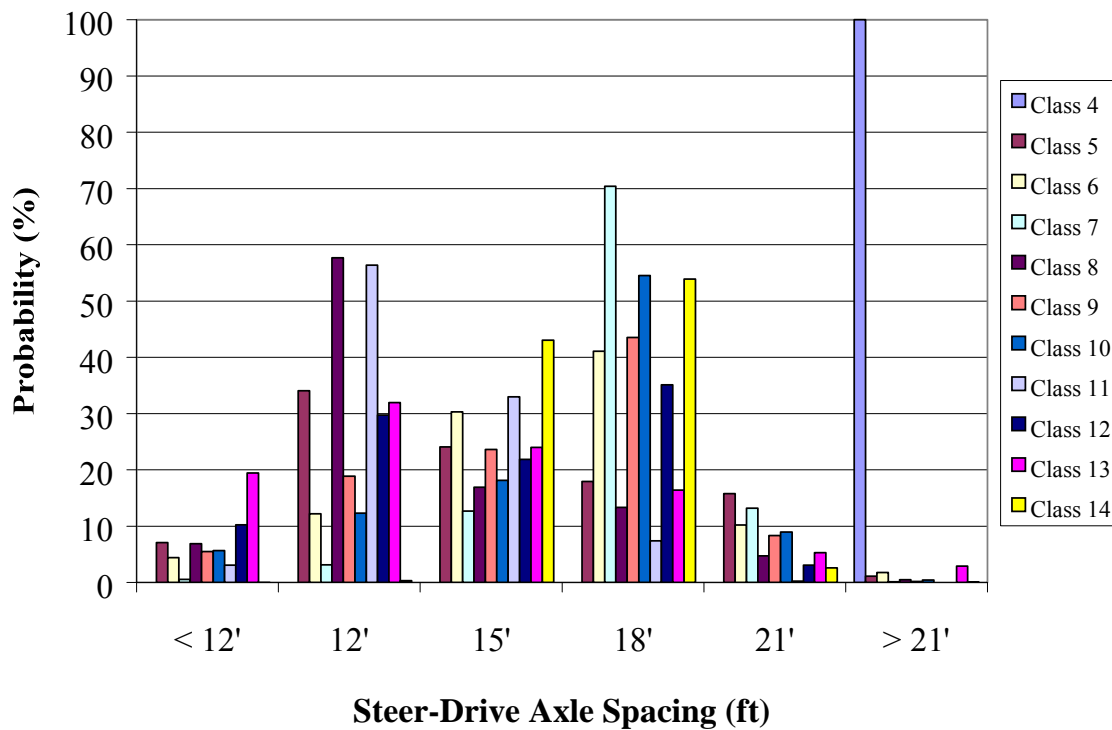


Figure E.6. Average steer-drive axle spacings for all California WIM stations (after Lu et al., 2001).

#### E.1.4 Climatic Influences

In order to easily incorporate climatic effects into the fatigue damage analyses, California was categorized into seven distinct climatic regions (Harvey et al., 2000a). Historical data from weather stations in each climatic zone was input into the Enhanced Integrated Climatic Model (Larson and Dempsey, 1997) to predict cyclical linear temperatures through the slab depth for several pavement sections.

An important input required for evaluating California rigid pavements is the inclusion of EBITD into the analysis. Rao (2005) defines the EBITD as all factors that affect curling and warping in the concrete slab (built-in temperature difference, reversible moisture warping, irreversible drying shrinkage) with the exception of cyclical temperature curling, which is accounted for in a backcalculation process. Rao builds upon previous work of Eisenmann and Leykauf (1990a, 1990b), Yu et al., 1998, and Yu and Khazanovich, 2001 in this area to develop a specific process using falling weight deflectometer testing. The EBITD level is treated as a linear temperature difference in this analysis, which shifts the frequency distribution of the cyclical, reversible slab linear temperature differences ( $\Delta T$ ) to an equivalent temperature difference, as demonstrated in Figure E.7 for the San Francisco Bay Area climatic region. For California, an EBITD level of  $-30^{\circ}\text{F}$  can shift the equivalent temperature difference distribution entirely into the negative region, as seen in Figure E.7. Only different levels of upward curl exist under this EBITD level, and the slab would never experience a downward curl or full contact with the underlying base layer.

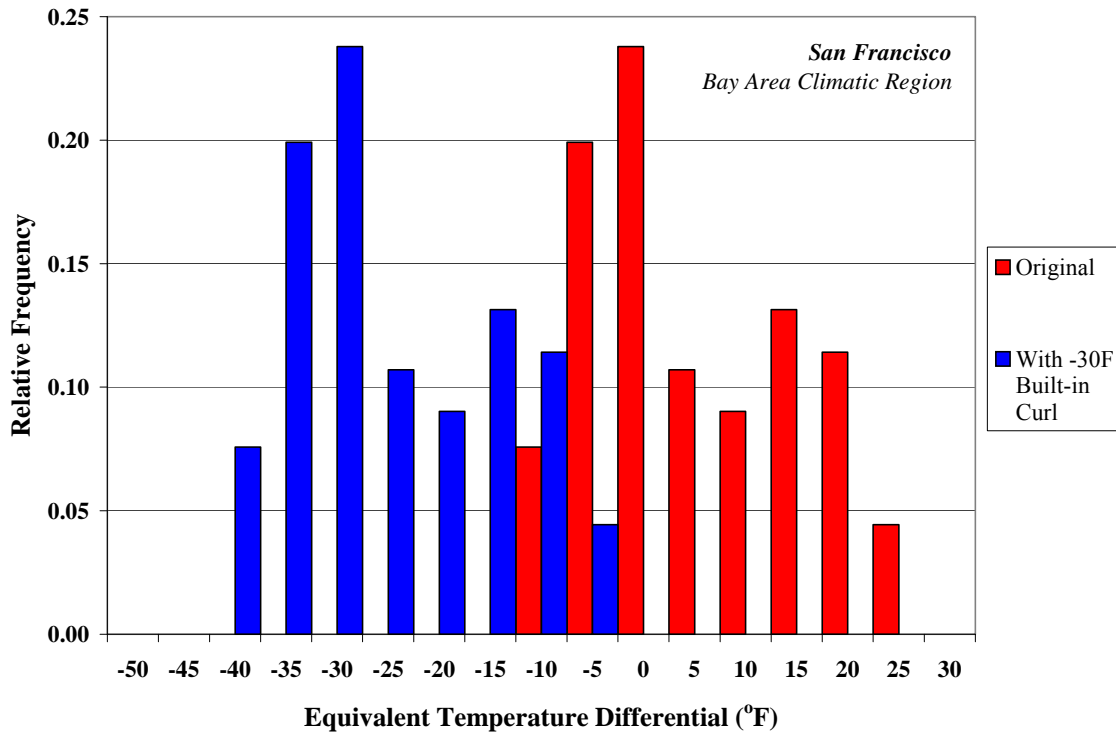


Figure E.7. Frequency distribution shift of temperature differential for San Francisco Bay Area due to effective built-in temperature difference.

### E.1.5 Fatigue Damage Determination

Damage levels at longitudinal and transverse joint nodes were determined using a phenomenological concrete fatigue relationship and employing Miner's Hypothesis of linear damage accumulation (Miner, 1945) for all nodes on the top and bottom of the slab at the transverse joint and along the longitudinal edge, as seen in Equation (E-2).

$$\text{Fatigue Damage}_{(x,y,z)} = \sum_i \sum_j \sum_k \sum_l \frac{n_{ijkl}}{N_{ijkl}} \quad (\text{E-2})$$

where:

- $n_{ijkl}$  = applied number of load applications at condition i, j, k, ...;
- $N_{ijkl}$  = allowable number of load applications at condition i, j, k, ...;
- $i$  = axle combination/spacing;
- $j$  = load level;
- $k$  = equivalent temperature difference;
- $l$  = wander; and
- $x, y, z$  = Cartesian coordinates for nodal location on slab.

The damage accumulation procedure was completed for up to 89 nodes for each influence line. By employing a damage accumulation procedure, the impact of the expected repetitions of each respective axle load can be assessed. The damage accumulation procedure



along the transverse joint and longitudinal edge determines the critical damage levels and locations leading to fatigue failure. The type of distress produced (top-down or bottom-up transverse, longitudinal, or corner cracking) depends on the interaction of the traffic, climate, and pavement geometry inputs.

To incorporate the cumulative damage analysis described above, a Visual Basic program called RadiCAL (Rigid pavement Analysis for Design In CALifornia) was developed (Hiller and Roesler, 2005b). A flow diagram detailing the process from input parameters to fatigue damage profiles along the transverse joint and longitudinal edge is shown in Figure E.8. This program allows for rigid pavements under California climatic conditions to be expeditiously analyzed for a variety of traffic inputs, climatic conditions, and pavement geometry. Two separate fatigue transfer functions based on maximum stress (zero maintenance as defined in Equation E-3; Darter, 1977) and Mechanistic-Empirical Pavement Design Guide (MEPDG; ARA, 2007), as well as one using stress range (Tepfers, 1979; Tepfers and Kutti, 1979) were incorporated into RadiCAL.

$$\text{Log}(N_f) = 17.61 - 17.61 \left( \frac{\sigma}{\text{MOR}} \right) \quad (\text{E-3})$$

where:

$N_f$  = number of load application until failure;  
 $\sigma$  = applied maximum stress level; and  
MOR = modulus of rupture of the concrete.

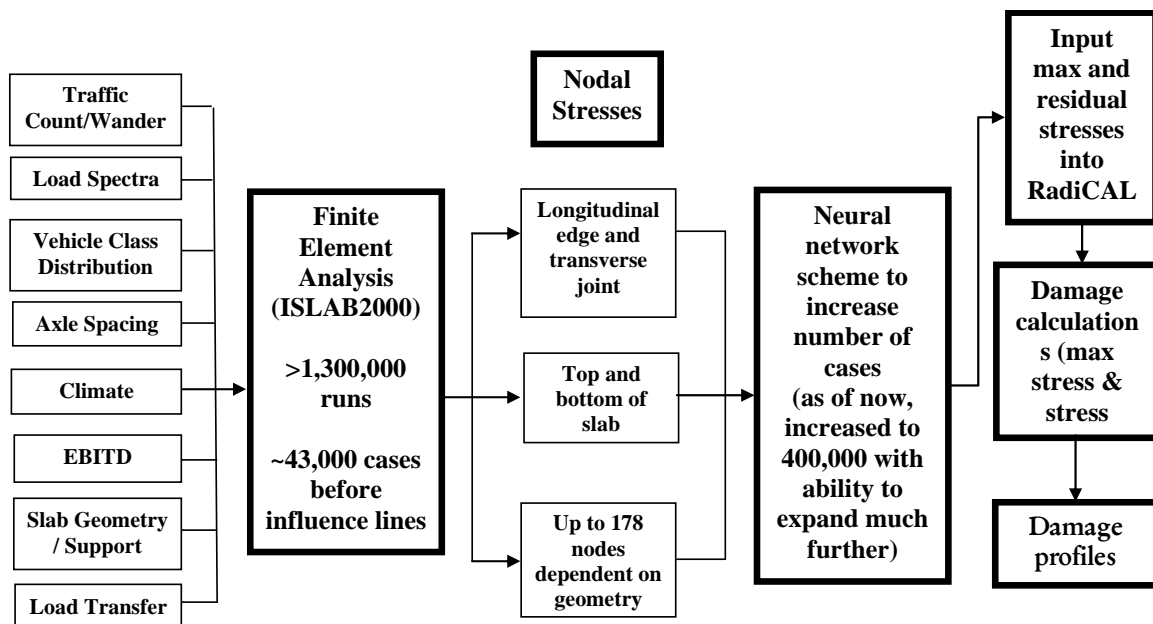


Figure E.8. RadiCAL flow diagram for mechanistic-empirical analysis of JPCP.

### E.1.6 Maximum Stress Determination

When employing an influence line analysis under fully supported slab conditions, the critical tensile stress locations for the pavement structure are typically at the bottom of the slab directly below the loaded area. Critical tensile stresses at the top of the slab for each node depend on the interactions between the slab geometry, curling, steer-drive axle spacing, joint load transfer, and load position on the slab. Figure E.9 demonstrates an example of the critical tensile stresses at the top of a slab for each node along the longitudinal slab edge using the

influence line approach for a 12-ft steer-drive axle spacing and a  $-50^{\circ}\text{F}$  equivalent temperature differential on a 15-ft slab length. With this particular axle spacing, 36 different loading positions are run in the influence line analysis in order for the full steer-tandem axle assembly to traverse the slab. Along the longitudinal edge at the slab surface, only six out of the 36 loading positions were required to produce the maximum tensile stresses for all node locations during this axle assembly pass. These six loading positions are represented in Figure E.9 by the distance from the starting position of the influence line analysis (the first load is 2 ft before transverse joint in order to have residual curling-related stresses present on the slab of interest).

RadiCAL employs a neural network approach to predict the stresses derived from these finite element analysis runs (Khazanovich et al., 2001). The neural network can determine the maximum stress levels for all nodes along the longitudinal edge and transverse joint of the design slab for each axle position. This assures that the damage determined from each axle pass is due to the maximum stress at each node, and does not rely on the stress values from only one load position, as traditional mid-slab edge design approaches have used (Packard, 1984; Zollinger and Barenberg, 1989a, 1989b).

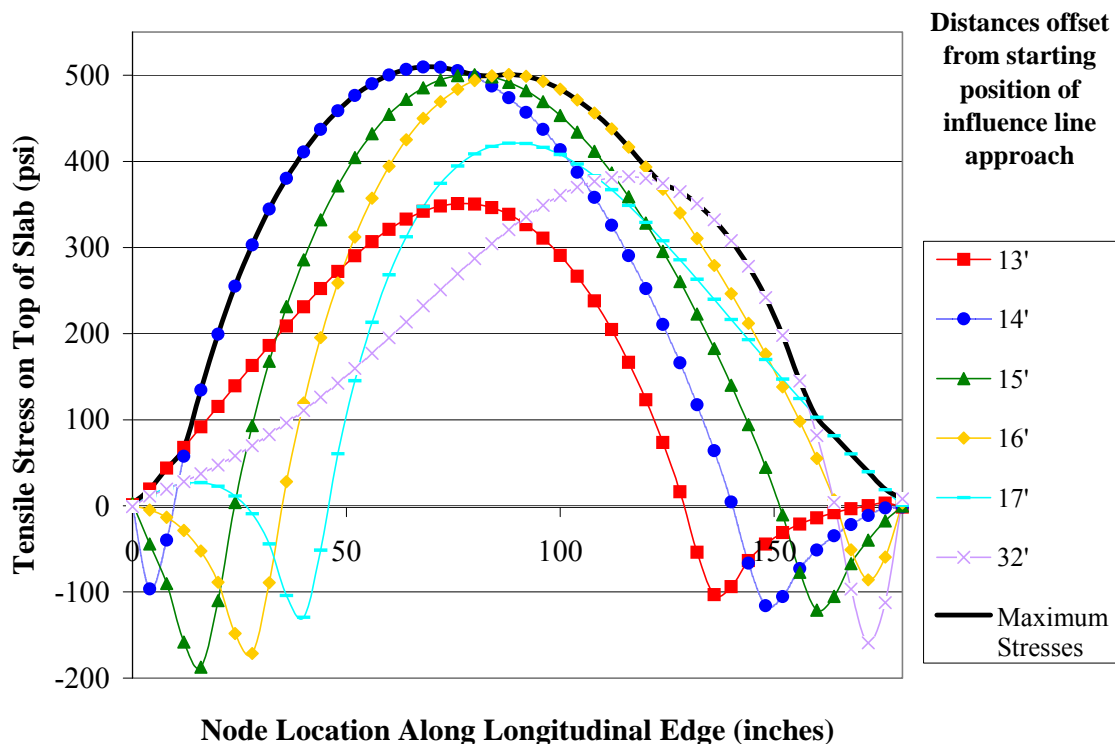


Figure E.9. Maximum stress values at all top-of-slab longitudinal edge nodes for influence line analysis with 12-ft steer-drive axle spacing and asphalt shoulders.

### E.1.7 Stress Range in Concrete Fatigue

When using the influence line approach, a range of stress can also be determined for each pass of an axle or set of axles. Many researchers (Murdock and Kesler, 1958; Awad and Hilsdorf, 1974; Tepfers, 1979; Tepfers and Kutti, 1979) have documented the influence of stress range on the fatigue life of concrete. Recently, Rufino (2003) suggested that the use of maximum stress only in airfield rigid pavements might not be the best tool for design, as it could incorrectly estimate the actual stress responsible for the concrete fatigue damage. By incorporating the stress range concept into fatigue-based design, residual stresses from EBITD and cyclical curling can be considered. Tepfers, 1979 and Tepfers and Kutti, 1979 proposed a stress range model

for concrete fatigue as seen in Equation (E-4), which is used in RadiCAL to determine the allowable number of loads for a given load and climate combination.

$$\frac{\sigma_{\max}}{MOR} = 1 - \beta(1 - R)\log_{10} N \quad (E-4)$$

where:

<i>MOR</i>	=	concrete modulus of rupture;
$\sigma_{\max}$	=	maximum flexural stress applied during cyclic loading;
$\sigma_{\min}$	=	residual flexural stress in slab before load application;
$\beta$	=	calibration coefficient (0.0685 for concrete by Tepfers, 1979a);
<i>R</i>	=	$\sigma_{\min} / \sigma_{\max}$ ; and
<i>N</i>	=	number of loading cycles to failure (at 50% reliability).

The idea of stress range in conjunction with an applied stress ratio concept in rigid pavement analysis was first proposed by Domenichini and Marchionna (1981). They used a modified Tepfers' equation by altering the  $\beta$ -coefficient from 0.0685 to 0.0954 to account for factors not present in laboratory beam testing, such as varying magnitudes of environmental stresses and rest periods in the field, as well as variations in concrete properties such as thickness and modulus of rupture. However, Domenichini and Marchionna limited their study to bottom-up transverse cracking at the mid-slab edge based on Westergaard's edge stress equation (1948). The RadiCAL program uses the finite element method for stress determination, enabling a large range of additional variables (steer-drive axle spacing, EBITD, wander, shoulder type, etc.) and potential failure locations that extends the work presented by Domenichini and Marchionna. More recently, researchers (Rao and Roesler, 2004; Rao, 2005) have found that the use of stress range in fatigue was the best predictor of the location of crack initiation from accelerated pavement testing studies in California.

When using the stress range approach in the RadiCAL program, the maximum stress is determined from the influence line analysis, while the minimum stress is taken as the residual stress from the combination of EBITD and the cyclical temperature gradient (no mechanical load condition). With 12-ft-wide by 15-ft-long slabs under a negative gradient, the residual equivalent temperature stresses are higher at the top of the slab along the longitudinal edge, as seen in Figure E.10. If the equivalent temperature difference were positive, the same geometry and restraint conditions would also force the maximum residual stress to be along the longitudinal edge, albeit at the bottom of the slab. These variations in residual stresses create different baselines for the change in stress concept in comparison to a traditional maximum stress analysis. While the maximum stress (load plus curl) along any slab may be at the mid-slab longitudinal edge, the largest change in stress may not be at the location of the highest residual equivalent temperature stress. A maximum stress analysis can be conducted with RadiCAL, where the minimum stress is taken as zero.

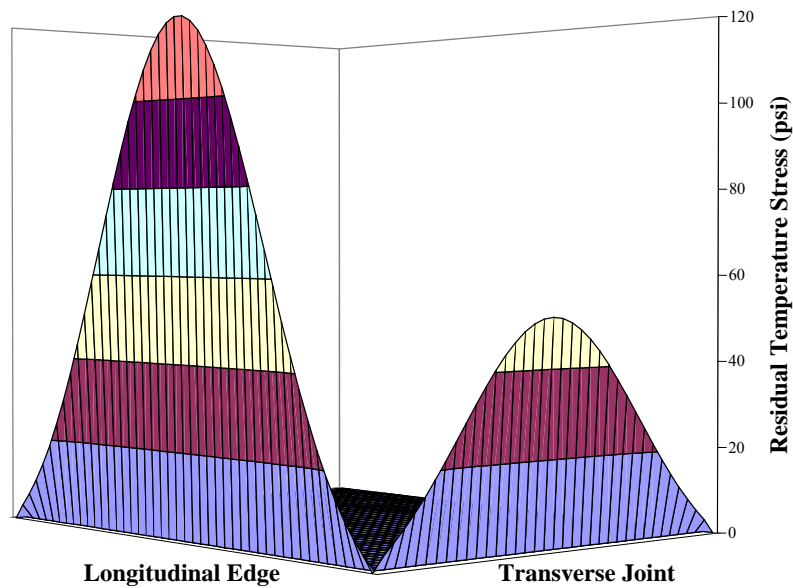


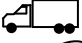

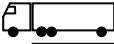
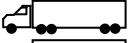
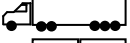

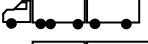




Figure E.10. Residual equivalent temperature stresses for EBITD =  $-30^{\circ}\text{F}$  on 12-ft-wide by 15-ft-long slab with asphalt shoulders.

## E.2. Results Using the RadiCAL Software

This study examines cases run using RadiCAL on 8-in. slabs with dimensions of 12 ft by 15 ft resting on a Winkler subgrade of 250 psi/in. Other constants with regard to traffic, geometry, materials, etc. can be viewed in Table E-2. The statistical distribution for traffic and axle spacing used in this analysis represent the average values found from all California WIM stations (Lu et al., 2001). The average annual daily truck traffic (AADTT) values are held constant in the damage accumulation analysis unless a deviation is otherwise noted. Fatigue damage values are presented as either “absolute damage” (specific damage level determined using Miner’s hypothesis, 1945) or “relative damage” (all damage normalized to highest damage level for a particular RadiCAL run).

Table E-2. Fixed Input Values and Range of Input Parameters Available in RadiCAL.

<i>Geometry</i>		<i>Traffic</i>	
Joint Spacing	12 or 15 ft	Two Way AADTT	Variable
Slab Width	12 or 14 ft	Trucks in Design Direction	Variable
Thickness	8, 10, or 12 in	Trucks in Design Lane	Variable
<i>PCC Materials / Support</i>		Design Life	Variable
Flexural Strength	Variable	<i>CA Avg. Vehicle Class Distribution</i>	
Elastic Modulus	$4 \times 10^6$ psi	Class 4	 1.14%
Thermal Expansion Coeff.	$5.5 \times 10^{-6}$ / °F	Class 5	 23.03%
Poisson's Ratio	0.15	Class 6	 5.18%
Mod. of Subgrade Reaction	250 psi/in	Class 7	 0.28%
Built-in Curl	0 to -40°F	Class 8	 6.66%
<i>Load Transfer Efficiency</i>		Class 9	 50.63%
Transverse Joints	20 to 90%	Class 10	 0.63%
Longitudinal Joints	50%	Class 11	 8.78%
<i>Lateral Wheel Wander Distribution</i>		Class 12	 1.06%
Mean	Variable	Class 13	 0.10%
Standard Deviation	Variable	Class 14	 2.52%
<i>Climatic Zones</i>			
Arcata (North Coast)	California	Carbondale	Illinois
Los Angeles (South Coast)		Chicago DuPage	
Daggett (Desert)		Chicago Midway	
Reno, NV (High Desert/Mountain)		Peoria	
Sacramento (Central)			
San Francisco (Bay Area)			

Absolute damage is reported to first locate the critical damage locations on the slab and to compare the damage magnitude with other input combinations. An absolute damage level of 1.0 does not necessarily mean slab failure in this analysis, as was postulated by Miner (1945). Relative damage is used to compare nodes with respect to the highest damage level node for a particular set of inputs. The following sections examine the relative damage and absolute damage level caused by changing inputs shown in Table E-2, as well as their effect on the critical damage location.

### **E.2.1 Maximum Stress Analysis**

A large percentage of older concrete pavements across the United States use an asphalt concrete shoulder. This shoulder type does not provide stress reduction to the concrete slab. With asphalt shoulders, axles applied near the mid-slab edge produce high tensile stresses at the bottom of the slab. Without restraint from a tied shoulder or doweled transverse joint, EBITD levels have been found to be more negative as well (Rao and Roesler, 2005b).

Figure E.11a demonstrates the fatigue damage profile along the bottom of the longitudinal edge for asphalt concrete shoulders without the influence of EBITD (0°F). In these relative damage profiles, a negative value indicates the damage is bottom-up, whereas a

positive value indicates the damage is top-down. The maximum fatigue damage location is at mid-slab edge and is predominantly caused by heavily loaded single axles. This finding supports the traditional analysis approach that the maximum stress and subsequent bottom-up, transverse fatigue cracking are caused by axles placed at the mid-slab edge.

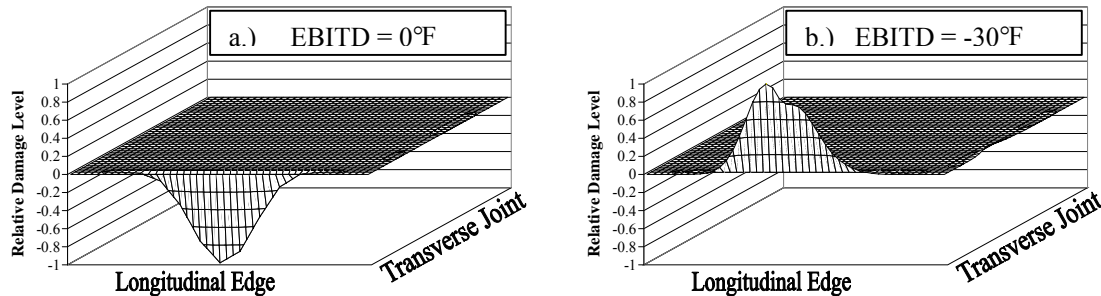


Figure E.11. Damage along top and bottom of slab with 0°F and -30°F effective built-in temperature difference in San Francisco Bay Area.

However, by adding a -30°F EBITD, the predicted fatigue behavior of the rigid pavement slab is greatly modified, as seen by the damage profile on the right in Figure E.11b. Due to steer-drive axle spacing effects and the lift-off at the slab corners, the critical fatigue damage location is found within 2 ft of mid-slab, but is top-down instead of the traditional bottom-up cracking mechanism. This result agrees well with the MEPDG for rigid pavements with respect to critical fatigue damage locations (Darter et al., 2001). The steer-drive axle combinations dominate the critical damage level for this case, while single axles contribute only a relatively small portion to the total damage.

As previously seen from Figure E.7, a -30°F EBITD results in a permanently curled-up slab for the San Francisco Bay Area climate. The crossover from bottom-up to top-down transverse cracking prediction occurs in the -20 to -25°F built-in curl range for this climatic region. Figure E.12 shows the fatigue damage levels for the six climatic regions found in California with increasing built-in curl levels. The absolute fatigue damage levels are minimized between built-in curl levels of -15 and -20°F. At EBITD levels less negative than this range, bottom-up cracking is predominant and the absolute damage level is high. At EBITD levels more negative than this range, the critical damage location results in top-down cracking. Without considering EBITD, predicted linear temperature differentials using the Enhanced Integrated Climatic Model (EICM) model range from -16°F to +21°F for the coastal climates and -23°F to +27°F for the harsher inland California climatic regions, as seen in Table E-3.

EBITD levels of -15 to -20°F tend to minimize the extreme stress-inducing events caused under positive linear temperature gradients which traditionally lead to bottom-up transverse cracking. However, this EBITD range also limits the most extreme stresses at the top of the slab from loading events under linear negative temperature gradients that are typically observed at equivalent temperature differentials greater than -30°F. This results in a minimization of total damage accumulation for the slab in comparison to an EBITD level of 0°F, but a less predictable failure location, as the relative damage levels are similar in several locations along the slab edges.

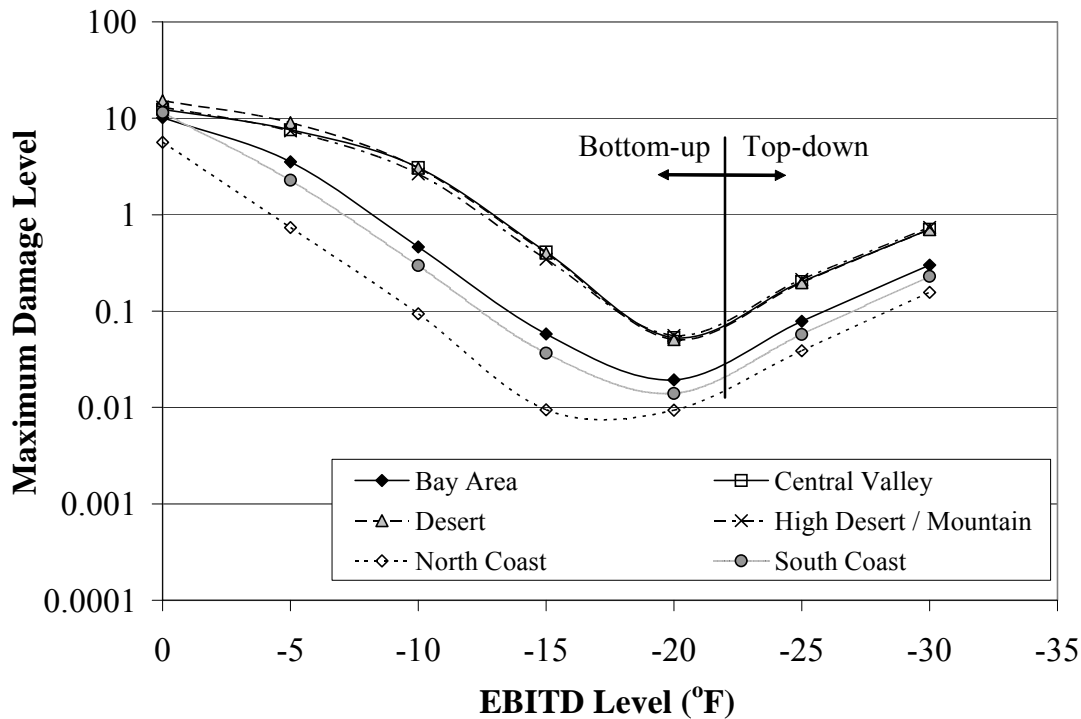


Figure E.12. Maximum damage levels with respect to EBITD magnitudes.

Table E-3. Predicted Temperature Differential Extremes (°F) for California Climatic Regions Using Enhanced Integrated Climatic Model with Daily Maximum and Minimum Temperature Values.

Slab Thickness		8 inches		12 inches	
Climatic Region	Representative Weather Station	Maximum	Minimum	Maximum	Minimum
Bay Area	San Francisco	21.6	-16.4	21.6	-17.1
Central Valley	Sacramento	27.7	-22.5	28.3	-23.4
Desert	Daggett	26.5	-20.9	26.5	-21.6
High Desert/Mountain	Reno, NV	27.4	-23	28.1	-23.8
North Coast	Arcata	16.9	-12.8	17.3	-13.3
South Coast	Los Angeles	19.4	-13.7	19.4	-14.2

### E.2.2 Stress Range Approach

Using the stress range concept without EBITD, the maximum damage location remains at the bottom of the mid-slab edge, just as in the maximum stress analysis. However, the absolute damage level is more than an order of magnitude less, as seen in Figure E.13. This trend also remains true for mean lateral wander distributions of 24-in. and 30-in. at lower negative EBITD levels. Conversely, at highly negative EBITD levels, where the critical damage locations change from bottom-up to top-down cracking, the difference in absolute magnitude of damage grows between the maximum stress and stress range fatigue function.

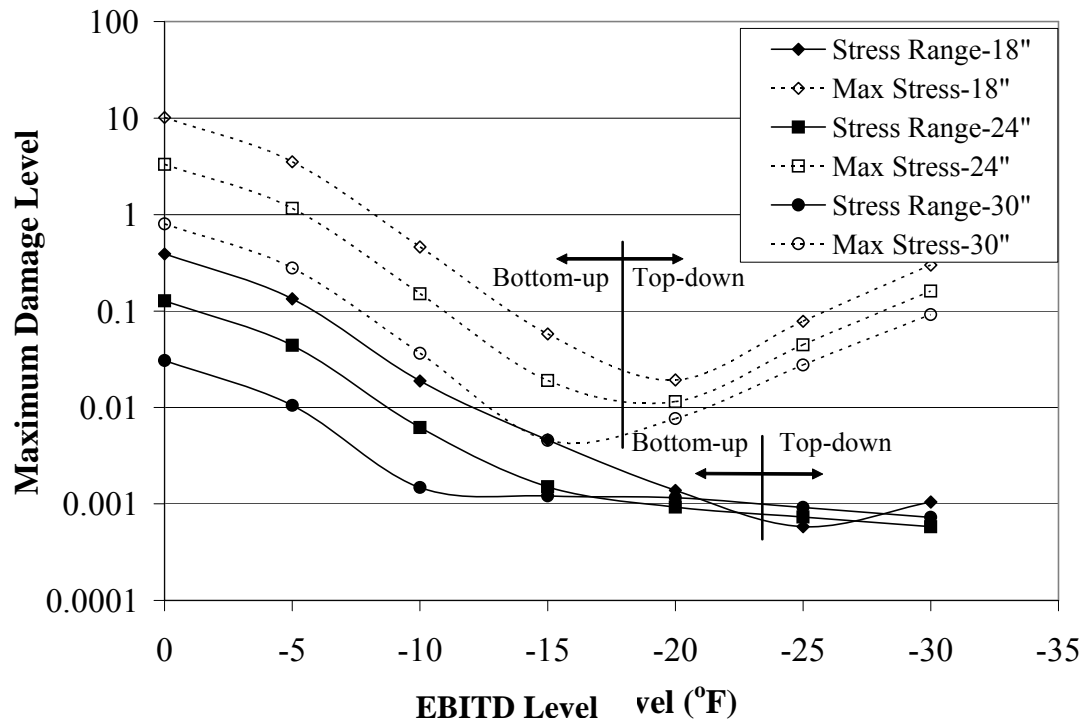


Figure E.13. Maximum damage levels with respect to EBITD and mean wander location (18-, 24-, 30-in.) for San Francisco Bay Area climate.

As the EBITD level becomes more negative, the damage level at the bottom of the mid-slab is decreased as the damage levels at other locations on the top of the slab are increased. These opposing trends allow for the critical damage mechanism to switch from the traditional bottom-up to top-down cracking. These lower levels of damage also contribute to the unpredictability of the critical damage location, as seen in Figure E-14. In this scenario, a  $-30^{\circ}\text{F}$  EBITD in the Bay Area climatic region is analyzed. With the maximum stress analysis, the predominant predicted cracking mechanism was top-down around the mid-slab position (see Figure E.11b). With the stress range concept, the critical damage location is at the top of the slab along the transverse joint. The cumulative damage at the transverse joint is unaffected by axle spacing effects and predicts a longitudinal crack 44 in. from the corner of the slab (between the wheel paths). However, the relative damage level at the top of the slab 64 in. from the corner along the longitudinal edge is 0.95, which suggests that the critical damage location could occur at this location as well, and potentially produce a corner crack. Bottom-up relative damage levels along the transverse joint and longitudinal edge are also high—0.37 and 0.47, respectively. The location of the damage along the top and bottom of the longitudinal edge corresponds well with findings from Hansen et al. (2001), who observed transverse cracking in Tracy, California (Central Valley climatic region) originating closer to the leave side of the transverse joint than the approach side.



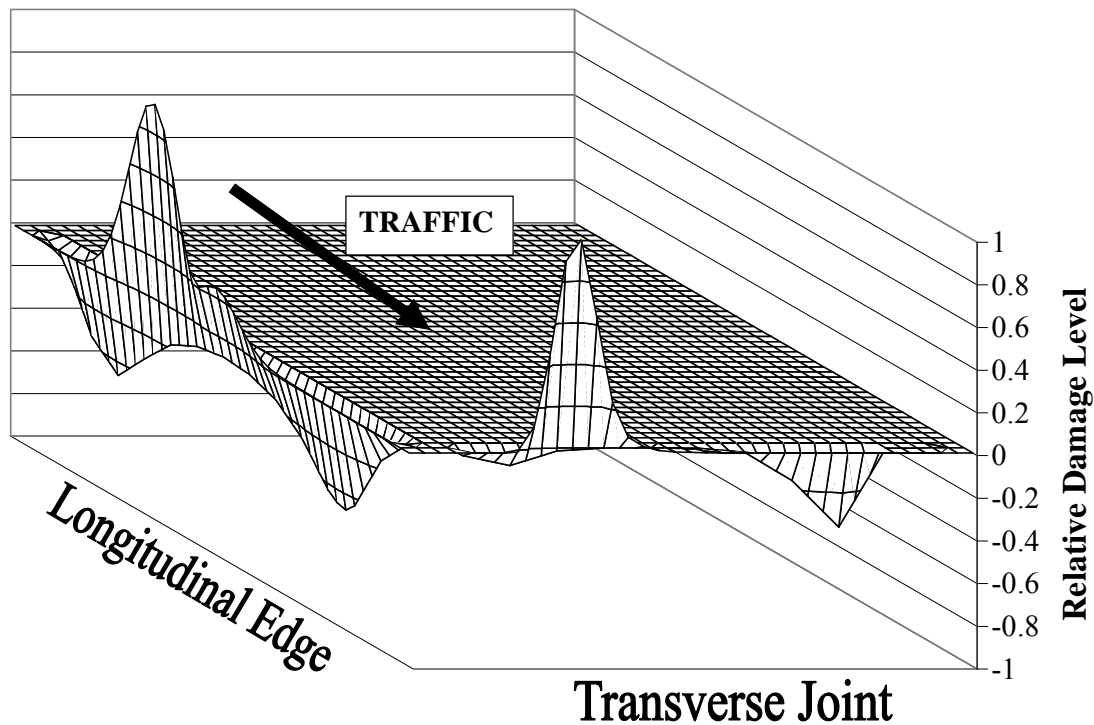


Figure E-14. Relative damage levels using stress range approach along top and bottom of slab with EBITD = -30°F in San Francisco Bay Area.

If the load transfer efficiency across the transverse joint is increased from 20 to 50% under highly negative EBITD levels, the maximum absolute damage level actually increases as the critical damage location changes to the bottom of the longitudinal edge less than 3 ft from the slab corner. Due to this added shear transfer at the transverse joint, the top-down relative damage levels are reduced to roughly 0.2 along both the transverse joint and longitudinal edge. If the load transfer is again increased to 70%, the absolute damage level is slightly increased, while the critical damage location stays the same. The damage levels along the top of the slab become fairly insignificant at the high joint load transfer efficiencies. Thus, if the load transfer efficiency across the transverse joints is at high levels (e.g., dowels), the potential failure locations are limited and more predictable with AC or tied PCC shoulder. This is not necessarily the case when designing concrete pavements with widened slabs, however. With the majority of existing California rigid pavement structures undoweled, the resulting unpredictable load transfer efficiencies across the transverse joints can lead to significant changes in the expected critical damage levels and locations, even within the same design section.

### E.3. Critical Damage Locations

One important goal of this research was to determine where critical damage can occur for California design and climates. Figure E.15 is a demonstration of the critical damage locations found by varying the EBITD level from 0° to -30°F in steps of 5°F, the mean lateral wheel load distribution at 18 in., 24 in., and 30 in., modifying load transfer efficiency, and changing the climatic region. In the asphalt shoulder case, the potential failure zones expand from two to six by using the stress range concept instead of the maximum stress analysis. The stress range concept also leads to potential longitudinal or corner cracking. When using tied shoulders, the potential failure zones expand to four with the stress range approach from the

two determined with the maximum stress analysis. The only top-down cracking mechanism for tied shoulders was found to be transverse cracking near the mid-slab edge from steer-drive axle spacing effects. With widened lanes, the maximum stress analysis actually exhibited more potential failure locations (three) relative to stress range (one).

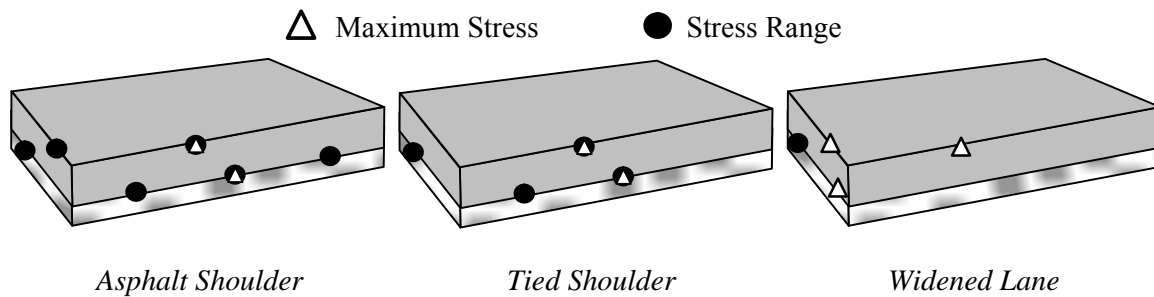


Figure E.15. Potential maximum damage locations using RadiCAL.

#### E.4. Design Parameters Resulting in Alternative Fatigue Failure Modes

Using the analysis described above in RadiCAL, the design parameters that influence the prediction of these alternative fatigue failure modes can be determined. Figure E.16 shows six damage profiles (stress range fatigue function) along the transverse joint and longitudinal edge for a typical 8-in. jointed plain concrete pavement with standard lane width and 15-ft joint spacing in the San Francisco Bay Area. The average load spectra–axle spacing distribution from California weigh-in-motion stations (Lu et al., 2001) was used in this analysis (see Appendix C). A normal distribution for lateral wheel wander was assumed, in addition to the predicted frequency distribution of  $\Delta T$  in the Bay Area found from the Enhanced Integrated Climatic Model (Larson and Dempsey, 1997). These damage profiles assumed low load transfer because the standard design in California for many years was aggregate interlock for load transfer between slabs. In Figure E.16, the only difference between these six damage profiles is the EBITD value. At lower EBITD levels (at 0°, -10°, and -20°F), the critical damage areas result in bottom-up transverse cracking. However, as the EBITD level approaches -30°F, the damage profile transforms to predict the occurrence of fatigue crack initiation at one of (but not necessarily all) multiple failure locations such as:

- top-down transverse cracking (roughly 30 in. from mid-slab point)
- bottom-up transverse cracking (40 in. from the transverse joint)
- top-down longitudinal cracking (44 in. from the shoulder corner between the wheels of an axle at the transverse joint)
- bottom-up longitudinal cracking (32 in. from the adjacent slab corner under the wheels of an axle placed at the transverse joint).

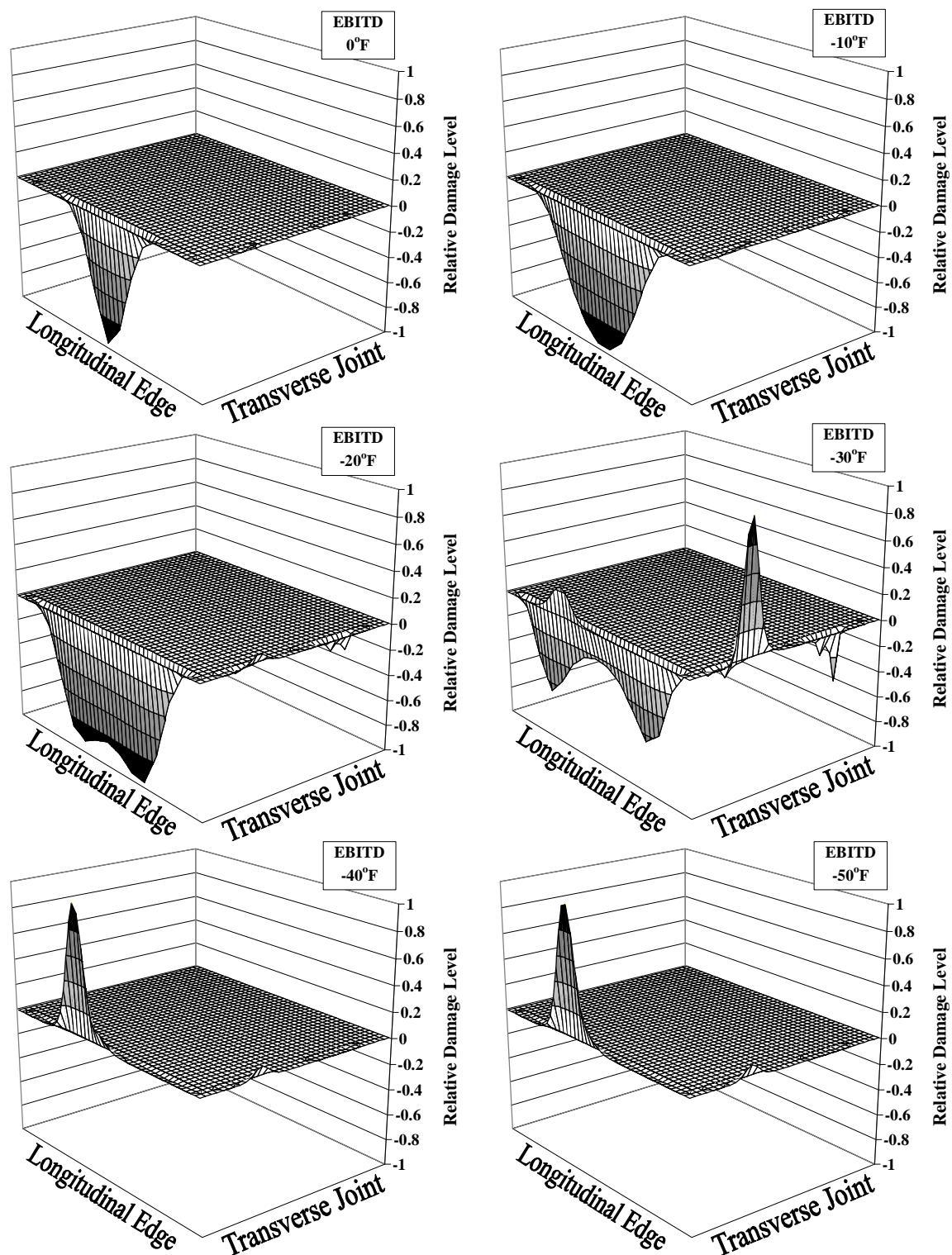


Figure E.16. Relative edge damage levels using stress range approach with variable EBITD under low load transfer (20% or undoweled) and 15-ft joint spacing in San Francisco Bay Area.

As the EBITD becomes even more negative, the primary fatigue failure mode becomes top-down transverse cracking (again within 30 in. of mid-slab) as the stresses from interaction between the steer-drive axle spacing and the slab lift-off becomes dominant. The location of

this top-down transverse cracking failure mode agrees well with the findings of the NCHRP 1-37A project (ARA, 2007).

Many California pavements have been designed with a random skewed joint spacing concept (12-, 13-, 19-, and 18-ft pattern) to reduce the effects of vehicle dynamics from the man-made joints. California's and many other transportation agencies are also constructing short joint spacing sections to promote lower curling stresses and achieve long-life designs. Thus, it is important to find the effects of this shorter joint spacing design approach on predicted fatigue performance. Figure E.17 shows the damage profiles for the same inputs as described for Figure E.16, except that the joint spacing shown is 12 ft instead of 15 ft. Just as with the 15-ft sections, RadiCAL predicts bottom-up transverse cracking at the lower EBITD levels and a transition towards alternative fatigue failure modes as this value approaches  $-30^{\circ}\text{F}$ . However, due to the reduced joint spacing, the top-down transverse cracking failure mode does not develop at large EBITD levels. Instead, top-down longitudinal cracking between the wheels of the axles becomes the predominant failure mode due to the unsupported corners as a result of the permanent curl. At EBITD levels less than  $-30^{\circ}\text{F}$ , the slabs will still be curled up (negative effective  $\Delta T$ ), even at the highest positive  $\Delta T$  expected.

When the long-term load transfer is improved by dowelling, the predicted damage profiles using RadiCAL do change. Figure E.18 looks at the effect of higher load transfer (70%) for the 15-ft joint spacing cases presented in Figure E.16. At the low levels of EBITD, the damage profiles mirror those with the low load transfer (20%) from Figure E.16. However, at  $-30^{\circ}\text{F}$  EBITD, reduced stresses from the load transfer across the transverse joint do not result in major fatigue damage accumulation which would produce longitudinal cracking. Instead, bottom-up transverse cracking from heavily loaded single axles that push the concave slab into contact with the base within 3 ft of the corner control the fatigue damage. At the larger levels of EBITD, the top-down transverse cracking mechanisms from steer-drive axle spacing effects tend to dominate. While these damage profiles were developed for the Bay Area climatic region, the general trends described above are applicable for all climatic regions in California, with some variance between the more extreme and temperate climates.

When adding dowels to the 12-ft joint spacing cases with asphalt shoulders, as seen in Figure E-19, the trends are different from the undoweled 12-ft slab length case from Figure E.17. Just as with the doweled case with 15-ft joint spacing, the fatigue damage at the transverse joint is severely limited. One difference in this case, however, is that very little top-down damage ensues due to the short joint spacing and interaction with the steer-drive axle spacing distribution. Instead, bottom-up transverse cracking is moved further away from the mid-slab location as EBITD becomes more severe, and instead, is located mid-way between the mid-slab edge and the corner of the slab.

It should be noted that with the added load transfer from dowel bars, added restraint is placed on the slab which limits the EBITD levels (Rao and Roesler, 2003). Therefore, extreme levels of EBITD ( $<-30^{\circ}\text{F}$ ) may not be possible with adequate load transfer. For interstate and state highways, most agencies use load transfer devices which should minimize the occurrence of alternative failure modes using asphalt shoulders with lower built-in curl levels. However, on lower volume roads where aggregate interlock is the sole method of load transfer between slabs, high EBITD levels and their resulting alternative failure modes are quite possible. This effect is exacerbated by the thinner slabs that are typically designed in these situations, as well.

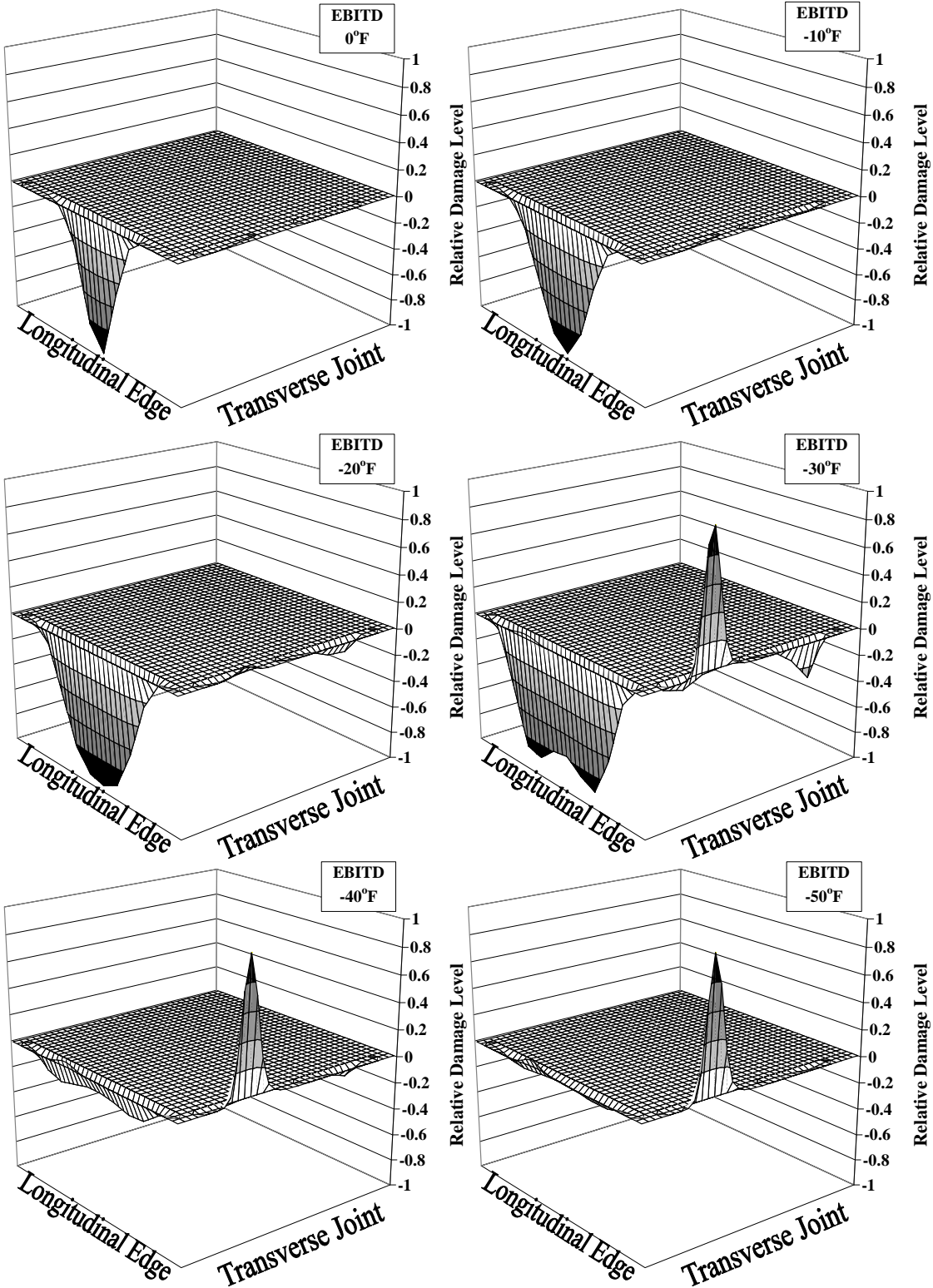


Figure E.17. Relative edge damage levels using stress range approach with variable EBITD under low load transfer (20% or undoweled) and 12-ft joint spacing in San Francisco Bay Area.



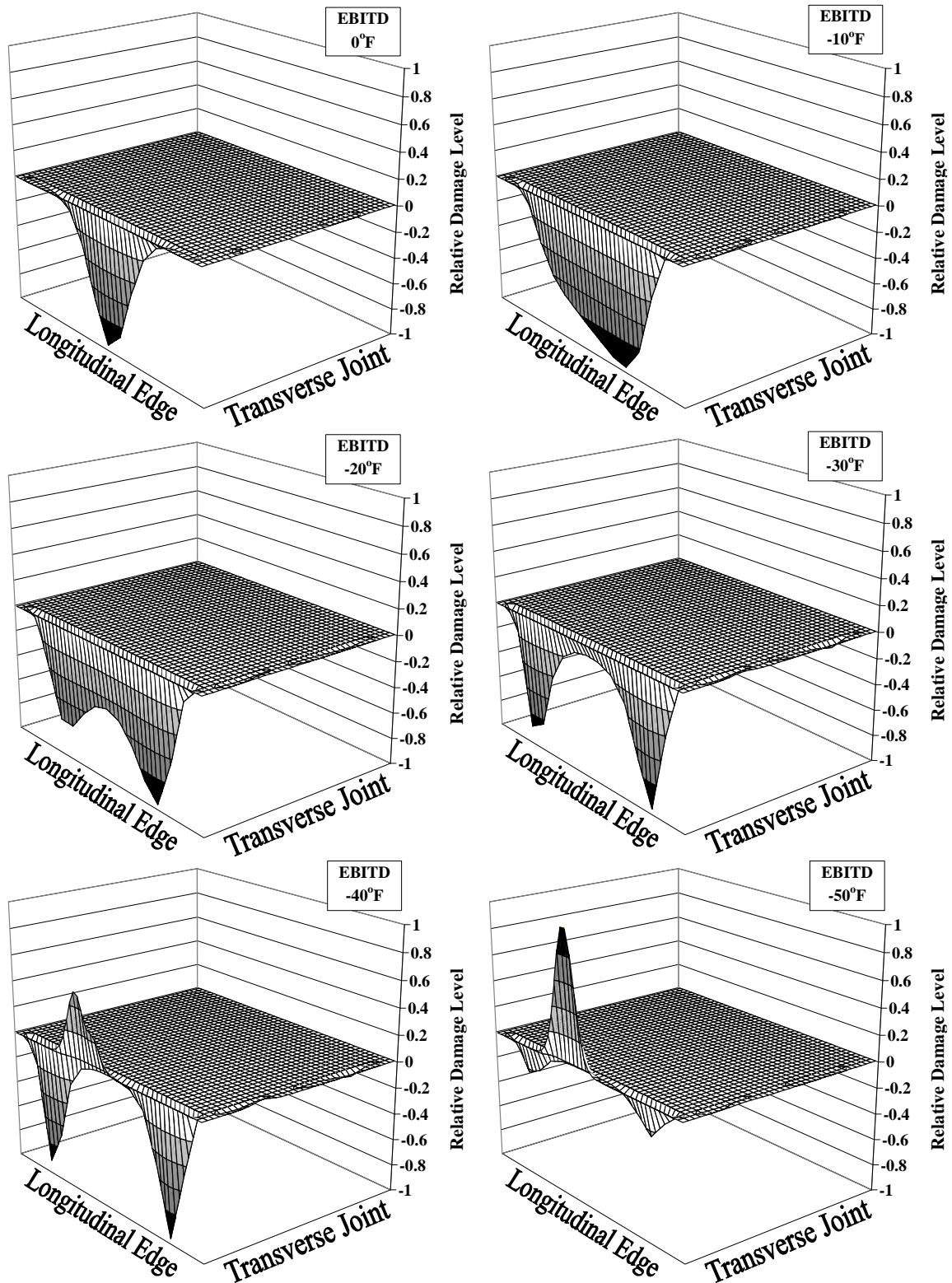


Figure E.18. Relative edge damage levels using stress range approach with variable EBITD under moderate load transfer (70% or doweled) and 15-ft joint spacing in San Francisco Bay Area.

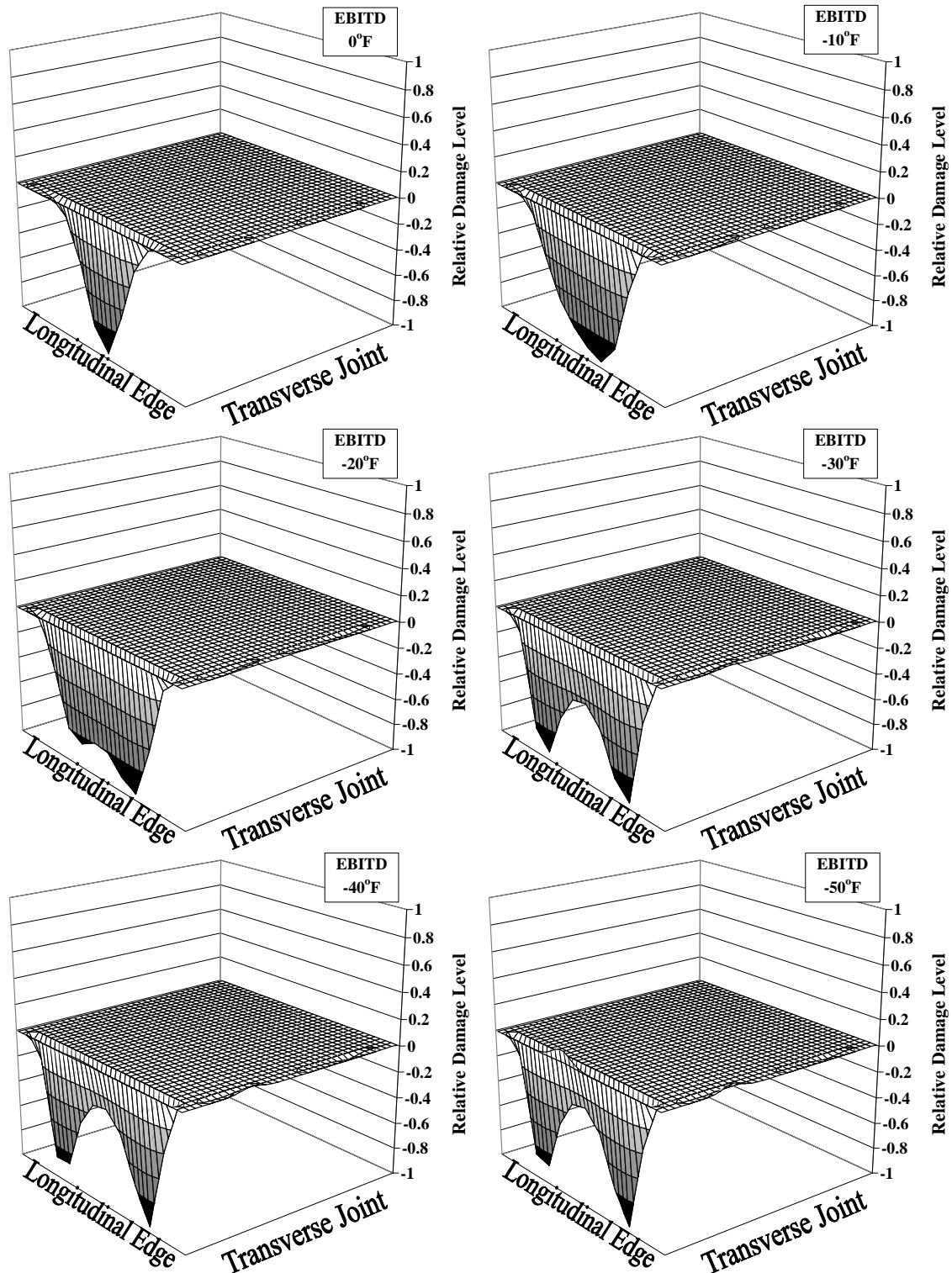


Figure E-19. Relative edge damage levels using stress range approach with variable EBITD under low load transfer (70% or doveled) and 12-ft joint spacing in San Francisco Bay Area.

### **E.5. Conclusions of Initial Mechanistic-Empirical Damage Study**

The design of rigid pavements has traditionally focused on mitigating fatigue cracking at the mid-slab edge. With the advances in characterizing built-in slab curling and proper modeling of steer-drive axle spacing effect, the location of maximum fatigue damage and subsequent cracking mode cannot easily be ascertained without a detailed analysis.

An influence line analysis using an existing finite element program was completed to model an axle or set of axles passing over a slab for a range of input parameters. The maximum and minimum stress levels at nodes along the longitudinal and transverse edges were recorded. A mechanistic analysis program was developed to predict these nodal stresses and complete a cumulative fatigue damage analysis based on Miner's hypothesis. The input parameters such as effective built-in temperature difference, stress range, shoulder type, joint type, and wander, as well as vehicle load and configuration, highly influenced the critical damage location and magnitude.

When employing a maximum stress concept in a fatigue transfer function, the inclusion of steer-drive axle spacing in combination with highly negative EBITD levels resulted in top-down, transverse cracking typically within 2 ft of mid-slab. This occurred when using asphalt or tied shoulders, although the absolute damage level benefited from the use of a tied shoulder. Heavy single-axle loads dominated fatigue damage at the bottom of the longitudinal edge, while the number of cumulative axles passing affected the fatigue damage at the transverse joint.

The stress range concept incorporates both the maximum and minimum stress level into the fatigue damage accumulation process, with the residual stresses generated from built-in and cyclical temperature differences assigned to the minimum stress level. The addition of EBITD level, axle spacing, lateral wander distribution, and changing load transfer levels to the stress range damage accumulation concept had a dramatic effect on the predicted fatigue failure levels and locations. Without using stress range, critical fatigue damage locations are typical to those of existing procedures from this limited study. However, using stress range more accurately portrays the multiple fatigue failure locations observed on existing California rigid pavements such as longitudinal, corner, and transverse cracking, which can initiate at the top or bottom of the slab. Due to the lower level of EBITD measured in Illinois, these alternative cracking locations are less likely to occur and for now, the maximum stress concept should be sufficient.



## APPENDIX F. NONLINEAR TEMPERATURE EFFECTS ON CONCRETE PAVEMENT SLAB RESPONSE

### F.1. Introduction

Since Westergaard's solution for temperature curling (1927) and the subsequent graphical solution for curling stresses (Bradbury, 1938), the assumption of a linear temperature change through the depth of the slab has been standard. As early as the 1930's, it was reported that actual temperature profiles through the slab thickness were highly nonlinear (Teller and Sutherland, 1935). With regard to the measured magnitude of the resultant stresses from temperature, Teller and Sutherland also noted that "stresses arising from restrained temperature warping are equal in importance to those produced by the heaviest legal wheel loads." Subsequent researchers have also noted the observed nonlinearity of the temperature profile on concrete slabs (Mirambell, 1990; Choubane and Tia, 1992, 1995; Harik et al., 1994; Mohamed and Hansen, 1997; Masad et al., 1996; Ioannides and Salsilli-Murua, 1999; Lee and Darter, 1993).

The first researcher to address the issue of stress development due to nonlinear temperature profile was Thomlinson in 1940. He proposed subdividing stresses due to the total nonlinear temperature profile into three parts (Figure F.1):

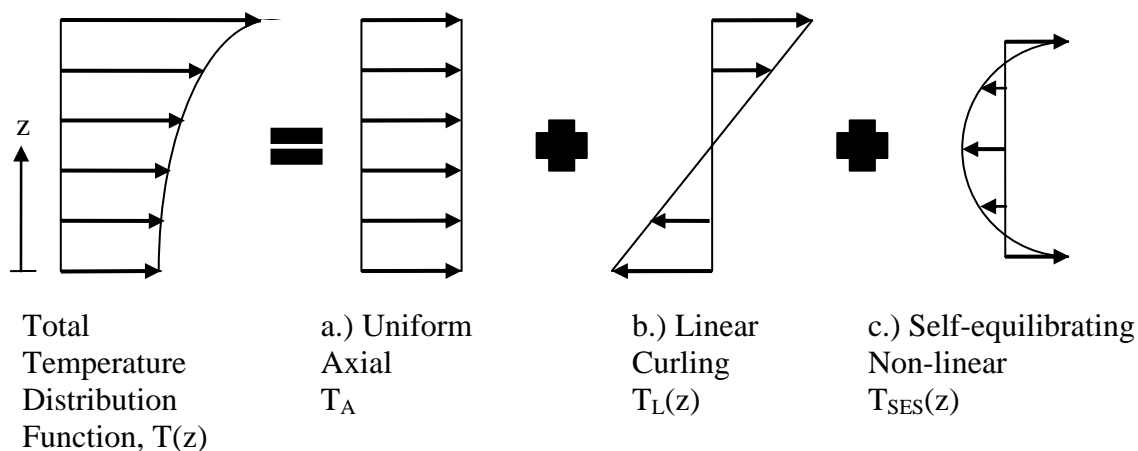


Figure F.1. Stress components due to nonlinear temperature profile.

The axial strain component (a) of the total temperature profile is that which is caused by uniform temperature changes, and results in either an expansion or contraction of the slab evenly through the thickness. Resistance to movement from underlying layers and neighboring slabs could generate stresses in the slab as a result of this uniform temperature profile. However, this restraint is generally assumed to be minimal, and therefore, this axial strain would not result in significant slab stresses and is generally ignored. However, at early concrete ages this assumption is not valid.

Component (b) is the equivalent linear bending strain derived from the nonlinear temperature profile by assuming that the slab is fully restrained or if there is significant slab self-weight. The equivalent linear bending strain can be quantified as an equivalent linear temperature difference. This equivalent linear temperature difference produces the same moment (stress) as the resultant total temperature profile minus the uniform temperature profile. Load-induced bending stresses also assume a linear stress profile in the medium-thick plate theory. According to Westergaard (1927), the maximum tensile stress in a concrete slab at the interior of the slab is traditionally defined as:

$$\sigma = \frac{E\alpha\Delta T}{2(1-\mu)} \quad (F-1)$$

where:

$E$  = modulus of elasticity of the concrete;  
 $\alpha$  = coefficient of thermal expansion of the concrete;  
 $\Delta T$  = linear temperature difference from top to bottom of slab; and  
 $\mu$  = Poisson's ratio of concrete

As this Westergaard solution is for an infinitely long slab, Bradbury (1938) implemented a correction factor to the Westergaard solution for slabs of finite dimensions. The tensile stress in a concrete slab then becomes

$$\sigma = \frac{E\alpha\Delta T}{2(1-\mu^2)}(C_1 + \mu C_2) \quad (F-2)$$

where:

$C_1$  = Bradbury coefficient in the direction under investigation; and  
 $C_2$  = Bradbury coefficient in the perpendicular direction.

When the slab is square  $C_1 = C_2 = C$ , the tensile stress simplifies to

$$\sigma = \frac{CE\alpha\Delta T}{2(1-\mu)} \quad (F-3)$$

where  $C$ , the Bradbury coefficient, can be written as

$$C = 1 - \frac{2 \cos \lambda \cosh \lambda (\tan \lambda + \tanh \lambda)}{\sin 2\lambda + \sinh 2\lambda} \quad (F-4)$$

where:

$$\lambda = \frac{L}{\ell\sqrt{8}} \quad (F-5)$$

and where:

$L$  = free length or width of the slab; and  
 $\ell$  = radius of relative stiffness

The radius of relative stiffness is then defined as:

$$\ell = \sqrt[4]{\frac{Eh^3}{12(1-\mu^2)k}} \quad (F-6)$$

where:

$h$  = depth of the concrete slab;  
 $E$  = modulus of elasticity of the concrete; and  
 $k$  = modulus of subgrade reaction

The final component (c) is the nonlinear self-equilibrating internal strains such that all forces and bending moments due to this component of the nonlinear temperature profile are self-balancing. While this nonlinear component will affect both the compressive and tensile strains in the slab at different depths, it does not affect the deflection profile of the slab (Ioannides and Khazanovich, 1998). It is this nonlinear stress component that routinely goes unaccounted for in stress prediction of concrete slabs. It is also very difficult to validate the magnitude of this stress component.

The strain-causing components of the true temperature profile can be expressed as the following individual temperature components as seen in Equation F-7.

$$T(z) = T_A + T_L(z) + T_{SES}(z) \quad (F-7)$$

where:

$T(z)$  = total temperature profile as a function of depth;  
 $T_A$  = axial temperature component;  
 $T_L(z)$  = linear temperature component as a function of depth; and  
 $T_{SES}(z)$  = nonlinear (self-equilibrating) temperature component as a function of depth

The shape of the temperature profile can be expressed as a polynomial function. The polynomial can be expressed to the order  $(n-1)$ , where  $n$  represents the discrete number of temperatures used to approximate the continuous temperature function.

## F.2. Quadratic Temperature Profile Method

While some researchers (e.g., Mohamad and Hansen, 1997; Jeong and Zollinger, 2005) have used a third-order polynomial to represent actual temperature profiles in concrete pavements, this complicates the interaction between the linear temperature stresses and the self-equilibrating stresses from the nonlinear temperature component. To properly use a third-order or higher polynomial to express the temperature-induced strains, one would need to determine an equivalent temperature difference ( $\Delta T_{eq}$ ) which is not equal to the actual  $\Delta T$ . The equivalent temperature difference can be derived through the use of a temperature moment concept (Janssen and Snyder, 2000), which is discussed later in this chapter.

Ioannides and Khazanovich (1998) note that if only a second-order polynomial is used to express the temperature profile, the actual difference in temperatures between the top and bottom of the slab ( $\Delta T$ ) is the only component that contributes to the linear bending strains in a concrete slab. Therefore, concrete slabs with either a linear or nonlinear (quadratic) temperature profile would have identical bending moments and deflection profiles, although the total stresses would be quite different due to effects of the nonlinear self-equilibrating stresses.

Choubane and Tia (1995) showed that many temperature profiles can be captured well by assuming this quadratic function of temperature through the depth of the slab. The quadratic temperature function can be expressed mathematically using Equation F-8.

$$T(z) = A + Bz + Cz^2 \quad (F-8)$$

where  $A$ ,  $B$ , and  $C$  are regression coefficients based on the measured slab temperature profile,  $z$  is the location from the bottom of the slab, and the temperature profile consists of the three strain-causing components discussed previously.

For the conditions defined in Figure F.2, given the temperatures at the top, middle, and bottom of the slab, the coefficients for quadratic temperature function presented in Equation F-8 can be derived as the following:

$$A = T_{bot} \quad (F-9)$$

$$B = \frac{4T_{mid} - 3T_{bot} - T_{top}}{h} \quad (F-10)$$

$$C = \frac{2(T_{bot} + T_{top} - 2T_{mid})}{h^2} \quad (F-11)$$

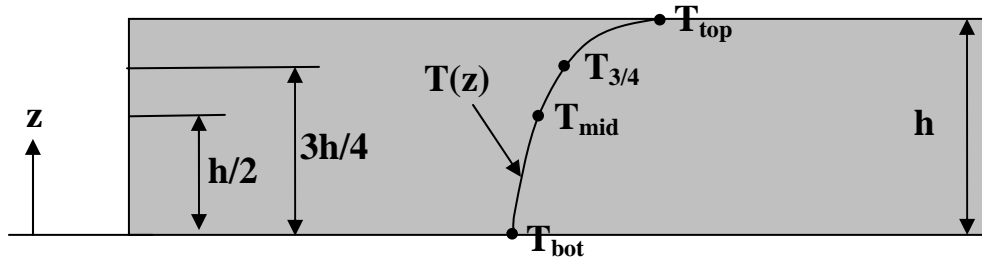


Figure F.2. Definition of terms for determination of quadratic temperature profile coefficients.

While the temperatures at the top, middle, and bottom of the slab were used in determining Equations F-9 through F-11, any three discrete temperatures through the depth of the slab could be used to characterize a continuous quadratic expression. In the vast majority of actual temperature profiles, the greatest change in measured temperature through the depth of the slab occurs within the top few inches of the slab due to the high impact of solar radiation, air temperature, and wind on the pavement surface temperature. This is true for both positive gradients in the daytime, as well as negative gradients in the nighttime. Thus, a quadratic expression that uses both the top and bottom temperatures of the temperature profile, in addition to a temperature at  $z = 3h/4$  ( $T_{3/4}$  as defined from Figure F.2), may better capture the nonlinearity of the total temperature profile. When doing this, the coefficients expressed in Equations F-9 through F-11 can be rewritten as seen in Equations F-12 through F-14.

$$A^* = T_{bot} \quad (F-12)$$

$$B^* = \frac{16T_{3/4} - 7T_{bot} - 9T_{top}}{3h} \quad (F-13)$$

$$C^* = \frac{4(T_{bot} + 3T_{top} - 4T_{3/4})}{3h^2} \quad (F-14)$$

The formulation for calculating the total curling stresses based on the axial, linear, and nonlinear components has been developed and presented by many researchers (Choubane and Tia, 1995; Mohamad and Hansen, 1997; Ioannides and Khazanovich, 1998; Rodden, 2006). The closed-form equations developed are presented herein to tie the determination of the quadratic temperature profile coefficients to the three components of temperature stress in concrete pavements.

Using the quadratic temperature profile  $T(z)$  from Equation F-8, the total stress  $\sigma_{T(z)}$  due to this temperature profile can be calculated as the following:

$$\sigma_{T(z)} = \frac{E\alpha T(z)}{1-\mu} \quad (\text{F-15})$$

The average axial stress can then be calculated as:

$$\bar{\sigma}_A = \frac{1}{h} \int_0^h \frac{E\alpha T(z)}{1-\mu} dz \quad (\text{F-16})$$

Substituting the relationship for  $T(z)$  and integrating gives a relationship between the quadratic coefficients and the average axial stress in the concrete slab as seen in Equation F-17.

$$\bar{\sigma}_A = \frac{E\alpha}{1-\mu} \left[ A + \frac{Bh}{2} + \frac{Ch^2}{3} \right] \quad (\text{F-17})$$

The next step is to solve for the equivalent linear moment that gives the difference between the total and average axial stress as defined below:

$$M_L = \int_0^h \left( \sigma_T - \bar{\sigma}_A \right) z dz = \frac{E\alpha}{1-\mu} \int_0^h \left[ \left( A + Bz + Cz^2 \right) - \left( A + \frac{Bh}{2} + \frac{Ch^2}{3} \right) \right] z dz \quad (\text{F-18})$$

Integrating over the depth of the slab gives the relationship in Equation F-19.

$$M_L = \frac{E\alpha}{1-\mu} \left( \frac{Bh^3}{12} + \frac{Ch^4}{12} \right) \quad (\text{F-19})$$

The equivalent linear stress component of the temperature can now be solved as follows:

$$\sigma_L = \frac{M_L}{I} = \frac{M_L \left( z - \frac{h}{2} \right)}{\frac{bh^3}{12}} = \frac{E\alpha}{1-\mu} \left[ B \left( z - \frac{h}{2} \right) + Ch \left( z - \frac{h}{2} \right) \right] \quad (\text{F-20})$$

When applying the set of coefficients from Equations F-9 through F-11 or F-12 through F-14 to the resulting relationship in Equation F-20, the equation matches the Westergaard solution seen in Equation F-3 for an infinite slab. This proves that the equivalent linear moment for a nonlinear temperature profile using a second-order polynomial matches that of one with an assumed linear temperature profile. However, this is not true for higher-order polynomials.

To find the self-equilibrating stress due to the nonlinearity in the temperature profile, the linear and average axial stress functions must be subtracted from the total temperature stress function, as seen in Equation F-21.

$$\sigma_{SES} = \sigma_T - \left( \sigma_L - \bar{\sigma}_A \right) \quad (\text{F-21})$$

Substituting Equations F-15, F-17, and F-20 into Equation F-21 yields a relationship between the quadratic temperature profile coefficients and the self-equilibrating axial stresses to compensate for the nonlinearity in the temperature profile with depth.

$$\sigma_{SES} = C \frac{E\alpha}{1-\mu} \left[ z^2 - hz + \frac{h^2}{6} \right] \quad (F-22)$$

It is important to note that this self-equilibrating component due to the nonlinear temperature profile does not cause bending or expansion of the slab, but is only due to thermal strains that distort the pavement cross-section (Khazanovich 1994).

### F.2.1 Example of Self-Equilibrating Stress Calculation using Quadratic Profile Function

Figure F.3 shows an example of a typical extreme daytime and nighttime temperature profile from the Enhanced Integrated Climatic Model, EICM (Larson and Dempsey, 1997). The predicted temperature profile data is for an 8-in. concrete slab in Los Angeles, California and the slab's temperature difference is also noted in Figure F.3.

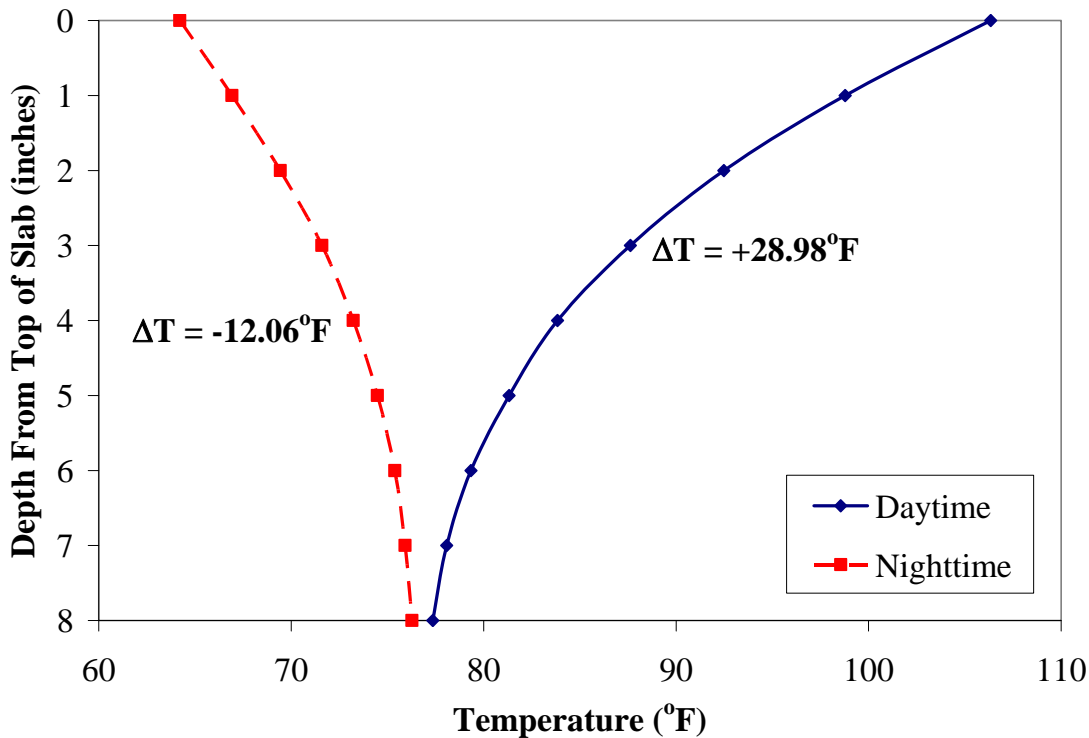


Figure F.3. Typical daytime and nighttime temperature profiles for Los Angeles, California.

Figure F.4 shows the change in stress distribution at the interior of the slab for the daytime temperature profile shown in Figure F.3 for a linear to nonlinear temperature profile assumption. The nonlinear profile used a quadratic assumption with temperature data taken from the top, bottom, and middle of the slab. This nonlinearity at the top of the slab is compensated for by adding compressive stresses near the top and bottom of the slab (a maximum of 125.6 psi at both the top and bottom of the slab), while adding tensile stresses in the middle portion of the slab. The added compressive stress at the top of the slab during the

daytime places the top of the slab in further compression. As concrete has excellent compressive strength properties, this additional compressive stress is negligible in fatigue of the slab. However, this 125.6-psi compressive stress addition to the bottom of the slab reduces the temperature stress from 341 psi to 215 psi. Using the temperatures at the bottom, three-quarters of the depth, and top of the slab would yield a maximum axial compressive stress component of 138.4 psi, reducing the tensile stress at the bottom of the slab even more. Regardless of the quadratic assumption methods used, the use of the nonlinear temperature profile would increase the predicted bottom-up fatigue cracking life.

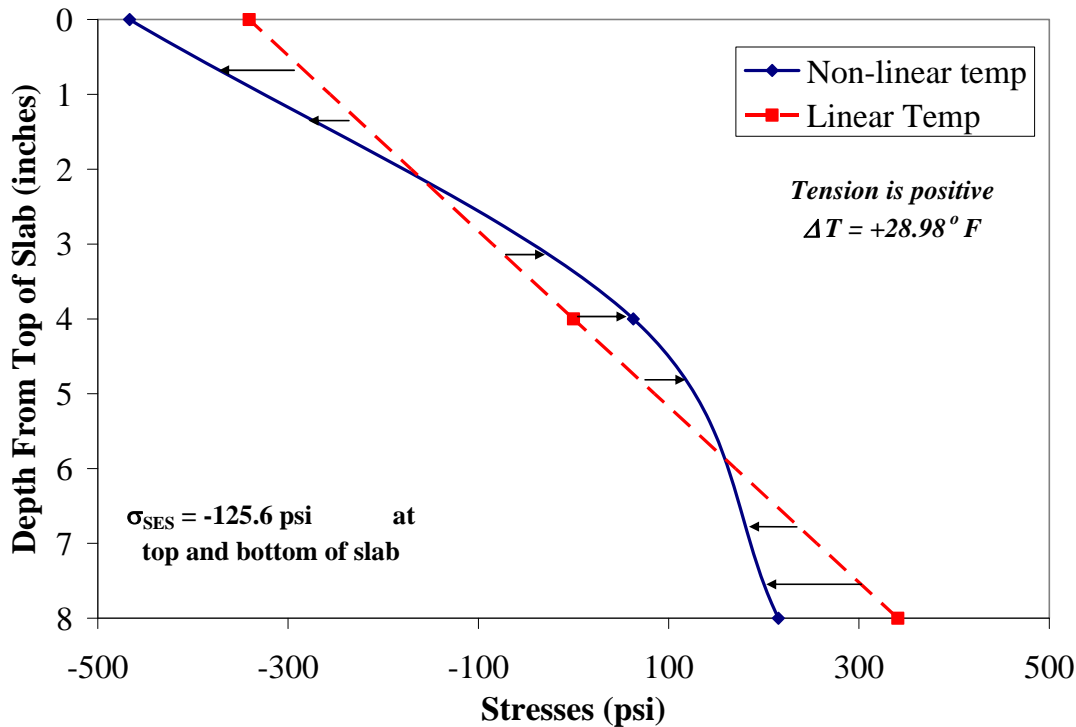


Figure F.4. Temperature stresses for nonlinear and linear profile assumptions for typical daytime Los Angeles, California temperature profile.

Conversely, Figure F.5 shows the effect of using nighttime nonlinear temperature profiles on temperatures stresses in the same slab. Using the nighttime nonlinear temperature profile from Figure F.3, tensile stresses are added at the top and bottom of the slab to the bending stresses found from the linear temperature assumption. In this case, the bottom of the slab was under compression (142 psi) and this stress in tension reduced the compression in the slab by 46.6 psi to a level of 95 psi in compression, assuming the quadratic profile assumption with the top, bottom, and middle slab temperatures. The top of the slab was previously assumed to be in tension at 142 psi under the linear temperature profile assumption. With the addition of the self-balancing stresses, the top of the slab undergoes a larger tensile stress of 188 psi. Using the temperatures at the top, one-quarter of depth, and bottom of the slab for the quadratic profile assumption yields a maximum tensile stress at the top and bottom of approximately 46.1 psi for the self-equilibrating stress. Nevertheless, this increase in tensile stress at the top of the slab should lead to a decrease in fatigue life for cracks that propagate

from the top down.

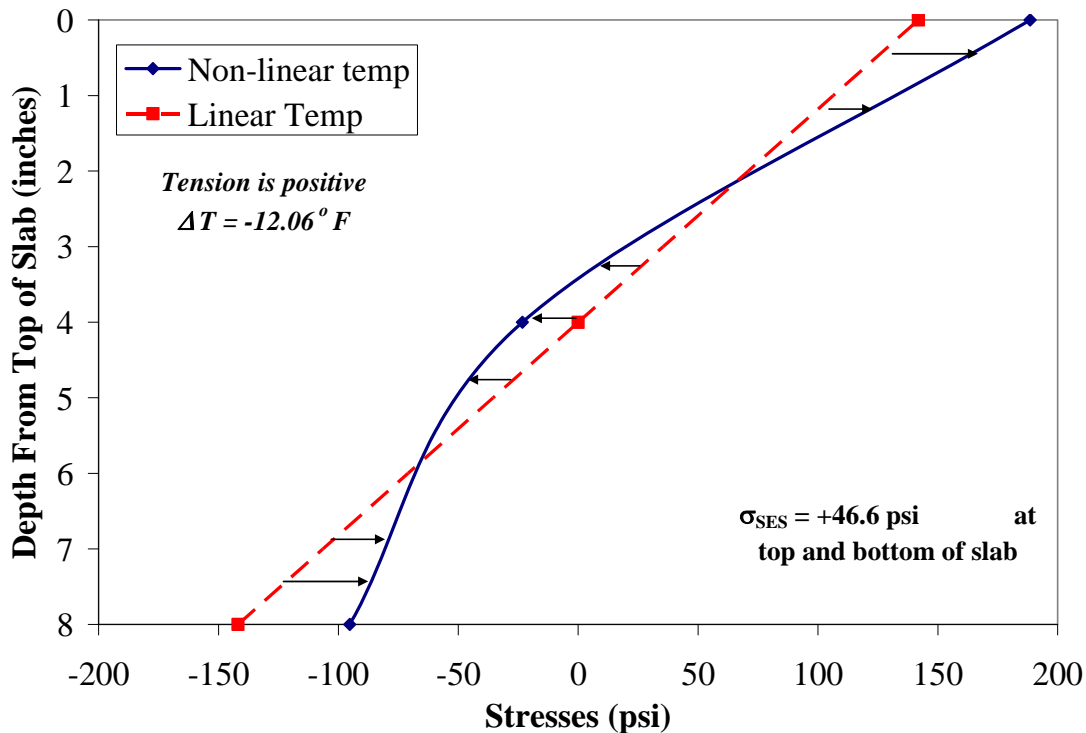


Figure F.5. Temperature stresses for nonlinear and linear profile assumptions for typical nighttime Los Angeles, California temperature profile.

### F.3. NOLA Concept

Since the use of nonlinear temperature profiles will likely have a significant impact on stress development and subsequent fatigue life predictions in concrete pavement slabs, a method for accounting for these self-equilibrating stresses is needed to assess predicted fatigue damage development using the RadiCAL software (Hiller and Roesler, 2005b). The consideration of nonlinear temperature distribution and built-in curling in the MEPDG (ARA, 2007) has resulted in a significant prediction of top-down fatigue cracking produced by the design software as confirmed through several cases run for the state of Illinois.

While nonlinear temperature stresses are accounted for in the MEPDG software, there are some limitations to the methodology employed. The MEPDG allows for the total stresses due to load and a nonlinear temperature profile to be correctly predicted, but only at five locations of interest (one at the bottom of the slab and four on the top of the slab along the longitudinal edge). However, since RadiCAL predicts stresses and calculates fatigue damage at up to 178 nodal locations at both the top and bottom of the slab, a generalized scheme to account for self-equilibrating stresses from the nonlinear portion of the temperature profile, in addition to load and temperature bending stresses, is required.

One such way to accomplish this is to develop a parameter to capture the level of nonlinearity in any given temperature profile that can be directly related to the self-equilibrating stresses. This allows for post-processing of finite element cases that have been conducted using a combined linear temperature difference and external load analysis. These self-equilibrating stresses can then be added or subtracted from the load and linear temperature cases at individual nodes to capture the effect of nonlinear temperature on fatigue damage development using RadiCAL.



To do this, a parameter named NOLA (NOnLinear Area) was developed. NOLA can be defined as the area between the actual temperature profile and a linear temperature assumption (using the top and bottom temperatures) on a plot of temperature and depth of the slab. It can also be defined as the difference between the average temperature stress and the linear temperature profile assumption. Mathematically, it can be expressed as seen in Equation F-23 where  $z = 0$  is the bottom of the slab.

$$NOLA = \int_0^h [T(z) - T_{linear}(z)] dz \quad (F-23)$$

where:

$T(z)$	=	Actual temperature profile function
$T_{linear}(z)$	=	Linear assumption temperature profile function ( $= \Delta Tz/h$ )
$h$	=	depth of the concrete slab

If the temperature profile is truly linear or uniform, then the NOLA term would indicate a value of zero, which means no internal self-equilibrating stresses are present. The NOLA term has a maximum value of  $\pm 1/2h\Delta T$  except in extremely rare instances.

Using the example temperature profiles from Figure F.3, the NOLA values can be calculated using a trapezoidal method of integration to be  $+41.5^\circ\text{F}\cdot\text{in.}$  and  $-15.2^\circ\text{F}\cdot\text{in.}$  for the positive and negative temperature profiles, respectively, as seen in Figure F.6. The positive NOLA would lead to a compressive stress at the top and bottom of the slab added to the stress found using linear temperature gradients, while a negative NOLA value would conversely add a self-equilibrating tensile stress at the top and bottom of the slab.

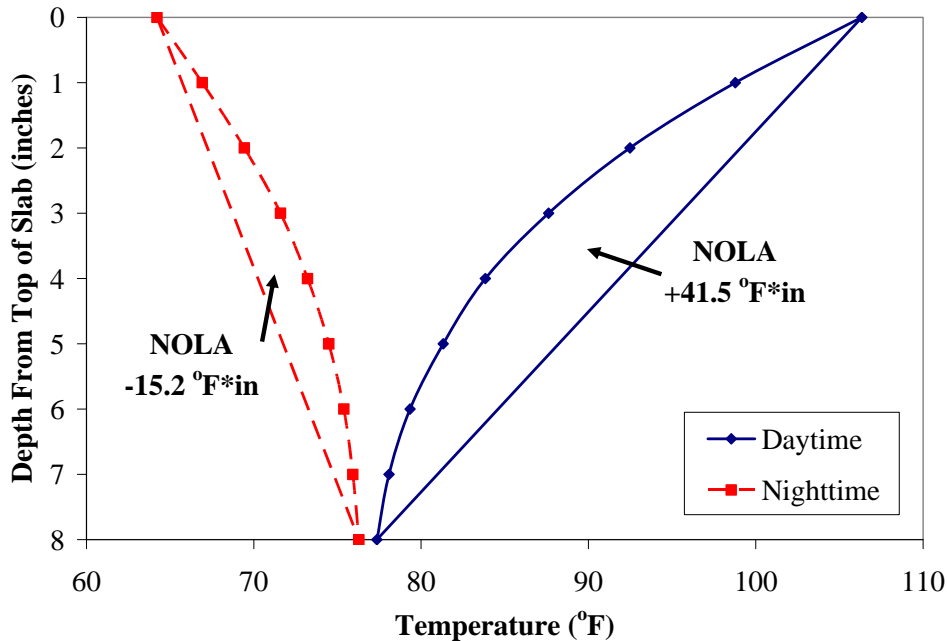


Figure F.6. Graphical representation of NOLA for two typical temperature profiles.

Using the derived coefficients to satisfy Equation F-8 using the temperatures at the top, middle, and bottom of the slab (Equations F-9 through F-11), the derivation of NOLA from Equation F-23 can be written as seen below for a quadratic temperature distribution. In this

equation, all temperatures are relative to the temperature at the bottom of the slab, thereby making the temperature at the top of the slab equal to  $\Delta T$ .

$$NOLA = \int_0^h \left[ \frac{4T_{mid} - \Delta T}{h} z + \frac{2\Delta T - 4T_{mid}}{h^2} z^2 - \frac{\Delta T}{h} z \right] dz \quad (F-24)$$

Integrating and evaluating the limits in Equation F-24 results in the NOLA term being directly related to  $\Delta T$  and a second relative temperature as seen in Equation F-25. Conducting the same formulation using the coefficients from Equations F-12 through F-14 for the top, three-quarters of slab depth, and bottom temperatures will result in a similar relationship as seen in Equation F-26.

$$NOLA_{mid} = \frac{2T_{mid} - \Delta T}{3} h \quad (F-25)$$

$$NOLA_{3/4} = \frac{8T_{3/4} - 6\Delta T}{9} h \quad (F-26)$$

where:

$\Delta T$	=	actual temperature difference from top to bottom of slab;
$T_{mid}$	=	temperature at middle of slab depth; and
$T_{3/4}$	=	temperature at one-quarter of the depth from top of slab.

To characterize the level of temperature nonlinearity expected, 30 years of hourly weather data from six weather stations across California and Nevada (Arcata, Daggett, Los Angeles, Reno, Sacramento, and San Francisco) were used in the EICM model to predict nonlinear temperature profiles to represent the seven climatic regions in California as seen in Figure F.7. Three of the weather stations represent more temperate weather influenced by the Pacific Ocean (Arcata, San Francisco, and Los Angeles), while the other three weather stations (Daggett, Reno, and Sacramento) have more extreme temperature swings on a daily basis and are protected from direct temperature influence of the ocean by mountain ranges and elevation differences.



Figure F.7. Locations of representative California weather stations.

While the NOLA value allows the level of nonlinearity to be expressed in a single variable with the assumption of a quadratic temperature profile, it is not a unique parameter, as it is dependent on  $\Delta T$ . Thus, a two-parameter model to characterize the level of nonlinearity was used for the California temperature profiles, which uses both the NOLA value and the temperature difference from the top of the slab to the bottom ( $\Delta T$ ). By discretizing the NOLA values by the actual  $\Delta T$  as seen in the three-dimensional plot in Figure F.8, similar temperature profiles that produce comparable self-equilibrating stresses can be discretized together to form statistical distributions for use in fatigue analysis in the RadiCAL program.

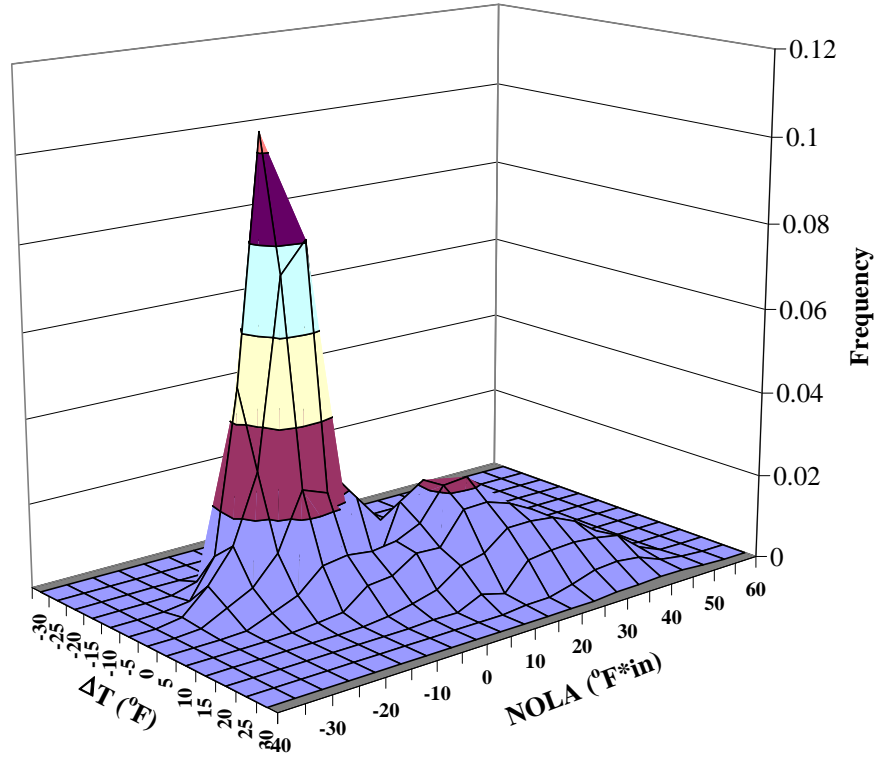


Figure F.8. Example plot of  $\Delta T$  and NOLA relationship for 8-in. JPCP in Los Angeles, California.

The self-equilibrating stresses for a quadratic temperature profile are dependent on one quadratic coefficient,  $C$ , as previously seen in Equation F-22. Solving the relationship in Equations F-25 and F-26 in terms of  $T_{mid}$  or  $T_{3/4}$  results in the following equations.

$$T_{mid} = \frac{3NOLA_{mid}}{2h} + \frac{\Delta T}{2} \quad (F-27)$$

$$T_{3/4} = \frac{9NOLA_{3/4}}{8h} + \frac{3\Delta T}{4} \quad (F-28)$$

Equations F-27 and F-28 can then be substituted into Equations F-11 and F-14 for the quadratic profiles using the middle and three-quarters depth temperatures, respectively. Both methods then result in the coefficient,  $C$ , being expressed in terms of only the NOLA value and the thickness of the slab.

$$C = \frac{-6NOLA_{mid\_or\_3/4}}{h^3} \quad (F-29)$$

Substituting Equation F-29 into the generalized Equation F-22 for self-equilibrating stresses under a quadratic temperature profile results in a direct relationship between NOLA and the self-equilibrating stress at any slab depth, as seen in Equation F-30. Equation F-31

provides this link for the self-equilibrating stress at either the top or bottom of the slab, while Equation F-32 is applicable at the mid-depth of the slab.

$$\sigma_{SES}(z) = \frac{-6NOLA}{h^3} \frac{E\alpha}{1-\mu} \left( z^2 - hz + \frac{h^2}{6} \right) \quad (F-30)$$

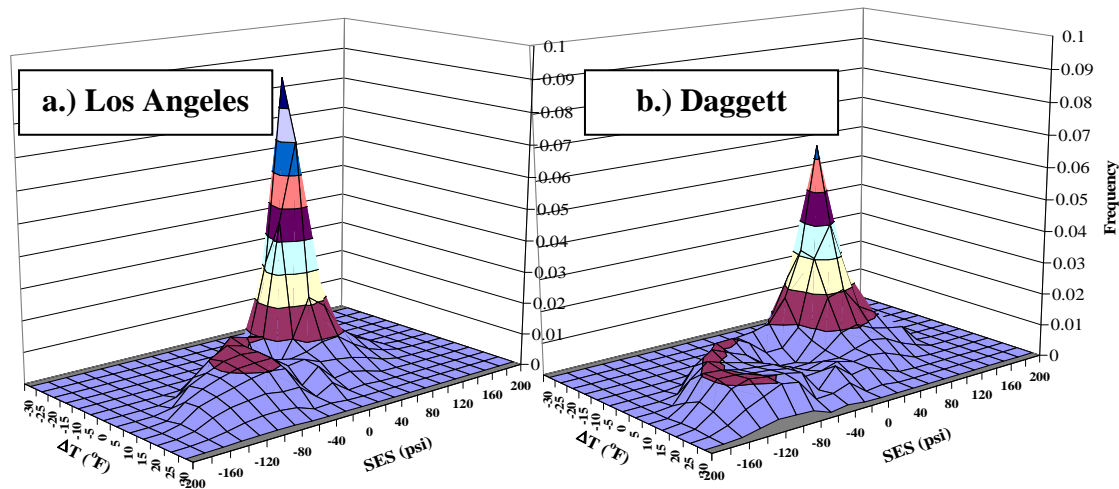
$$\sigma_{SES\_at\_top/bottom} = \frac{-NOLA}{h} \frac{E\alpha}{1-\mu} \quad (F-31)$$

$$\sigma_{SES\_at\_mid-depth} = \frac{NOLA}{2h} \frac{E\alpha}{1-\mu} \quad (F-32)$$

Using this three-dimensional frequency relationship between NOLA and  $\Delta T$ , Equation F-31 can be used to directly calculate the level and frequency of the maximum self-equilibrating stresses at the top and bottom of the slab for any climatic location. Figure F.9 shows a direct relationship between self-equilibrating stress and  $\Delta T$  for Los Angeles (a), Daggett (b), San Francisco (c), Sacramento, (d), Arcata, California (e), and Reno, Nevada (f) without having to plot the frequency of NOLA. The coastal climates are to the left of Figure F.9, while the inland climates are on the right of this same figure.

The coastal climate profiles show a higher frequency of low self-equilibrating stresses and  $\Delta T$  relative to the inland climate profiles. The inland profiles not only show a greater range of expected  $\Delta T$ , but also a greater range of maximum self-equilibrating stresses. More extreme climates can produce both high levels of curling ( $\Delta T$ ), as well as large maximum self-equilibrating stresses at the top and bottom of the slab due to more sudden environmental changes.

The three-dimensional plots in Figure F.9 can show multiple peaks of temperature difference and self-equilibrating stresses. This is due to the hysteresic nature of heating and cooling of slabs, particularly in cases such as concrete slabs where the influence of the sun and wind on the top of the slab is much more significant than that at the bottom.



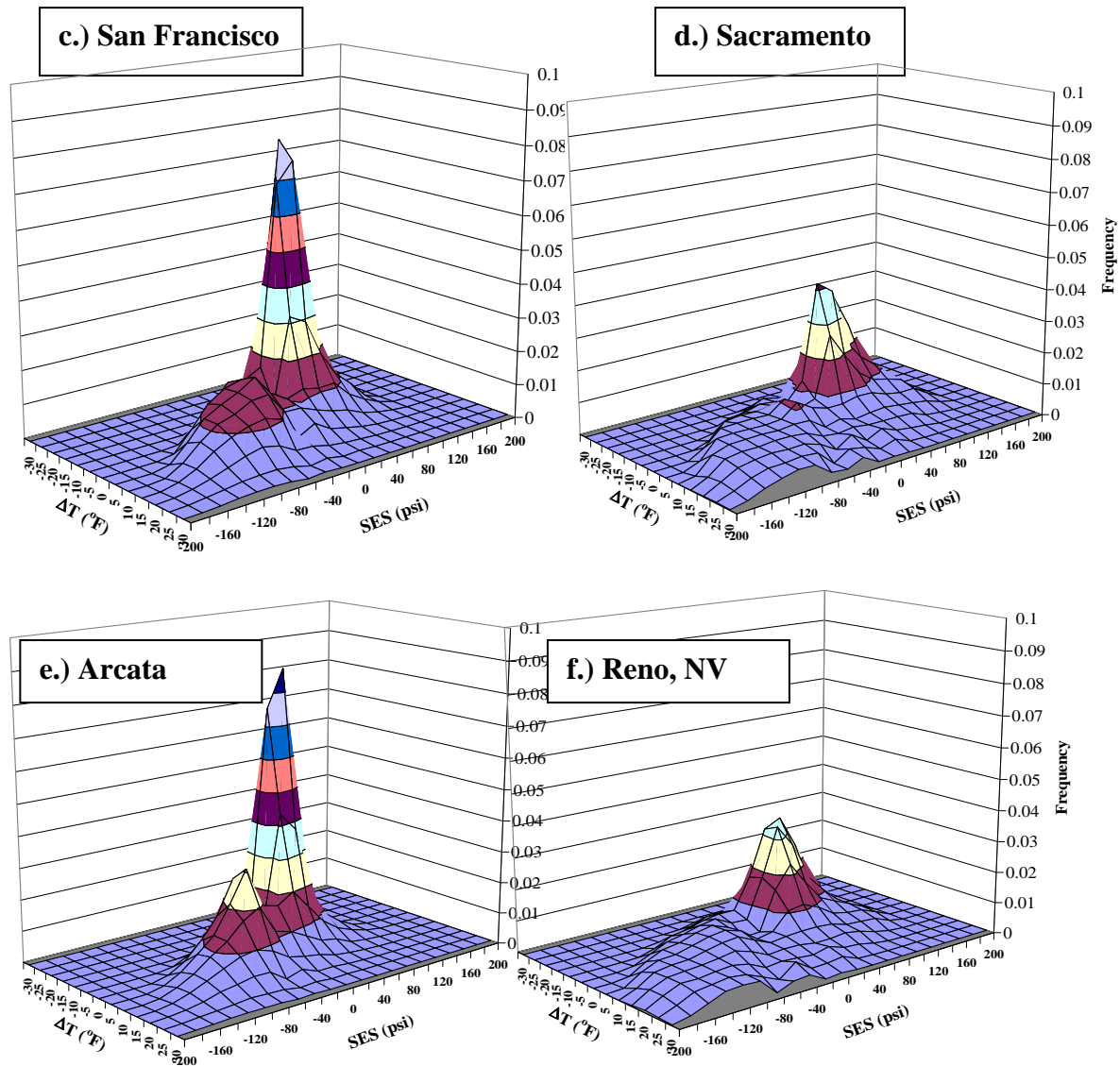


Figure F.9. Comparison of  $\Delta T$  and self-equilibrating stress frequency relationship for (a.) Los Angeles, (b.) Daggett, (c.) San Francisco, (d.) Sacramento, (e.) Arcata, California, and (f.) Reno, Nevada.

While large positive NOLA values increase the maximum compressive self-equilibrating stresses and subsequently reduce the combined temperature and load-induced stresses at the bottom of the slab, top-down tensile stresses are greatly exacerbated under high EBITD and negative NOLA values such as those in arid climates. Similar designs under the same traffic would generally lead to reduced fatigue life in the more extreme locations, such as Daggett. Since Los Angeles is a coastal climate along the Pacific Ocean, large temperature swings are less likely than an area more inland such as Daggett (roughly 140 mi from Los Angeles). This difference in proximity to the tempering effects of the ocean, the influence of mountain ranges between these two locations (San Gabriel and San Bernadino Mountains), and elevation differences (roughly 2,000 feet) can drastically change the expected distribution of both the temperature difference and maximum self-equilibrating stresses. This same trend is observed between San Francisco and Sacramento, as well as Arcata and Reno.

#### F.4. Piecewise Nonlinear Temperature Profile Stress Calculation

Another process to calculate self-equilibrating stresses from a nonlinear temperature profile is to use a piecewise integration approximation by assuming linear temperature change from known discrete temperatures through the depth of the concrete slab. This process was first used in the rigid pavement finite element code ILLISLAB (Khazanovich, 1994) to calculate nonlinear temperature stresses in the slab. This method is considered to be inherently more accurate than a quadratic temperature profile, since many temperature profiles cannot be properly matched with the quadratic assumption. A comparison between the piecewise method and the simpler NOLA method can assist in assessing the potential viability of using the quadratic temperature profile assumption for the analysis and design of rigid pavements.

Just as with the quadratic temperature profile method, the piecewise method involves the division of the total temperature profile into three temperature components: average axial, linear bending, and self-equilibrating. However, the complex task in this method is the calculation of the linear gradient that induces the equivalent bending moment from any given nonlinear temperature profile. This is achieved through the use of the temperature moment.

##### F.4.1 Temperature-Moment Concept

The theory of a temperature moment (TM) in concrete slabs and beams has been explored in many fundamental textbooks over the years (Timoshenko and Lessells, 1925; Bradbury, 1938; Boresi, 1965). Janssen and Snyder (2000) recently used the temperature-moment concept to characterize the equivalent linear temperature stress based on the nonlinear temperature profile.

Figure F.10 shows an example temperature profile and the calculation of the temperature moment. The temperature profile is divided into small sectional areas with the units of Temperature\*distance. The thickness of each specific area is defined by the thickness of slab that the specific area represents. The temperature for each distinct area is defined as the difference between the average temperature for that particular area and the average temperature of the entire profile. The average temperature of the profile is calculated using the trapezoidal method as seen in Equation F-33.

$$T_{avg} = \frac{\frac{1}{2}T_0 + \sum_{i=1}^{n-1} T_i + \frac{1}{2}T_n}{n} \quad (F-33)$$

where:

$T_{avg}$	=	average temperature of profile through depth;
$T_0 \dots T_n$	=	temperature at top and bottom of slab, respectively;
$T_i$	=	discrete temperature reading; and
$n$	=	number of discrete temperatures in profile at equal spacing.

Each area is multiplied by the moment arm from the bottom of the slab to the centroid of the area using the right-hand rule to derive the temperature-moment contribution for each specific area. The TM for the entire temperature profile can then be found by summing the individual area's temperature moments with units of temperature\*distance<sup>2</sup>. A slab with a uniform temperature will have TM = 0. In general, TM is negative if the top of the slab is warmer than the bottom and positive if the slab is warmer on the bottom. As the temperature profile becomes more nonlinear, the TM will start to approach zero as an extremely nonlinear profile starts to approach a uniform temperature profile.

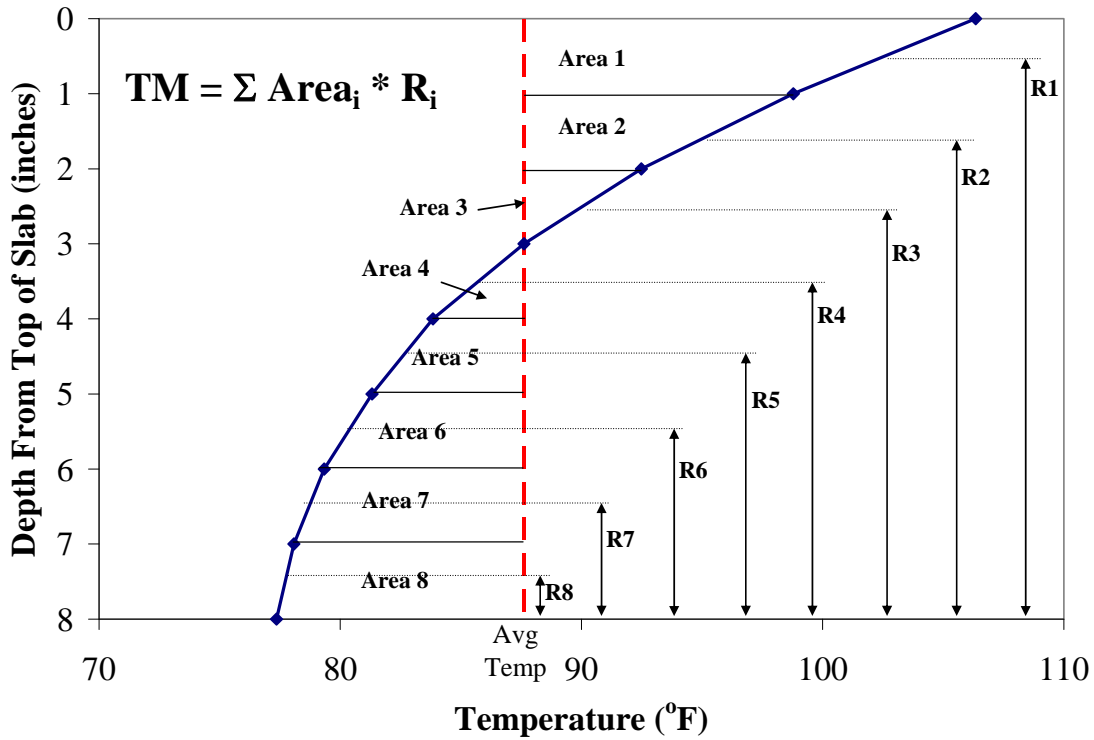


Figure F.10. Example temperature-moment calculation (after Janssen and Snyder, 2000).

TM has a direct relationship to the equivalent linear temperature difference ( $\Delta T_{eq}$ ), which can be defined as the temperature difference which gives the same bending moment as the nonlinear temperature profile as seen in Equation F-34 (Janssen and Snyder, 2000).

$$\Delta T_{eq} = \frac{-12 * TM}{h^2} \quad (F-34)$$

where:

$\Delta T_{eq}$	=	equivalent linear temperature difference from top to bottom of slab;
$TM$	=	temperature moment; and
$h$	=	thickness of the slab

When the temperature profile is either linear or uniform, or can be expressed as a quadratic function, then the actual  $\Delta T (T_{top} - T_{bottom})$  is equal to the  $\Delta T_{eq}$ . If these conditions are not true however, then  $\Delta T_{eq}$  and  $\Delta T$  are unequal.

From the equivalent linear temperature difference, the equivalent linear temperature for any point through the slab can be determined from Equation F-35. Equation F-35 assumes that the temperature at middle of the slab is zero and all the temperatures through the depth of the slab are relative to this value.

$$T_{linear}(z) = \frac{\Delta T_{eq}}{2} - \frac{\Delta T_{eq}}{h} z \quad (F-35)$$



where:

$$\begin{aligned} T_{linear}(z) &= \text{relative temperature as a function of } z; \\ \Delta T_{eq} &= \text{equivalent linear temperature difference from top to} \\ &\quad \text{bottom of slab; and} \\ z &= \text{distance from top of slab to specified depth.} \end{aligned}$$

For the top and bottom of the slab, Equation F-35 simplifies to Equations F-36 and F-37, respectively, which again is relative to the middle slab temperature of zero.

$$T_{linear}(h) = \frac{\Delta T_{eq}}{2} \quad (F-36)$$

$$T_{linear}(0) = \frac{-\Delta T_{eq}}{2} \quad (F-37)$$

where:

$$\begin{aligned} T_{linear}(h) &= \text{equivalent linear temperature at bottom of slab; and} \\ T_{linear}(0) &= \text{equivalent linear temperature at top of slab} \end{aligned}$$

#### **F.4.2 Piecewise Nonlinear Self-Equilibrating Stresses**

After the average and equivalent linear temperatures have been calculated, the nonlinear temperature component can be calculated at any depth using Equation F-38, which follows the form of Equation F-7, and as graphically noted in Figure F.1. Equation F-38 takes into account the average, equivalent linear, and actual temperatures at a specified depth with respect to the reference temperature at the bottom of the slab ( $T_n$ ). Note that the derivations for the average temperature and equivalent linear temperature are already relative to this bottom temperature.

$$T(z) - T_n = [T_{avg}] + [T_{linear}(z)] + [T_{nl}(z) - T_n] \quad (F-38)$$

This equation can more simply be re-written as:

$$T_{nl}(z) = T(z) - T_{avg} - T_{linear}(z) \quad (F-39)$$

where:

$$\begin{aligned} T_{nl}(z) &= \text{relative nonlinear temperature component at specified} \\ &\quad \text{depth;} \\ T_{avg} &= \text{average temperature of profile through depth;} \\ T(z) &= \text{actual temperature at specified depth;} \\ T_n &= \text{actual temperature at bottom of slab.} \end{aligned}$$

Equation F-39 simplifies to Equations F-40 and F-41 for the top and bottom of the slab, respectively.

$$T_{nl}(h) = -T_{avg} - T_{linear}(h) \quad (F-40)$$

$$T_{nl}(0) = \Delta T - T_{avg} - T_{linear}(0) \quad (F-41)$$

where:

$$\begin{aligned} \Delta T &= \text{actual temperature difference from top to bottom of slab;} \\ T_{nl}(h) &= \text{relative nonlinear temperature component at bottom; and} \\ T_{nl}(0) &= \text{relative nonlinear temperature component at top.} \end{aligned}$$

These relative nonlinear temperatures can then be converted into nonlinear self-equilibrating stress at any specified depth using Equation F-42.

$$\sigma_{SES}(z) = \frac{E\alpha}{1-\mu} T_{nl}(z) \quad (\text{Equation F-42})$$

where  $\sigma_{SES}(z)$  are the self-equilibrating stresses at specified depth.

For nonlinear temperature implementation in RadiCAL, only stresses at the top and bottom of the slab are analyzed. Therefore, Equations F-43 and F-44 can be used in this process to calculate the self-equilibrating stresses due to any given nonlinear temperature profile, and to provide an accurate comparative value to assess the validity of the NOLA method to account for self-equilibrating stresses due to nonlinear temperature profiles in concrete slabs.

$$\sigma_{SES}(h) = \frac{E\alpha}{1-\mu} T_{nl}(h) \quad (F-43)$$

$$\sigma_{SES}(0) = \frac{E\alpha}{1-\mu} T_{nl}(0) \quad (F-44)$$

### F.5. Comparison of Quadratic to Piecewise Nonlinear Temperature Stresses

Using the example temperature profiles from Figure F.3, the nonlinear self-equilibrating stresses can be found using both the NOLA method and the piecewise method as seen in Figure F.11. For both the daytime and nighttime profiles using any method, the self-equilibrating stresses at mid-depth and the shape of these profiles appear to be similar. Since the stresses at the top and bottom are critical for crack initiation, Table F.1 shows the summary of self-equilibrating stresses at the top and bottom of the slab for each method used. For the nighttime condition, both NOLA methods reasonably match the piecewise method at both the top and bottom of the slab, producing self-equilibrating axial tension between 43 and 47 psi at the top and bottom of the slab, depending on the method used. Since the nighttime profile in Figure F.3 was matched quite closely using a quadratic temperature profile, it is no surprise that the three techniques produce similar results.

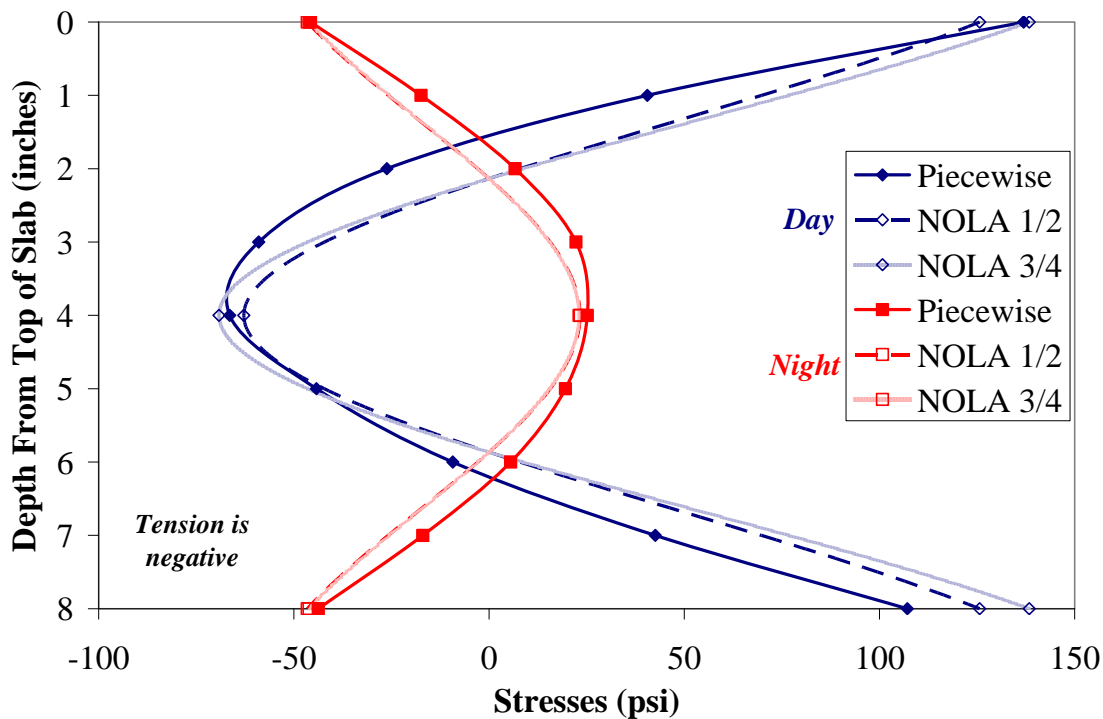


Figure F.11. Comparison of self-equilibrating stresses by method of calculation through slab depth.

Table F.1. Comparison of Self-Equilibrating Stresses by Method of Calculation at Top and Bottom of Slab.

	Actual $\Delta T$ (°F)	$\Delta T_{eq}$ (°F)	$\sigma_{SES-top}$ (psi)			$\sigma_{SES-bottom}$ (psi)		
			NOLA <sub>mid</sub>	NOLA <sub>3/4</sub>	Piecewise	NOLA <sub>mid</sub>	NOLA <sub>3/4</sub>	Piecewise
Night	-12.06	-11.98	-46.6	-46.1	-45.7	-46.6	-46.1	-43.7
Day	28.98	27.71	125.6	138.4	136.9	125.6	138.4	107.1

NOTE: Tension is negative.

The nonlinear stress components calculated from the daytime temperature profile do not match as closely as they did for the nighttime profile. At the top of the slab, the NOLA<sub>3/4</sub> method matches the piecewise method quite well (1.5 psi difference), while the NOLA<sub>1/2</sub> method is slightly more imprecise (11.3 psi difference). At the bottom of the slab, both quadratic methods do not match the piecewise method well. Since the quadratic temperature profile assumption produces no change in the equivalent bending moment ( $\Delta T = \Delta T_{eq}$ ), the self-equilibrating stresses are the same at the top and bottom of the slab. This assumption is not true with the piecewise method, as the self-equilibrating stress at the top (136.9 psi compression) does not match the bottom (107.1 psi compression). With most daytime temperature profiles, this bottom stress is most important, since there is a better chance of the stress at the bottom of the slab being the most critical stress. In this example, both NOLA methods would reduce the total tensile bending stress due to curling at the bottom of the slab by more than is suggested using

the piecewise method, thereby artificially decreasing the projected fatigue damage from bottom-up cracking. This difference will be somewhat compensated by the difference in  $\Delta T_{eq}$  in the NOLA and piecewise methods (28.98°F and 27.71°F in this case, respectively), but that is not enough to fully compensate for the difference in self-equilibrating stresses at the bottom of the slab.

### F.5.1 Comparison of Quadratic NOLA to Piecewise Total Nonlinear Temperature Stresses

While the use of the NOLA concept demonstrated varied success in matching self-equilibrating stresses of the piecewise solution, this section looks at both the NOLA<sub>1/2</sub> and NOLA<sub>3/4</sub> methods in comparison with the more accurate piecewise method in terms of total temperature stress prediction ( $\sigma_{linear} + \sigma_{SES}$ ).

Using five years of predicted hourly temperature profiles from ICM (Larson and Dempsey, 1997) for Daggett, California, Figure F.12 shows a direct comparison between the total temperature stress ( $\sigma_{linear} + \sigma_{SES}$ ) using the NOLA<sub>1/2</sub> and piecewise calculation methods at the top of the slab. Subsequently, Figure F.13 shows this comparison for the NOLA<sub>1/2</sub> method at the bottom of the slab. To find the total temperature stresses, the linear temperature bending stress was calculated using Westergaard's equation for maximum curling stresses at the bottom edge of the slab (Equation F-1), while the NOLA<sub>1/2</sub> method, assuming a quadratic temperature profile Equation F-30, was used to compensate for the self-equilibrating stresses.

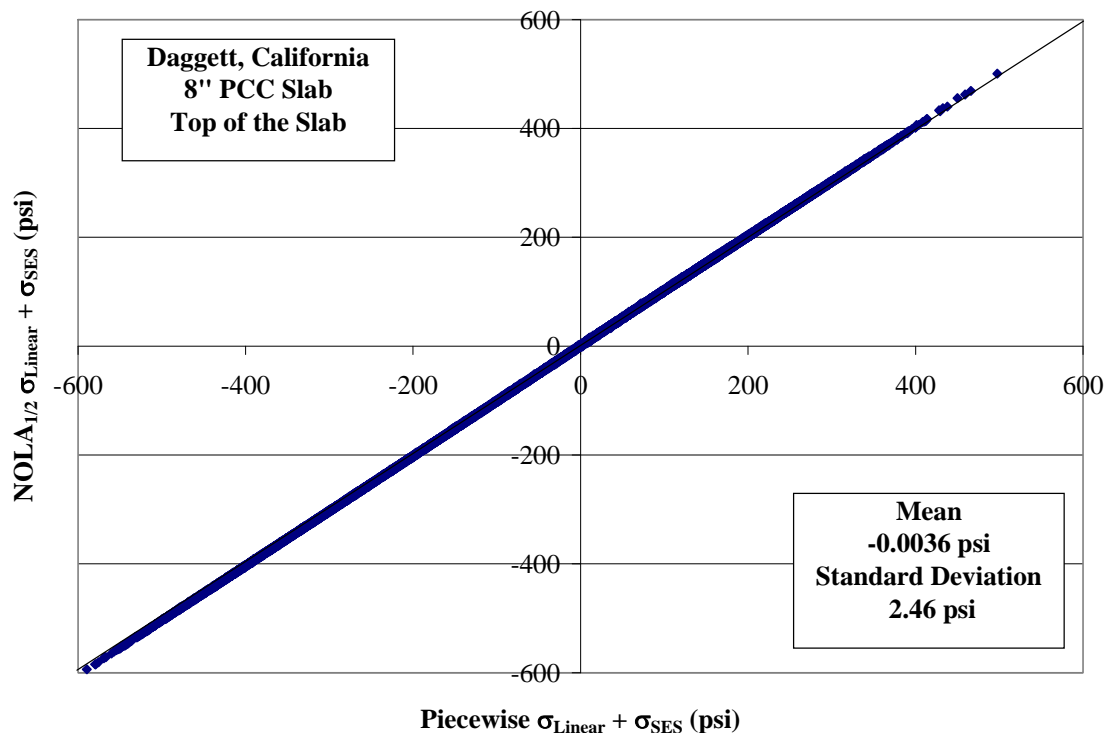


Figure F.12. Comparison of total temperature stresses using piecewise method and NOLA<sub>1/2</sub> quadratic method at top of slab using hourly data from 1986–1990 in Daggett, California.

For both the top and bottom of the slab, the total temperature stresses show a tremendous match between the two methods, with a mean difference of nearly zero and a

standard deviation of 2.46 and 3.70 psi, respectively. This shows that the  $NOLA_{1/2}$  self-equilibrating stress approximation method should provide an accurate representation of almost any nonlinear temperature profile in terms of temperature stress prediction.

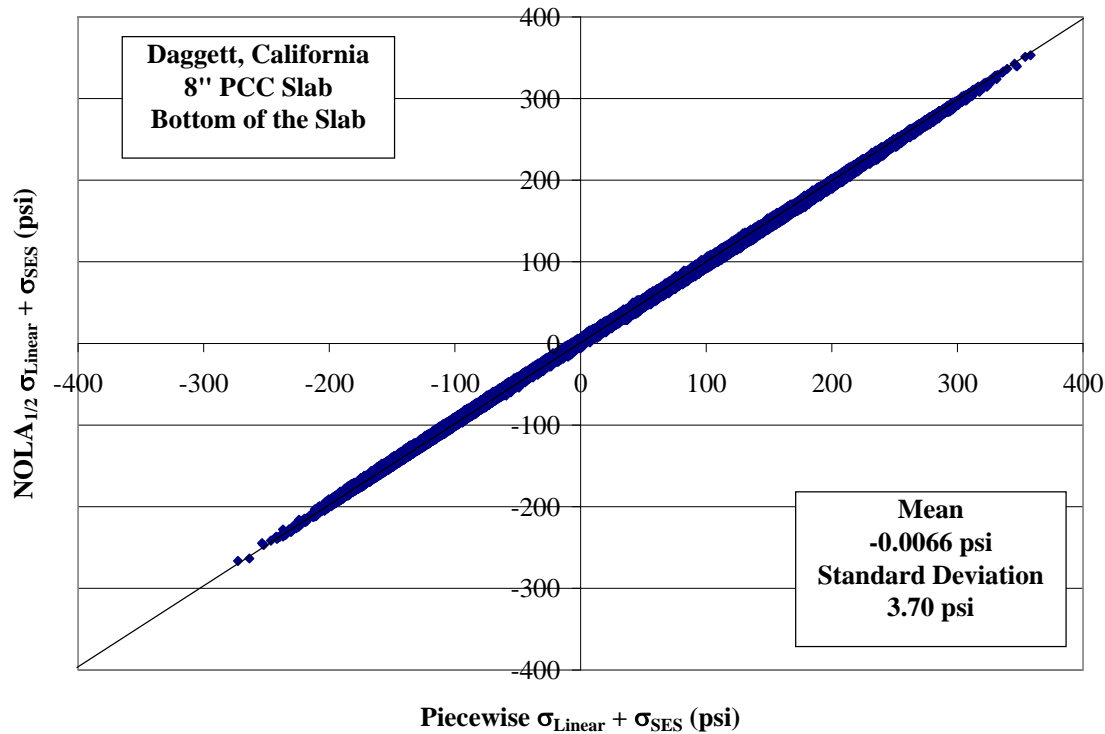


Figure F.13. Comparison of total temperature stresses using piecewise method and  $NOLA_{1/2}$  quadratic method at bottom of slab using hourly data from 1986–1990 in Daggett, California.

Using the same process to verify the accuracy of the total temperature stress prediction, the  $NOLA_{3/4}$  method was tested as seen in Figure F.14 and Figure F.15 for, respectively, the top and bottom of the slab. While the mean difference for this method was also found to be nearly zero, the scatter of these predictions is more visibly noticeable. Due to this scatter, the standard deviations of the total temperature stress differences were found to be 20.13 and 16.39 psi for the top and bottom of the slab, respectively.

While the purpose of the  $NOLA_{3/4}$  method was to better match the actual temperature profile near the top of the slab with a quadratic approximation, the profile at all depths of the slab are generally not matched as accurately as using the mid-depth temperature used in the  $NOLA_{1/2}$  method. By forcing the profile to fit the points near the top of the slab, the assumption of a quadratic temperature profile tends to overcompensate at depths in the bottom half of the slab depth. This results in more erroneous predictions of NOLA and the subsequent self-equilibrating stresses in the slab.

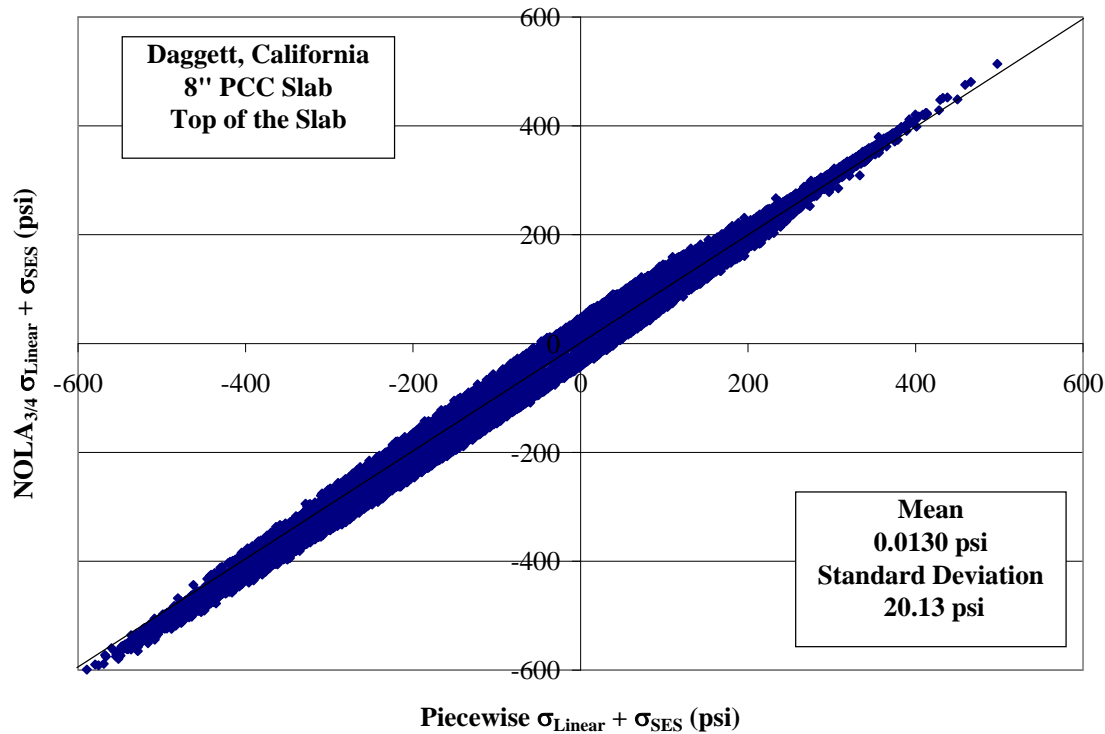


Figure F.14. Comparison of total temperature stresses using piecewise method and NOLA<sub>3/4</sub> quadratic method at top of slab using hourly data from 1986–1990 in Daggett, California.

It should be noted that while the piecewise method requires the calculation of the equivalent temperature difference ( $\Delta T_{\text{eq}}$ ) from the nonlinear temperature profile, this approximation method using the quadratic-based NOLA must use the actual temperature difference ( $\Delta T$ ). This allows for a more simple calculation of self-equilibrating stresses. However, when introducing load in addition to temperature effects in concrete pavements, the equivalent temperature difference would control the actual bending of the slab and its associated lift-off from the underlying layers. This slab lift-off behavior can have a major effect on critical stresses when all stress-related factors are considered.

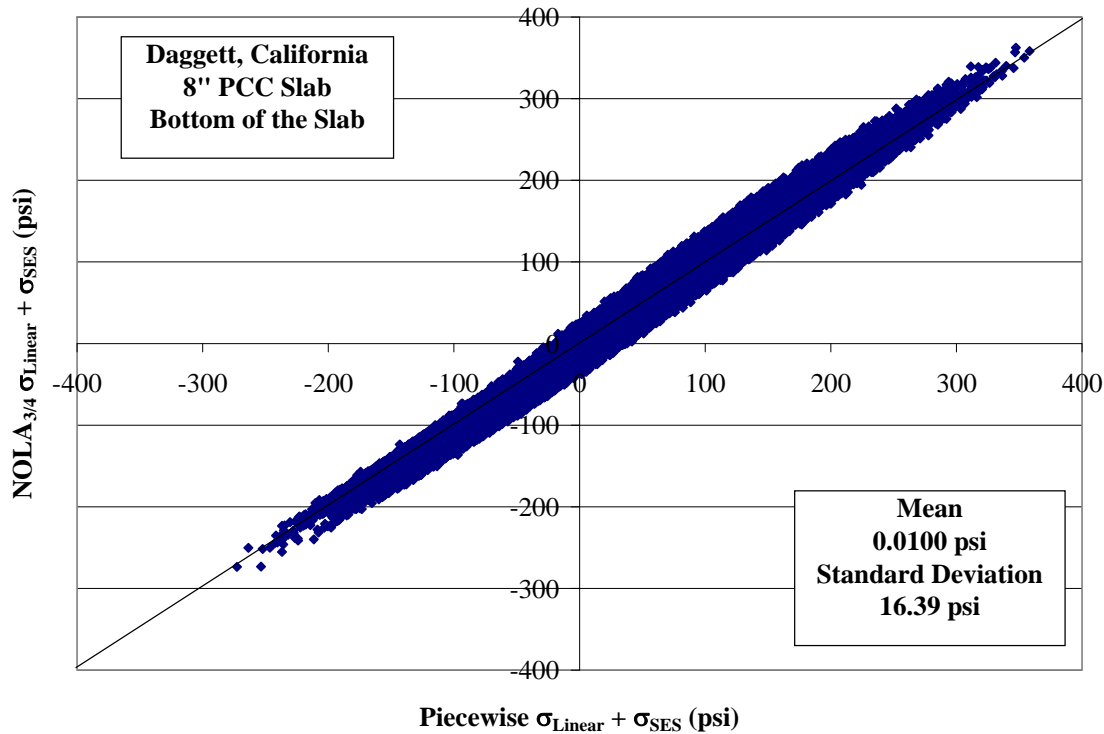


Figure F.15. Comparison of total temperature stresses using piecewise method and NOLA<sub>3/4</sub> quadratic method at bottom of slab using hourly data from 1986–1990 in Daggett, California.

#### F.6. Comparison of True NOLA to Piecewise Nonlinear Temperature Stresses

The closed form quadratic solution was tested to assess its potential as an approximation method to find the self-equilibrating stresses. This was done by using the actual area between the temperature profile and the linear assumption, instead of assuming a quadratic profile through the depth of the slab. This actual difference in area will be defined as the “True NOLA.” The True NOLA can be estimated easily through a trapezoidal area approximation similar to that used in the temperature-moment concept in the previous section. Figure F.16 shows a comparison between the self-equilibrating stresses using the piecewise method with those using Equation F-30 and the True NOLA for five years of hourly ICM temperature data from Daggett, California at the top of the concrete slab. While the average difference between these two methods is nearly zero, the standard deviation is 18.7 psi for this set of data. Since RadiCAL uses a discretization level of 20 psi to categorize self-equilibrating stresses into equal bins, this level of error appears to be unacceptable to match the more precise piecewise method to account for nonlinear temperature profiles.

In addition to the high level of error using this method of approximation, the positive self-equilibrating stresses (tension) are underpredicted in comparison to the piecewise method. Conversely, the cases in which compressive self-equilibrating stresses, were generated at the top of the slab, were overpredicted. Thus, the use of this approximation method would result in the greatest amount of error in the most extreme cases that determine the majority of fatigue damage in concrete pavements.

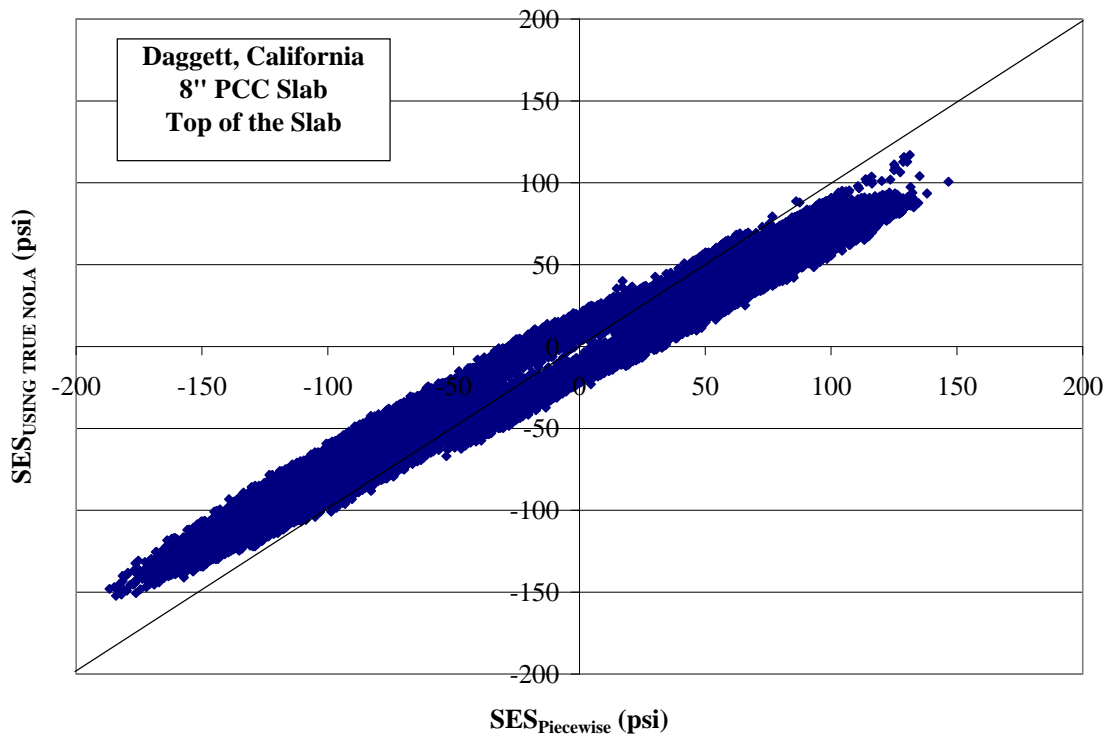


Figure F.16. Comparison of piecewise self-equilibrating stresses to computed self-equilibrating stresses at top of slab using True NOLA using hourly data from 1986–1990 in Daggett, California.

Using the piecewise method, the self-equilibrating stresses at the top of the slab do not necessarily match those values found for the bottom of the slab, unless the profile is matched by a second-order-or less-polynomial. Thus, the bottom of the slab must also be checked using this approximation method as well. In this location, the exact opposite trend is found (Figure F.17). The tension cases are underpredicted while the compressive self-equilibrating stresses are overpredicted. Consequently, this method of approximation appears unfit for adaptation in RadiCAL for bottom-up fatigue damage.



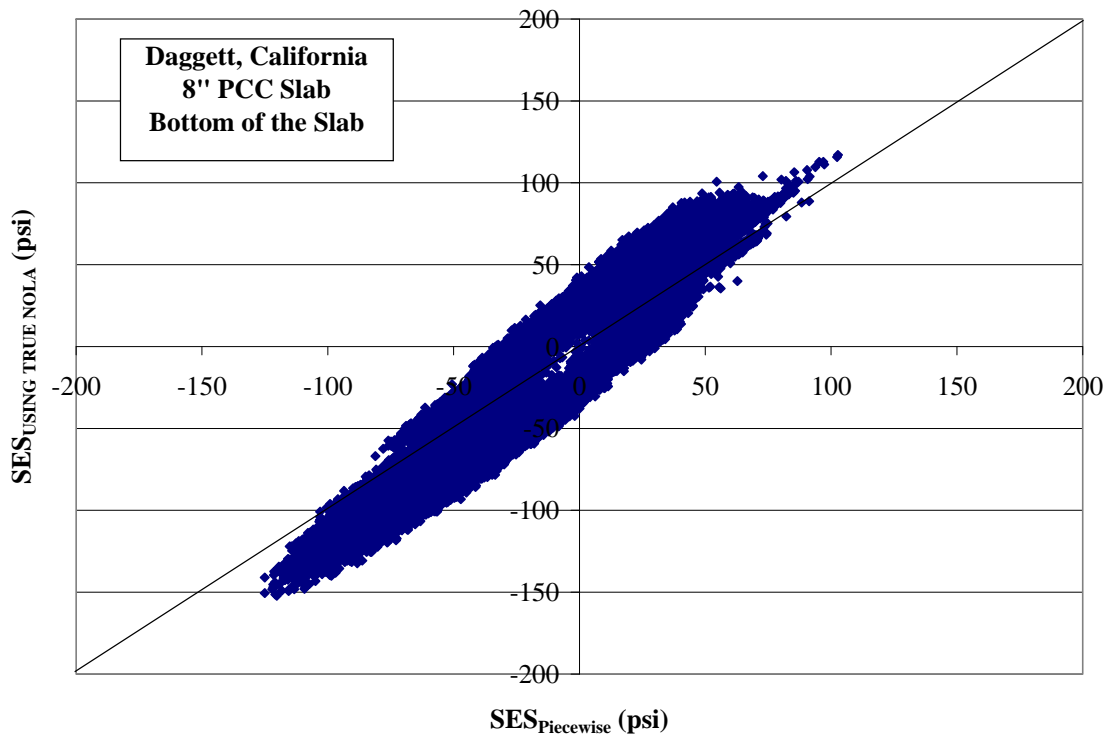


Figure F.17. Comparison of piecewise self-equilibrating stresses to computed self-equilibrating stresses at bottom of slab using True NOLA using hourly data from 1986–1990 in Daggett, California.

However, when looking at the predictive power of using the True NOLA in terms of total temperature stress (linear bending stress from Equation F-1, in addition to the respective self-equilibrating stress), the result is much different. An excellent approximation is found in comparison to the total temperature stresses using the piecewise method, as seen in Figure F.18 and Figure F.19. The mean difference for the top and bottom comparison was found to be almost zero, with a small standard deviation of 1.87 psi. This direct total temperature stress comparison shows good promise for a simple and accurate approximation of self-equilibrating stresses for post-processing finite element analyses of curled concrete slabs undergoing loading.

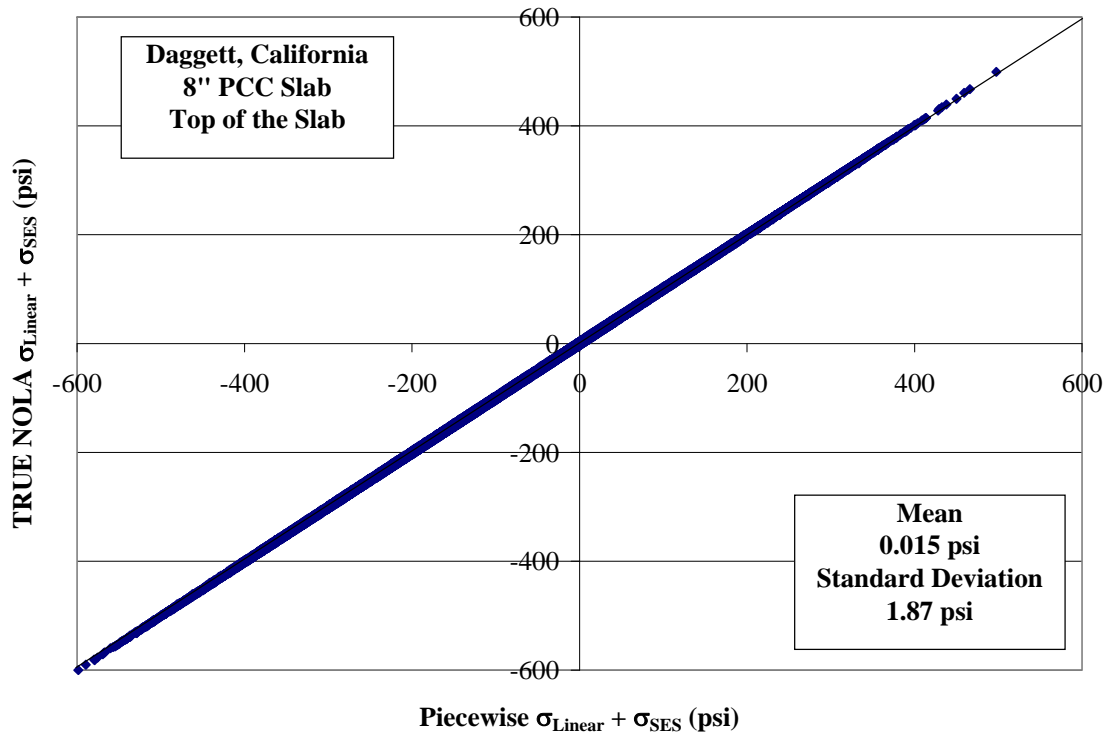


Figure F.18. Comparison of total temperature stresses using piecewise method and True NOLA quadratic method at top of slab using hourly data from 1986–1990 in Daggett, California.

By using the  $\text{NOLA}_{1/2}$  or True NOLA method to compensate for self-equilibrating stresses, a very good approximation of total temperature stresses can be achieved at the critical points at the top and bottom of the slab, as seen in the summary in Table F.2. Due to its poor matching of the total temperature stress prediction relative to the other quadratic-based approximations, avoiding the use of the  $\text{NOLA}_{3/4}$  method in this capacity is recommended.

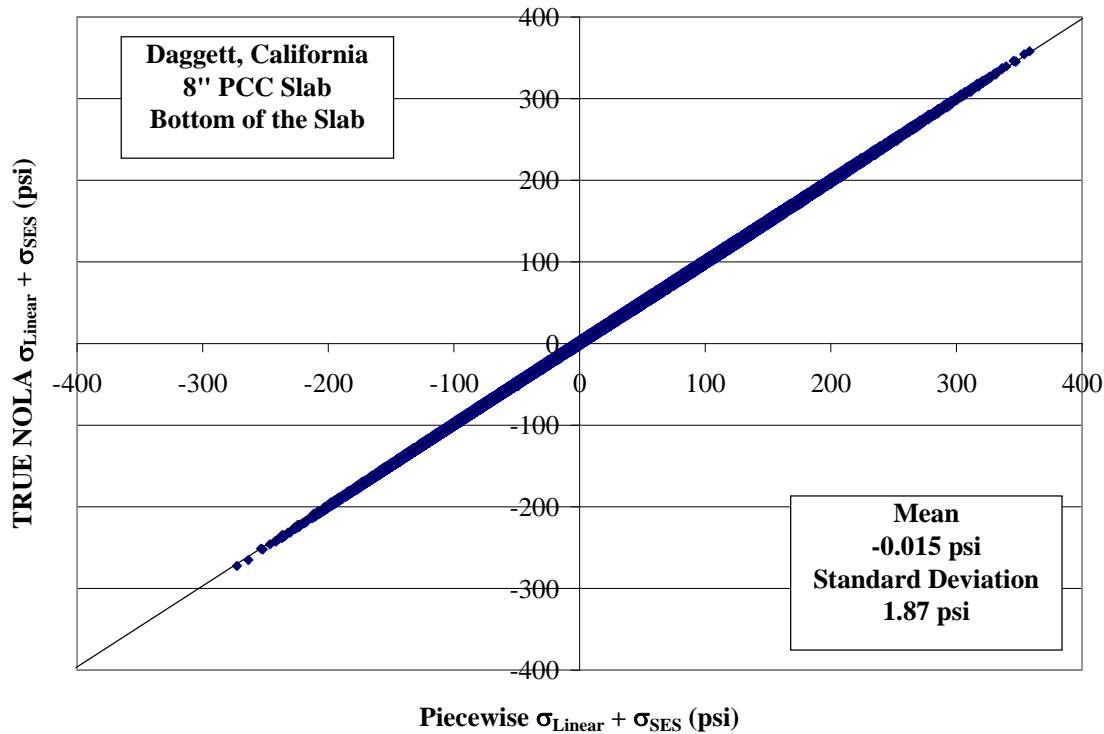


Figure F.19. Comparison of Total Temperature Stresses using the Piecewise Method and the True NOLA Quadratic Method at the Bottom of the Slab using Hourly Data from 1986-1990 in Daggett, California.

Table F.2. Comparison of Total Temperature Stresses using NOLA Methods to the Piecewise Method.

	Top of Slab			Bottom of Slab		
	NOLA <sub>1/2</sub>	NOLA <sub>3/4</sub>	NOLA <sub>TRUE</sub>	NOLA <sub>1/2</sub>	NOLA <sub>3/4</sub>	NOLA <sub>TRUE</sub>
<b>Mean Difference (psi)</b>	-0.0036	0.0130	0.0015	-0.0066	0.0100	-0.0015
<b>Standard Deviation (psi)</b>	2.46	20.13	1.87	3.70	16.39	1.87

### F.7. Effect of Nonlinear Temperature Stresses on Fatigue Damage

While the preceding section focused on differences in stresses due to the incorporation on self-equilibrating stresses from nonlinear temperature profiles, the next step in this analysis is to assess differences in fatigue damage profiles and magnitudes. This will provide a better understanding of the impact of accounting for nonlinear temperature in fatigue-based pavement analysis.

### F.7.1 Damage Profile Comparison

For this analysis, an undoweled, 8-in. slab with a standard lane width of 12 ft and joint spacing of 15 feet will be used with a k-value of 250 psi/in., and a modulus of rupture of 700 psi. A moderate EBITD level of -10°F with the location in Los Angeles will also be utilized. For traffic, an average annual daily truck traffic (AADTT) of 10,450 trucks for a 30-year design as well as an average load spectra and axle spacing distribution from over 100 weigh-in-motion stations (Lu et al. 2001) will be utilized in RadiCAL (Appendix C). For fatigue analysis, the Zero Maintenance fatigue transfer function (Darter, 1977) will also be employed.

When a linear temperature assumption is used in RadiCAL, the damage profile from Figure F.20a is found. At this lower level of EBITD, almost all of the fatigue damage is focused at the mid-slab location, thereby predicting bottom-up transverse fatigue cracking as the critical location. However, when self-equilibrating stresses from the nonlinear profiles are accounted for, as in Figure F.20b using the NOLA<sub>1/2</sub> method, the damage profile changes significantly. Figure F.20b shows high levels of fatigue damage at the traditional mid-slab bottom location, but also significant fatigue damage near mid-slab at the top of the slab and at the the transverse joint between the wheelpaths on the top of the slab. This damage profile suggests multiple potential failure locations: bottom-up transverse cracking, top-down transverse cracking, or top-down longitudinal cracking initiating from the transverse joint. Using the more robust piecewise method to account for self-equilibrating stresses (Figure F.20c), a similar profile to the NOLA method is found. In terms of locations of potential failure, the much simpler NOLA method matches the piecewise method quite well.

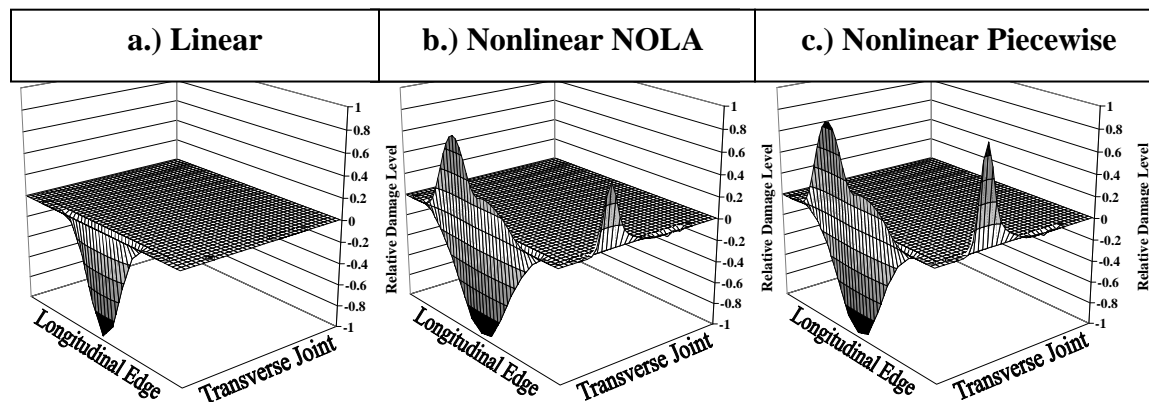


Figure F.20. Damage profile comparison incorporating nonlinear self-equilibrating stresses for Los Angeles, California using (a.) linear temperature differences, (b.) quadratic nonlinear temperature, and (c.) piecewise nonlinear temperature profiles.

Figure F.21 looks at the same nonlinear temperature comparison in terms of fatigue damage profiles for the more extreme Daggett climate inland from the Pacific Ocean and Los Angeles. The linear temperature assumption at EBITD of -10°F and use of the Zero Maintenance maximum stress fatigue transfer function (Darter, 1977) indicates bottom-up transverse cracking as probable, thereby matching the Los Angeles climate prediction. However, accounting for self-equilibrating stresses completely changes the predicted fatigue mechanisms to top-down transverse cracking with only slight probabilities of formation of bottom-up transverse cracking or top-down longitudinal cracking. More important, the use of the NOLA method matches the predicted damage profile from the piecewise method exceptionally

well, further corroborating the use of this quadratic-based, self-equilibrating stress method for nonlinear temperature stress prediction.

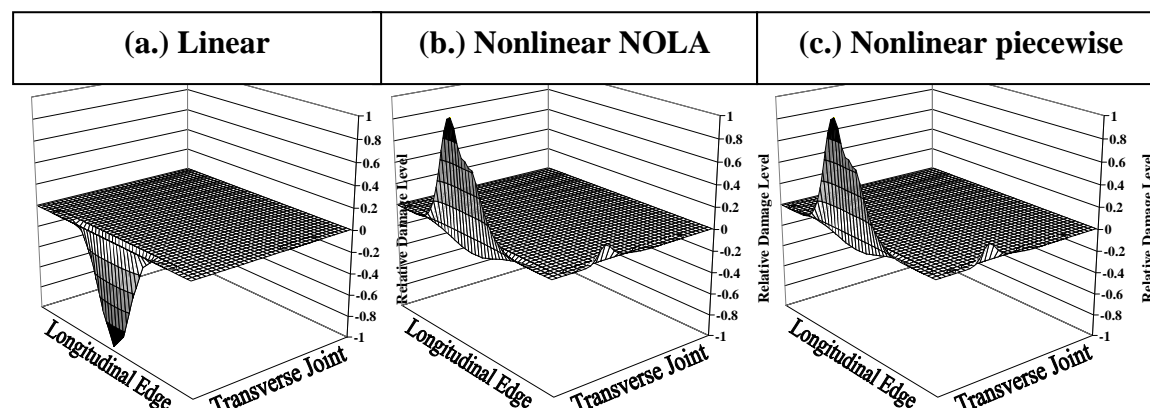


Figure F.21. Damage profile comparison incorporating nonlinear self-equilibrating stresses for Daggett, California using (a.) linear temperature differences, (b.) quadratic nonlinear temperature, and (c.) piecewise nonlinear temperature profiles.

### F.7.2 Damage Level Comparison

While the damage profiles give a good indication of where damage will occur, the level of damage or damage magnitude is indicative of when that damage will manifest itself as a physical crack in the pavement slab. Using Miner's hypothesis (Miner, 1945) for damage accumulation in RadiCAL, this level of fatigue damage can also be predicted. The assumption using Miner's hypothesis is that fatigue damage of 1.0 equates to fatigue cracking failure. Using this standard case for traffic, geometry, etc. described in the previous section, the fatigue damage level at an EBITD of  $-10^{\circ}\text{F}$  using the  $\text{NOLA}_{1/2}$  method and piecewise method are very similar at  $6.8 \times 10^{-4}$  (Figure F.22) for the Los Angeles climate. Conversely, the damage level assuming linear temperature differences at this EBITD level is 55 times higher at 0.038. The self-equilibrating stresses reduce the level of stress at the critical tensile bottom locations and increase the damage at other tensile stress locations on the top of the slab. Figure F.22 also shows that the use of the  $\text{NOLA}_{3/4}$  method (using temperature at the top, bottom, and  $h/4$  from the top of the slab) does not yield results that match the damage levels of the piecewise method to account for self-equilibrating stresses.

For the Los Angeles climate with no EBITD, Figure F.22 predicts that the slab would have a much higher probability of being cracked using a linear temperature assumption, and uncracked using any of the methods accounting for nonlinear temperature profiles. The converse is true at levels of EBITD more extreme than  $-30^{\circ}\text{F}$  where accounting for nonlinear temperature exacerbates temperature and load-induced stresses at the top of the slab and results in top-down fatigue failure.

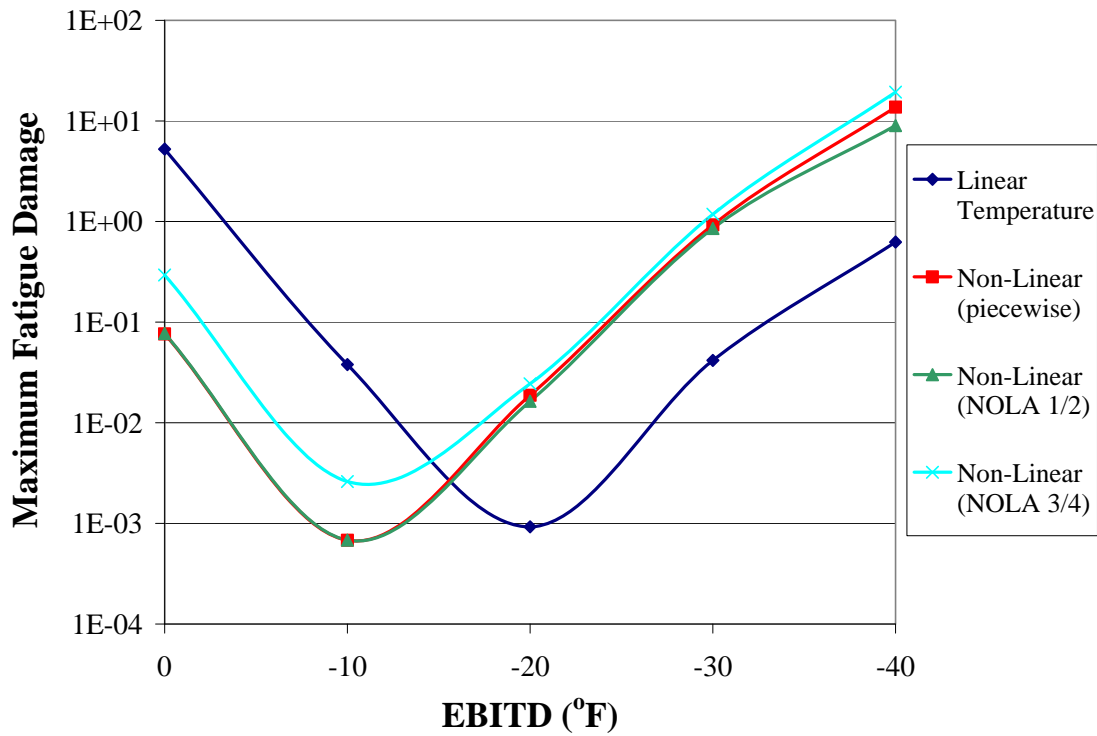


Figure F.22. Maximum fatigue damage level by built-in curl level using several nonlinear self-equilibrating stress methods and maximum stress fatigue for Los Angeles, California.

Figure F.23 shows this same maximum stress damage comparison for the desert climate of Daggett, with similar results to the Los Angeles comparisons. While the damage locations were confirmed—as well predicted—from the damage profiles in Figure F.21 using the  $NOLA_{1/2}$  method, the actual absolute fatigue damage level is also closely matched to the piecewise solution at all levels of EBITD. Thus, it can be concluded that the  $NOLA_{1/2}$  method provides an adequate accommodation of self-equilibrating stresses and its subsequent relationship to predicted fatigue damage level.

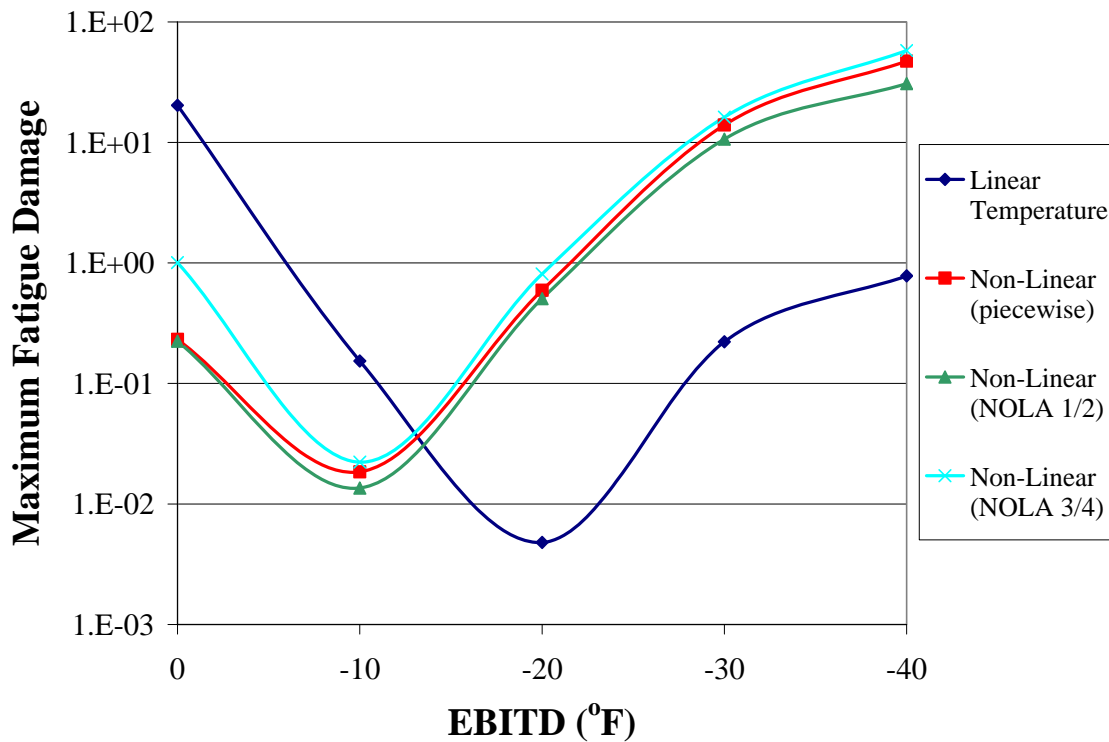


Figure F.23. Maximum fatigue damage level by built-in curl level using several nonlinear self-equilibrating stress methods and maximum stress fatigue for Daggett, California.

The “flip point” value between bottom-up fatigue damage and top-down fatigue damage occurs as the magnitude of EBITD increases. However, the flip point magnitude varies depending on the temperature profile assumption made. This flip point usually occurs as the level of bottom-up fatigue damage at mid-slab becomes minimized to the point where top-down damage becomes critical and is represented roughly by the minimum points in Figure F.22 and Figure F.23. To the left of these minima, the critical fatigue mechanism is bottom-up and the opposite is true to the right of these minima. With a linear temperature difference assumption, this flip point is between an EBITD level of -20°F and -25°F (Hiller and Roesler, 2005a, 2006). However, when the self-equilibrating stresses are accounted for, the tensile stresses at the bottom of the slab are usually reduced while the tensile stresses at the top of the slab are increased (Figure F.4 and Figure F.5) due to the majority of nonlinearity occurring near the top of the slab. This promotes a flip point in a range of -10°F to -15°F depending on traffic, geometry, climate, etc. This approach tends to generally agree with fatigue damage results using the MEPDG where top-down cracking becomes more prevalent around the default built-in curl level of -10°F and almost exclusively occurs at higher levels of built-in curling.

When a stress range approach is used to assess fatigue damage (Tepfers, 1979) instead of a maximum stress approach, this flip point difference is less pronounced for the Los Angeles (Figure F.24) and Daggett (Figure F.25) climates. The flip point using nonlinear temperature and stress range transfer function for fatigue is usually in the range of -15°F to -20°F, while the linear assumption yields a flip point anywhere in the range of -15°F to -25°F. Note that it is expected that this flip point should not be constant, but should be a function of the temperature profile nonlinearity and its interaction with the pavement geometry and load transfer between slabs.

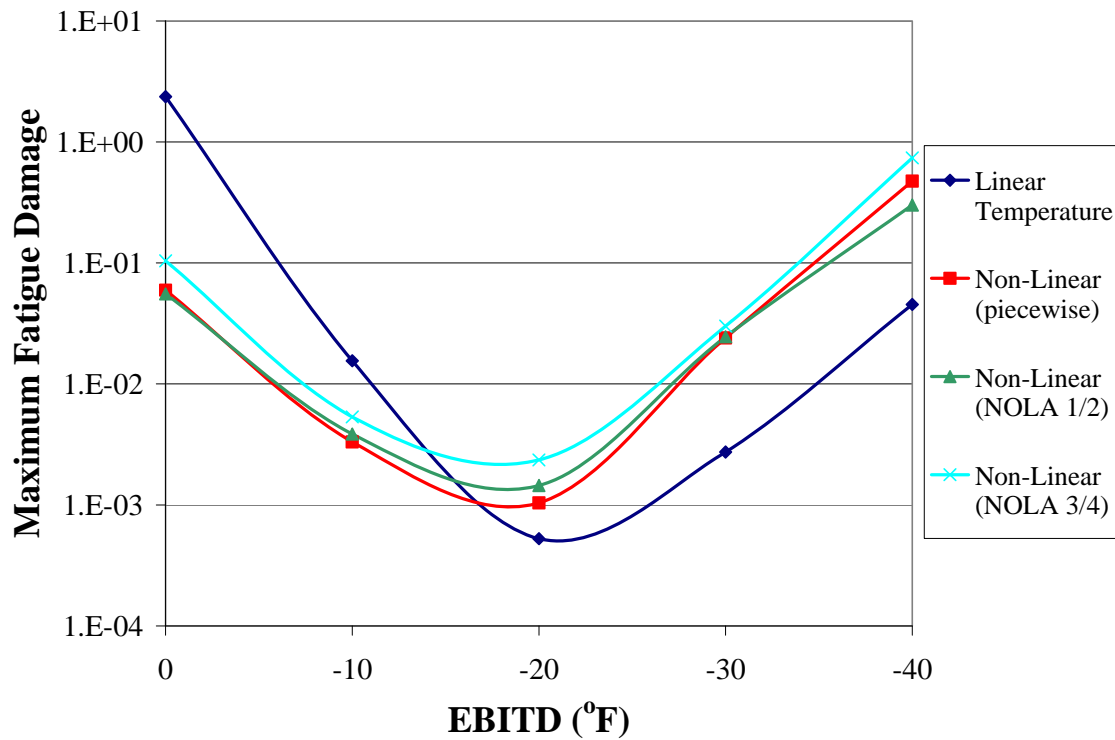


Figure F.24. Maximum fatigue damage level by built-in curl level using several nonlinear self-equilibrating stress methods and stress range fatigue for Los Angeles, California.

It is important to note that the stress range approach does reduce the predicted damage magnitude by dampening extreme temperature and load-induced stress events and the subsequent fatigue damage accumulation. However, the NOLA<sub>1/2</sub> method still matches the piecewise absolute fatigue damage levels quite well. In addition, the use of a reduced-strength concept (McCullough and Dossey, 1999; McCullough et al., 2000; S. Rao, 2005) for the top of the slab due to surface shrinkage cracking may further reduce the true flip point for field sites in arid climates or situations with poor curing of the concrete during placement.



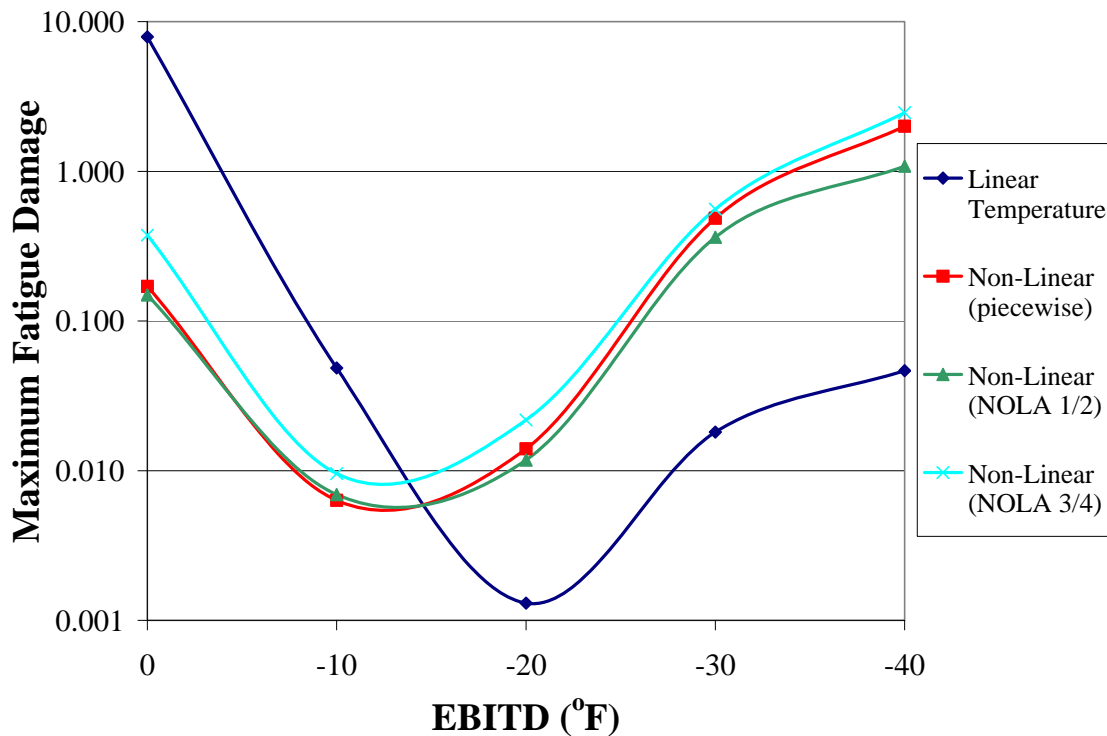


Figure F.25. Maximum fatigue damage level by built-in curl level using several nonlinear self-equilibrating stress methods and stress range fatigue for Daggett, California.

### F.8. Summary on Nonlinear Temperature

The use of self-equilibrating stresses in concrete pavement analysis and design is critical to properly characterize the total thermal stresses and likely timing and position of fatigue cracking. By using only the linear temperature differences in these analyses, bottom-up stresses are generally overpredicted and top-down stresses are subsequently underpredicted. This omission will typically lead to an underprediction of fatigue life in cases with no to low built-in curl (bottom-up failures) and overprediction of fatigue life in high built-in curl cases (top-down cracking mechanisms).

Using EICM results, it was shown that for any given temperature difference to which a pavement slab is subjected, a variety of self-equilibrating stresses may occur, since an infinite number of temperature profile shapes exist for a given temperature difference. To account for these self-equilibrating stresses, a parameter named NOLA was developed that represents the difference in area between a quadratic temperature profile (3 temperatures at three depths) and an assumed linear profile (temperature at top and bottom of the slab). The NOLA method allows for a simple visualization of the level of nonlinearity even though the more theoretically rigorous piecewise solution can be used. This simple visualization of the NOLA can give pavement engineers a simple tool to assess the importance of accounting for self-equilibrating stresses in their analyses. A closed-form solution was derived to account for the self-equilibrating stresses based on the NOLA parameter that allows pavement engineers to easily account for temperature nonlinearity in analyses.

Comparisons using the NOLA method were made to the more rigorous and precise piecewise method for self-equilibrating stress determination. In terms of self-equilibrating stresses, the NOLA method using the mid-slab depth temperature matched the piecewise method quite well. The use of the actual area between the linear assumption and the actual

temperature profile (True NOLA), in conjunction with the closed form solution for self-equilibrating stresses, tended to match the total temperature stresses found using the piecewise method the best. An excellent trend between total temperature stresses with the NOLA<sub>1/2</sub> method and piecewise solution was obtained, while the NOLA<sub>3/4</sub> method was less accurate in this respect due to the overcompensation of the temperature profile prediction in the bottom portion of the slab.

When comparing the temperature profile characterization techniques in terms of fatigue damage, both the fatigue damage level and the fatigue damage profiles matched well for both the NOLA<sub>1/2</sub> and piecewise methods for two distinct climates in California. This indicates that the NOLA method would be an appropriate approximation for the piecewise method for correctly predicting both where and when fatigue damage would occur in comparison with the piecewise method.

Comparisons in the flip point of fatigue cracking mechanisms (from bottom-up to top-down cracking as the EBITD level is increased) found that the use of self-equilibrating stresses in the damage analysis reduced the level of built-in curl required to cause top-down cracking to become predominant. For a maximum stress fatigue damage approach using nonlinear temperature profiles, this flip point occurred in the range of -10°F to -15°F. For the stress range approach to fatigue damage, this flip point was slightly more extreme at a range of -15°F to -20°F. These flip point ranges are slightly less extreme than those found using strictly linear temperature profiles.

It was also found that the use of nonlinear temperature profiles with an EBITD concept generally reduces the fatigue damage level in comparison to its linear counterpart, except for the scenarios with more extreme EBITD level than -15°F, where accounting for self-equilibrating stresses exacerbates temperature and load-induced stresses at the top of the slab, and results in top-down fatigue failure earlier.

The use of a nonlinear temperature profile assumption for Illinois can offer advantages if top-down stresses are going to be predicted, since underprediction of top tensile stresses result for linear temperature assumption. However, if bottom-up stresses control the thickness design (the current situation for IDOT design of rigid pavements), then the nonlinear temperature stresses will reduce the critical tension at the bottom of the slab and result in thinner slabs.

## **APPENDIX G. DESIGN VERIFICATION OF IN-SERVICE JOINTED PLAIN CONCRETE PAVEMENTS**

### **G.1. Introduction**

The development of RadiCAL (Hiller and Roesler, 2005b) and the subsequent addition of self-equilibrating stresses from nonlinear temperature profiles provides an excellent analytical tool for evaluating the impact of individual input parameters on both the level and location of critical fatigue damage in JPCPs. However, one major drawback is that the stress prediction algorithm, damage calculation procedure, and fatigue models used in RadiCAL are not calibrated with in-service field sites. This appendix aims to assess the predictive power of RadiCAL in terms of matching fatigue damage mechanisms of several California sites through a “design verification” process. This design verification process essentially uses RadiCAL as a forensic tool to match fatigue cracking types, while ignoring the timing element of crack propagation required to conduct a full calibration of RadiCAL or any analysis/design software. For this analysis, site-specific load spectra, geometry, EBITD, and climate were used. A set value for the level of traffic was used as this analysis focuses on relative damage, so that all damage levels are normalized to the maximum damage level found in a particular RadiCAL run.

### **G.2. RPPR Sections**

Using the Rigid Pavement Performance/Rehabilitation (RPPR) database (Smith et al., 1998), two projects in California with the occurrence of fatigue cracking at multiple locations on the slab were examined as a preliminary design confirmation of the predicted damage locations. These sections are referred to as CA1-3 and CA2-3, using the RPPR database terminology.

#### **G.2.1 Section CA1-3**

Section CA1-3 is a 1,045-ft section of a larger test section on northbound I-5 in Tracy, California (Central Valley climatic region). It was built in 1971 as a jointed plain concrete pavement with random joint spacing (12, 13, 19, and 18 ft) and a 12-ft slab width with an asphalt shoulder. The slabs were designed to be 8.4-in. on top of a 5.4-in. cement-treated base and 24-in. aggregate subbase. The joints were designed to be skewed with no load transfer devices. Falling-weight deflectometer testing conducted in 1987 and 1992 revealed a wide range of average load transfer (87% and 20%, respectively) and a high number of corners with voids (50% to 100%, respectively). Some of this variation may be explained by the difference in the temperature at which the section was tested (63°F and 78°F, respectively). Condition surveys revealed the following information as seen in Table G.1.

Table G.1. Condition Survey for RPPR Sections CA1-3 in Tracy and CA2-3 in Los Angeles, California (after Smith et al. 1998).

Project ID	FWD Corner Deflection (9 kips)		Load Transfer (%)		Estimated Corners with Voids		Transverse Cracking		Longitudinal Cracking	
	Under Load (mils)		Average		(%)		% Slabs Cracked		Linear ft/mi	
	1987	1992	1987	1992	1987	1992	1987	1992	1987	1992
CA1-3	13.7	35.5	87	20	50	100	9	18	872	812
CA2-3	24.4	n/a	19	n/a	90	n/a	66	68	0	0

The EBITD value was estimated from the FWD corner deflection in 1992 using the method from Rao and Roesler (2003, 2005a). FWD testing is typically conducted at times to limit the actual  $\Delta T$  in the slab. Since no  $\Delta T$  was reported (Smith et al., 1998), this value was assumed to be zero. Thus, the backcalculated value of curl was completely attributed to the EBITD value, as seen in Figure G.1 to be  $-24^{\circ}\text{F}$  at the previously backcalculated  $k$ -value of 250 psi/in for CA1-3. If a positive temperature gradient was actually present, which is the most likely scenario, this value would be added to the backcalculated value found in Figure G.1 to find the adjusted EBITD value (i.e., an increased EBITD value). Likewise, the opposite would be done if a negative  $\Delta T$  existed in the slab during testing, i.e., during nighttime FWD testing. It should be noted that if erosion of the underlying material exists, the EBITD process would erroneously equate the additional deflections to a more extreme EBITD value.

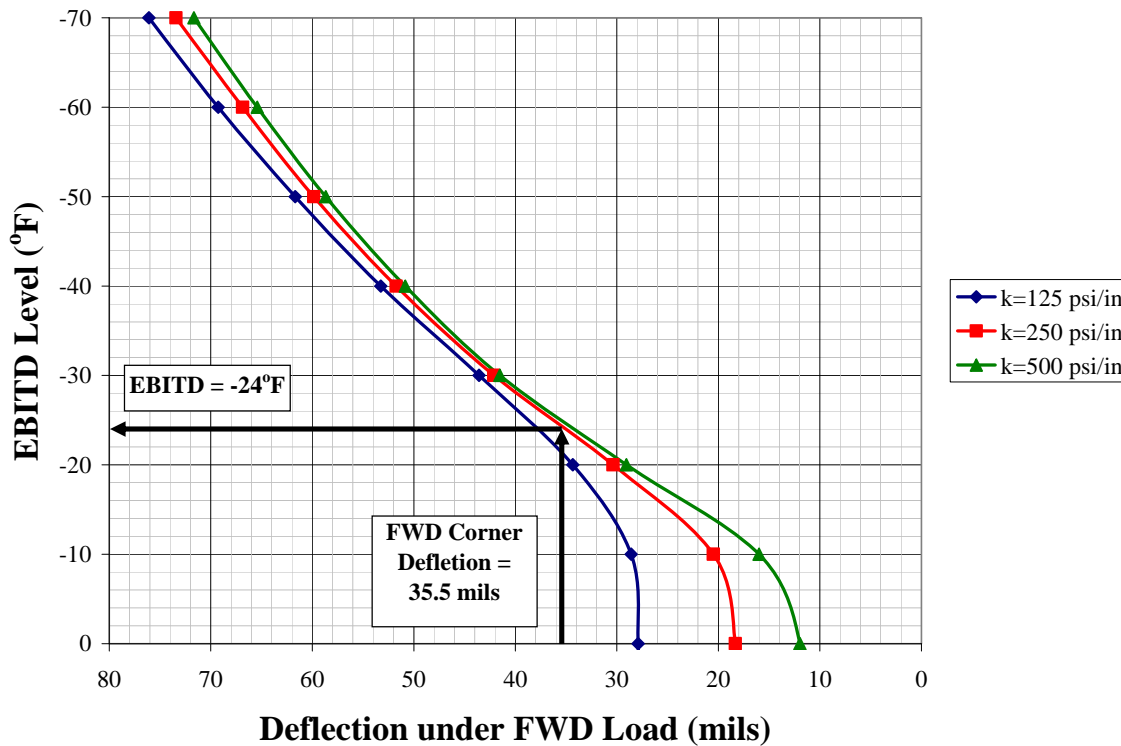


Figure G.1. Backcalculation procedure for EBITD under geometry, support conditions and load transfer in CA 1-3 (9,000-lb FWD load).

#### G.2.1.1 Linear Analysis

A predicted damage profile using a stress range fatigue approach and linear temperature assumptions was generated, as seen in Figure G.2a, using the backcalculated EBITD value, measured load transfer across the transverse joint, climatic zone, slab geometry and thickness, stress range transfer function, and site-specific load spectra from northbound I-5 in Tracy, California (Lu et al., 2001),.

Table G.1 shows that 18% of slabs in this particular section exhibited transverse cracking. Hansen et al. (2001) noted that the observed transverse cracking in Tracy on I-5 originated between the mid-slab edge and leave joint of the slab. Since the database for this site exhibits longitudinal cracking in terms of linear ft/mi, longitudinal cracks were assumed to be equally distributed among the different slab lengths and span the entire slab length. Using this assumption, this section would exhibit 15% of the slabs with longitudinal cracking. The damage profile in Figure G.2a using a stress range approach would project a higher percentage of top-down transverse cracking with a smaller probability of longitudinal cracking (both top-down between the loads on the axles and bottom-up under the loaded areas) or bottom-up transverse cracking. In this relative damage profile, the traffic would be coming out of the page. While this damage profile does not exactly match the distresses found on CA 1-3, the probability for both transverse and longitudinal cracking is shown. With the assumption of no temperature gradient during testing, this may lead to an improper calculation of EBITD. Daytime testing of this section could possibly add -5°F to -10°F to the EBITD level, thereby predicting more longitudinal cracking potential.

Using a maximum stress approach with linear temperature differences (Figure G.2b), the predicted damage profile predicts only top-down transverse cracking near midslab. This does

not appear to match the cracking distresses found on section CA 1-3, as well as the stress range approach in this case.

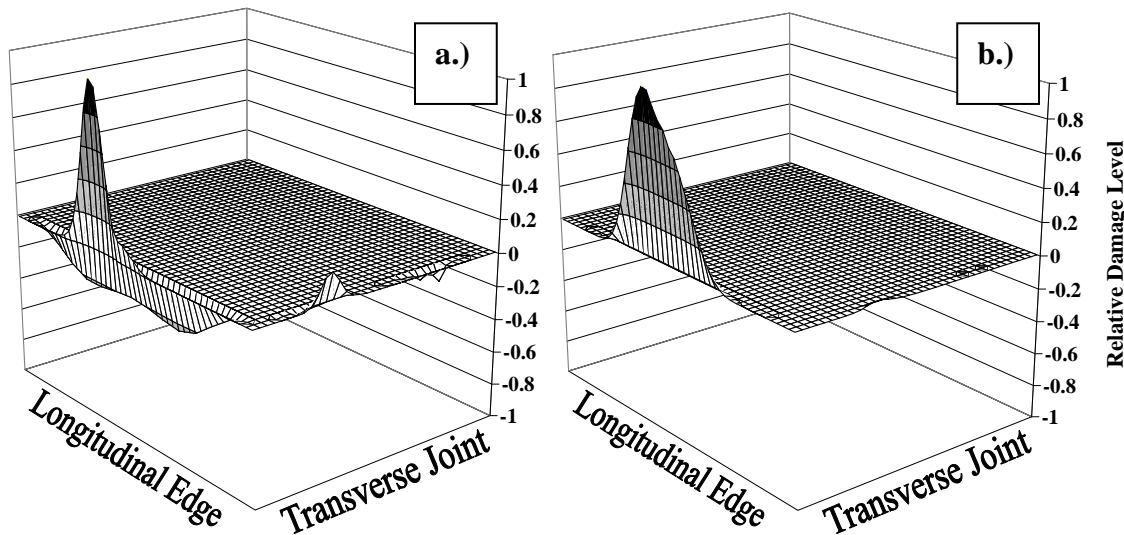


Figure G.2. Relative damage profile using linear temperature profiles of Section CA 1-3 with (a.) stress range and (b.) MEPDG maximum stress damage analysis.

#### G.2.1.2 Nonlinear Analysis

Using the piecewise method for assessing self-equilibrating stresses from nonlinear temperature profiles, the damage profiles in Figure G.3 were developed. Figure G.3a represents the damage profile using the stress range approach, while Figure G.3b indicates the predicted fatigue damage profile using the MEPDG maximum stress fatigue approach (ARA, 2007). Interestingly, both of these profiles focus the critical damage top-down near midslab. However, the MEPDG maximum stress transfer function for fatigue does predict a slight amount of damage between the wheel paths, while the stress range fatigue approach predicts little fatigue damage at locations outside the mid-slab edge area. Just as with the linear temperature damage profile predictions from Figure G.2a using stress range, the damage profile using the nonlinear MEPDG function matches the magnitude of longitudinal cracking that is exhibited in section CA 1-3 most closely.

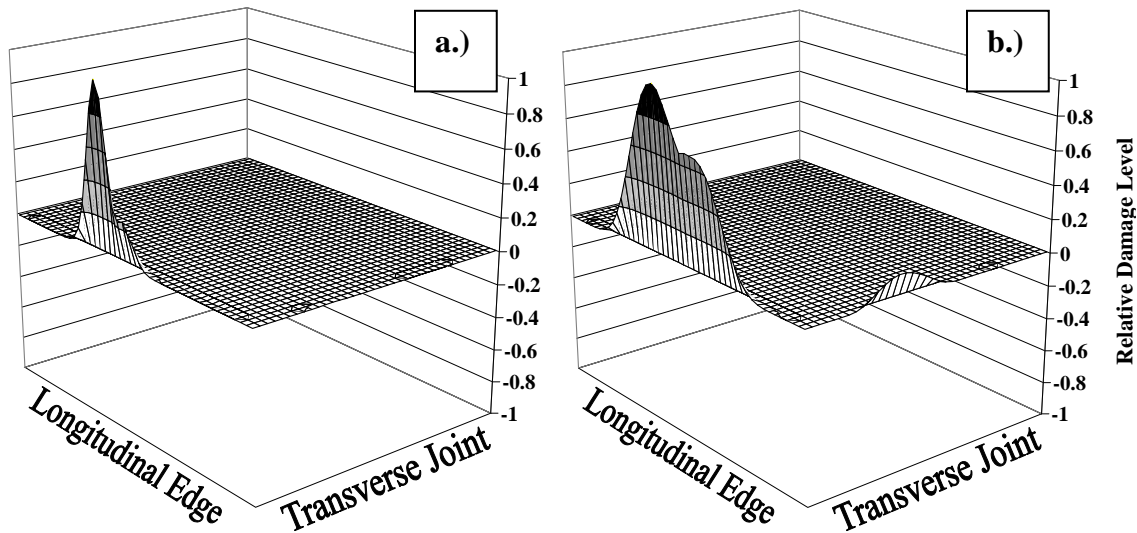


Figure G.3. Relative damage profile using nonlinear temperature profiles of Section CA 1-3 with (a.) stress range and (b.) MEPDG maximum stress damage analysis.

## G.2.2 Section CA2-3

Section CA2-3 is a 918-ft section of a larger test section on eastbound I-210 in Los Angeles, California (South Coast climatic region). It was built in 1980 as a jointed plain concrete pavement with random joint spacing (12, 13, 19, and 18 ft) and a 12-ft slab width with an asphalt shoulder just as with the section CA1-3 in Tracy. The slabs were also designed to be 8.4-in. on top of a 5.4-in. cement-treated base and a 24-in. aggregate subbase. The joints were designed to be skewed with no load transfer devices. The results of the condition survey and falling weight deflectometer testing can be seen in Table G.1.

### G.2.2.1 Linear Analysis

Using the previously mentioned backcalculation procedure, the EBITD value was determined from the 1987 FWD testing to be -11°F. Again using site-specific information (Los Angeles climate zone), including load spectra, the damage profile in Figure G.4 was developed. Even with the extremely low load transfer values (less than 20%), the relatively small EBITD value forces the maximum damage to be at the bottom of the slab, mid-way between the joints. The damage levels at the transverse joint are negligible and would not result in prediction of longitudinal cracking. This correlates quite well with the condition survey of CA 2-3 which noted that roughly two-thirds of slabs cracked transversely and no longitudinal cracking. Slight reduction of the strength at the top of the slab made little difference in this case, as the top-down fatigue damage was still negligible. While these two sections (CA 1-3 and CA 2-3) had the same structural designs, the difference in climate zone and EBITD from construction and shrinkage effects would predict (and verify) quite different failure locations.

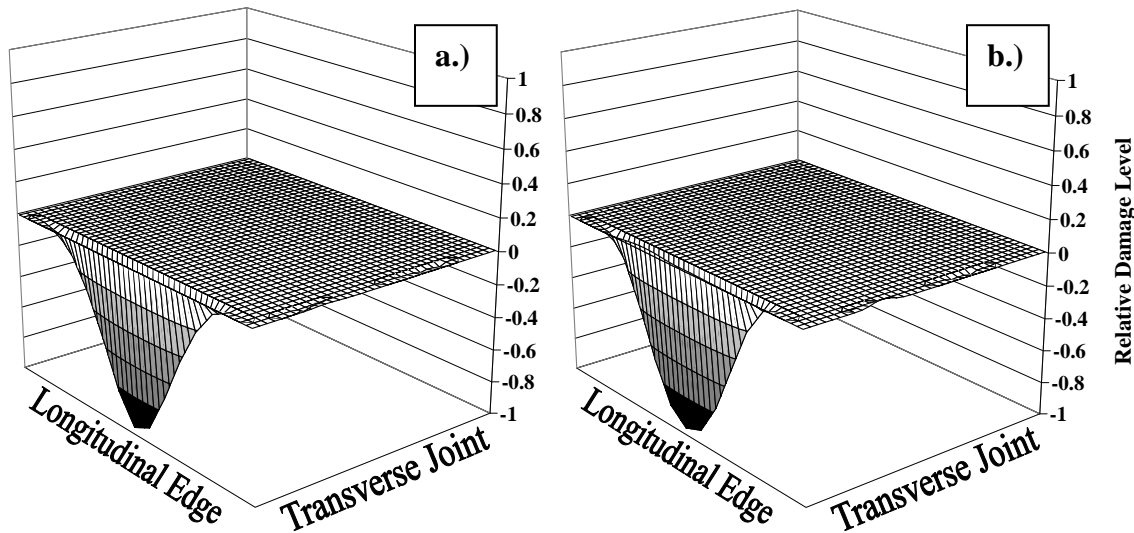


Figure G.4. Relative damage profile using linear temperature profiles of Section CA 2-3 with (a.) stress range and (b.) MEPDG maximum stress damage analysis.

#### G.2.2.2 Nonlinear Analysis

Using the input parameters for section CA 2-3 in RadiCAL with nonlinear temperature profile assumption, a slightly different damage profile is predicted as seen in Figure G.5. In Figure G.5a, the Tepfers' stress range approach is used and predicts results similar to the linear analysis with stress range (Figure G.4a) and linear temperature differences. The focus on this damage profile reveals a high probability of bottom-up cracking along a large portion of the slab, initiating from the longitudinal edge.

If a maximum stress approach using the MEPDG fatigue function is used in combination with nonlinear temperature for this site (Figure G.4b), the resulting predicted damage profile is much different with high damage levels in multiple locations that could initiate as top-down or bottom-up transverse cracking or even top-down longitudinal cracking in the wheelpath closest to the shoulder. For this particular site, the flip-point from bottom-up to top-down fatigue damage becoming critical is between an EBITD of  $-10^{\circ}\text{F}$  and  $-15^{\circ}\text{F}$ . Since this scenario is approaching this flip-point for nonlinear temperature cases, the damage profile has multiple locations of high-fatigue damage potential. However, this does not match the transverse-only cracking noted on section CA 2-3 (see Table G.1) as the stress range approach does.



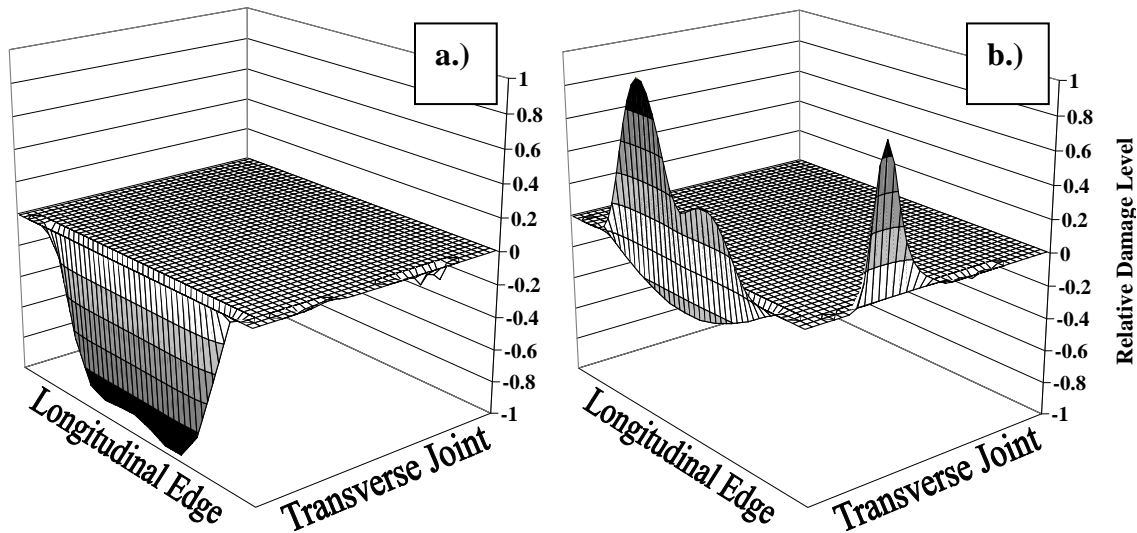


Figure G.5. Relative damage profile using nonlinear temperature profiles of Section CA 2-3 with (a.) stress range and (b.) MEPDG maximum stress damage analysis.

### G.3. UCPRC Sections

The University of California Pavement Research Center (UCPRC) has overseen a vast data acquisition process conducted by Stantec for numerous flexible, rigid, and composite pavement sections within the state of California. Correspondingly, the UCPRC has shared much of this data to conduct some trial design verification studies of RadiCAL. From this data, nine sections of in-service jointed plain concrete pavements (Table G.2) with a variety of fatigue cracking mechanisms were analyzed using site-specific climatic data, EBITD, geometry, and load spectra (where available) in RadiCAL and compared with the actual cracking patterns noted during recent condition surveys conducted by Stantec for UCPRC. The general location of these sections in California can be seen in Figure G.6. While all nine of these sections are within 100 miles of each other, they represent three climatic zones of northern California.

Table G.2. Inventory Data for Nine UCPRC JRCP Sections.

<b>Section #</b>	<b>Route / Direction</b>	<b>County</b>	<b>Climatic Region</b>	<b>PCC Thickness (in.)</b>	<b>Base Thickness (in.) / type</b>	<b>Subbase Thickness (in.)</b>	<b>Joint Spacing (ft)</b>
<b>04-N201</b>	CA-85 NB	Santa Clara	Bay Area	10	3 / AC	24	14
<b>04-N249</b>	I-80 EB	Solano	Central Valley	10	3 / CTB	20	14
<b>04-N250</b>	I-80 EB	Solano	Central Valley	10	4 / CTB	10	14
<b>04-N251</b>	I-80 EB	Solano	Central Valley	8.5-10	4 / CTB	N/A	12,17
<b>04-N252</b>	I-80 EB	Solano	Central Valley	8.5	7.5 / CTB	6	14
<b>04-N253</b>	I-80 EB	Solano	Central Valley	10	7.5 / CTB	10	15
<b>04-N282</b>	US-101 NB	Sonoma	North Coast	11.25-11.75	2 / AC	7	13, 15, 12, 14
<b>04-N284</b>	US-101 NB	Sonoma	North Coast	10	4.5 / AC	6	13, 15, 12, 14
<b>04-N288</b>	US-101 SB	Sonoma	North Coast	9.5-10	4.5 / AC	14	13, 15, 12, 14

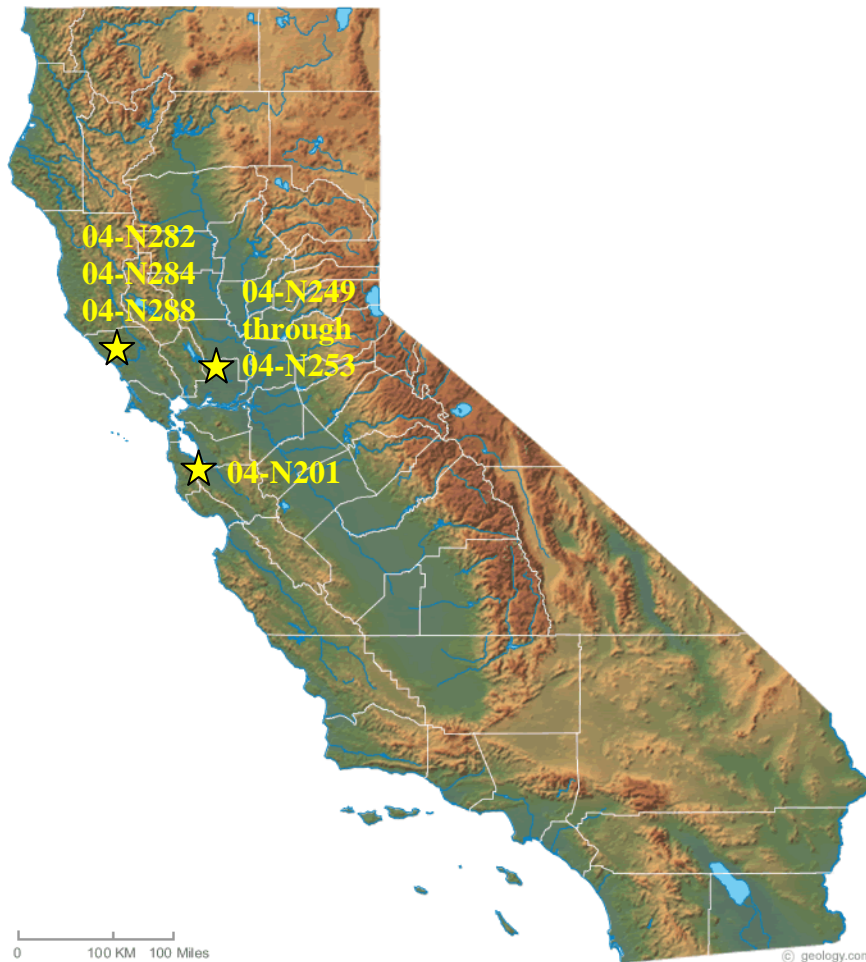


Figure G.6. General locations of UCPRC JPCP design verification sections.

Each of these nine UCPRC sections exhibit varying types and levels of fatigue-related distresses, as seen in Table G.3. Each of these sections was analyzed using RadiCAL using both linear and nonlinear temperature profiles under both stress range (Tepfers, 1979) and maximum stress (ARA, 2007) fatigue damage approaches, to attempt to match predicted and observed distresses on these sections. Table G.3 also shows that the average calculated load transfer across the transverse joints in these sections is in a range similar to that of the RPPR sections previously analyzed, with the exception of section 04-N288 at 80%. The low load transfer between slabs is expected, as all of these sections are undoweled and rely only on aggregate interlock for reducing stresses and deflections at the joints. These sections also exhibit a wide range of backcalculated EBITD values from a moderate -7°F to a highly curled -25°F from backcalculation of FWD tests.

Table G.3. Cracking Mechanisms, Severities, and FWD Backcalculated Values for Nine UCPRC JRCP Sections from Stantec Data Collection.

Section #	Transverse (% slabs cracked)	Longitudinal (% slabs cracked)	Corner (% slabs cracked)	Average EBITD (°F)	Average LTE (%)	Average k-value (psi/in.)
04-N201	3	--	6	-25	30	150
04-N249	14	14	8	-24	30	100
04-N250	56	28	11	-7	35	225
04-N251	64	25	8	-15	40	125
04-N252	11	--	8	-7	40	100
04-N253	82	88	9	-9	50	150
04-N282	3	--	3	-14	30	200
04-N284	6	11	3	-10	50	200
04-N288	6	--	3	-20	80	150

### G.3.1 Section 04-N201

Section 04-N201 is a 500-ft segment located between mile posts (MP) 13.90 and 14.01 on northbound California State Route 85 (CA-85), just southwest of San Jose in Santa Clara County (Bay Area climate). This section consisted of a 14-ft skewed joint spacing with standard 12-ft lane widths and an asphalt shoulder. Analysis of cores and design records revealed this section as a 10-in. PCC slab resting on a 3-in. AC base and 24-in. aggregate subbase. Condition surveys at this site show that a small amount of transverse and corner cracking exists on this 500-ft section, as seen in Figure G.7. However, the majority of the section is in excellent condition less than 15 years from construction (Table G.3).



Figure G.7. Corner cracking on section 04-N201 on CA-85NB in Santa Clara County, California.

Backcalculation of FWD testing at this site indicates highly curled slabs at EBITD of -25°F after accounting for the actual slab temperature gradient during the FWD testing. Several researchers have noted higher built-in curl levels for concrete slabs without restraint from dowels or tied PCC shoulders (Poblete et al., 1988, 1990; Byrum, 2000; S. Rao and Roesler, 2005b; C. Rao et al., 2001). FWD testing analysis also shows an average load transfer across the transverse joints at about 30% due to the absence of dowels in the joints.

### G.3.1.1 Linear Analysis

The damage profiles in Figure G.8 were developed using linear temperature differences in conjunction with site-specific load transfer, geometry, and boundary conditions for section 04-N201 in RadiCAL. Since site-specific load spectra was not available on CA-85, the average load spectra and vehicle class distribution for all of California were used in these analyses (see Appendix C).

In Figure G.8a, using the stress range fatigue damage approach, the damage profile suggests transverse or corner cracking developing near the corners of the slab in question. Since a high level of damage exists at both the transverse joint and longitudinal edge near the corner, the potential for corner cracking is increased. This profile tends to match the few slabs in this section that have exhibited cracking (3% of slabs transversely cracked and 6% of slab cracked at the corner).

The maximum stress approach with linear temperature differences does not necessarily match existing distresses well, as seen in Figure G.8b, since only top-down transverse cracking near midslab is exhibited. However, due to the limited number of cracked slabs in this section, it is difficult to conclude that a maximum stress approach is not valid.

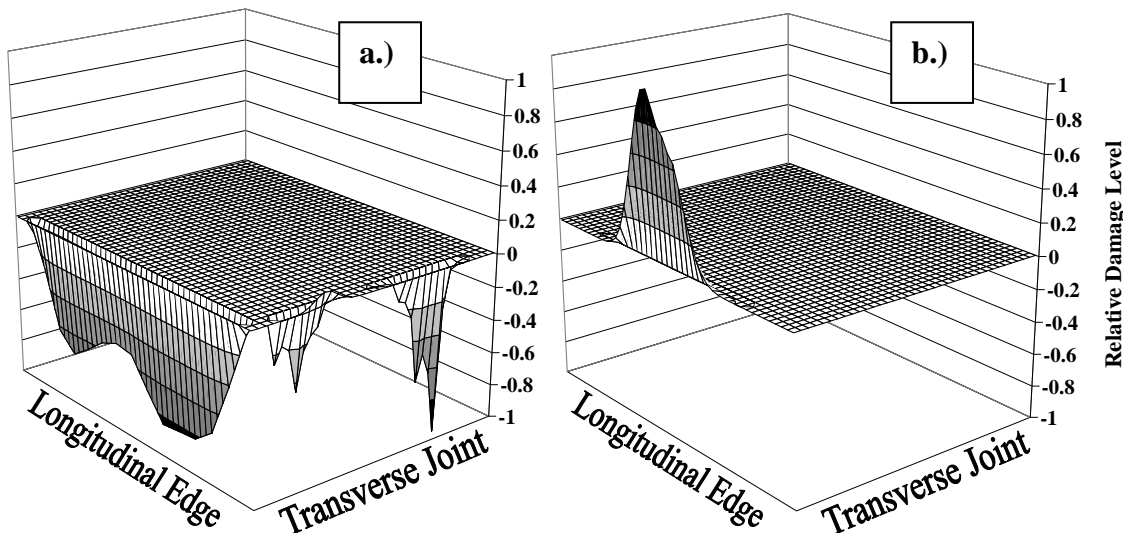


Figure G.8. Relative damage profile using linear temperature profiles of section 04-N201 with (a.) stress range and (b.) MEPDG maximum stress damage analysis.

### G.3.1.2 Nonlinear Analysis

Using the nonlinear temperature profiles with the piecewise self-equilibrating stresses for the Bay Area climatic region, RadiCAL reveals damage profiles (see Figure G.9) similar to the linear temperature option above. Thus, for section 04-N210, the stress range approach seems to better match the existing damage profiles based on the limited cracking exhibited in this section. It should be noted that, while the damage profiles appear to be similar for both the linear and nonlinear temperature analyses, the absolute damage levels for the nonlinear profiles are about 2.2 and 48 times greater than the corresponding linear profiles using stress range and



maximum stress fatigue damage approaches, respectively. Thus, the timing of the crack initiation prediction would be greatly affected by the choice of fatigue transfer function, as well as by how temperature stresses are accounted for in the fatigue analysis.

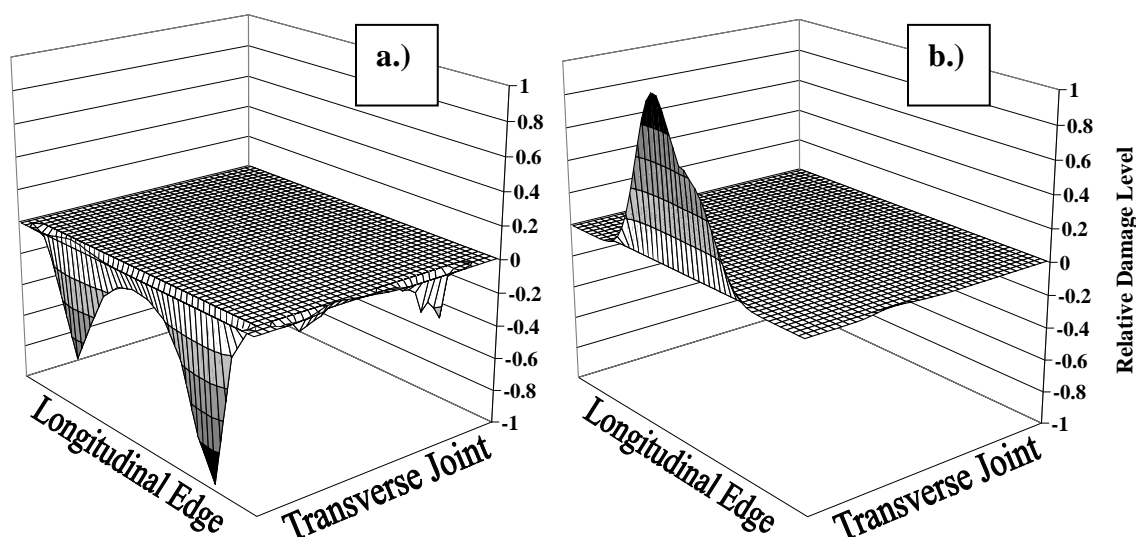


Figure G.9. Relative damage profile using nonlinear temperature profiles of section 04-N201 with (a.) stress range and (b.) MEPDG maximum stress damage analysis.

### G.3.2 Section 04-N249

Section 04-N249 is located between MP 19.56 and 19.67 on eastbound Interstate 80 in Solano County, between San Francisco and Sacramento (Central Valley climate). This section consisted of a 14-ft skewed joint spacing with standard 12-ft lane widths and an asphalt shoulder. This 500-ft section consists of a 10-in. PCC slab resting on a 4-in. cement-treated base (CTB) and 20-in. aggregate subbase. Constructed in 1965, this section of I-80 has been in service for over 40 years and has had several fatigue-related cracking distresses develop over this time, as seen in Figure G.10. Table G.3 indicates that 14% of slabs are cracked transversely, 14% of slabs are cracked longitudinally, and 8% of slabs exhibit corner cracking on this site, all in varying stages of severity. Backcalculation of FWD data indicates that this site has an average EBITD value of -24°F, which suggests a large amount of slab lift-off at the corners at most times during any given day.



Figure G.10. Transverse, longitudinal, and corner cracking on section 04-N249 on I-80EB in Solano County, California.

### G.3.2.1 Linear Analysis

Since EB I-80 has a nearby WIM station, site-specific load spectra was used in this and all other RadiCAL analyses for the I-80 sections (04-N249 through 04-N253). This site had some positive attributes, in that a significant amount of cracking initiated sufficient to make a solid judgment on the types of cracking expected, while enough uncracked slabs existed so that a proper determination of the EBITD for this section could be made.

An interesting characteristic is that all of the transverse cracks on this site appear to initiate along the longitudinal edge of the slab and begin closer to the leave joint of the slab (back of the damage profile) than to the approach joint (front of the damage profile). This would indicate that cracking did not initiate from the bottom-up mid-slab maximum stress location predicted by traditional damage analyses, which are dominated by single-axle critical stresses. Figure G.11a and b exhibit the predicted damage profiles using stress range and maximum stress fatigue accumulation approaches, respectively. Both fatigue damage methods predict alternative failure modes for transverse cracking for this site. However, only the stress range approach (Figure G.11a) indicates some significant amount of damage along the transverse joint that could initiate as either longitudinal or corner cracking (bottom-up), depending on the crack propagation direction into the interior of the slab. This stress range approach also matches the location of the potential longitudinal cracking along the inside wheel path.

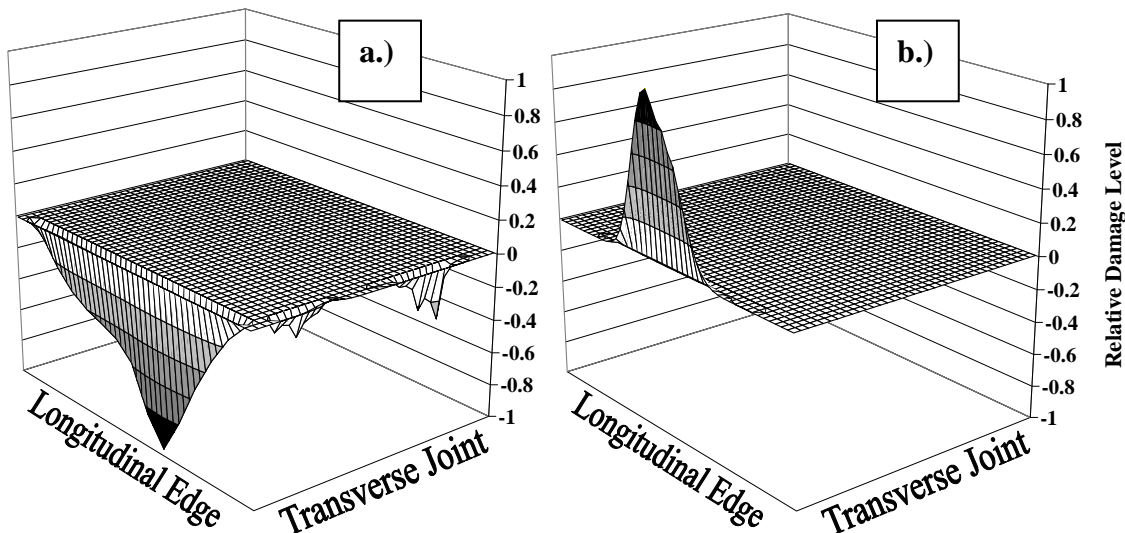


Figure G.11. Relative damage profile using linear temperature profiles of section 04-N249 with (a.) stress range and (b.) MEPDG maximum stress damage analysis.

### G.3.2.2 Nonlinear Analysis

The analyses of section 04-N249 using nonlinear temperature yield the damage profiles in Figure G.12. These profiles match the linear temperature approaches fairly well, with the exception that no significant fatigue damage occurs along the transverse joint in the stress range approach. For this section, the nonlinear profiles are about 1.6 and 145 times greater than the corresponding linear profiles using stress range and maximum stress fatigue damage approaches, respectively. Again, this would greatly affect the timing of the predicted crack initiation, as the self-equilibrating stresses generally exacerbate the top of the slab stresses when considering the maximum stress only in the fatigue transfer function. The use of stress range in addition to self-equilibrating stresses fatigue complicates this relationship, as both the stress ratio and ratio of minimum to maximum stress is affected by accounting for nonlinear temperature profiles.

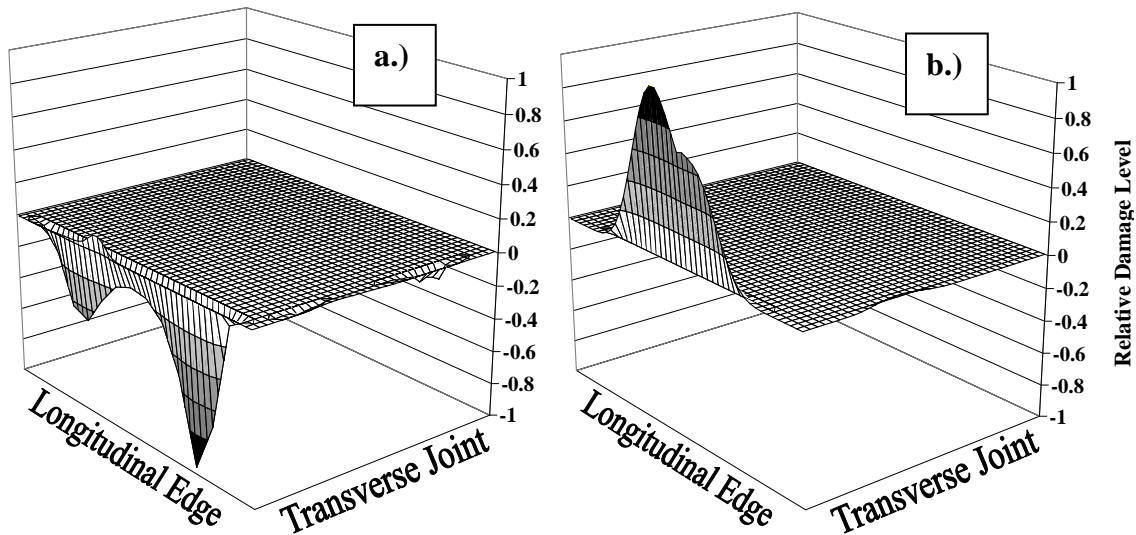


Figure G.12. Relative damage profile using nonlinear temperature profiles of section 04-N249 with (a.) stress range and (b.) MEPDG maximum stress damage analysis.

### G.3.3 Section 04-N250

Roughly one mile east of section 04-N249, section 04-N250 is another 500-ft segment located between MP 20.52 and 20.63 on eastbound I-80 (Central Valley climatic zone). This section consisted of a 14-ft skewed joint spacing with standard 12-ft lane widths and an asphalt shoulder. Analysis of cores and design records revealed that this section is a 10-in. PCC slab resting on a 4-in. CTB and a 10-in. aggregate subbase.

Transverse cracks were found to be consistently nearer the leave joint of the slab in section 04-N250. Analysis using RadiCAL would indicate this crack location to be more in line with top-down cracking mechanisms found in high EBITD-level scenarios due to steer-drive axle spacing effects. Visual analysis of the site reveals 56% of slabs with transverse cracks, 28% of slabs with longitudinal cracks, and 11% of the slabs exhibiting corner cracking (Figure G.13). A closer look at many of these slabs also indicates the transverse cracks to be the initial cracks that formed, with the longitudinal and corner cracking appearing at a later date, as many of these cracks become arrested as they intersect the transverse cracks.

Backcalculation of FWD data indicates only a minimal level of EBITD (-7°F). Since very few slabs in this section are fully intact and many of the cracked slabs are of high severity, the calculation of EBITD did not have many replicates. There is less confidence in the backcalculated values obtained from this section, but they may be corrected as shown in the next section.





Figure G.13. Transverse, longitudinal, and corner cracking on section 04-N250 on I-80EB in Solano County, California.

#### G.3.3.1 Linear Analysis

RadiCAL was again used to analyze an I-80 section with site-specific load spectra, geometry, load transfer, and boundary conditions. The resulting damage profiles using linear temperature differences are shown in Figure G.14a for stress range fatigue and Figure G.14b for maximum stress fatigue. In both of these figures, the damage profile predicts only bottom-up, mid-slab transverse cracking as traditionally found from analyses going back to the 1920s (Westergaard, 1927). This is due to the low EBITD value of  $-7^{\circ}\text{F}$  found from the limited FWD data.

Cracking patterns for this site more closely match analyses using larger EBITD values, such as that from section 04-N249, roughly one mile west of this section. However, due to a lack of FWD data to validate this level of EBITD, it must be concluded that RadiCAL cannot match all of the cracking mechanisms seen in this field section. However, since most of the longitudinal and corner cracks on this site appear to be secondary in nature, it is possible that the transverse cracks on this section could have developed from the bottom of the slab and fully propagating across the slab, as predicted by RadiCAL. These subsequent shorter “slabs” would alter the intact slab stress states and lower bending stresses that would produce less transverse cracking. Due to this phenomenon, the critical damage location could switch to along the transverse joint. This could potentially form these longitudinal and corner cracks that propagate until they reach the structural transverse cracks, as noted in the field evaluation of site 04-N250 (see Figure G.13).

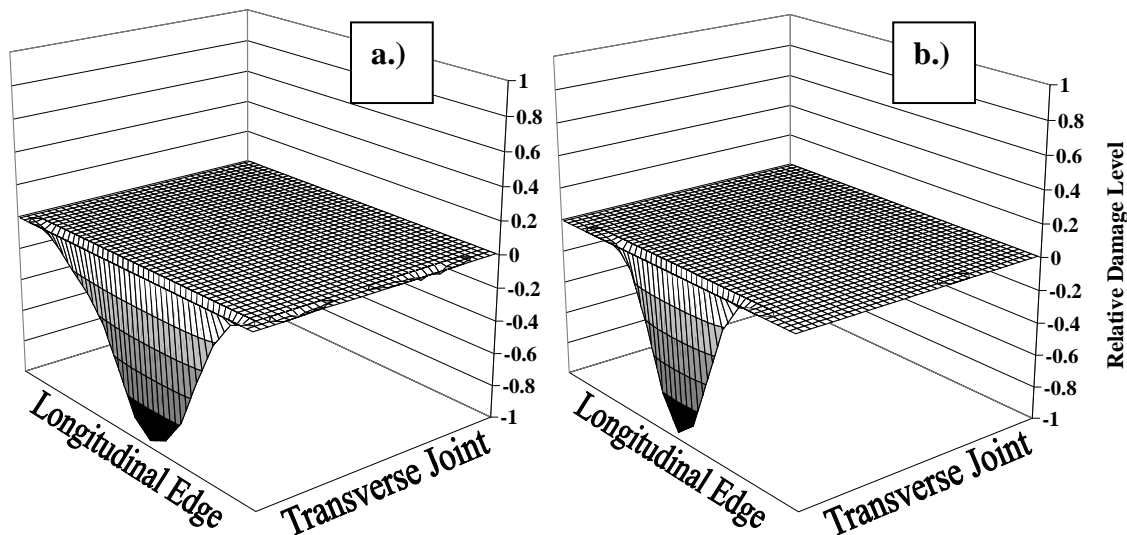


Figure G.14. Relative damage profile using linear temperature profiles of section 04-N250 with (a.) stress range and (b.) MEPDG maximum stress damage analysis.

#### G.3.3.2 Nonlinear Analysis

Using nonlinear temperature profiles and their associated self-equilibrating stresses for section 04-N250, the damage profiles in Figure G.15 are developed in RadiCAL. While the stress range approach (see Figure G.15a) yields results very similar to its linear temperature analysis counterpart, the use of a maximum stress approach to fatigue finds a different mechanism of fatigue failure (see Figure G.15b). If the initial transverse cracking on section 04-N250 was found to be top-down in nature, this would not change the process that would cause secondary longitudinal and corner cracking on this site. It should be noted that the maximum stress analysis using the MEPDG fatigue transfer function with nonlinear temperature does predict critical damage to be closer to the leave joint and thereby provides a more accurate representation of cracking location in this case. While the critical absolute damage of the nonlinear profile using stress range is quite close (86% of the linear corresponding profile), the ratio of nonlinear to linear absolute damage using a maximum stress fatigue approach is only 2.6. Thus, the predicted timing of cracking using either linear or nonlinear temperature profile assumptions would be quite similar for this section.

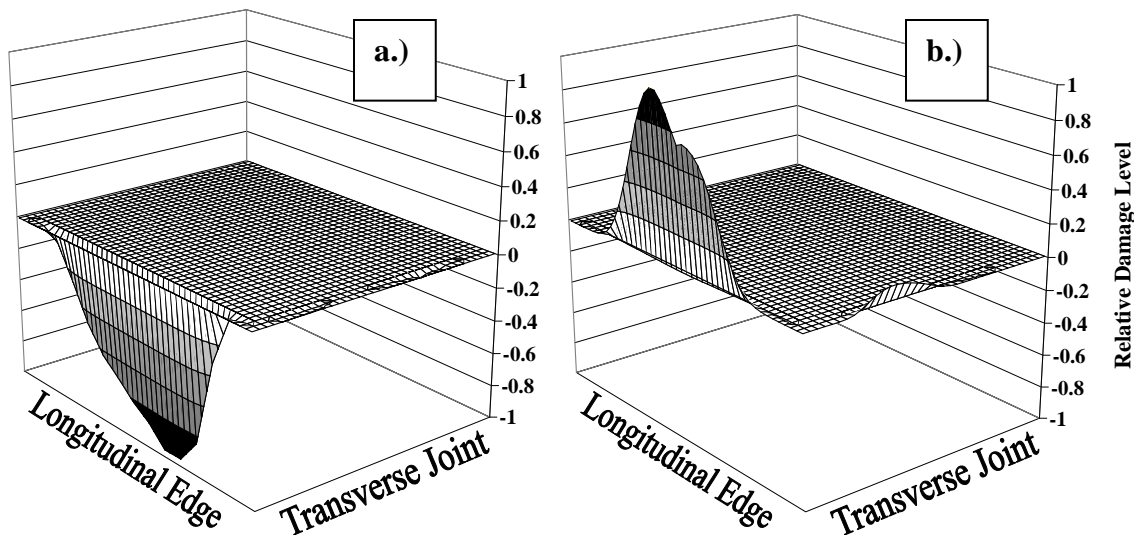


Figure G.15. Relative damage profile using nonlinear temperature profiles of section 04-N250 with (a.) stress range and (b.) MEPDG maximum stress damage analysis.

#### G.3.4 Section 04-N251

Another five miles east of section 04-N250 is section 04-N251 between MP 25.59 and 25.69 on eastbound I-80 in the Central Valley climatic zone. This section varies from the others previously mentioned on I-80 in that repeated 12- and 17-ft skewed joint spacing exist with a standard 12-ft lane width and asphalt shoulder. The thickness of the PCC slab ranges from 8.5 to 10 in. and rests on a 4-in. CTB with an unknown subbase thickness or condition. This section predates the previously analyzed I-80 sections, as it was originally constructed in 1952, with a widening of the outside lane in 1963.

As with section 04-N250, the transverse cracking patterns were near midslab, but consistently closer to the leave joint, indicating potential for top-down cracking mechanisms. Section 04-N251 also exhibited numerous cracking mechanisms (Figure G.16), with 64% of slabs with transverse cracks, 25% of slabs with longitudinal cracks, and 8% of slabs with corner cracks. Just as with section 04-N250, the transverse cracks were of the highest severity and appeared to be the primary cracking mechanism, with longitudinal and corner cracks forming at a later date. These transverse cracks were more prevalent on the 17-ft length slabs, although transverse cracking also existed on some of the shorter 12-ft slabs as well.

The backcalculated EBITD value was found to be  $-15^{\circ}\text{F}$ , but again, this was with a limited number of intact slabs. Due to more 12-ft slabs being intact, this level of EBITD may not be completely representative of the longer 17-ft joint spacing slabs.



Figure G.16. Transverse and longitudinal cracking on section 04-N251 on I-80EB in Solano County, California.

#### G.3.4.1 Linear Analysis

Due to the two-joint spacing used on site 04-N251, fatigue damage analyses were conducted for a shorter joint spacing (Figure G.17) and longer joint spacing (Figure G.18) using linear temperature profiles. Just as with section 04-N250, the primary damage mechanism in fatigue is predicted to be bottom-up transverse cracking. This is true for both fatigue transfer functions, as well as both joint spacings.

Also like section 04-N250, the process of longitudinal and corners cracks forming after initiation of a full-length transverse crack developed is definitely possible. This would help explain the presence of a large percentage of alternative cracking mechanisms forming from the transverse joint. However, it should be noted that most transverse cracks are not at midslab for the longer joint spacing, but instead are between the midslab and leave joint of the slab. This would indicate non-traditional top-down transverse crack formation, as seen in Figure G.18. For the shorter 12-ft slab lengths, transverse cracks appeared to be closer to midslab for the few occurrences noted, which matches both fatigue damage accumulation methods shown in Figure G.17 well.

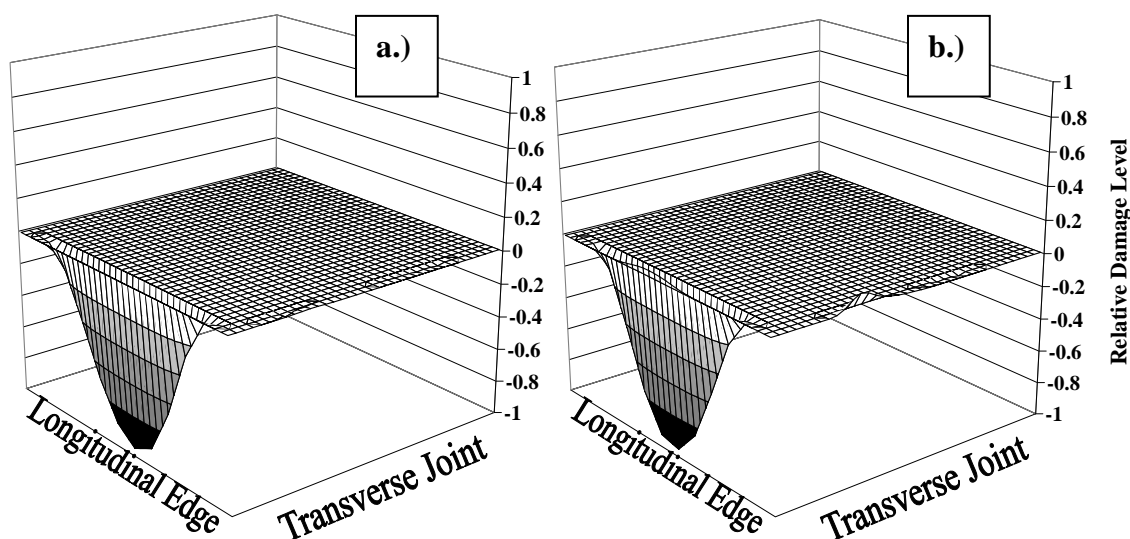


Figure G.17. Relative damage profile using linear temperature profiles of section 04-N251 at 12-ft joint spacing with (a.) stress range and (b.) MEPDG maximum stress damage analysis.

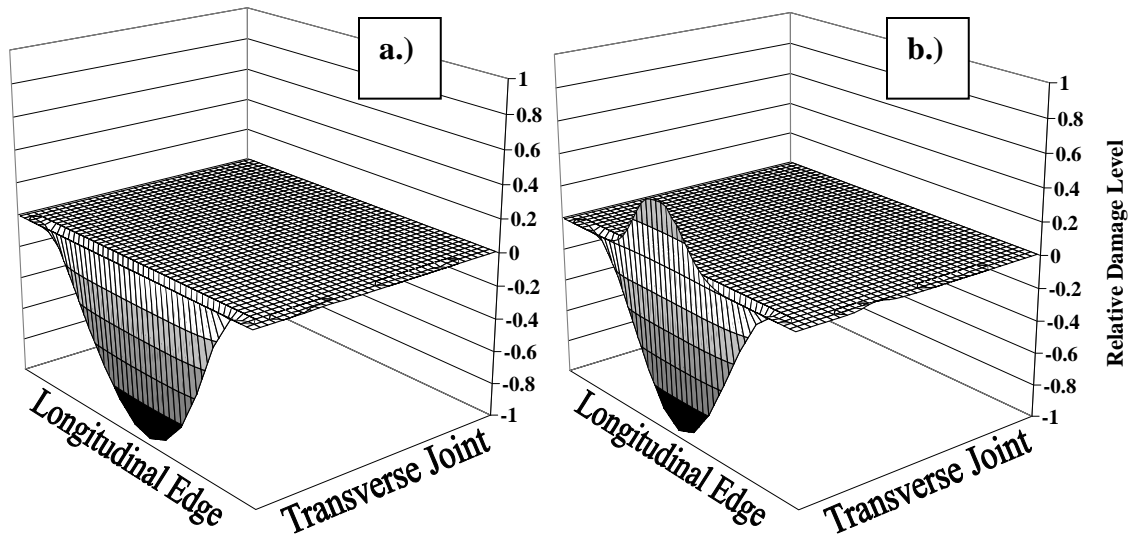


Figure G.18. Relative damage profile using linear temperature profiles of section 04-N251 at 15-ft joint spacing with (a.) stress range and (b.) MEPDG maximum stress damage analysis.

#### G.3.4.2 Nonlinear Analysis

Using nonlinear temperature analysis for the short (Figure G.19) and long (Figure G.20) JPCP joint spacing yield damage profiles that exhibit cracking in both traditional and alternative mechanisms. Figure G.19a uses stress range fatigue for the shorter 12-ft slabs and predicts only bottom-up transverse cracking over a wide area, with the critical damage near the approach joint. Changing the transfer function to accommodate maximum stress only (Figure G.19b) in fatigue alters the damage profile so that top-down damage at the transverse joint between the wheel paths is the most critical location, but with a high probability of top-down mid-slab transverse cracking to initiate as well.

Looking at the longer slabs, the predicted fatigue damage profiles predict different mechanisms. When using stress range, bottom-up transverse cracking near the leave and approach joints is predicted (Figure G.20a). Using the maximum stress fatigue algorithm on the longer slabs, the critical damage is now top-down transverse cracking near the leave joint, but there is still a likelihood of top-down longitudinal cracking at transverse joint loading locations, as shown in Figure G.20b. In this case, both the maximum stress and stress range fatigue approach yield results that can match exhibited distresses on site 04-N251. However, the MEPDG function does predict a greater probability of longitudinal cracks forming, as seen in Figure G.16 for this site.

The timing of the linear and nonlinear crack initiation is quite different in this case. For the shorter 12-ft slabs, the ratio of absolute fatigue damage using nonlinear temperature to that of its linear counterparts is 0.8 and 17.5, respectively, for the stress range and maximum stress approaches,. For the longer slabs, these ratios are 0.57 and 27, respectively. This represents the dampening power of the stress range approach to reduce extreme damage-inducing events in a JPCP fatigue analysis to produce reasonable thicknesses regardless of temperature profile assumptions.

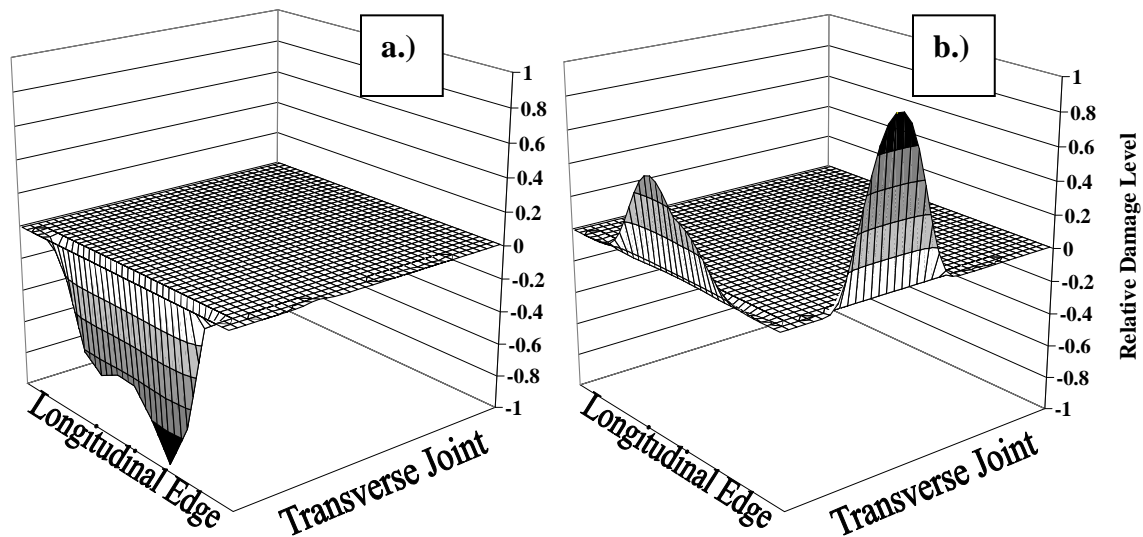


Figure G.19. Relative damage profile using nonlinear temperature profiles of section 04-N251 at 12-ft joint spacing with (a.) stress range and (b.) MEPDG maximum stress damage analysis.

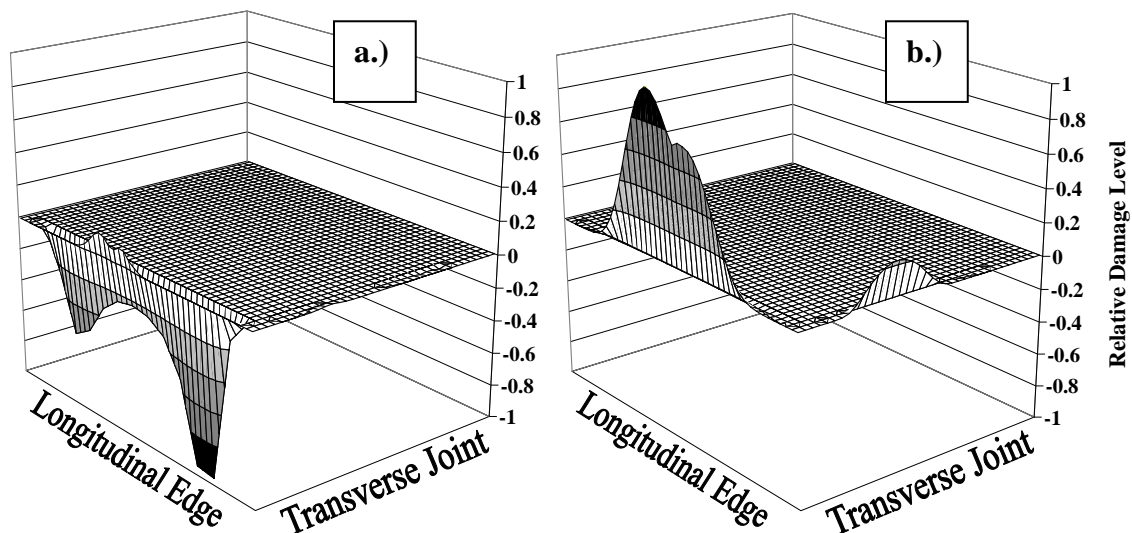


Figure G.20. Relative damage profile using nonlinear temperature profiles of section 04-N251 at 15-ft joint spacing with (a.) stress range and (b.) MEPDG maximum stress damage analysis.

### G.3.5 Section 04-N252

Section 04-N252 is a 500-ft segment located between MP 26.75 and 26.86 near section 04-N251 (Central Valley climatic zone). This section resumes the 14-ft skewed joint spacing with standard 12-ft lane widths and an asphalt shoulder. However, the PCC thickness remains 8.5 in. on a 7.5-in. CTB and a 6-in. aggregate subbase. Constructed in 1952 and widened in 1963, this section of I-80 has been in service for over 40 years, but has held up extremely well, as seen in Figure G.21. Table G.3 indicates that only 11% of slabs are cracked transversely and 8% of slabs exhibit corner cracking on this site. No longitudinal cracking exists on section 04-N252. Backcalculation of FWD data indicates that this site has a very low average EBITD value of -7°F, which would lead to the corners being supported at most times of the day.



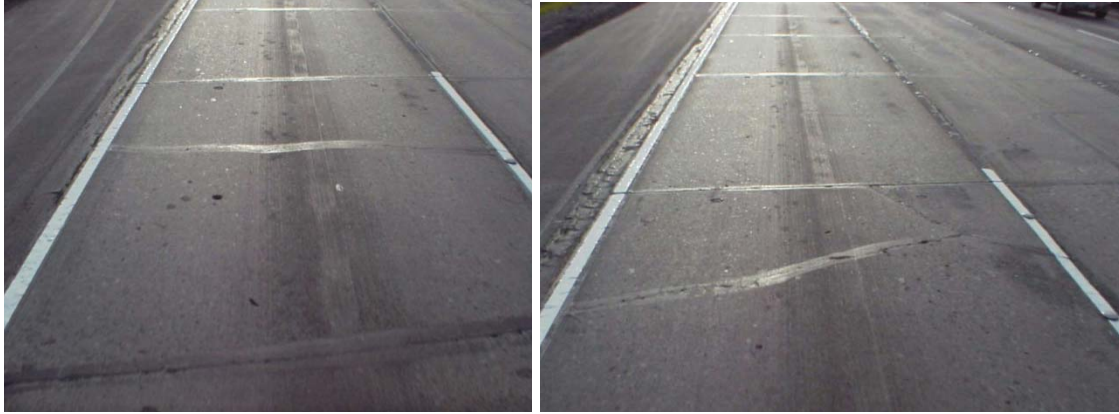


Figure G.21. Transverse and corner cracking on section 04-N252 on I-80EB in Solano County, California.

#### G.3.5.1 Linear Analysis

RadiCAL analyses using linear temperature differences from the Central Valley for section 04-N252 yield damage profiles as seen in Figure G.22. Both the stress range (Figure G.22a) and maximum stress approaches (Figure G.22b) predict transverse cracking initiating solely from the bottom of the slab due to the low EBITD level of this section. Due to the majority of slabs being in good condition, the  $-7^{\circ}\text{F}$  EBITD backcalculated for this section was verified on several slabs with little variation. While this section does exhibit transverse cracking initiating from near midslab, neither linear temperature damage profile addresses the corner cracking observed on several slabs in this section.

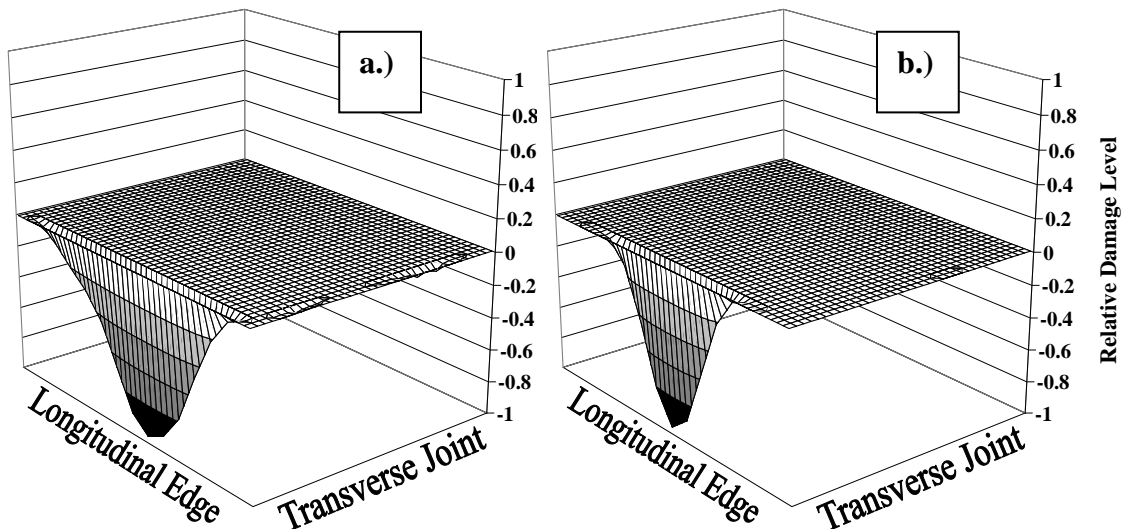


Figure G.22. Relative damage profile using linear temperature profiles of section 04-N252 with (a.) stress range and (b.) MEPDG maximum stress damage analysis.

#### G.3.5.2 Nonlinear Analysis

With nonlinear temperature profiles in the fatigue damage analysis, the predicted damage profiles were found to be fairly similar using stress range (Figure G.23a). However, the nonlinear temperature damage profile using maximum stress (Figure G.23b) indicates a significantly different profile to that of its corresponding linear temperature damage profile. The primary mechanism for damage in this case is predicted to be top-down transverse mid-slab

cracking, with a moderate probability of top-down longitudinal cracking between the wheel paths as well. Since this damage at the transverse joint could manifest itself as corner cracking if the crack propagated towards the longitudinal edge of the slab, this particular site exhibits no longitudinal cracking, and therefore, the use of maximum stress in conjunction with nonlinear temperature profiles seems to predict a more accurate cracking pattern than the other fatigue transfer function/temperature profile combinations in this case.

Due to the low EBITD level, the ratio of absolute damage of the linear temperature analyses for both the stress range and maximum stress approaches were roughly 0.86 and 2.6 times that of the nonlinear temperature cases for the stress range and MEPDG functions, respectively.

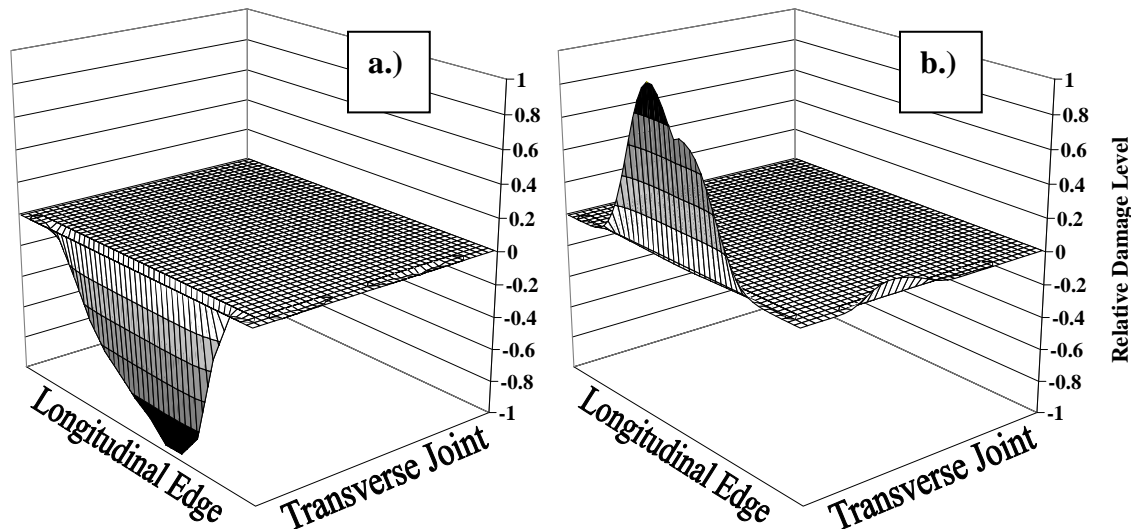


Figure G.23. Relative damage profile using nonlinear temperature profiles of section 04-N252 with (a.) stress range and (b.) MEPDG maximum stress damage analysis.

### G.3.6 Section 04-N253

Five miles east of section 04-N252 is the final eastbound I-80 section noted as section 04-253. This 500-ft segment is located between MP 30.83 and 30.94, and was originally constructed in 1946, with a widening of the outside lane in 1963, along with sections 04-N251 and 04-N252. This section consists of a 15-ft skewed joint spacing with standard 12-ft lane widths and an asphalt shoulder. Analysis of cores and design records revealed this section as a 10-in. PCC slab resting on a 7.5-in. CTB and 6-in. aggregate subbase.

Unlike the previous section, 04-N252, this 500-ft section is severely damaged with respect to fatigue cracking, with 82% of slabs with transverse cracking, 88% of slabs with longitudinal cracking, and 9% of the slabs with corner cracking. One difference between this site and previously mentioned sites with a large amount of both transverse and longitudinal cracking is that the longitudinal cracks appear to be the original fatigue failure mechanism, as most of the transverse cracks are arrested when approaching the longitudinal cracks (Figure G.24).

Only one slab was found in the 500-ft site that was fully intact for FWD backcalculation. This one slab exhibited an EBITD value of -9°F. However, this value can be deemed as fairly unreliable, as no replicates were available to assess the level of permanent built-in curling for the entire length of site 04-N253.





Figure G.24. Transverse, longitudinal, and corner cracking on section 04-N253 on I-80EB in Solano County, California.

#### G.3.6.1 Linear Analysis

Figure G.25 shows damage profiles for the linear temperature profile assumption for (a.) stress range fatigue and (b.) maximum stress approach using the MEPDG fatigue equation. In both of these cases, the only fatigue damage is concentrated at the bottom of midslab, thereby producing only transverse cracking. Since this site exhibits a large amount of longitudinal cracking that appears to be the primary cracking mechanism, neither method using linear temperature profiles match this well.

As the calculated EBITD value is quite moderate at -9°F, this predicted critical damage mechanism is not unexpected. To produce longitudinal cracking for this geometry, load spectra, climate, and shoulder type, an EBITD value around -25°F to -30°F would need to exist. Even though only one slab was fully intact for EBITD backcalculation, direct evidence does not necessarily exist that this level of EBITD previously existed on this section before fatigue cracking initiated.

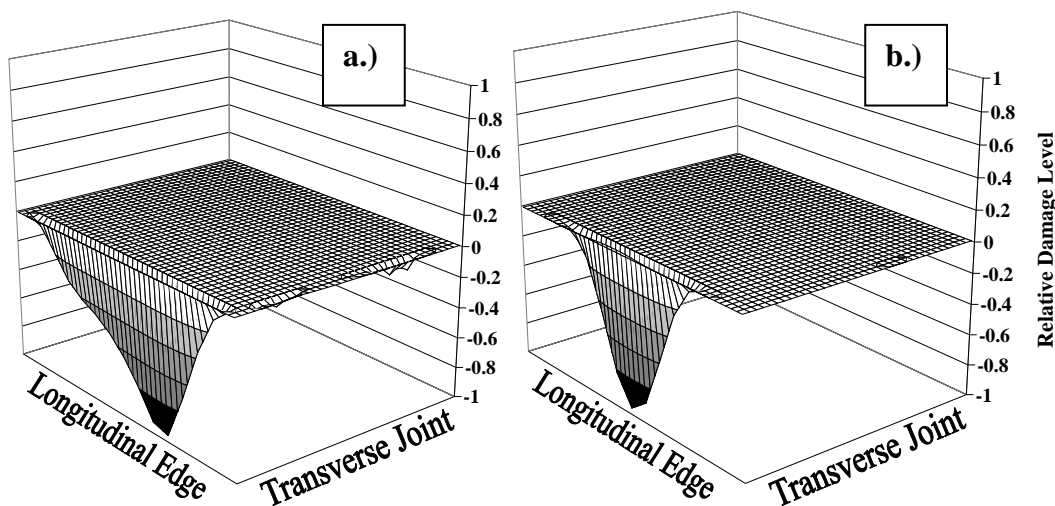


Figure G.25. Relative damage profile using linear temperature profiles of section 04-N253 with (a.) stress range and (b.) MEPDG maximum stress damage analysis.

#### G.3.6.2 Nonlinear Analysis

Just as with the linear analyses, the damage profiles using nonlinear temperature profiles (Figure G.26) do not signify significant longitudinal cracking potential for the input parameters for this section. Again, using the nonlinear temperature profiles, longitudinal

cracking damage would start to appear at a smaller EBITD value of -15°F for the maximum stress approach (Figure G.27) and for this thickness. Otherwise, it must be concluded that no RadiCAL fatigue function properly portrays these damage profiles.

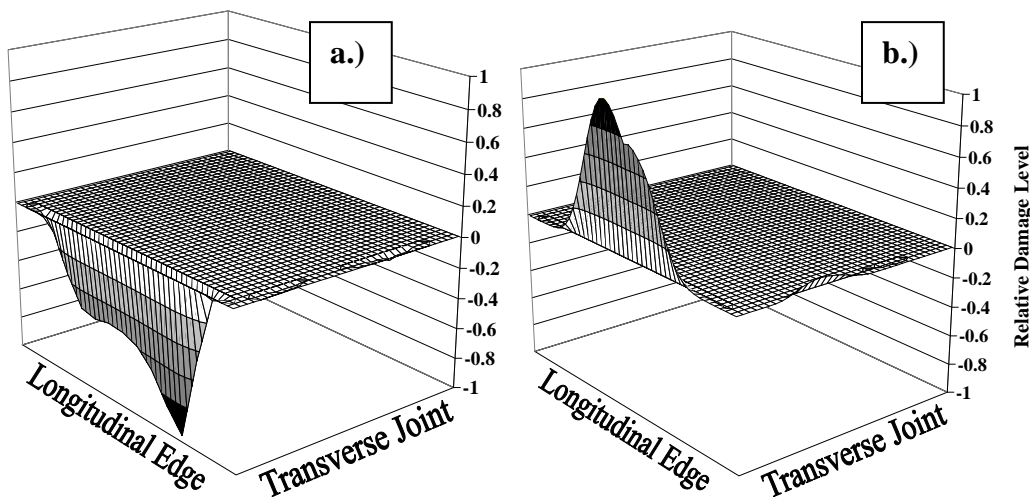


Figure G.26. Relative damage profile using nonlinear temperature profiles of section 04-N253 with (a.) stress range and (b.) MEPDG maximum stress damage analysis.

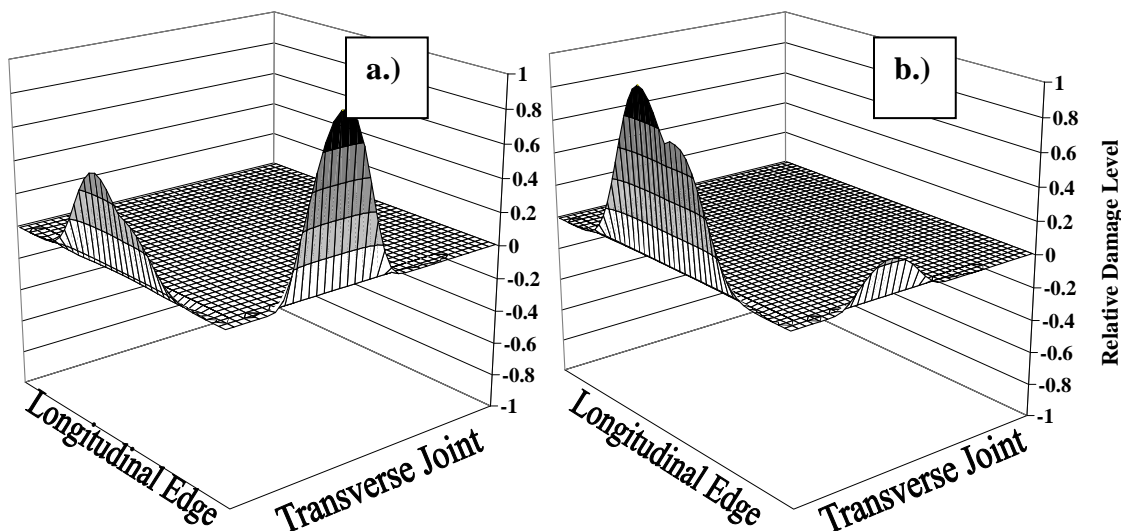


Figure G.27. Relative damage profile using nonlinear temperature profiles of section 04-N253 and an assumed EBITD value with (a.) MEPDG maximum stress damage analysis (-15°F EBITD) and (b.) MEPDG maximum stress damage analysis (-20°F EBITD).

### G.3.7 Section 04-N282

The first of three sections on US-101 is in the northbound direction and noted as section 04-N282. This section is located between MP 50.52 and 50.63, north of San Francisco in Sonoma County (North Coast climate). The PCC thickness of this section ranges from 11.25 to 11.75 in. resting on a 2-in. AC base and a 7-in. thick aggregate subbase. This section uses a repeating joint spacing pattern of 13, 15, 12, and 14 ft with standard 12-ft lane widths and an asphalt shoulder. Constructed in 1993, section 04-N282 appears in good condition overall after more than a decade of trafficking (Figure G.28). Approximately 3% of slabs are cracked transversely and 3% exhibit corner cracking (Table G.3). Currently, site 04-N282 exhibits no

longitudinal cracking. Backcalculation of FWD data indicates a moderate equivalent temperature difference due to permanent built-in curling of  $-14^{\circ}\text{F}$ .



Figure G.28. Transverse cracking on section 04-N282 on US-101NB in Sonoma County, California.

#### G.3.7.1 Linear Analysis

For 12-ft joint spacing and using linear temperature profiles, RadiCAL predicts bottom-up transverse cracking between the midslab and joints, with potential for longitudinal cracking in the wheel paths using a stress range approach for fatigue, as seen in Figure G.29a. The combination of high damage near the corner of the slab may manifest itself as bottom-up corner cracking. When using maximum stress approach to fatigue on the 12-ft slabs (Figure G.29b), the resulting damage profile exhibits potential for only bottom-up transverse cracking in a very localized area. However, unlike the stress range approach, corner cracking potential is low, as damage along multiple edges of the slab does not exist.

Figure G.30a and b show the damage profiles for the longer 15-ft slabs which exist in this repeating joint spacing section. When the joint spacing is lengthened, the stress range approach (Figure G.30a) shows a profile similar to the shorter slabs, with high longitudinal and transverse cracking potential from the bottom of the slab. However, the maximum stress approach reveals little damage at the transverse joint, thereby eliminating the potential for longitudinal cracking.

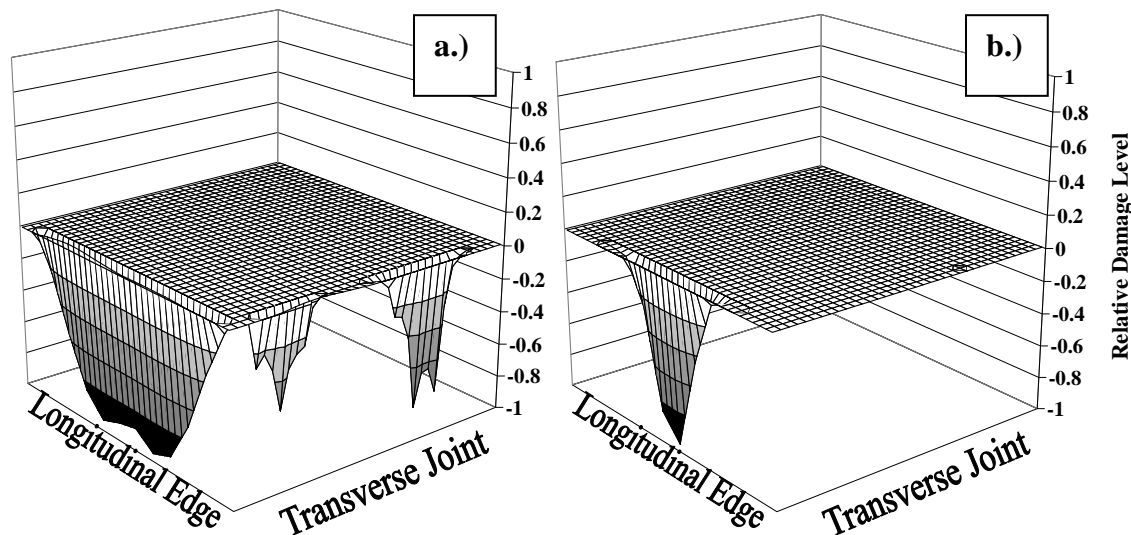


Figure G.29. Relative damage profile using linear temperature profiles of section 04-N282 at 12-ft joint spacing with (a.) stress range and (b.) MEPDG maximum stress damage analysis.

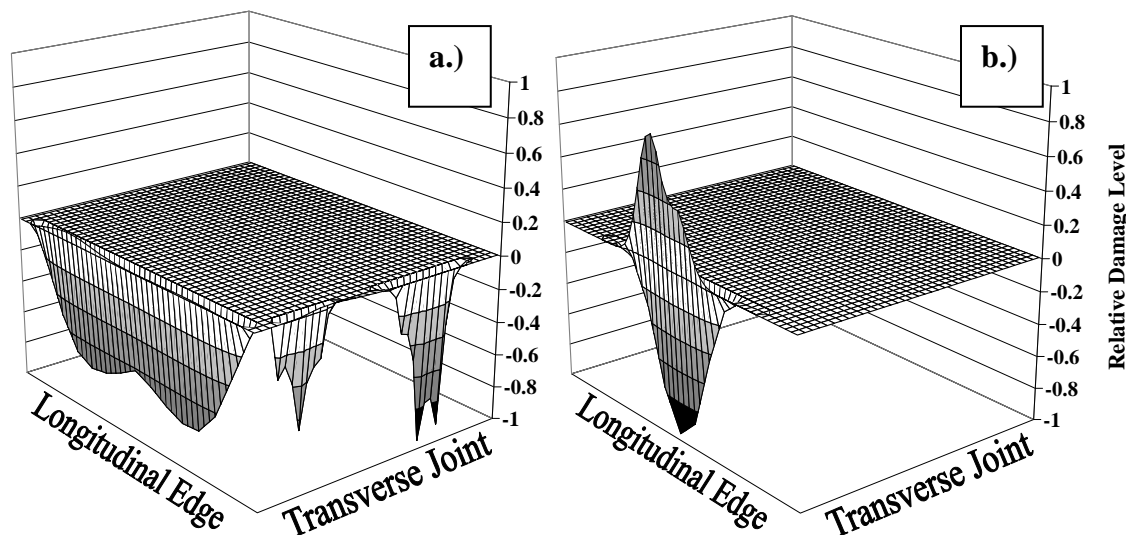


Figure G.30. Relative damage profile using linear temperature profiles of section 04-N282 at 15-ft joint spacing with (a.) stress range and (b.) MEPDG maximum stress damage analysis.

#### G.3.7.2 Nonlinear Analysis

Just as with the linear profiles for the stress range fatigue transfer function on the shorter 12-ft slabs, Figure G.31a shows a significant amount of fatigue damage for both bottom-up transverse and longitudinal cracking using the nonlinear temperature profiles. This trend is similar for the 15-ft joint spacing slabs, as seen in Figure G.32a. Due to the positioning of the damage in these cases, RadiCAL predictions for fatigue damage using stress range is conducive to bottom-up transverse cracking, with the small possibility of bottom-up corner cracking developing.

Using the maximum stress MEPDG transfer function for 12-ft slabs (Figure G.31b) and longer slabs (Figure G.32b), very little damage is shown at the transverse joint. The only major difference between the predicted transverse cracking in the short- and long-joint spacing cases is that both top-down and bottom-up transverse cracking damage is predicted on the 15-ft slabs,



unlike the 12-ft joint spacing counterpart. While this section has very little cracking and no longitudinal cracking has formed as of the most recent field survey, this fatigue transfer function does address the corner cracking (large top-down cracks) that this site exhibits for 12-ft slabs. Based on this limited data for fatigue cracking on this section, the maximum stress approach to fatigue tends to predict more accurate critical damage locations in relationship to observed distresses.

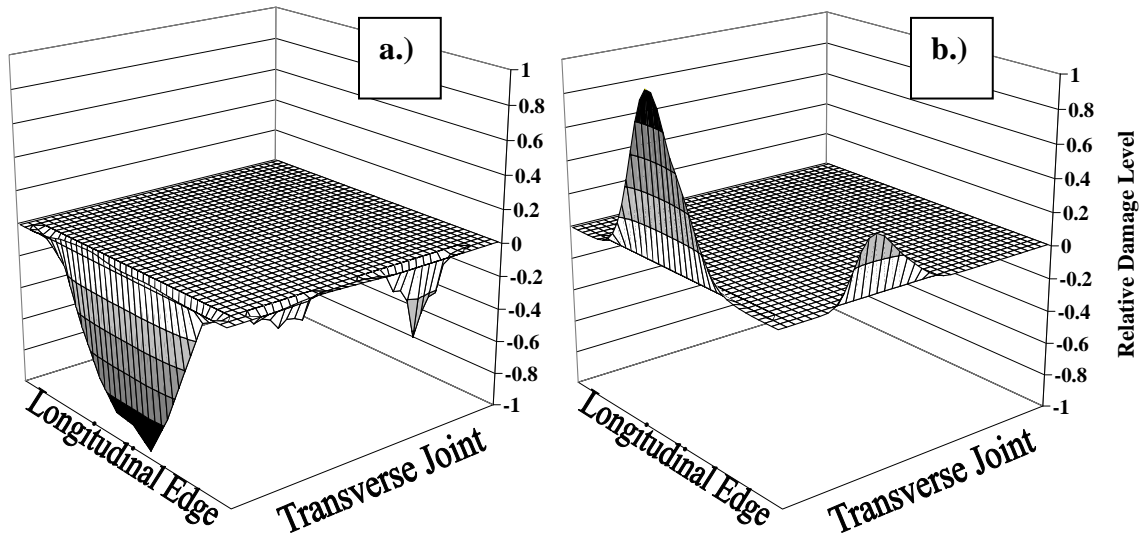


Figure G.31. Relative damage profile using nonlinear temperature profiles of section 04-N282 at 12-ft joint spacing with (a.) stress range and (b.) MEPDG maximum stress damage analysis.

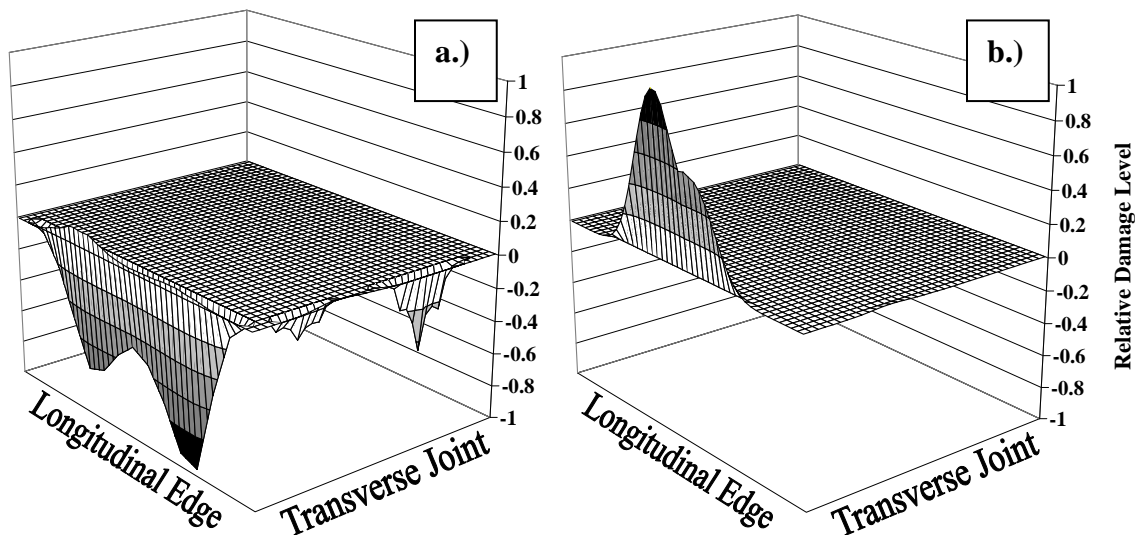


Figure G.32. Relative damage profile using nonlinear temperature profiles of section 04-N282 at 15-ft joint spacing with (a.) stress range and (b.) MEPDG maximum stress damage analysis.

### G.3.8 Section 04-N284

One mile north of section 04-N282 is section 04-N284 (MP 51.69 to 51.79) in the North Coast climatic zone. This section uses the same repeating joint spacing pattern of section 04-N282, with standard 12-ft lane widths and an asphalt shoulder. Cores revealed this pavement section had a 10-in. PCC slab resting on a 4.5-in. AC base and a 6-in. aggregate subbase. Also

constructed in 1993, section 04-N284 exhibits slightly more fatigue cracking than 04-N282, as seen in Figure G.33. Approximately 6% of slabs are cracked transversely, 11% of slabs are cracked longitudinally, and 3% exhibit corner cracking (Table G.3). Backcalculation of FWD data reveals an EBITD level of -10°F similar to that of section 04-N282 (-14°F).



Figure G.33. Transverse and longitudinal cracking on section 04-N284 on US-101NB in Sonoma County, California.

#### G.3.8.1 Linear Analysis

Due to the two-joint spacing used on site 04-N284, fatigue damage analyses were conducted for a shorter joint spacing (Figure G.34) and longer joint spacing (Figure G.35) using linear temperature profiles. As this site exhibits transverse, longitudinal, and corner cracking, the fatigue algorithm employed in RadiCAL must be able to predict all three distresses.

For both the shorter (Figure G.34a) and longer (Figure G.35a) joint spacing using linear temperature profiles, the critical damage location is transverse cracking offset from the mid-slab edge. Using the stress range fatigue algorithm, bottom-up longitudinal cracking is probable for both joint spacing (relative damage level near 0.12). The locations of these damages in relation to the damage along the longitudinal edge could potentially lead to corner cracking initiating roughly 2 ft from the corner of the slab, as high bottom-up damage along the transverse joint is also predicted near the same corner. While the potential for longitudinal cracking using this method is small, this site does exhibit this distress as the primary cracking mechanism for the most part. This suggests that the stress range approach is more appropriate for linear temperature scenarios on this site.

Using the MEPDG fatigue function for both joint spacings (see Figure G.34b and Figure G.35b), the predicted critical damage locations result only in bottom-up transverse cracking, with negligible damage elsewhere. This damage prediction does not tend to agree with the observed cracking distresses on section 04-N284.

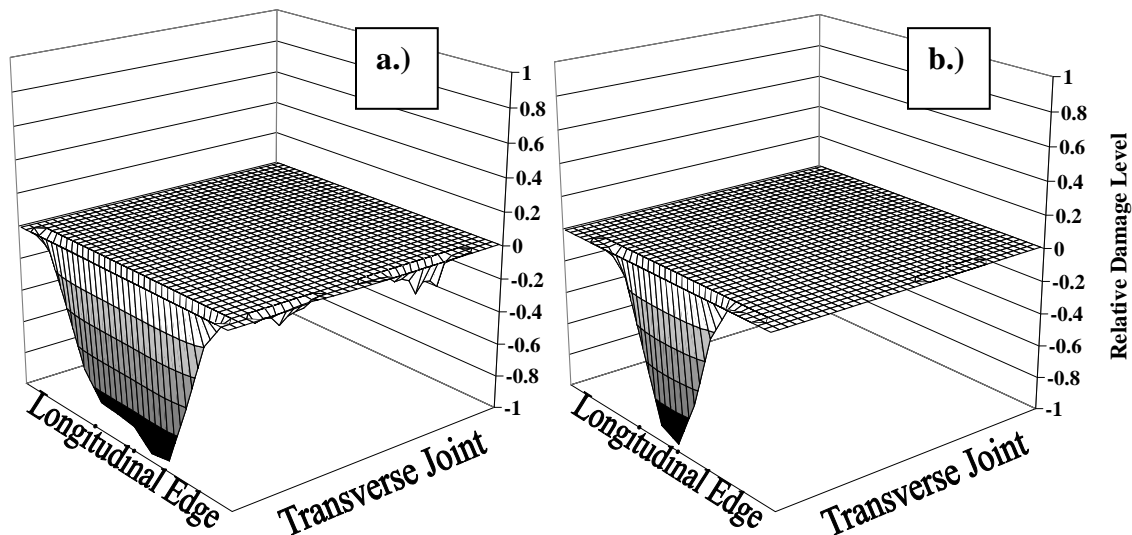


Figure G.34. Relative damage profile using linear temperature profiles of section 04-N284 at 12-ft joint spacing with (a.) stress range and (b.) MEPDG maximum stress damage analysis.

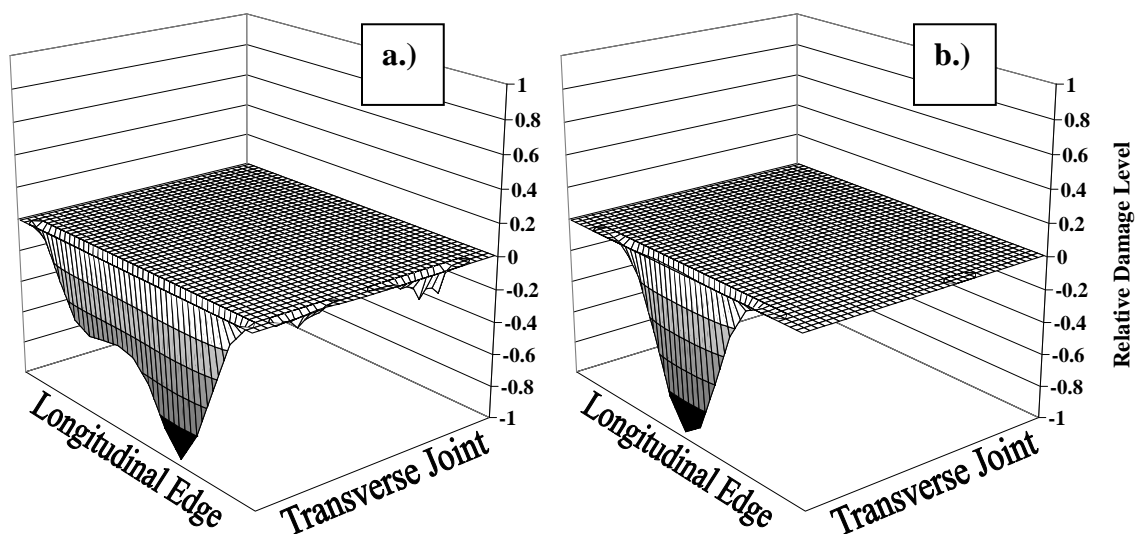


Figure G.35. Relative damage profile using linear temperature profiles of section 04-N284 at 15-ft joint spacing with (a.) stress range and (b.) MEPDG maximum stress damage analysis.

#### G.3.8.2 Nonlinear Analysis

RadiCAL predicts similar damage profiles using nonlinear temperature profiles and stress range fatigue as it did with linear profiles, while the ratio of relative damage along the transverse joint differs, as seen in Figure G.36a for shorter joint spacing, and Figure G.37a for longer joint spacing. The damage along the transverse joint for both the nonlinear stress range is quite reduced relative to the linear temperature cases, since the self-equilibrating stresses tend to reduce the overall damage at the bottom of the slab.

For 12-ft joint spacings, the MEPDG transfer function predicts a high level of damage (Figure G.36b) at both the transverse joint (top-down between the wheel paths) and the longitudinal edge of the slab (top-down near midslab). In section 04-N284, the longitudinal cracking appears to be prevalent on the slabs with shorter joint spacing. This trend using the MEPDG appears to be a better predictor of longitudinal cracking for this site conditions. On this

site, the observed corner cracks are quite large in nature, initiating 4 to 6 feet from the corner of the slab. This also matches the trend predicted by RadiCAL using the MEPDG fatigue function.

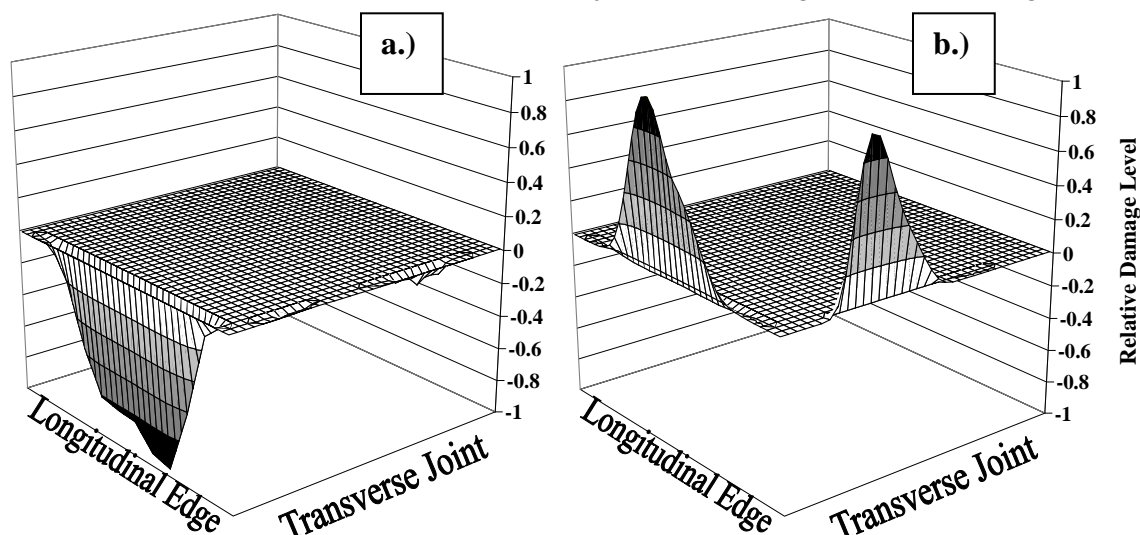


Figure G.36. Relative damage profile using nonlinear temperature profiles of section 04-N284 at 12-ft joint spacing with (a.) stress range and (b.) MEPDG maximum stress damage analysis.

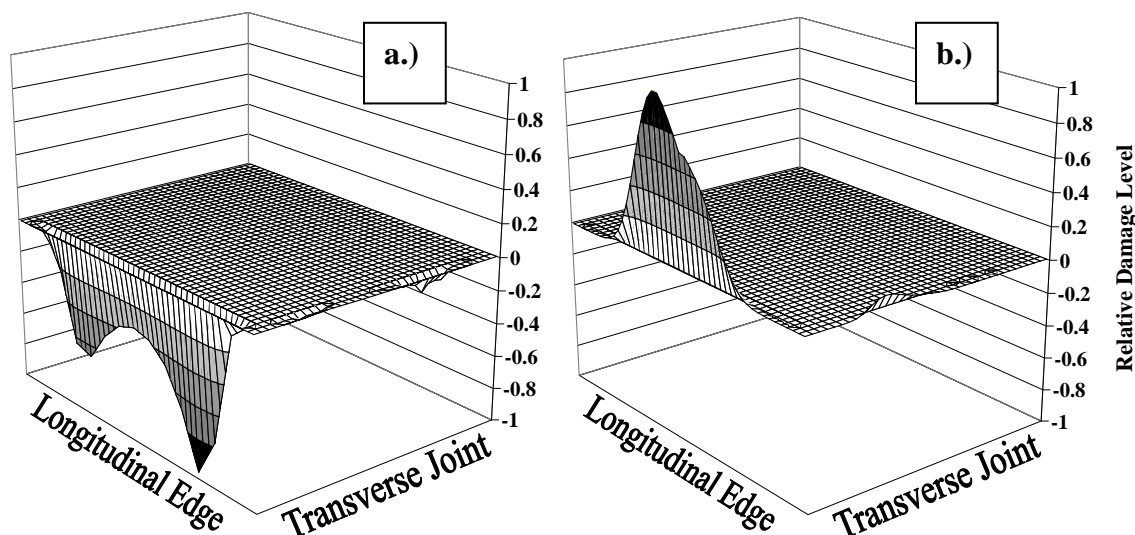


Figure G.37. Relative damage profile using nonlinear temperature profiles of section 04-N284 at 15-ft joint spacing with (a.) stress range and (b.) MEPDG maximum stress damage analysis.

### G.3.9 Section 04-N288

Adjacent to section 04-N284 is section 04-N288 (MP 51.75 to 51.86) in the southbound direction on US-101 in the North Coast climatic zone. This section also uses the repeating joint spacing pattern of section 04-N282 with standard 12-ft lane widths and an asphalt shoulder. The cores showed this section had PCC thickness ranging from 9.5 to 10 in. on top of a 4.5-in. AC base and a 14-in. aggregate subbase. Section 04-N288 was constructed in 1993 and is in overall good condition (Figure G.38). Approximately 6% of slabs are cracked transversely and 3% exhibit corner cracking (Table G.3). Currently, site 04-N288 exhibits no longitudinal cracking. Backcalculation of FWD data shows a slightly larger EBITD value (-20°F) on this particular site in comparison with the northbound US-101 sites adjacent to this one.





Figure G.38. Corner cracking on section 04-N288 on US-101SB in Sonoma County, California.

#### G.3.9.1 Linear Analysis

Using linear temperature profile predictions for stress range in RadiCAL, the damage profiles for the shorter 12-ft slabs (Figure G.39a) and longer 15-ft slabs (Figure G.40a) indicate a high likelihood of bottom-up transverse cracking between the mid-slab point and the corner of the slab. In both joint spacing scenarios, a moderate level of relative fatigue damage (up to 0.19) is shown at the transverse joint that could manifest itself as either longitudinal or corner cracking, matching existing fatigue cracking on this site.

A significant difference is noticed in the predicted damage locations using the MEPDG maximum stress fatigue algorithm for the shorter (Figure G.39b) and longer (Figure G.40b) joint spacings. On the 12-ft slabs, top-down (midway between the midslab and corner of the slab) and bottom-up transverse cracking (near midslab) are predicted. RadiCAL also predicts a significant amount of relative fatigue damage along the transverse joint that could potentially manifest itself as top-down longitudinal or corner cracking. However, as the slab length gets longer (Figure G.40b), the bottom-up damage along the longitudinal edge and top-down damage at the transverse joint is not predicted. While only a limited number of cracked slabs exist on section 04-N288, the MEPDG fatigue transfer function seems to predict field surveys fairly well.

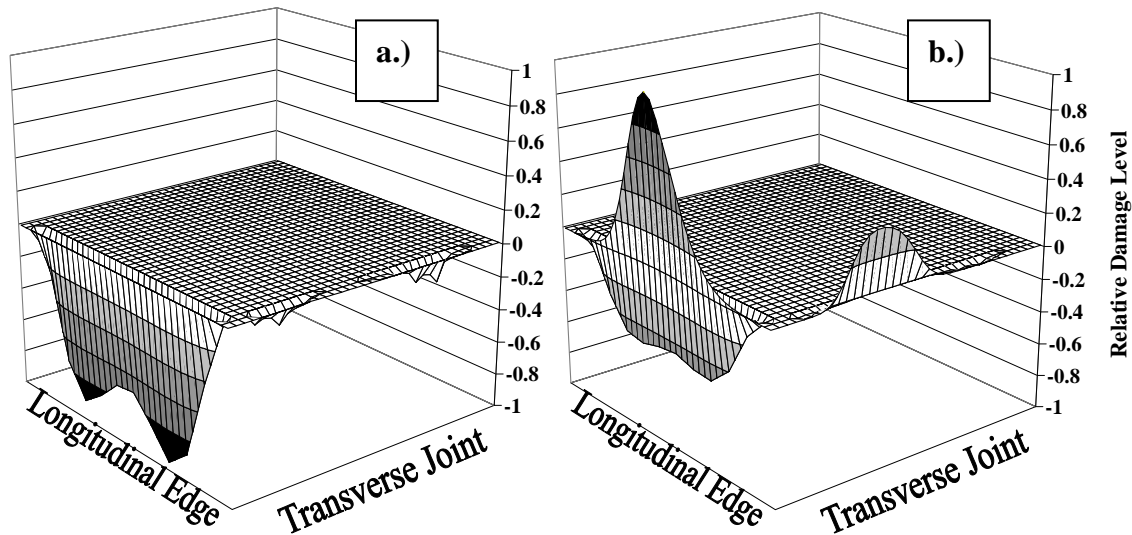


Figure G.39. Relative damage profile using linear temperature profiles of section 04-N288 at 12-ft joint spacing with (a.) stress range and (b.) MEPDG maximum stress damage analysis.

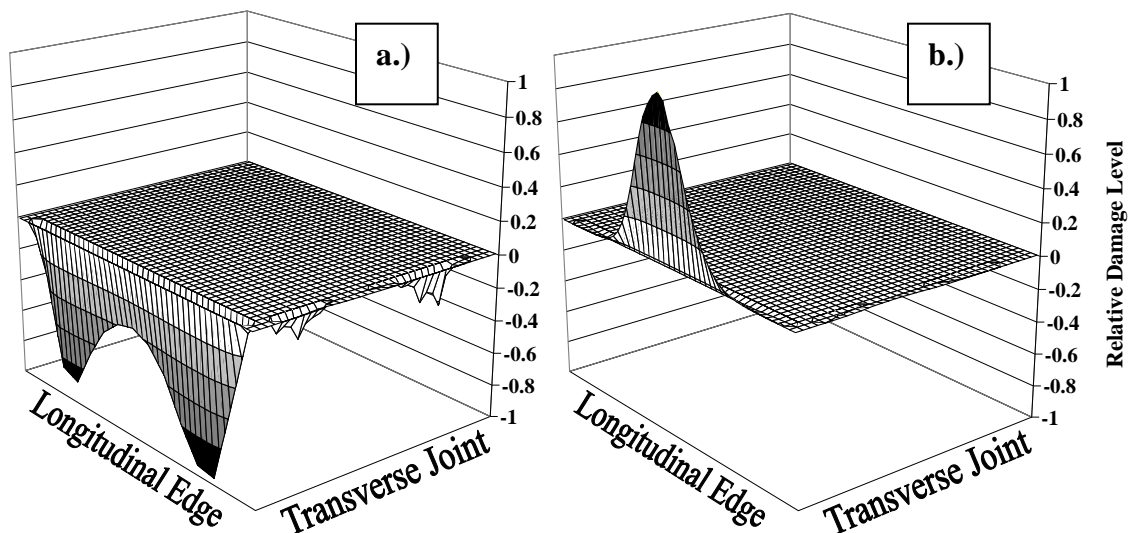


Figure G.40. Relative damage profile using linear temperature profiles of section 04-N288 at 15-ft joint spacing with (a.) stress range and (b.) MEPDG maximum stress damage analysis.

#### G.3.9.2 Nonlinear Analysis

For both the stress range and maximum stress fatigue damage process in RadiCAL, the results are quite similar to their linear counterparts. For both the 12-ft (Figure G.41a) and 15-ft (Figure G.42a) joint spacings, the damage profiles predict the same location of transverse cracking. However, no significant damage along the transverse joint is predicted relative to the linear temperature cases. This is due to the self-equilibrating stresses that tend to reduce stresses on the bottom of the slab in comparison with the linear temperature assumption cases.

With the MEPDG maximum stress fatigue function, the longitudinal damage at the bottom of the slab for the shorter joint spacing is reduced under nonlinear temperature profiles, as seen in Figure G.41b. The nonlinear temperature assumption and 15-ft joint spacing produces a damage profile (Figure G.42b) similar to the linear temperature profile (Figure G.40b). However, the predicted absolute fatigue damage level is much larger due to the

addition of self-equilibrating stresses at the top of the slab, predicting a shorter fatigue life than the linear case.

With very little cracking data available on this section, it is difficult to assess the best fatigue algorithm to predict both transverse and corner cracking that exists on this site. However, using nonlinear temperature, only the MEPDG maximum stress fatigue function predicts any likelihood of corner cracking potentially occurring, although the location and subsequent size of the corner crack predicted does not match the limited cracking data from Stantec field surveys of section 04-N288.

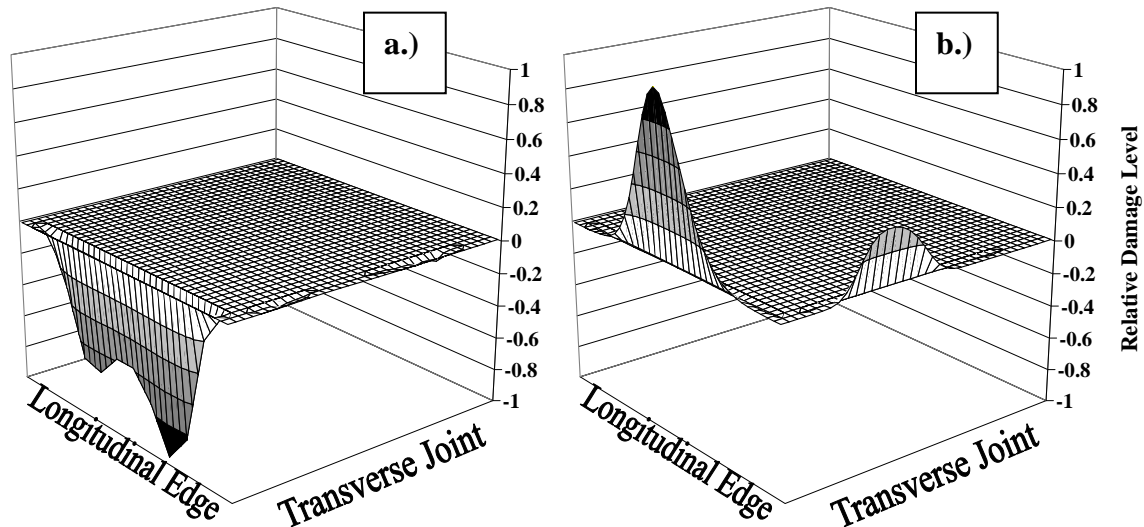


Figure G.41. Relative damage profile using nonlinear temperature profiles of section 04-N288 at 12-ft joint spacing with (a.) stress range and (b.) MEPDG maximum stress damage analysis.

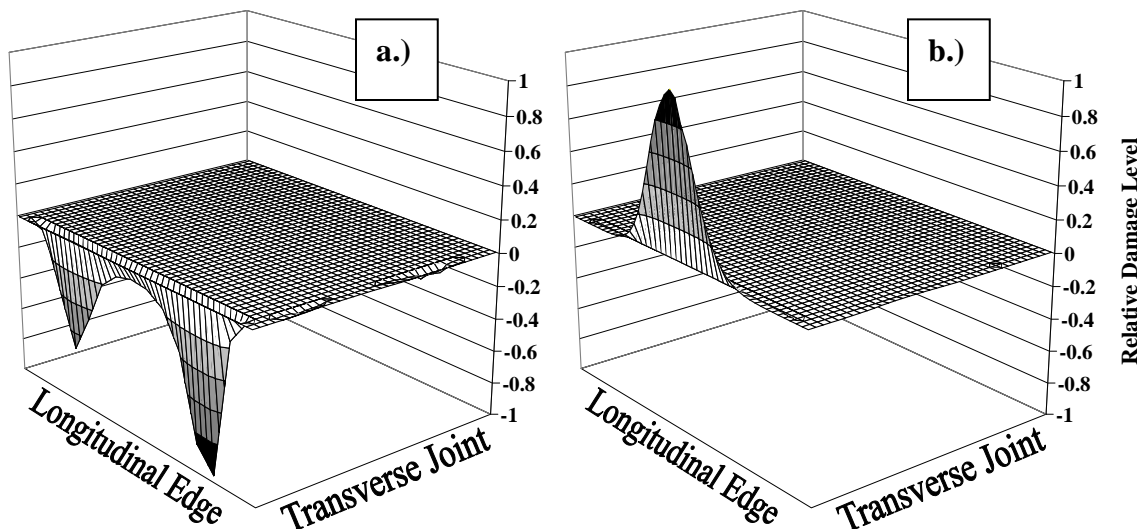


Figure G.42. Relative damage profile using nonlinear temperature profiles of section 04-N288 at 15-ft joint spacing with (a.) stress range and (b.) MEPDG maximum stress damage analysis.

#### G.4. Conclusions on Design Verification of In-Service California JPCP Sites

Eleven JPCP sections in California covering four different climatic zones (South Coast, Bay Area, North Coast, and the Central Valley) were analyzed with site-specific geometry, shoulder considerations, and load spectra (when available) to attempt to validate the RadiCAL

predictive power in terms of fatigue cracking locations. Backcalculation using a FWD on each of these sites permitted site-specific load transfer and EBITD values to use in RadiCAL as well. Each of these sites was analyzed with two temperature consideration methods (linear and nonlinear piecewise solution) for both the Tepfers' stress range and MEPDG fatigue transfer functions to determine the best predictor of crack location. Unfortunately, a wealth of data did not exist for either the RPPR or UCPRC sites in terms of the timing of crack initiation or changes in traffic levels and load spectra, and thus, engineering judgment was used on cracking mechanisms.

When numerous replications of EBITD were available, the stress range approach using linear temperature considerations tended to produce fairly realistic damage profiles, in comparison with observed cracking patterns (Table G.4). When considering nonlinear temperature, the MEPDG fatigue algorithm did predict existing longitudinal cracking in several locations, most notably the US-101 sites on the North Coast. For the sections with only a few intact slabs for EBITD backcalculation (shaded in Table G.4), the MEPDG fatigue transfer function using nonlinear temperature did predict some level of damage along the transverse joint that could manifest itself as either longitudinal or corner cracking.

Table G.4. Summary of Fatigue Transfer Functions that Represent Distresses Noted on California Sections.

	Temperature	Linear		Non-Linear	
	Fatigue Function	Stress Range	MEPDG	Stress Range	MEPDG
Site ID	CA 1-3	x			x
	CA 2-3	x	x	x	
	04-N201	x		x	
	04-N249	x		x	
	04-N250				x
	04-N251				x
	04-N252				x
	04-N253				x
	04-N282	x		x	x
	04-N284	x			x
	04-N288	x	x		x

As many of these sites did exhibit corner cracking, the stress range approach to damage tended to predict this possibility more frequently with high amounts of damage along the transverse joint (in wheel path) and along the longitudinal edge (midway between the midslab and corner of the slab). The ability to predict this cracking mechanism set the use of this fatigue function apart in most scenarios. The stress range approach also allows for transverse cracking prediction away from the mid-slab area, which matched the location of several of observed transverse cracking patterns. The corner cracking mechanism using the MEPDG fatigue function would result in large corner cracks, as the initiation point would be roughly 4 ft from the corner of the slab. While less likely, the size of the corner cracks predicted in this scenario were noticed on some of these sections, thereby lending credence to the use of the MEPDG function as a predictive means for alternative cracking mechanisms.

The use of nonlinear temperature in combination with stress range tended to produce cases that could potentially cause longitudinal or corner cracking, but not as significantly as with

the use of linear temperature differences only. As the stress range function developed by Tepfers (1979) was calibrated for beam data, it may not be an accurate representation of slab fatigue behavior. Calibration of the  $\beta$  coefficient to field data may help solve this somewhat. Domenichini and Marchionna (1981) calibrated this  $\beta$  coefficient for field slabs and found a change from Tepfers' default value of 0.0685 to 0.0954 to account for factors not present in laboratory beam testing. This increase in the  $\beta$  coefficient would create a steeper fatigue curve, thereby reducing the number of repetitions required to initiate fatigue damage.

The use of more advanced mechanics-based factors such as stress range and nonlinear temperature should be further explored in terms of forensic analysis and calibration of JPCP sections. These factors are just a few pieces of a larger picture that is needed to more accurately predict the timing of and prevent fatigue failures in JPCPs. While a clear picture was not found in terms of the best fatigue transfer function to predict locations of cracking, the results show that the use of several functions can be used in conjunction with calibration to design against both traditional and alternative cracking mechanisms for JPCPs.

# APPENDIX H. COMPARISON OF JOINTED PLAIN CONCRETE PAVEMENT DESIGN PREDICTION METHODS

## H1. INTRODUCTION

A comparison with RadiCAL can be made in terms of predicted thickness design by using the MEPDG Version 1.0 (ARA, 2007) design software, in addition to the existing IDOT mechanistic-empirical design method (Zollinger and Barenberg 1989a, 1989b). Both the MEPDG and IDOT methods are similar to RadiCAL, except that a stress-based approach to fatigue failure is used and a variety of statistical distributions of input parameters are accounted for in a Miner's Hypothesis-based fatigue damage accumulation design.

In terms of design, JPCP slabs are designed to prevent bending fatigue failure. Due to the stochastic nature of fatigue failure, all slabs will not crack at the mean time to failure predicted by a mechanistic-empirical design methodology. Thus, reliability concepts are used to complement this mean failure approach, to account for this probability distribution of failure and also to design to a certain level of reliability. In doing so, probability assures that the number of slabs cracked will not be exceeded during the design period of a JPCP. Both the MEPDG and IDOT methods employ a reliability-based process for their designs—albeit different—to account for variance in the timing of fatigue failure in JPCP slabs.

### H1.1. MEPDG JPCP Thickness Design Method

The MEPDG (ARA, 2007) was developed under NCHRP 1-37A as robust software for the design of new or rehabilitation of asphalt and concrete pavements. This program uses engineering mechanics to find stress, strains, and deflections and uses these outputs to predict performance of the pavement over its design life. Traffic is characterized using a load spectra concept while accounting for steer-drive axle spacings, as well as the individual axle spacing on a tandem, tridem, and quad axle. The MEPDG has the ability to predict environmental (climate) impacts on pavement response and design at virtually any location in the United States. One of the unique features of the MEPDG is the ability to account for a variety of material inputs and their impact on pavement response to better capture deterioration of the pavement and improve design predictions. For JPCPs, the MEPDG uses a nationally-calibrated fatigue equation, as seen in Equation H-1 below, originally derived from field slab test results of the U.S. Army Corps of Engineers.

$$\text{Log}(N) = 2.0 \left( \frac{\text{MOR}}{\sigma} \right)^{1.22} \quad (\text{H-1})$$

where:

$N$	=	number of repetitions to failure;
$\text{MOR}$	=	modulus of rupture of the concrete; and
$\sigma$	=	applied maximum stress level.

In conjunction with this fatigue transfer function, the MEPDG uses a stress prediction neural network in a real-time setting to predict either bottom-up or top-down

transverse fatigue cracking near the mid-slab edge. The MEPDG also allows for user-specified failure criteria, in terms of both reliability and percentage of slabs cracked.

## H1.2. Illinois Department of Transportation JPCP Thickness Design Method

As one of the earlier mechanistic-empirical methods developed, the IDOT method for design of JPCPs employs a simplified stress-based approach that accounts for both load and temperature in fatigue. Stresses are determined using charts or regression equations (Salsilli-Murua, 1991; Thompson and Barenberg, 1992) developed from finite element analyses using ILLISLAB (Tabatabaie and Barenberg, 1978; Ioannides, 1984; Korovesis, 1990; Khazanovich, 1994). Traffic is represented by an 18-kip ESAL with the lateral wheel wander of these trucks being represented by a normal distribution with mean of 18 in. from the edge and a standard deviation of 10 in. IDOT JPCP designs are designed to a reliability level of 95% and limiting the percentage of slabs cracked from bottom-up at the mid-slab edge during the design life to 20% for higher volume facilities (TF>10).

Temperature stresses are superimposed on load-related stresses using an *R*-factor to account for the effect of slab lift-off on stress development. The IDOT method assumes three different temperature gradients of +1.65 °F/in., -0.65 °F/in., and 0 °F/in. to account for daytime, nighttime, and transition periods of the day. This method assumes that the daytime gradient condition occurs 25% of the time, the nighttime gradient condition 35% of the time, and the transition period 40% of the time. For a 12-in. JPCP slab, these gradients would represent a  $\Delta T$  of 19.8 °F and -12.9 °F, which do not necessarily represent the extreme conditions that may drive fatigue damage development using a Miner's Hypothesis-based approach.

Subgrade support can also be modified for changing conditions through the year by assuming a percentage of time under a given *k*-value.

The number of repetitions until failure is determined using the Zero Maintenance equation (Darter, 1977). To develop this concrete fatigue function, Darter compiled 140 fatigue beam results from three published studies—Kesler (1953), Raithby and Galloway (1974), and Ballinger (1972)—into one least-square regression in Equation H-2:

$$\text{Log}(N_f) = 17.61 - 17.61 \left( \frac{\sigma}{\text{MOR}} \right) \quad (\text{H-2})$$

where:

$N_f$	=	number of load application until failure;
$\sigma$	=	applied maximum stress level; and
MOR	=	modulus of rupture of the concrete.

Many fatigue transfer functions for concrete fatigue exhibit a semi-logarithmic relationship such as shown above. This presents a dilemma in rigid pavement analysis using a linear damage accumulation method such as Miner's Hypothesis. The predicted damage accumulated using this method tends to be primarily due to the heaviest axle loads and their associated stresses on the pavement, thereby neglecting a vast majority of loads in the damage accumulation.

Using this fatigue transfer function, one can easily assess the impact of stress differences on the number of applied loads until failure. Assuming a mean 14-day modulus of rupture of 650 psi, as is done in the IDOT method, and an applied repeated stress of 500 psi (stress ratio of 0.77), this transfer function would predict 11,584

repetitions at this stress level until failure. A 20% reduction in stress to 400 psi (stress ratio of 0.62) would predict almost 6,000,000 repetitions until failure. This essentially means that one repetition at 500 psi would equate to 512 repetitions at 400 psi in this fatigue counting routine. Consequently, an applied stress of 300 psi would require over 260,000 repetitions to equal one applied stress load of 500 psi. Thus, these lower applied stresses are dominated by a few single high-stress applications and essentially do not add considerable damage under these assumptive conditions.

Using the Tepfers-type transfer function in rigid pavement analysis can help dampen this effect somewhat, as the areas of the slab that undergo the highest applied stress levels also exhibit the highest curling stresses. Therefore, the change in stress when the load is applied is not as great and does not dominate the damage development as much.

### **H1.3. RadiCAL JPCP Thickness Design Method**

The development of RadiCAL as a damage accumulation method for multiple locations along the transverse joint and longitudinal edge was presented in Appendix E. However, to design for a given failure level in terms of slabs cracked at a specified reliability level higher than the mean, fatigue damage must be related to a field calibrated cracking model. The following section overviews the method to achieve this for use of RadiCAL to determine design thicknesses in JPCPs.

#### ***H1.3.1. Adaptation of MEPDG Mean Cracking Levels Prediction in RadiCAL***

As RadiCAL is currently in an uncalibrated state and based on only mechanistic responses, its only output is fatigue damage magnitude. Using reliability-based functions developed for the MEPDG (ARA, 2007), these fatigue damage levels can be converted into a level of cracking to attempt to provide thickness design comparisons against existing mechanistic-empirical based procedures.

The MEPDG uses a sigmoid function to convert fatigue damage level to a mean level of slabs that would be cracked in a given section, as seen in the equation below. This function was developed using LTPP data and is calibrated for the MEPDG analysis program. Graphically, this can be represented as an s-shaped curved, as seen in Figure H.1. This sigmoid function assumes that a fatigue damage level of 1.0 represents a mean cracking level (50% probability that crack will occur on a given slab at this damage level).

$$CRK = \frac{1}{1 + (DI_F)^{-1.98}} \quad (H-3)$$

where:

$CRK$	=	predicted amount of bottom-up or top-down slab cracking (fraction); and
$DI_F$	=	fatigue damage level after design period using Miner's Hypothesis for linear fatigue damage accumulation.



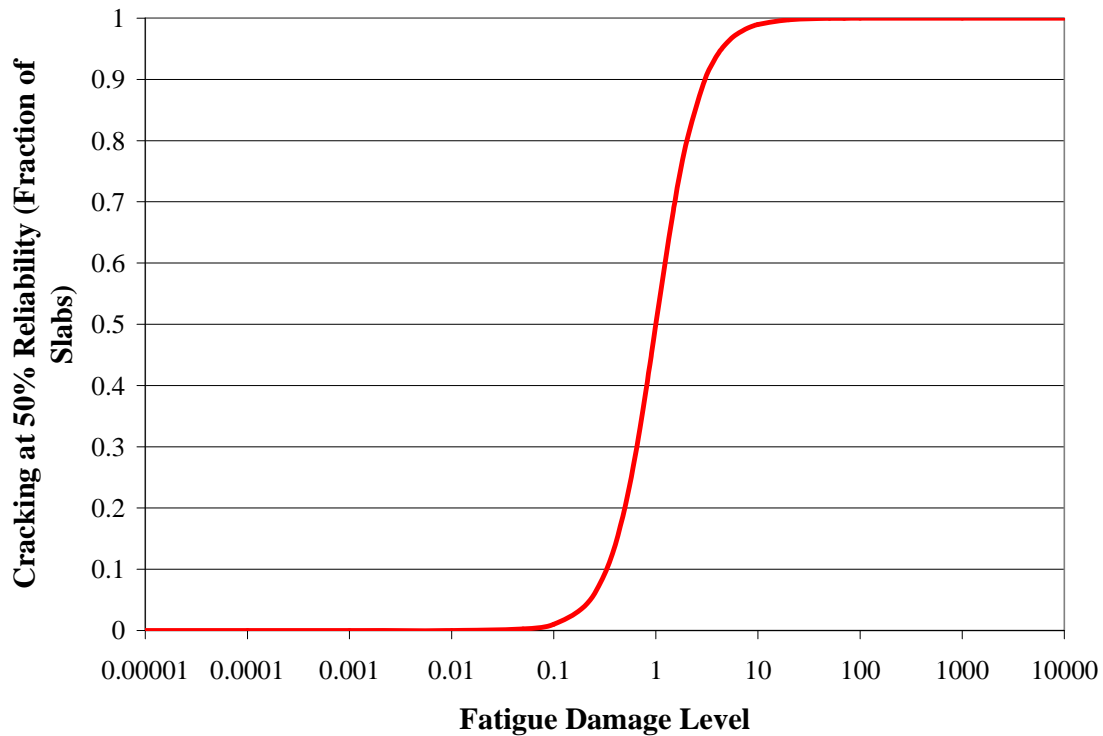


Figure H.1. Sigmoid function for converting fatigue damage level into slabs cracked in the MEPDG (after ARA, 2007).

#### ***H1.3.2. Incorporation of MEPDG Reliability in RadiCAL***

Both the MEPDG and RadiCAL have the ability to calculate damage at the top and bottom of the JPCP slab. However, the MEPDG only examines four nodal locations at the top of the slab (near midslab along the longitudinal edge) and at one node at the exact mid-slab edge at the bottom of the slab. RadiCAL has the ability to examine fatigue damage at every 4-in. increment along the top and bottom of both the longitudinal edge and transverse joint, resulting in up to 178 potential fatigue cracking initiation points (89 on both the top and bottom of the slab), depending on geometry of the slab. Equation H-4 assumes that a slab can crack either from the bottom to the top of the slab or from the top of the slab down to the bottom. However, this equation assumes that the slab cannot crack from both of these mechanisms. It should be noted that while the MEPDG developed and uses this equation to convert to a mean level of cracking expected from both top-down and bottom-up mechanisms, this program expresses the maximum *CRK* level of four top-down locations in conjunction with the bottom-up *CRK* level to find the mean level of cracking for a particular analysis. In RadiCAL, the top-down and bottom-up *CRK* values are always paired at the same location in the x-y (surface) plane of the slab. For these 89 pairs of fatigue damage levels in RadiCAL, Equation H-4 is used to predict the cracking level at that given location on the slab.

$$CRACK = (CRK_{BU} + CRK_{TD} - CRK_{BU} * CRK_{TD}) * 100\% \quad (H-4)$$

where:

$CRACK$	=	total amount of transverse or longitudinal cracking of all severities (%);
$CRK_{BU}$	=	predicted amount of bottom-up cracking (fraction); and
$CRK_{TD}$	=	predicted amount of top-down cracking (fraction).

Statistical principles state that since the cracking must occur from one direction, the probability of cracking occurring from both directions must be subtracted to properly account for this single cracking mechanism, as seen in Figure H.2.

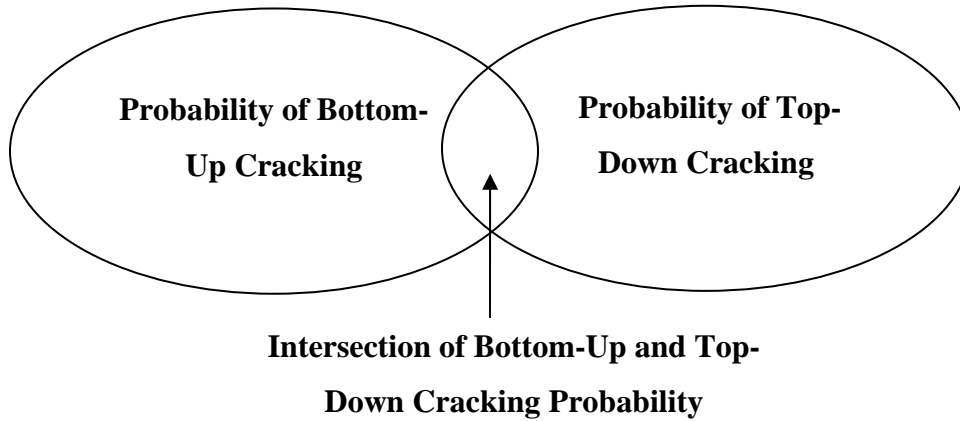


Figure H.2. Venn diagram accounting for single cracking mechanism in cracking prediction model (after ARA, 2007).

The MEPDG estimate of the standard error for the cracking prediction follows a power function as related to the mean level of cracking for a given section, as seen in Equation H-5. This model was adapted for use in RadiCAL.

$$s_e = (5.3116 * CRACK)^{0.3903} + 2.99 \quad (H-5)$$

where  $s_e$  is the standard error of estimate for cracking at mean predicted level

As most JPCP designs are not designed at 50% reliability for the design period, the standard error can be multiplied by the z-value for a given reliability level to determine the predicted level of fatigue cracking at this specified reliability. For 95% reliability of a single-tailed distribution, the z-value would be 1.645. This level of reliability is used in the comparisons between the MEPDG, IDOT M-E, and RadiCAL methods for thickness design. This value from Equation H-6 would result in a 95% probability that a certain level of cracking will be less than this calculated level.

$$CRACK_{95} = CRACK + 1.645 * s_e \quad (H-6)$$

where  $CRACK_{95}$  is the predicted level of cracking at 95% reliability for a given JPCP section.

#### H1.4. Design Methodology Comparison

A design comparison was conducted between the MEPDG, IDOT, and RadiCAL methods for a variety of design parameters to compare predicted cracking locations and actual slab thickness values. Input parameters were modified to determine the minimum JPCP thickness (in 0.5-in. increments) to achieve less than 20% of slabs cracked after 20 years of service at 95% reliability. The variables modified are as follows:

- Joint spacing: 12 and 15-ft
- Shoulder type: AC shoulder, tied PCC, widened slab (AC shoulder)
- Subgrade type: A-3 granular and A-7-6 clay
- Built-in curl level: -10 °F (part of the study varies from 0 to -40°F)
- Traffic level: 1,600 (moderate) and 9,575 (high) two-way AADTT corresponding to 10 and 60 million ESALs over the design life, respectively

The load spectra used in this study was the MEPDG default. The steer-drive axle spacing distribution for this study was also kept at the MEPDG default, with 33% of these spacings at 12 ft, 33% at 15 ft, and 34% at 18 ft. Other traffic characteristics kept at constant values for these analyses include the following:

- Number of lanes in design direction: 2
- Percent of trucks in design direction (%): 50
- Percent of trucks in design lane (%): 95
- Yearly growth factor: no growth

However, the vehicle class distribution for several weigh stations in Illinois found very different results than the MEPDG default values, as seen in Table H.1. In this case, the Illinois weigh stations note an extremely high number of Class 9 vehicles in comparison with national averages. An average vehicle class distribution from over 100 WIM sites in California also shows a higher percentage of Class 9 vehicles than the default MEPDG distribution (Lu et al., 2001). Therefore, the average Illinois vehicle class distribution was used in the design comparison.

Table H.1. Vehicle Class Distribution for Illinois, California, and MEPDG Program Default.

<b>Vehicle Classification</b>	<b>Illinois Average (%)</b>	<b>California Average (%)</b>	<b>MEPDG Default (%)</b>
Class 4	1.4	1.1	1.8
Class 5	3.8	23	24.6
Class 6	2.3	5.2	7.6
Class 7	0	0.3	0.5
Class 8	3.8	6.7	5
Class 9	84.4	50.6	31.3
Class 10	0.5	0.6	9.8
Class 11	2.8	8.8	0.8
Class 12	0.3	1.1	3.3
Class 13	0.3	0.1	15.3

Lateral wheel wander for this comparison was also kept at default levels for both the MEPDG and RadiCAL (normal distribution with mean 18 in. from the lane delineation and standard deviation of 10 in.).

Material values for the PCC layer were kept constant at the default value, with the exception of the modulus of rupture. The MEPDG program uses a growth factor dependent on age for strength of concrete according to Equation H-7.

$$GF = 1 + 0.12 * \log\left(\frac{AGE}{0.0767}\right) - 0.01566 * \left[\log\left(\frac{AGE}{0.0767}\right)\right]^2 \quad (H-7)$$

where:

$GF$  = growth multiplication factor to convert 28-day strength to strength at specified time; and  
 $AGE$  = age of concrete at time of interest (years).

The IDOT specifies a minimum 14-day center-point flexural bending strength (ASTM C293, 2003b) of 650 psi. Assuming a standard growth of this bending strength, this typically can be equated with a 90-day third-point bending strength (ASTM C78, 2003c). However, the MEPDG requires a 28-day third-point modulus of rupture value as an input. A 10% reduction of this 90-day strength was therefore used (585 psi) in these analyses (Zollinger and Barenberg, 1989b). Using a 28-day flexural strength of 585 psi, the MEPDG growth function would predict an increase to 692 psi at 10 years or half the design life. Since RadiCAL does not employ a growth function for strength and performs damage calculations assuming a constant strength, this 692 psi was used for these design comparisons. The IDOT method assumes a constant flexural strength of 650 psi for its design thickness charts. Thus, design JPCP thicknesses using this method should inherently be slightly thicker than either the RadiCAL or MEPDG methods.

For each of these design comparisons, the Zero Maintenance, MEPDG, and Tepfers' stress range fatigue transfer functions were employed in RadiCAL for both linear and nonlinear temperature profiles. However, the thickness comparisons shown are using only the MEPDG fatigue function with nonlinear temperature profiles for the

thicknesses derived in RadiCAL. However, critical damage locations using RadiCAL are noted for all three fatigue damage functions later in the discussion.

### H1.5. Climatic Impact

The first variable on which this design thickness comparison focuses is that of climate. Varying the location of the weather station used for the EICM (Larson and Dempsey, 1997) in both the MEPDG and RadiCAL can modify the temperature profiles and subsequent stress states and unsupported areas of the slab. However, the IDOT method assumes a constant climate for the entire state of Illinois, as described earlier. A design comparison was conducted among the MEPDG, IDOT, and RadiCAL methods for the four Illinois locations seen in Figure H.3 (Chicago Midway, Chicago DuPage, Peoria, and Carbondale) to represent the northern, central, and southern portions of the state.



Figure H.3. Climate location of Illinois JPCP design comparisons.

#### H1.5.1. Thickness Trends

Figure H.4. shows the resulting design thickness for a JPCP with 15-ft joint spacing and an asphalt concrete shoulder under a moderate level of traffic (10 million ESALs) for the four locations in Figure H.3. For the MEPDG method, the resulting design thickness is quite variable depending on location, resulting in a 24% reduction in required thickness from Chicago Midway in comparison to Chicago DuPage and Carbondale. The IDOT method predicts a constant thickness for all locations in Illinois, which is quite conservative in terms of absolute thickness in comparison to the other mechanistic-empirical methods. The use of RadiCAL with the MEDPG fatigue transfer function predicts a constant design thickness like the IDOT method, which does not address climate in its thickness design charts.

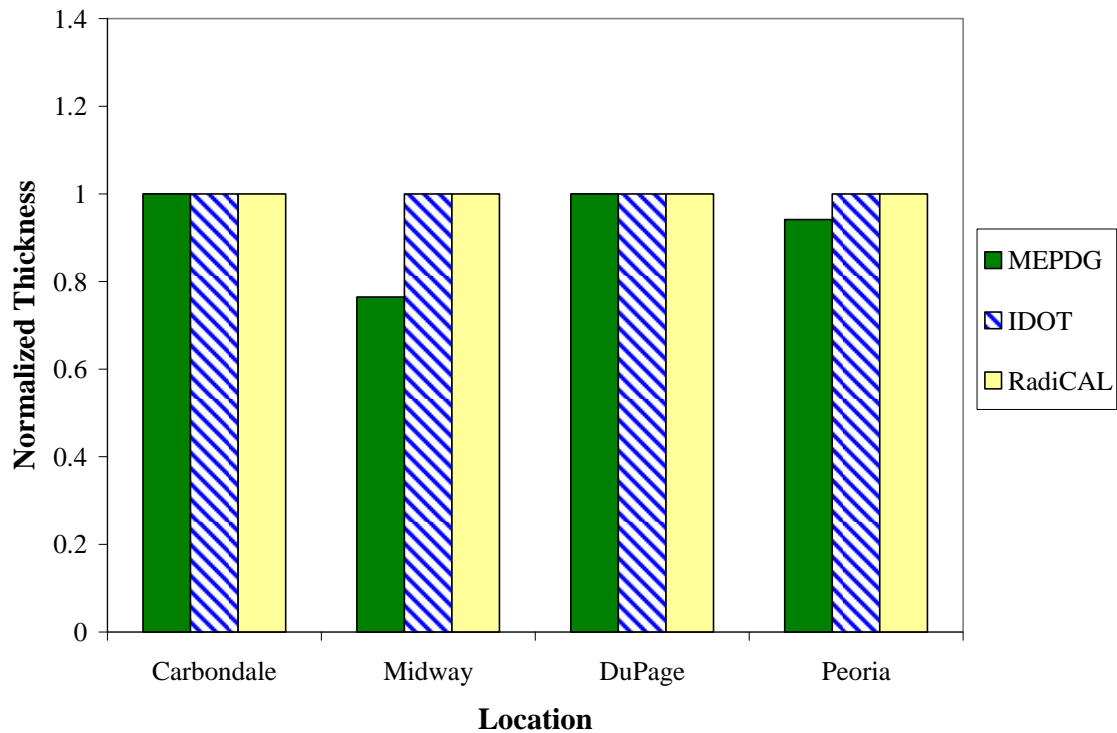


Figure H.4. Impact of climatic location on JPCP relative thickness for 15-ft joint spacing, AC shoulder, and 1,600 AADTT.

Figure H.5 compares the normalized thicknesses for the three methods at traffic volume that equates to 60 million ESALs. While the same trends exist for the IDOT and MEPDG design methods, RadiCAL predicts relatively thinner concrete slab at Chicago Midway in comparison with all other locations in the state of Illinois. Further analysis shows that for the lower traffic level from Figure H.4., the cracking level at 95% reliability was also significantly less at Midway than at other locations.

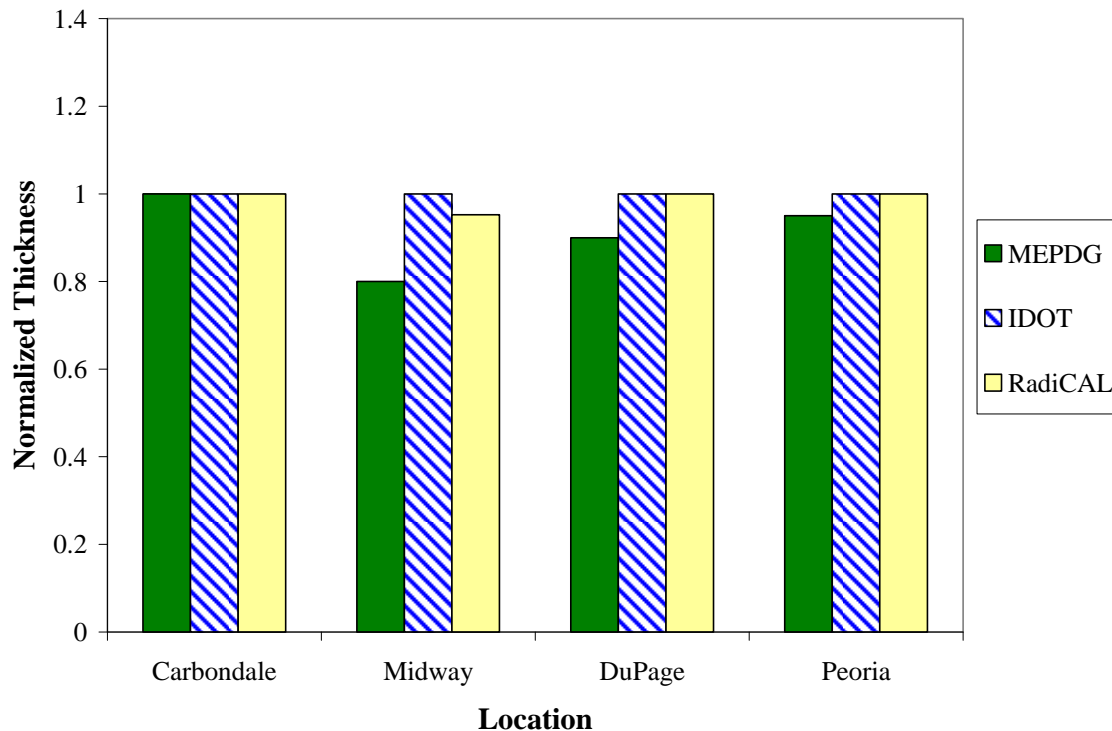


Figure H.5. Impact of climatic location on JPCP relative thickness for 15-ft joint spacing, AC shoulder, and 9,575 AADTT.

The straight-line distance between the Chicago Midway and Chicago DuPage weather stations is roughly 25 mi. However, for the high-AADTT scenario, the difference in required design thickness using RadiCAL is a 5% reduction and a 20% reduction using the MEPDG. This shows the tempering influence of large bodies of water on local climates in the Chicago area, as Midway is only 7 mi from Lake Michigan, while DuPage is roughly 30 mi from the lake. This effect can be seen by looking at the predicted frequency plot of  $\Delta T$  for these four locations in Illinois (see Figure H.6.) using hourly output data from EICM for years 2000 to 2004. While DuPage, Carbondale, and Peoria show similar predicted temperature difference frequencies, Midway shows a slightly different distribution. This is most noticeable at the extreme ends of both the positive and negative  $\Delta T$  where Midway is virtually absent in comparison with the other three sites. The tails of this distribution drive the highest stress levels and their subsequent damage accumulations, thereby requiring an increased thickness to compensate. With comparatively few of these extreme events, the Midway weather station would suggest that thinner slabs could be constructed in the city of Chicago with all other input parameters being equal. However, JPCP designs in a city such as Chicago would tend to require the highest level of reliability in order to reduce potential for rehabilitation and reconstruction of these sections under extremely heavy traffic levels. In this case, an increase of reliability from 95% to 99% using RadiCAL would increase the design thickness at Midway by 0.5 in.

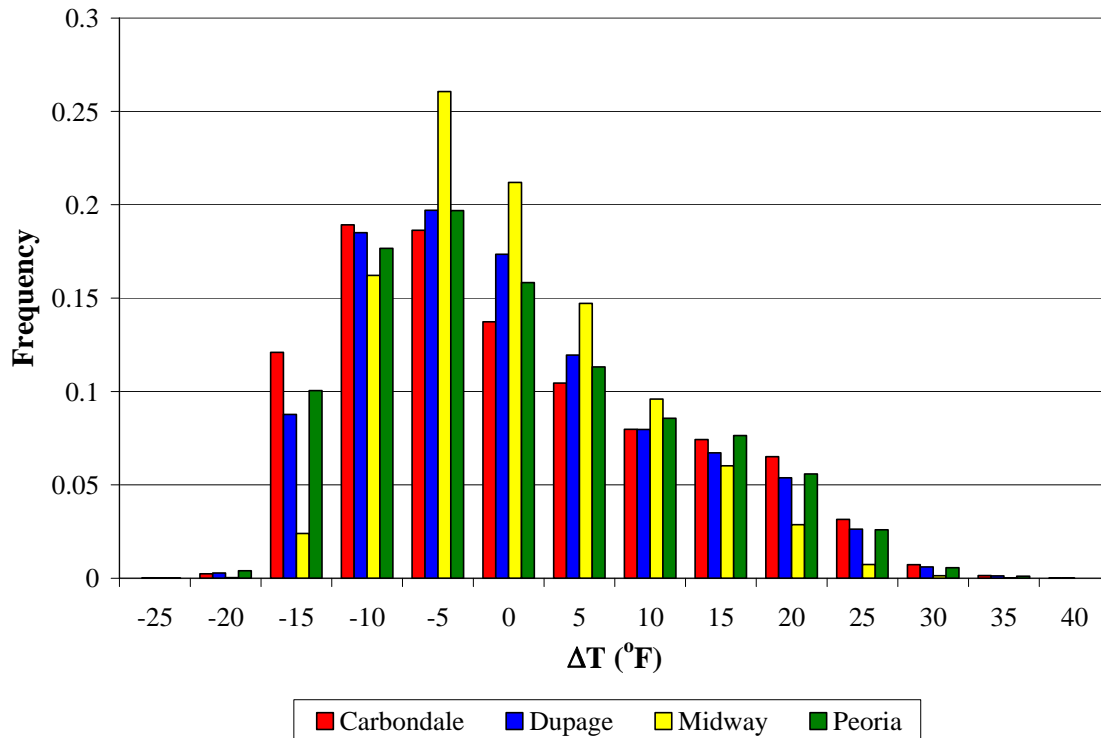


Figure H.6. Frequency of hourly temperature differences for four Illinois sites using EICM for years 2000-2004.

#### H1.5.2. Locations of Critical Fatigue Damage

Using linear temperature differences in RadiCAL, Table H.2 shows the comparison of critical damage locations in comparison to the MEPDG and IDOT methods for three different fatigue transfer functions, in terms of climatic location. The low and high traffic levels refer to 1,600 and 9,575 AADTT (10 and 60 million ESALs, respectively). Due to its limitations, the IDOT method will predict bottom-up transverse cracking to be critical in all cases.

Table H.2. Predicted Critical Damage Locations for Four Illinois Cities using Three M-E Design Methods with Linear Temperature Profile in RadiCAL.

	MEPDG		IDOT		RadiCAL				
	Transverse Cracking		Transverse Cracking		Transverse Cracking			Longitudinal	
	Bottom-up mid-slab	Top-down mid-slab	Bottom-up mid-slab	Top-down mid-slab	Bottom-up mid-slab	Top-down mid-slab	Bottom-up alternativ	Bottom-up wheelpath	Top-down between wheelpath
Carbondale	1600 <sup>a</sup>	9575 <sup>a</sup>	x	x	All				
	9575 <sup>ab</sup>	1600 <sup>ab</sup>							
DuPage	x	x <sup>b</sup>							
Midway	x								
Peoria	x	x <sup>b</sup>	x	x	ZM ME				
					SR				

<sup>a</sup> Refers to the level of AADTT

<sup>b</sup> Refers to the significant level of relative damage (>0.15) at secondary location

SR=Tepfers stress range, ZM=Zero Maintenance, ME=MEPDG fatigue transfer function in RadiCAL



In most cases, the use of any fatigue function in RadiCAL predicted bottom-up cracking at midslab. However, the use of the stress range function found slightly offset critical damage location (closer to the transverse joint) that was not found using the other methods. The effect of greater traffic levels did not affect the critical damage location for these cases in RadiCAL despite the increase in slab thickness.

For the cases analyzed in this climatic study (AC shoulder, 15-ft joint spacing, A-7-6 subgrade) the MEPDG generally predicted the critical transverse cracking location to be at the bottom of the slab, with the exception of the high-traffic level cases found at Carbondale. All sites except for the Chicago Midway location also showed a significant amount of relative damage (0.15 or greater) indicating top-down cracking near midslab, which wasn't predicted by RadiCAL in these cases using linear temperature differences.

For this study, the Carbondale location predicted the thickest section of any location in Illinois using the MEPDG. For cases found in this comparison, the MEPDG method will predict bottom-up transverse cracking to be critical at thicknesses less than 9.5 in. on a A-7-6 subgrade, while thicker slabs tend to have top-down transverse cracking becoming dominant. This difference in cracking mechanism lies with the interaction between the radius of relative stiffness ( $\ell$ ) and the slab length ( $L$ ). With thinner slabs, the ratio  $L/\ell$  is higher than with thicker slabs for a fixed slab length ( $L$ ). The larger this ratio becomes, the closer to an infinite slab condition exists and the tensile stresses on the top of the slab interact less at near the mid-slab location when analyzing steer-drive axle load cases. This increase in stress therefore leads to higher probability of bottom-up cracking occurring in thinner JPCP sections with all other factors being equal.

Table H.3 shows the same comparison of critical damage locations as Table H.2, except that the piecewise method to account for self-equilibrating stresses from nonlinear temperature profiles is used for the RadiCAL cases. When doing so, the stress range fatigue function tends to predict bottom-up transverse cracking at the mid-slab location, just like the Zero Maintenance and MEPDG fatigue functions. This critical damage location matches both the IDOT and MEPDG and is indicated by the shaded cells of Table H.3. However, both the Zero Maintenance and MEPDG transfer function show a significant amount of relative damage indicating top-down transverse cracking as a possibility. As both the MEPDG and RadiCAL used ILLISLAB for stress prediction algorithms and maximum stress fatigue functions in this case, there is a positive correlation that helps validate each method to some degree.

Table H.3. Predicted Critical Damage Locations for Four Illinois Cities using Three M-E Design Methods with Nonlinear Temperature Profile in RadiCAL.

	MEPDG		IDOT		RadiCAL				
	Transverse Cracking		Transverse Cracking		Transverse Cracking			Longitudinal	
	Bottom-up mid-slab	Top-down mid-slab	Bottom-up mid-slab	Top-down mid-slab	Bottom-up mid-slab	Top-down mid-slab	Bottom-up alternativ	Bottom-up wheelpath	Top-down between wheelpath
Carbondale	1600 <sup>a</sup> 9575 <sup>ab</sup>	9575 <sup>a</sup> 1600 <sup>ab</sup>	x		All				
DuPage	x	x <sup>b</sup>	x		All	ZM <sup>b</sup> ME <sup>b</sup>			
Midway	x		x		All				
Peoria	x	x <sup>b</sup>	x		All	ZM <sup>b</sup> ME <sup>b</sup>			

<sup>a</sup> Refers to the level of AADTT

<sup>b</sup> Refers to the significant level of relative damage (>0.15) at secondary location

SR=Tepfers stress range, ZM=Zero Maintenance, ME=MEPDG fatigue transfer function in RadiCAL

## H1.6. Joint Spacing Impact

The next parameter this comparison focuses on is joint spacing. A few limitations exist between the three methods. The statewide IDOT design method does not compensate directly for thickness changes with joint spacing, and instead assumes that all designs will be for a joint spacing of 15 ft. RadiCAL is limited to joint spacing of 12 ft and 15 ft, as the initial development of the program was for new designs in California, and joint spacing is now limited considerably in that state. In contrast, the MEPDG has the ability to analyze any joint spacing ranging from 12 to 20 ft. for JPCPs. Due to this limitation, only 12- and 15-ft joint spacings are analyzed. For the joint spacing and shoulder type studies, the Carbondale climatic location with A-7-6 subgrade soil was also used.

### H1.6.1. Thickness Trends

A comparison of the impact of joint spacing on design thickness for JPCPs can be seen in Table H.4 with the 12-ft joint spacing cases, with an AC shoulder being the reference thickness. For AC shoulder cases, the MEPDG predicts an increase in thickness of 42% and 18% for the moderate and high truck-traffic values, respectively, as the joint spacing increases from 12 to 15 ft. Conversely, RadiCAL predicts 0 and 5% increase of required thickness for the same scenarios. The sensitivity to curling-related effects in terms of thickness design in the MEPDG can also be aggravated by factors directly affecting the temperature profile (absorptivity) or curling-related stresses (coefficient of thermal expansion), as noted by Kannekanti and Harvey (2006).

While the thicknesses are reduced when using a tied PCC shoulder, RadiCAL still predicts a 0 to 6% reduction of required thickness when joint spacing is reduced from 15 ft to 12 ft. The MEPDG shows a similar trend as thickness is reduced 12.5% for the high-volume traffic and tied concrete shoulder, and there is no reduction at the moderate traffic level due to the program's minimum thickness requirement of 6 in.. The sensitivity of joint spacing on thickness for RadiCAL is similar for all shoulder types.

Using a widened slab with an asphalt shoulder, the same trends exist for the MEPDG, while RadiCAL shows no sensitivity for joint spacing in terms of minimum required thickness. It should be noted that for both the moderate and high traffic-level scenarios, the cracking predicted does increase in RadiCAL, but not enough to affect design thickness.

Table H.4. Impact of Joint Spacing on JPCP Relative Thickness for Carbondale, Illinois using Three M-E Design Methods

AADTT 1600									
Joint Spacing (ft)	AC Shoulder			Tied PCC Shoulder			Widened Slab w/ AC Shoulder		
	MEPDG	IDOT	RadiCAL	MEPDG	IDOT	RadiCAL	MEPDG	IDOT	RadiCAL
12	1	1	1	1	0.95	0.84	1	0.88	0.84
15	1.42	1	1	1	0.95	0.89	1	0.88	0.84
AADTT 9575									
Joint Spacing (ft)	AC Shoulder			Tied PCC Shoulder			Widened Slab w/ AC Shoulder		
	MEPDG	IDOT	RadiCAL	MEPDG	IDOT	RadiCAL	MEPDG	IDOT	RadiCAL
12	1	1	1	0.82	0.98	0.95	0.82	0.90	0.95
15	1.18	1	1.05	0.94	0.98	0.95	0.94	0.90	0.95

\* normalized to 12-ft joint spacing with AC shoulder for each method and traffic level

## H1.7. Shoulder Type Impact

The next factor that affects both thickness and critical damage location is that of the shoulder type. This analysis looks at three different types of shoulders for the three mechanistic-empirical design methods: standard slab width (12-ft) with an asphalt concrete shoulder, standard slab width with a tied PCC shoulder (LTE=50% in RadiCAL), and a widened slab (14-ft) with the lane delineation painted two ft from the true slab edge.

### H1.7.1. Thickness Trends

For this analysis, the analysis of shoulder type on required thickness and location of cracking is broken down into two categories based on traffic levels: the moderate traffic level (1,600 AADTT) and the heavy traffic level (9,575 AADTT).

#### H.1.7.1.1 Moderate Traffic Levels

For moderate traffic levels, the trend of required thickness to satisfy less than 20% of slabs cracked at 95% reliability can be seen in Figure H.7 for 12-ft joint spacing and Figure H.8 for 15-ft joint spacing. RadiCAL predicts a decrease of 16% in thickness when using a tied PCC shoulder or widened slab, while the IDOT method predicts a 5% reduction for tied shoulders and 12% for the widened lane with 12-ft joint spacing (Figure H.7). The MEPDG does not predict any thickness difference at this level of traffic due to the predicted thickness requirements being less than the minimum 6 in. for this design method.

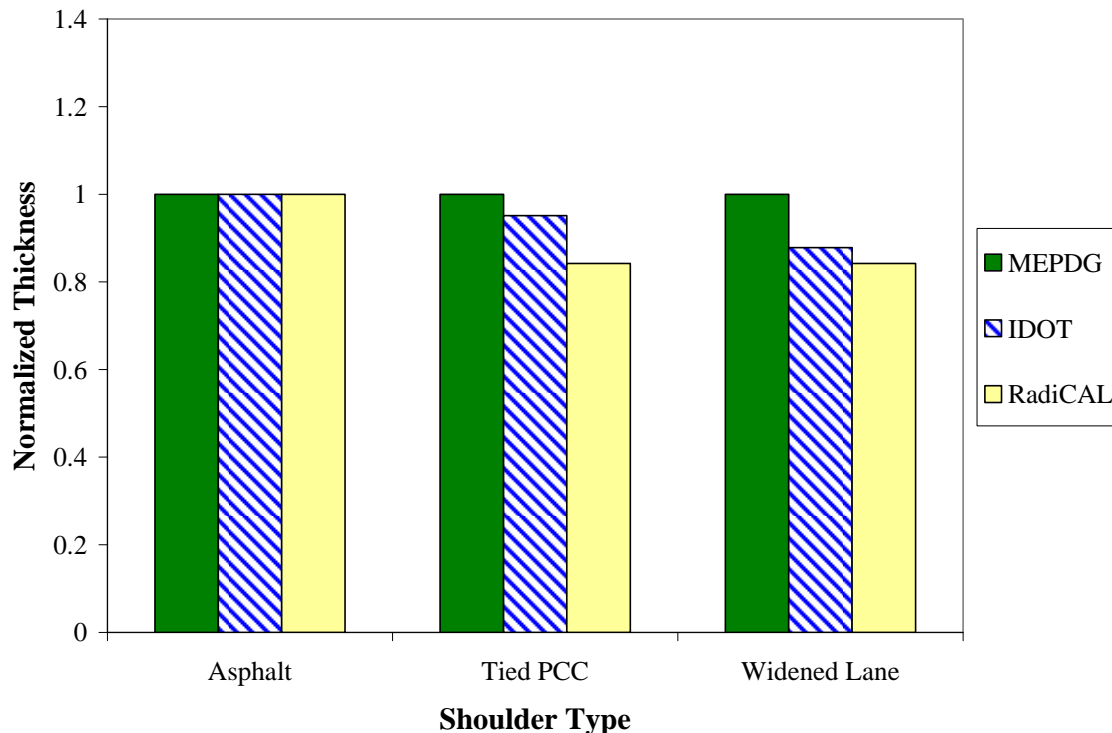


Figure H.7. Impact of shoulder type on JPCP relative thickness for Carbondale, Illinois, 12-ft joint spacing, and 1,600 AADTT.

Using a 15-ft joint spacing as seen in Figure H.8, the trends are a little more apparent, as the MEPDG predicts a 29% decrease in required thickness from the standard lane width with AC shoulders to either the tied PCC shoulder or widened slab case. The same trend is noted in RadiCAL, with an 11% thickness reduction for adding a tied PCC shoulder and a 16% reduction for using a widened slab. IDOT's current method should demonstrate behavior similar to RadiCAL.

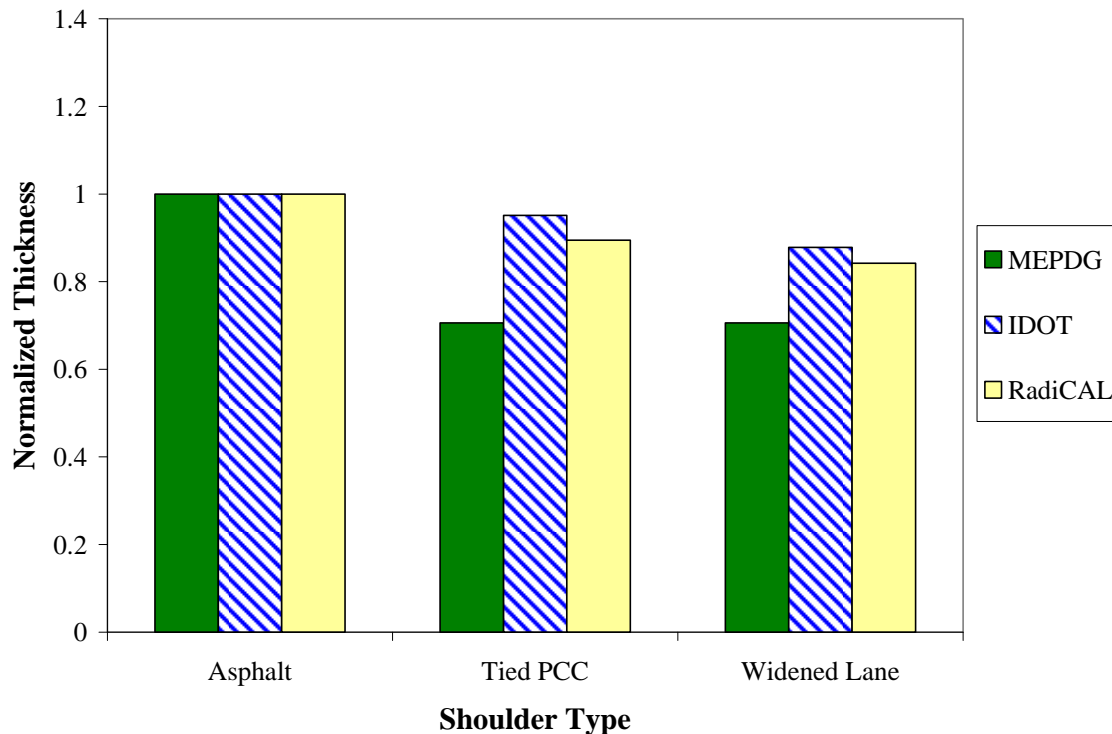


Figure H.8. Impact of shoulder type on JPCP relative thickness for Carbondale, Illinois, 15-ft joint spacing, and 1,600 AADTT.

#### H.1.7.1.2 Heavy Traffic Levels

At higher traffic levels, similar trends in terms of thickness are noted for all three design methods. Using RadiCAL, the thickness reduction for adding a tied PCC shoulder or widening the slab width results is 5% for a 12-ft joint spacing design (Figure H.9) and 10% at a joint spacing of 15 ft (Figure H.10). The MEPDG predicts a reduction of 18% for 12-ft joint spacing, regardless of whether tied shoulders or widened slabs are employed. For 15-ft slab size, the thickness reductions using the MEPDG are 20% for tied shoulder and widened slab designs relative to AC shoulder designs. The IDOT method demonstrates a 2% and 12% thickness reduction when using tied shoulder and widened slabs, respectively.

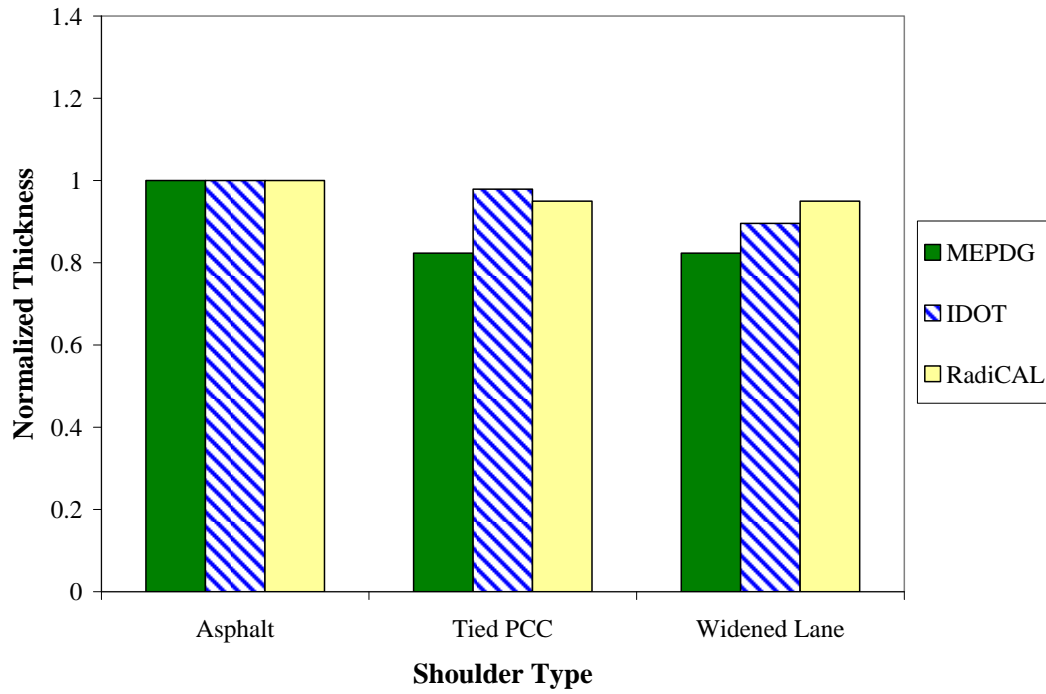


Figure H.9. Impact of shoulder type on JPCP relative thickness for Carbondale, Illinois, 12-ft joint spacing, and 9,575 AADTT.

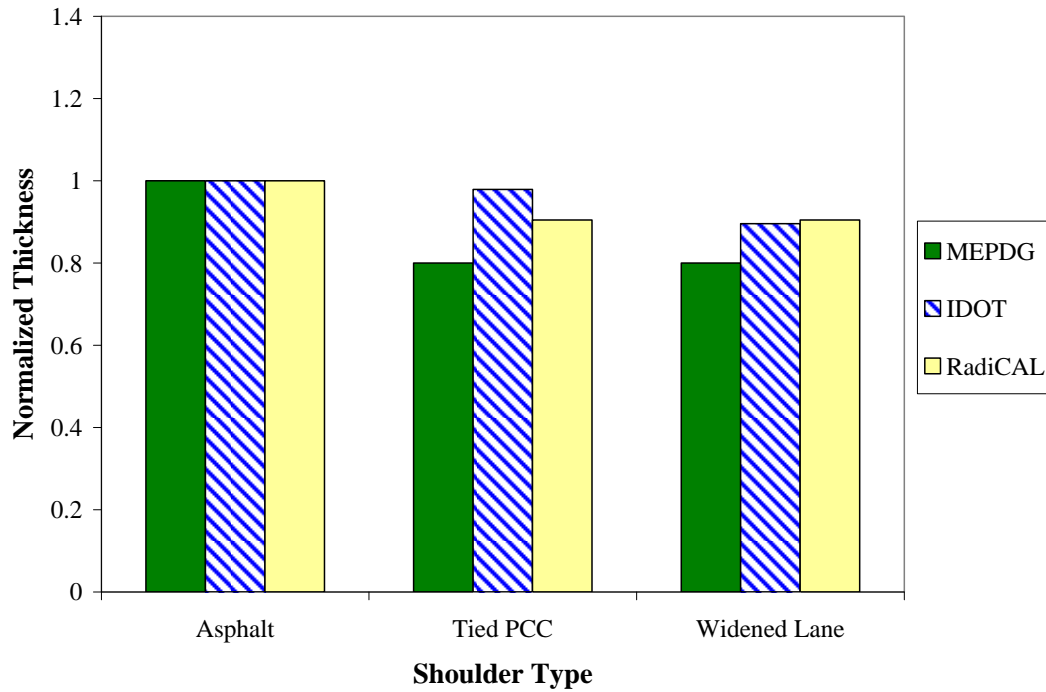


Figure H.10. Impact of shoulder type on JPCP relative thickness for Carbondale, Illinois, 15-ft joint spacing, and 9,575 AADTT.

### ***H1.7.2. Locations of Critical Fatigue Damage***

*Table H.5* Table H.5 compares the critical and secondary damage locations with for two traffic levels (1600 and 9575 AADTT), two joint spacings (12 ft and 15 ft), and three shoulder types (AC shoulder, tied PCC shoulder, and widened slab with AC shoulder) using the three mechanistic-empirical design methods. Table H.5 also assumes a linear temperature profile for the RadiCAL designs regardless of fatigue transfer function used and assumes that critical damage locations for the Tepfers' and Zero Maintenance fatigue functions were analyzed for the design thicknesses determined using the MEPDG fatigue function. In general, the MEPDG, IDOT, and RadiCAL methods tended to match critical fatigue damage locations at the bottom of mid-slab when using AC or tied PCC shoulders with shorter 12-ft joint spacings, regardless of traffic level. This is designated by the shaded cells in Table H.5. However, when changing the joint spacing to 15 ft, critical damage locations are not necessarily the same. In many of these cases, the Tepfers' stress range predicts an alternative bottom-up crack initiating along the longitudinal edge, but not at the mid-slab location. Instead, this location is roughly halfway between the midslab and corner of the slab. Due to high stresses from both single and tandem axles placed at this location and the relatively low residual temperature stresses in comparison with the mid-slab edge location, the stress range approach accounts for a significant amount of fatigue damage accumulation at these locations.

In general, the MEPDG predicts critical damage locations similar to RadiCAL when using a maximum stress fatigue approach, such as the Zero Maintenance or MEPDG fatigue function for standard lane widths.

When considering widened slabs, in almost all cases, RadiCAL predicts the critical damage location to be at the transverse joint under either the inner or outer wheel path. Since the extended lane width effectively keeps axle loads away from the true slab edge, the importance of loads at the transverse joint becomes imperative. In comparison, the critical location for damage accumulation in the MEPDG for widened slabs is at the mid-slab edge, but at the adjacent lane (and not the AC shoulder). This difference in potential critical locations can result in different design thicknesses.

In high-traffic cases with 15-ft joint spacing and widened slabs, the Zero Maintenance function in RadiCAL does predict top-down transverse cracking emanating from the shoulder to be critical. However, in this case, the level of relative damage in the wheel path along the transverse joint was also quite significant (0.5).

With RadiCAL's ability to predict fatigue mechanisms at alternative locations, the program may not necessarily predict the same thickness reduction for adding either a tied PCC shoulder or extending the slab width. It is important to note that the fatigue damage mechanism that is being designed against in RadiCAL may not correspond to that of either the IDOT or MEPDG design methods.

Table H.5. Predicted Critical Damage Level Locations by Joint Spacing, Shoulder Type, and Truck Traffic Level using Three M-E Design Methods with Linear Temperature Profile in RadiCAL.

Joint Spacing (ft)	MEPDG		IDOT		RadiCAL				
	Transverse Cracking		Transverse Cracking		Transverse Cracking			Longitudinal	
	Bottom-up mid-slab	Top-down mid-slab	Bottom-up mid-slab	Top-down mid-slab	Bottom-up mid-slab	Top-down mid-slab	Bottom-up alternative	Bottom-up wheelpath	Top-down between wheelpath
<b>AC Shoulder</b>									
<b>AADTT 1600</b>									
12	x		x		All				
15	x	x <sup>a</sup>	x		All				
<b>AADTT 9575</b>									
12	x	x <sup>a</sup>	x		ZM ME		SR		
15	x <sup>a</sup>	x	x		ZM ME	ZM <sup>a</sup>	SR	SR <sup>a</sup>	
<b>Tied PCC Shoulder</b>									
<b>AADTT 1600</b>									
12	x		x		All				
15	x		x		ZM ME	ZM <sup>a</sup>	SR	SR <sup>a</sup> ZM <sup>a</sup>	
<b>AADTT 9575</b>									
12	x		x		All				
15	x	x <sup>a</sup>	x		ZM ME		SR	SR <sup>a</sup> ME <sup>a</sup>	
<b>Widened Slab with AC Shoulder</b>									
<b>AADTT 1600</b>									
12	x		x					All	
15	x		x					All	ZM <sup>a</sup>
<b>AADTT 9575</b>									
12	x		x					All	
15	x	x <sup>a</sup>	x			ZM		SR ME ZM <sup>a</sup>	ZM <sup>a</sup>

<sup>a</sup> Refers to the significant level of relative damage (>0.15) at secondary location

SR=Tepfers stress range, ZM=Zero Maintenance, ME=MEPDG fatigue transfer function in RadiCAL

Table H.6 shows the same comparison as Table H.5, except that the RadiCAL cases are run considering nonlinear temperature profiles. For cases with AC shoulders, the three design methods predict similar critical damage locations at the bottom of the mid-slab edge, with the exception of the stress range cases with 15-ft joint spacing.

The same trend exists for tied PCC shoulder cases, as the Zero Maintenance and MEPDG fatigue functions in RadiCAL tend to predict the critical damage location at the bottom of the mid-slab edge at -10 °F built-in curl. The stress range function tends to predict bottom-up transverse cracking closer to the corner of the slab in these scenarios.

Table H.6. Predicted Critical Damage Level Locations by Joint Spacing, Shoulder Type, and Truck Traffic Level using Three M-E Design Methods with Nonlinear Temperature Profile in RadiCAL.

Joint Spacing (ft)	MEPDG		IDOT		RadiCAL				
	Transverse Cracking		Transverse Cracking		Transverse Cracking			Longitudinal	
	Bottom-up mid-slab	Top-down mid-slab	Bottom-up mid-slab	Top-down mid-slab	Bottom-up mid-slab	Top-down mid-slab	Bottom-up alternative	Bottom-up wheelpath	Top-down between wheelpath
<b>AC Shoulder</b>									
<b>AADTT 1600</b>									
12	x		x		All				
15	x	x <sup>a</sup>	x		ZM ME	ZM <sup>a</sup> ME <sup>a</sup>	SR		
<b>AADTT 9575</b>									
12	x	x <sup>a</sup>	x		All	ZM <sup>a</sup>			
15	x <sup>a</sup>	x	x		ZM ME	ZM <sup>a</sup> ME <sup>a</sup>	SR	SR <sup>a</sup>	
<b>Tied PCC Shoulder</b>									
<b>AADTT 1600</b>									
12	x		x		ZM ME		SR	ZM <sup>a</sup> ME <sup>a</sup>	
15	x		x		ZM ME	ZM <sup>a</sup>	SR	All <sup>a</sup>	ZM <sup>a</sup>
<b>AADTT 9575</b>									
12	x		x		ZM ME		SR	ME <sup>a</sup>	
15	x	x <sup>a</sup>	x		ZM <sup>a</sup> ME <sup>a</sup>	ZM ME	SR	SR <sup>a</sup>	
<b>Widened Slab with AC Shoulder</b>									
<b>AADTT 1600</b>									
12	x		x					All	ZM <sup>a</sup> ME <sup>a</sup>
15	x		x					All	ZM <sup>a</sup> ME <sup>a</sup>
<b>AADTT 9575</b>									
12	x		x					All	ZM <sup>a</sup> ME <sup>a</sup>
15	x	x <sup>a</sup>	x		ZM ME <sup>a</sup>			SR ME	ZM <sup>a</sup>

<sup>a</sup> Refers to the significant level of relative damage (>0.15) at secondary location

SR=Tepfers stress range, ZM=Zero Maintenance, ME=MEPDG fatigue transfer function in RadiCAL

A major difference between the RadiCAL method and the MEPDG and IDOT methods is that a significant amount of secondary relative damage is located in several locations, including the top of the longitudinal edge, as well as the top or bottom of the slab at the transverse joint. These significant secondary relative damage levels could exacerbate themselves as alternative cracking mechanisms that cannot be designed against in either the MEPDG or IDOT method. With tied PCC shoulder scenarios, the stress at the bottom of the mid-slab edge is reduced in comparison with the AC shoulder scenario, while the stresses at the transverse joint are relatively similar. Even with an assumed load transfer efficiency of 70%, this reduction in bottom-up mid-slab stresses increases the importance of the consideration of longitudinal cracking potential in design of JPCPs. These secondary locations are especially important if a lower concrete strength were to be assumed at the slab surface relative to the bottom, or if a higher level of built-in curling value was assumed in many instances.

It is also important to note the differences in safety and rehabilitation options between slabs containing transverse or longitudinal cracking. While transverse cracking can reduce ride quality if rehabilitation options such as dowel bar retrofitting are used, it



is generally not considered to be a safety hazard except in the most significant cases of faulting at these cracks. However, longitudinal cracking is a distress with which vehicles must contend for a longer period of driving time if this continues for several slabs. Faulting along these cracks (particularly those emanating in the wheelpath) can cause severe control problems for trucks, cars, and particularly motorcycles. The rehabilitation options for these longitudinal cracks are also limited to grout insertion and stitching, which is costly and time consuming.

Just as with the linear temperature profile scenarios in RadiCAL, the nonlinear temperature cases also showed that widened slab cases with AC shoulder predict longitudinal cracking emanating from the wheel path at the transverse joint to be critical, regardless of the fatigue transfer function used. This important finding can allow for proper consideration of alternative fatigue cracking mechanisms for thickness design. It should be noted that while the critical damage location in RadiCAL is shown to be at the transverse joint for widened slab cases, there is still a reduction of thickness required in comparison with the standard lane width scenarios, but not as significant as the current IDOT or MEPDG would suggest.

### H1.8. Subgrade Soil Impact

The impact of subgrade soil type is investigated in this analysis for two soil types: A-3 (granular) and A-7-6 (clay). It should be noted that RadiCAL does not currently model changes in subgrade support and uses only a constant  $k$ -value of 250 psi/in. Thus, the use of RadiCAL will show no impact to soil type changes.

The IDOT method uses an empirical method based on particle size of the unbound materials to classify subgrade support into three categories: poor, fair, and granular, as seen in Figure H.11. For this analysis, the A-3 subgrade was classified as granular, while the A-7-6 subgrade was classified in the poor category.

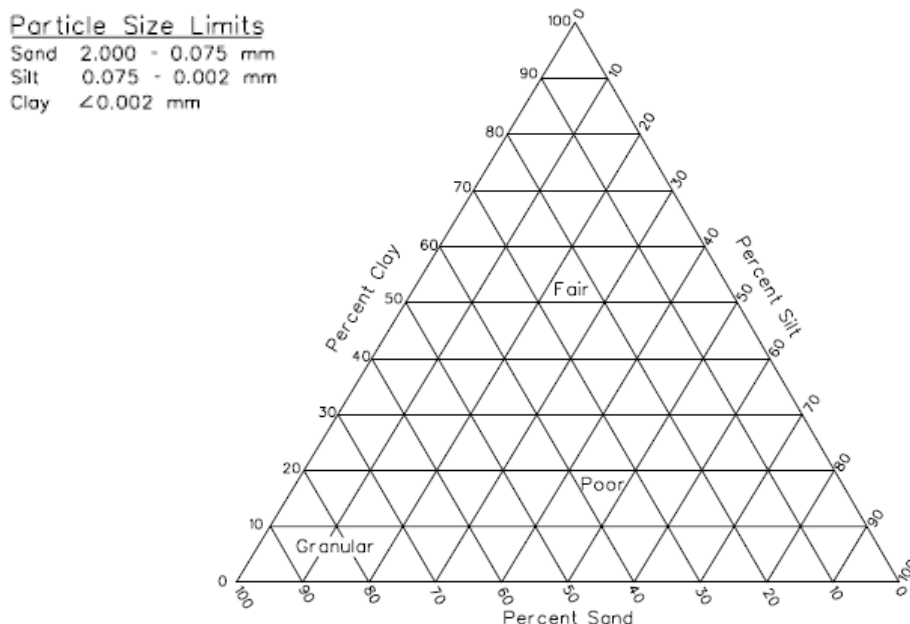


Figure H.11. Determination of subgrade soil support level for IDOT design of JPCP (from IDOT, 2002).

The MEPDG method allows the user to select a subgrade type classified by the AASHTO method of soil classification (ASTM D 2487, 2003). The program then uses default values for the resilient modulus which is then converted to an equivalent  $k$ -value that is not directly input by the user. For the A-3 soil, a default resilient modulus value of 16,500 psi is suggested. This value was modified to 15,000 psi. For the A-7-6 soil, a default value of 13,000 psi is suggested, although a specified value of 7,500 psi was used in the analyses. This present analysis was limited to Carbondale, Illinois and 15-ft joint spacings with an AC shoulder in order to see trends of all design methods.

### H1.8.1. Thickness Trends

For moderate truck traffic levels, Figure H.12 shows that the MEPDG results in no change in thickness for an A-3 and A-7-6 subgrade, although the predicted cracking levels at this thickness is slightly larger for the A-3 granular subgrade. However, the IDOT method shows a 10% reduction in required thickness with granular subgrade support.

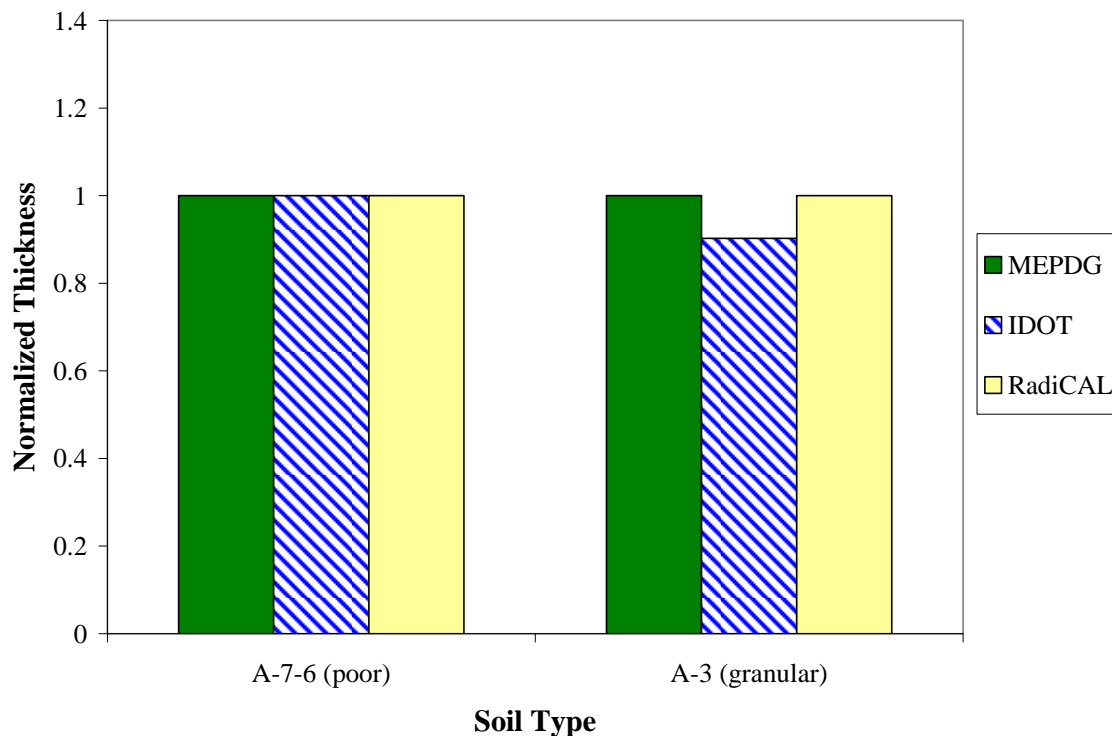


Figure H.12. Impact of soil type on JPCP relative thickness for Carbondale, Illinois, AC shoulder, 15-ft joint spacing, and 1,600 AADTT.

For the heavier traffic scenarios (Figure H.13), the IDOT method results in an 8% thickness reduction for a higher soil support value, while the MEPDG method shows an increase thickness requirement of 10%. In fact, the use of an A-3 soil is the only scenario from this factorial that predicts the same thickness or higher for the MEPDG in comparison with the RadiCAL (using the MEPDG fatigue and cracking models) or IDOT methods at the default built-in curl level of -10 °F.

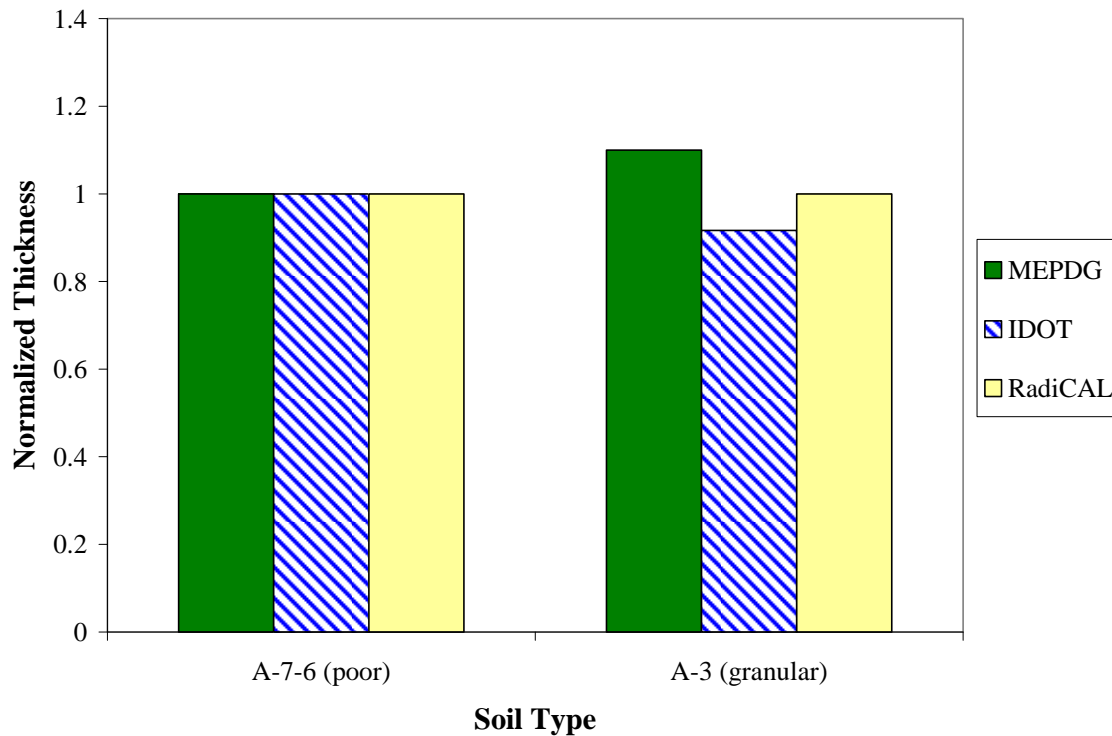


Figure H.13. Impact of soil type on JPCP relative thickness for Carbondale, Illinois, AC shoulder, 15-ft joint spacing, and 9,575 AADTT.

Intuitively, the use of higher-quality subgrade support materials should reduce the required slab thickness—at least the mechanical load stresses—as shown by the IDOT method in Figure H.13. However, as subgrade support becomes stiffer, mechanics show that the area of the slab that undergoes slab lift-off actually increases, thereby causing higher stresses when load and temperature are considered. This supports the trend exhibited by MEPDG and by analysis conducted during the development of RadiCAL.

### H1.9. Built-in Curling Impact

The level of built-in curl has a dramatic effect on stress, fatigue damage level, and critical damage locations in JPCPs. This section aims to look at how the factors in turn affect the required design thickness for the MEPDG and RadiCAL. The IDOT design method for JPCP does not have the ability to account for built-in curl, and therefore would show no sensitivity to this parameter.

#### H1.9.1. Thickness Trends

Figure H.14 shows the impact of increasing the level of built-in curl to more extreme values using nonlinear temperature profiles for Carbondale. The MEPDG method predicts an increase in required thickness as the level of built-in curl becomes more negative. While RadiCAL shows a similar trend of increasing thicknesses for most of the built-in curl levels, there is one exception. At a built-in curl level of 0 °F, the required thickness according to RadiCAL is actually thicker than is required at a built-in

curl level of -10 °F. This follows the same trend for fatigue damage level for nonlinear temperature profiles in Los Angeles and Daggett, California. It was found that the fatigue damage level tended to minimize in the EBITD range of -10 °F to -15 °F as the “flip point” of damage from bottom-up to top-down became critical. This trend apparently is also reproduced in terms of required thickness using the MEPDG fatigue and cracking models.

At built-in curl levels more extreme than -20 °F, both the MEPDG and RadiCAL design method would tend to require thicker JPCP sections than required by the IDOT method. However, this level of built-in curl is fairly rare and would probably require a drier climate, extreme positive temperature gradient during setting, and poor curing conditions after concrete placement to occur. The use of restraint mechanisms such as dowels and tie bars has also shown a correlation to reduced built-in curl levels (Rao, 2005).

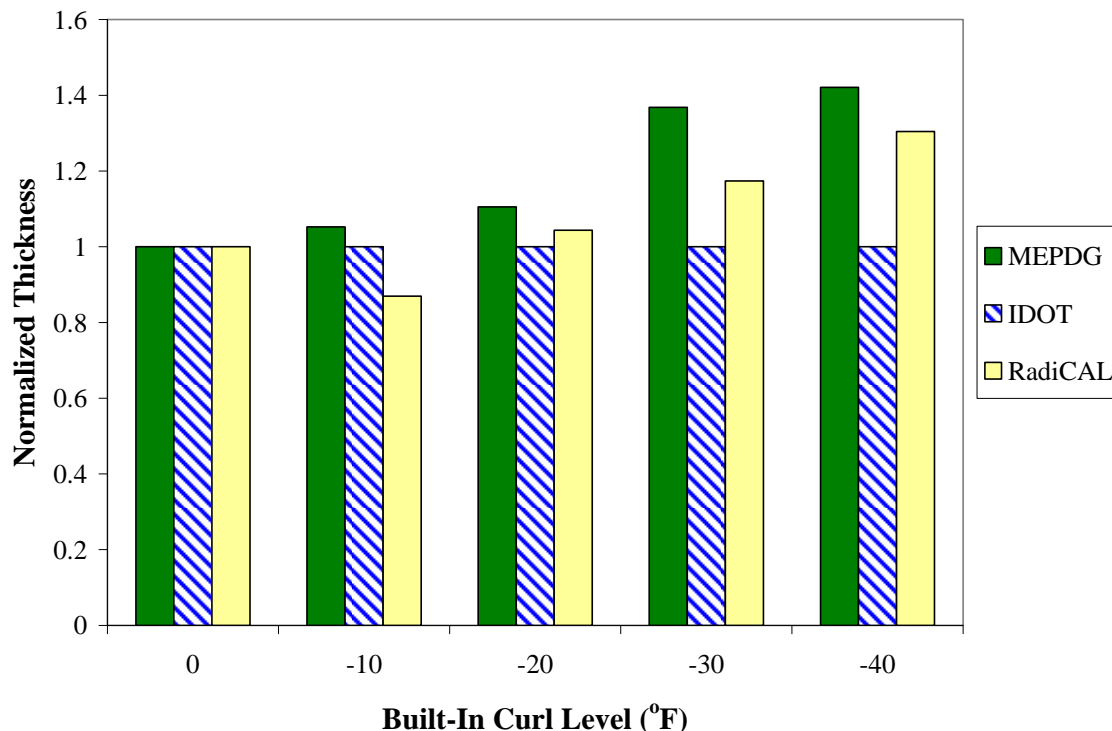


Figure H.14. Impact of built-in curl level on JPCP relative thickness for Carbondale, Illinois, AC shoulder, 15-ft joint spacing, and 9,575 AADTT with nonlinear temperature profiles.

#### **H1.9.2. Locations of Critical Fatigue Damage**

In both the MEPDG and RadiCAL (using the MEPDG fatigue and cracking functions with nonlinear temperature) methods, the flip point for when critical fatigue damage changed from bottom-up to top-down transverse cracking was found to be -10°F with very little damage at the transverse joint. This flip point occurs due to the reduction of stresses at the traditional mid-slab edge location from single axles and the increased importance of steer-drive axle spacing effects with a negative built-in curl.

For example, using the average axle load spectra found from all California WIM stations, in conjunction with the probabilities of load levels and steer-drive axle spacings for a typical California rigid pavement design, the probability of stresses can be predicted, as seen in Figure H.15. This particular plot shows the probabilities of stresses at the bottom of the slab at the mid-slab edge. It can be seen that the EBITD value greatly affects the distribution of stresses predicted at this location, which is typically assumed to be critical. Using transfer functions under a high EBITD value, this location would essentially have infinite life in fatigue as the stress ratio is kept below a value of 0.50 using a flexural strength of 700 psi. When assuming no EBITD value, the maximum stress at this location produces a stress ratio of 0.85 when using the same flexural strength, and this would lead to a much quicker fatigue failure. Due to this reduction in stresses at the traditional bottom-up transverse cracking initiation point, stresses at other locations, such as those causing top-down transverse or longitudinal cracking, become more critical.

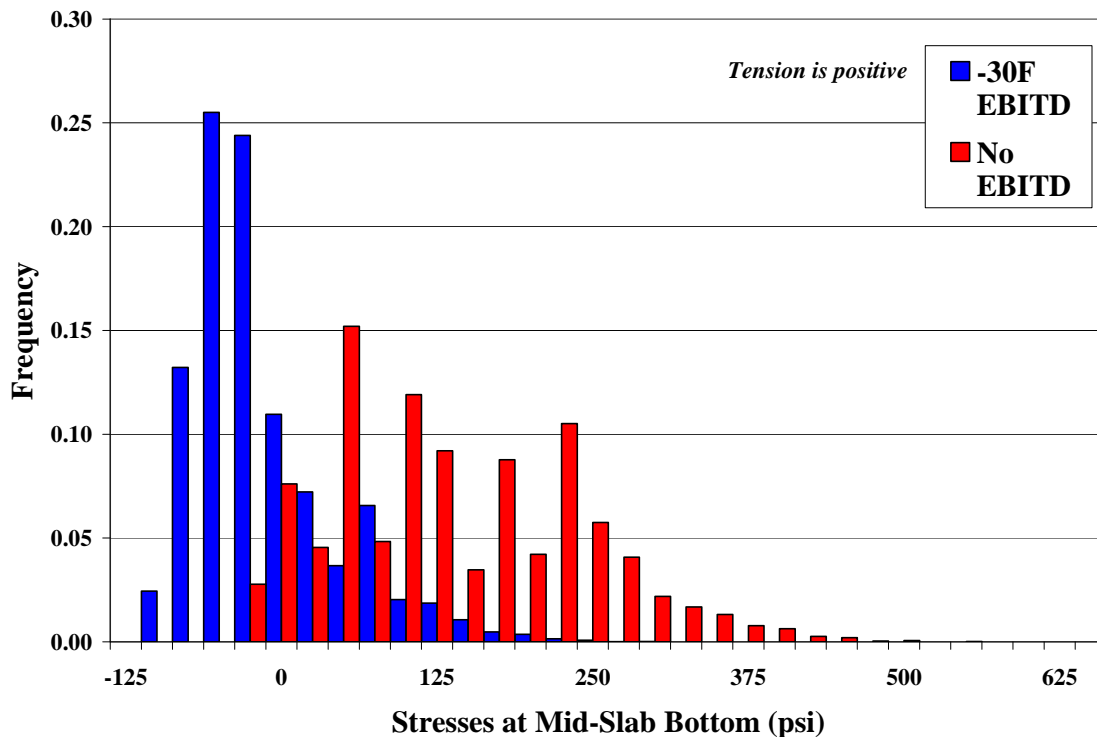


Figure H.15. Probabilities of stresses occurring at bottom of the mid-slab edge of the slab for different EBITD values.

Looking at a key location at the top of the slab along the longitudinal edge (2 ft from the mid-slab location), the exact opposite trend is noted in Figure H.16. At the top of the slab, the probability distribution for stresses is magnified by the inclusion of a -30 °F EBITD value in this example. This inclusion of EBITD intensifies the tensile stresses at this location significantly, thereby causing significant fatigue damage using RadiCAL or any other fatigue analysis program.

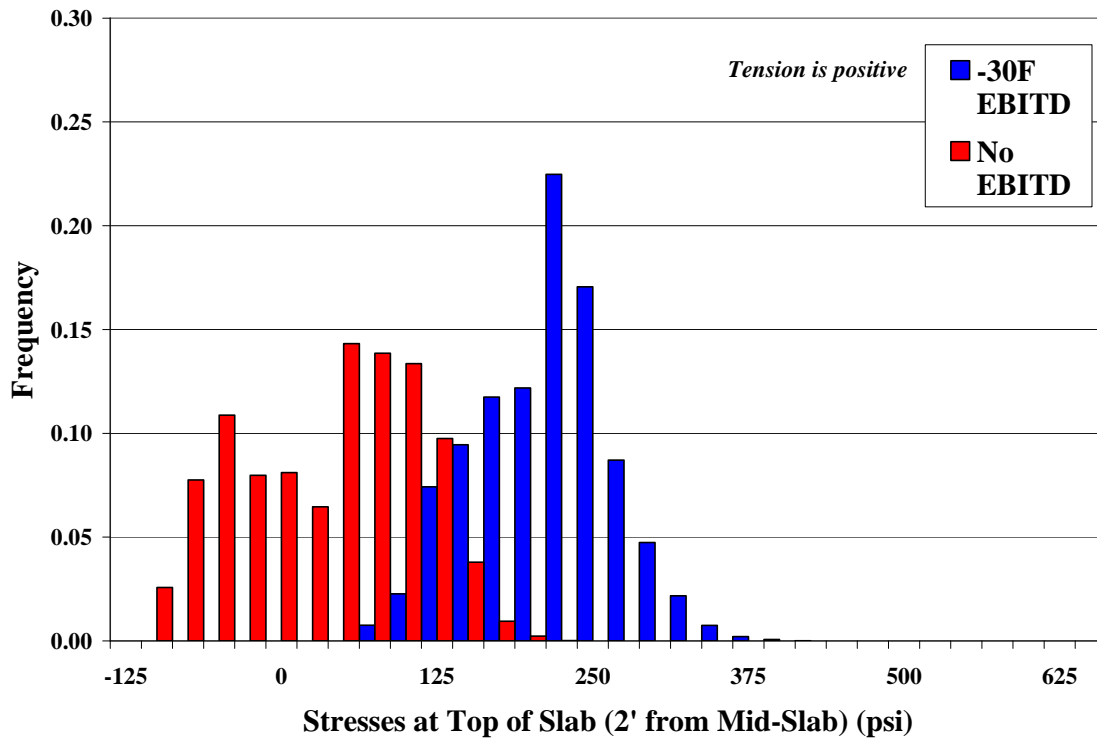


Figure H.16. Probabilities of stresses occurring at top of slab (2 ft from mid-slab) for different EBITD values.

It is these maximum stresses (and their associated stress ratios) that control fatigue life most directly, and are what largely need to be accounted for in design as the majority of loads produce stresses in the pavement that are deemed insignificant. It is important to note that these probability distributions were created using only high load levels (>10,500 lb for single axles, >26,000 lb for tandem axles) and already exclude the vast majority of traffic that highway pavements would experience.

## H2. CONCLUSIONS ON DESIGN METHODOLOGY COMPARISON

Several trends were noticed in terms of minimum design thickness when comparing the MEPDG, IDOT, and RadiCAL design methods. For Illinois sites, the Chicago Midway location was found to have a thinner required thickness using both the MEPDG and RadiCAL design methods, in comparison with all other locations in Illinois. Due to the tempering effects of Lake Michigan on air temperature and subsequent temperature profiles in the pavement slabs, this effect was not noticed at the Chicago DuPage location roughly 25 miles away from Midway and 30 miles from Lake Michigan.

The MEPDG and IDOT methods were found to have opposite effects in terms of the impact of subgrade support on required design thickness for the cases analyzed. The MEPDG requires thicker sections with stiffer subgrades, as the level of curling is exacerbated by this and less support is available, as with softer subgrades.

The MEPDG was found to be very sensitive to joint spacing in terms of thickness design in comparison with RadiCAL using the same fatigue, cracking, and reliability functions. This extreme sensitivity is also exacerbated by parameters that affect curling stresses, such as the coefficient of thermal expansion or surface layer absorptivity.

Using the MEPDG for design at a built-in curl level of  $-10^{\circ}\text{F}$  with 15-ft joint spacing and an AC shoulder, the failure mechanism for fatigue cracking tends to change from bottom-up transverse cracking to top-down transverse cracking as thickness increases to 9.5 in. This trend is not necessarily observed using RadiCAL, as the failure mechanism is quite dependent on the fatigue function used, and can become critical for longitudinal or corner cracking as well.

The level of built-in curl significantly affects the required thickness in the MEPDG and RadiCAL methods. While both of these methods flipped from bottom-up to top-down transverse cracking to be critical at a built-in curl level of  $-10^{\circ}\text{F}$ , a slightly different trend of required thickness was noticed using RadiCAL. In RadiCAL cases without built-in curl, the required thickness was larger than that of  $-10^{\circ}\text{F}$ .

In terms of critical cracking locations, the MEPDG, IDOT, and RadiCAL methods tended to match quite well in AC shoulder cases for every fatigue transfer function available in RadiCAL. When tied shoulders were used, the critical damage locations were generally similar, although RadiCAL predicts a variety of secondary fatigue cracking locations at significant damage levels, producing a high potential for either bottom-up or top-down longitudinal cracking. For widened lane cases, RadiCAL generally predicted that the critical damage location remains at the transverse joint, producing longitudinal cracking emanating along the wheelpath. In comparison, both the IDOT and MEPDG predict bottom-up transverse cracking to be critical in these cases. The results from RadiCAL suggest that special attention be paid to widened slab designs using the MEPDG or IDOT methods, as the critical damage location in these methods probably does not protect against these alternative cracking mechanisms.

# APPENDIX I. RAMP REINFORCEMENT FOR JOINTED PLAIN CONCRETE PAVEMENTS

## I1. INTRODUCTION

The primary purpose of reinforcement across longitudinal joints is to prevent lane separation between a PCC shoulder and mainline pavement. This allows for a safe joint between these two slabs and limits water infiltration in the underlying layers as well. An added effect is also to provide stress reduction in the mainline slab through increased load transfer.

Many on- and off-ramps using jointed concrete pavements have exhibited longitudinal cracking in Illinois. While many factors may possibly contribute to this phenomenon, including fatigue, poor saw-cut timing, settlement issues with underlying materials, etc., this technical memo focuses on the restraint levels that typical reinforcement design schemes would provide and their potential to be over-restraining the mainline slab. This over-restraint may possibly limit movement of the mainline and shoulder slabs, thereby resulting in stress build-up and longitudinal cracking development.

## I2. ANALYSIS OF MINIMUM STEEL REQUIRED

Subgrade drag theory is generally used to determine the amount of steel required to hold joints or cracks together as the slab undergoes contraction. In this theory, the minimum steel reinforcement is calculated based on the weight of the concrete, the friction between the PCC and underlying layer, and the allowable stress in the steel (to prevent yielding of the steel). The required steel content provides resistance equal to or greater than the concrete stress generated by subgrade drag. This theory is represented in Equation I-1 below:

$$A_s = \frac{\gamma h L f_a}{2 f_s} \quad (I-1)$$

where:

$A_s$	=	cross-sectional area of steel required to hold joint tight per lineal foot of slab length (in. <sup>2</sup> );
$\gamma$	=	unit weight of concrete (lb/in. <sup>3</sup> ), assumed to be 150 lb/ft <sup>3</sup> ;
$h$	=	slab thickness (in.);
$L$	=	largest uncracked slab length (in.);
$f_a$	=	friction coefficient between PCC slab and base (assumed 1.5);
$f_s$	=	allowable stress in steel, usually 0.75 of yield strength (psi)

It should be noted that the value  $L$  (slab length) used in the subgrade drag theory Equation I-1 represents the distance between the free ends of the slab that can move due to shrinkage contraction or thermal expansion. The frictional coefficient ( $f_a$ ) is also highly dependent on the material compatibility between the PCC slab and the underlying layer, as seen in Figure I.1, as an example for thinner slabs. Since “frictional coefficient” is defined as the ratio between the frictional and normal force, the thickness of the slab should not theoretically affect it. In this analysis, in all cases, the frictional coefficient was assumed to be 1.5, based on the suggested average value from Huang (1993). The number two in the denominator of Equation I-1 is not designed for conservatism, but



assumes that the slab will contract or expand equally in both directions ( $L/2$ ) and restraint is equal on both sides, which may not always be true. This particularly could be the case in jointed concrete pavement ramps, as the vertical curves (up to 5% grade) either approaching or leaving the main road would provide gravitational normal force restraint in one direction, in addition to the frictional subgrade components in both directions.

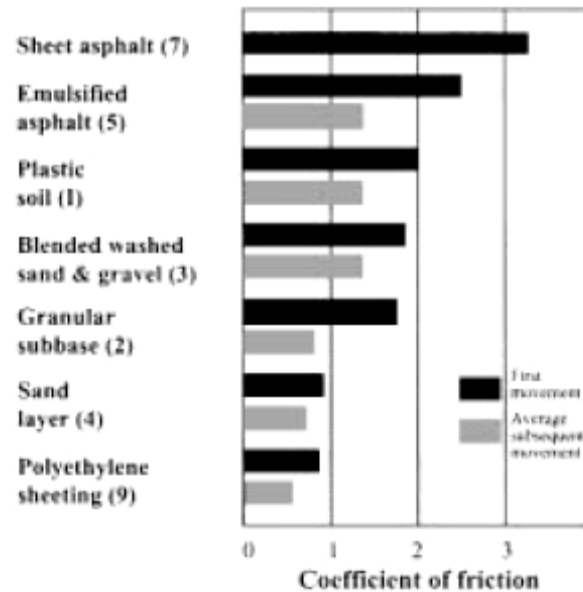


Figure I.1. Variation in values of coefficient of friction ( $f_a$ ) for 5-in. slabs on different bases and subbases for first slip and average friction value (from Post-Tensioning Institute, 1991).

In this analysis of typical steel contents used in shoulder–mainline slab reinforcement in ramps, a typical design of ramps is used, as seen in Figure I.2. This includes a 16-ft mainline PCC pavement slab with 8- and 4-ft PCC slabs tied into this mainline slab. Using different thickness as well as two allowable steel stress limits, the cross-sectional area of steel reinforcement per lineal foot of PCC slab should be limited to the values seen in Table I.2. For 16-ft slabs, 0.0022 in.<sup>2</sup> is required for an 8-in.-thick slab with higher yield strength steel and 0.0058 in.<sup>2</sup> for a 14-in. PCC slab with lower yield strength steel.

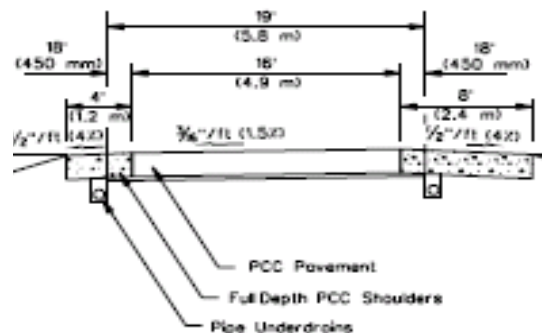


Figure I.2. Typical ramp shoulder and mainline slab design lengths in Illinois.

Table I.1. Minimum Amount of Steel (in.<sup>2</sup>) per Lineal Foot of PCC Slab Length to Hold Joint Tight.

		$f_s=30,000$ psi			$f_s=45,000$ psi		
Spacing (feet)		16	20	28	16	20	28
Slab thickness (inches)	8	0.0033	0.0042	0.0058	0.0022	0.0028	0.0039
	10	0.0042	0.0052	0.0073	0.0028	0.0035	0.0049
	12	0.0050	0.0063	0.0088	0.0033	0.0042	0.0058
	14	0.0058	0.0073	0.0102	0.0039	0.0049	0.0068

By comparison, Table I.2 shows the actual cross-sectional areas of steel for different reinforcement bar sizes and center-to-center spacings between tie bars. Even using #4 tie bars spaced at 36 in. would far exceed the minimum steel required to hold the mainline and shoulder slabs tight using subgrade drag theory.

Table I.2. Area of Steel (in.<sup>2</sup>) per Lineal Foot of PCC Slab Length by Tie Bar Spacing and Nominal Bar Size.

Tie Bar Size		#8	#7	#6	#5	#4
Tie Bar Spacing	12"	0.79	0.60	0.44	0.31	0.20
	18"	0.52	0.40	0.29	0.20	0.13
	24"	0.39	0.30	0.22	0.15	0.10
	30"	0.31	0.24	0.18	0.12	0.08
	36"	0.26	0.20	0.15	0.10	0.07

In a national synthesis of PCC pavement joint design, McGhee (1995) noted that a shoulder tie bar design consisting of 30-in.-long #5 bars spaced at 30 in. was adequate for most moderate to heavily trafficked highways. This area of steel (0.12 in.<sup>2</sup> per lineal foot of PCC slab) would be more than adequate using subgrade drag theory calculations. However, McGhee (1995) also notes that in cases in which a large amount of lane crossing may occur, both close spacing as well as larger diameter tie bars should be considered. With heavy trucks often using ramp shoulders for parking rest areas overnight, this may be a legitimate concern. However, the longitudinal joints should then be dowelled to handle load transfer more effectively instead of relying on tie bars.

### I2.1. District 1 Ramp Reinforcement Alternatives

IDOT District 1 employs a few alternatives to help control random longitudinal cracking in jointed concrete pavement ramps. Typically, the construction of JPCP ramps involves three separate concrete pours, two PCC shoulders (4 and 8 ft) and the 16-ft mainline ramp slab. The shoulders are tied to the mainline slabs with #8 tie bars spaced at 24 in., which are drilled and grouted to provide separation resistance.

One alternative method that has been used is to saw cut the middle of the 16-ft ramp slab and use #6 tie bars at 18-in. spacing on chairs to reduce the subgrade drag by half in the mainline slab. This reduces the randomness of longitudinal cracking by forcing the crack to initiate at the weakened plane of the saw cut.

Another alternative could also be to conduct two concrete pours and one drill and grout operation, as suggested by Tom Matousek of District 1. This could be achieved by

having one pour spaced at 14 ft (outside 6 ft striped as shoulder and the inside 8 ft for half of the driving lane). The next pour would consist of a 12-ft pour with the other 8 ft of the driving lane and striped for a 4-ft striped shoulder. A gravel or asphalt shoulder could then be placed alongside the 4-ft striped shoulder to add safety. This would eliminate the 16-ft slab with two slabs that are slightly smaller and less likely to incur longitudinal cracking. It would also require only one drill and grout operation, reduce the number of tie bars placed, and only two passes of the concrete paver instead of three.

Another possibility, suggested at the Technical Review Panel meeting by Dave Lippert, would be to pour the ramp pavement 24 ft wide and subsequently saw down the middle and stripe the shoulders where they need to be. This would place most of the loaded truck traveling away from the edges of the slab to prevent high bottom-up tensile stresses, while reducing subgrade drag by having a limited uncracked slab width of 12 ft. The shoulder width would also be reduced.

Several other alternatives are to significantly reduce the size of the tie bar, closer to the recommended values shown in Table I.1; i.e., sizes closer to #4 or #5 at 36 in., or use 1-in. dowel bars at 18- to 24-in. spacing to transmit the load across the lane-shoulder joint, which is currently a construction joint.

### **I3. SUMMARY**

According to subgrade drag theory, the amount of steel required to hold the mainline and PCC shoulder together without yielding steel is far exceeded using any combination of standard tie bars at spacings less than 36 in. It is possible that this over-restraint of the slabs could limit any movement and cause internal stresses to develop, which may manifest themselves as longitudinal cracks in jointed concrete pavement ramps.

Some Illinois districts have used alternative designs of ramp reinforcement to prevent these longitudinal cracks from forming, including using saw-cutting the 16-ft ramp slab at 8 ft, or the use of two concrete pours with the longitudinal joint in the center of the ramp's driving lane. IDOT may consider re-evaluating their specifications for tying the shoulders to the mainline ramp. This may include alternative construction procedures such as two concrete pours, or the usage of dowels at the longitudinal construction joint between the ramp and shoulder.

